Laser Doppler Velocimetry Measurements of Particle Velocity Fluctuations in a Concentrated Suspension

by
Nina Claire Shapley

A.B. Physics, Harvard University (1993)

Submitted to the Department of Chemical Engineering in partial fulfillment of
the requirements for the degree of

DOCTOR OF PHILOSOPHY
at the
MASSACHUSETTS INSTITUTE OF TECHNOLOGY
February, 2000

Author...
Department of Chemical Engineering
September 29, 1999

Certified
by...
Robert C. Armstrong
Professor of Chemical Engineering
Thesis Supervisor

Certified
by...
Robert A. Brown
Professor of Chemical Engineering
Thesis Supervisor

Accepted
by...
Robert E. Cohen
Professor of Chemical Engineering
Chairman, Committee for Graduate Students

Laser Doppler Velocimetry Measurements of Particle Velocity Fluctuations in a Concentrated Suspension

by
Nina Claire Shapley

Submitted to the Department of Chemical Engineering on September 29, 1999,
in partial fulfillment of the requirements for the degree of
Doctor of Philosophy in Chemical Engineering

Abstract

Recent statistical constitutive models of suspensions of neutrally buoyant, non-Brownian, non-colloidal, solid spheres in Newtonian fluids suggest that the particles migrate in response to gradients in "suspension temperature," defined as the average kinetic energy contained in the particle velocity fluctuations. These models have not yet been compared systematically with experimental data.

In addition, the "temperature" models assume isotropic particle velocity fluctuations, since the "suspension temperature" is given as a scalar, in analogy to molecular systems. However, highly anisotropic particle velocity fluctuations have been observed in settling suspensions, which suggests that a "suspension temperature" tensor would be more realistic.

We used laser Doppler velocimetry (LDV) to make a set of experimental observations of particle velocity fluctuations arising from inter-particle collisions in a concentrated non-colloidal suspension under nearly homogeneous shear flow in a narrow-gap concentric cylinder Couette device. We compared the relative sizes of the fluctuating velocity components and observed the variation of each component with particle volume fraction, shear rate, and radial position. In addition, we assessed the implications of these observations for suspension temperature models.

The data indicate that the suspension temperature is anisotropic. The flow direction component is overwhelmingly the largest at every concentration and shear rate, followed by the neutral and then the gradient components. Meanwhile, each fluctuating velocity component demonstrates a distinct variation with the shear rate and with the particle volume fraction, but only slight variation with radial position, over the region of the flow accessible to measurement.

Comparison between model predictions and measured shear rate and particle volume fraction profiles shows that several models capture the measured profiles qualitatively but not quantitatively, with better agreement for moderately concentrated suspensions than for highly concentrated suspensions. Also, comparison between predicted scalar suspension temperature profiles and the sum of the measured velocity fluctuation components demonstrates that most of the models underpredict the sum of the temperature components by a large factor. Finally, comparison among the models shows that the models are quite sensitive to the choice of transport coefficients that are functions of the particle volume fraction.

Thesis Supervisor: Robert C. Armstrong
Title: Professor of Chemical Engineering

Thesis Supervisor: Robert A. Brown
Title: Professor of Chemical Engineering

Acknowledgements

I want to express my deep gratitude to so many people for helping me with this project. First, I want to thank my advisors Bob Armstrong and Bob Brown, particularly Bob Armstrong, for his dedication and encouragement throughout the long years when it seemed like nothing was ever working and for always being able to ask the essential question that clarified a confusing situation. My thesis committee, Professors Howard Brenner, Gareth McKinley, and Ken Smith, also contributed valuable input to the project.

None of the experiments in this thesis would have been possible without the help of Peter Morley and Mark of the MIT Central Machine Shop, who expertly advised me on the design of the Couette flow cell and did a wonderful job in building it. The design process was made a lot easier for me thanks to the generosity of Professors Howard Stone (Division of Engineering and Applied Sciences, Harvard University) and Sameer Madanshetty (Mechanical and Aerospace Engineering Department, Boston University) for lending me a Couette cell which became the prototype for the one I designed and which I used for preliminary experiments.

In addition, I want to credit the LDV/suspension colleagues whose expertise in these difficult experimental methods helped me get started on the project: Anubhav Tripathi, Mike Lyon, Anat Shauly, Bir Kapoor, and Gokul Krishnan. Their advice concerning particle procurement, fluid recipes, refractive index matching, and LDV data interpretation was critical in designing almost every aspect of the experiments. Also, their friendliness and willingness to share information (and commiseration!) really impressed me.

I want to thank my fellow members of the Bob & Bob group for an unforgettable grad school experience. Thanks to: Dave, Fred, Gokul, Radha, Garrett, Mark, Indranil, Jason, Tatsuo, Talid, Howard, Zihong, Maria, Tony, Yong, Alice, Todd, Lars, and everyone else I overlapped with, for all the good ideas and fun times. Meanwhile, it was a joy to work with the ChemE support staff, especially Arline, Elaine, Janet, Linda, Emmi, Patsy and Carol. Also, my terrific roommates Ginger and Daniel and my other friends at MIT, in Boston and elsewhere have made my time here very happy.

Two people mentioned here deserve extra special thanks, and they are Professor Gareth McKinley and my former labmate David Lee. Gareth advised me on many of the tricky experimental issues in the project and was a mentor to me throughout grad school (and even before, when I worked in his lab as an undergrad). Dave is a fantastic lab partner and friend, always thinking of good solutions to problems in the lab or in life, and I learned so much from him. My current and former labmates Fred and Gokul also made the lab a pleasant home and gave me tons of moral support.

Finally, I want to give the most thanks of all to my parents and my sister Alice, who are the most wonderful family I could ever have. They even contributed scientifically to this project, and always gave me love and encouragement the whole way through. I could not have gotten to this point without you guys, and my thesis is dedicated to you!

Table of Contents

List of Figures

List of Tables

Chapter 1

Introduction

1.1 Motivation

Suspensions, or fluids with solid particles of comparable density mixed into them, surround us in our daily lives. These mixtures appear in industrial processes for manufacturing such familiar and essential items as concrete, molded plastics, ceramic superconductors, packaging for computer chips, paper pulp, chromatography beds, and chocolate. Sand slurries, a type of suspension, also are used in the oil drilling process. Highly filled suspensions also are used in exotic applications such as solid propellants for rocket engines; solid propellants are also used as the inflation mechanism for emergency air bags in automobiles.

An even larger group of industrially relevant substances is granular materials, such as powders, which alone account for 40% of the total "value added" by the chemical industry in the U.S. (Ennis et al., 1994) Thus, any development in granular flow processing has a large industrial impact. Granular materials are also extremely abrasive to piping systems set up to transport them. A smoother way to transport these materials is to suspend them in liquids which lubricate their contacts with pipe walls and therefore reduce wear on machinery. In this way, suspensions may play a role in granular material processing. Finally, suspensions are critical in biomedical engineering, since the most important biological fluid of all, blood, is clearly a mixture of liquid blood plasma and solid red and white blood cells.

Although people come into frequent contact with suspensions and depend on them to satisfy many needs, the dynamics of these mixtures is poorly understood. Current industrial processes involving flowing suspensions typically operate at rates of 40 to 50% of their designed efficiency. In addition, these flow processes often experience long startup times and frequent problems simply because the flow and stress properties of the materials involved are not known and thus cannot be controlled in order to optimize the efficiency and safety of the processes

(Knowlton et al., 1994). Economic losses, waste, and safety hazards result from this ignorance. In order to improve the processing of particulate materials and suspensions, it is necessary to understand the fluid dynamics of suspensions and be able to predict suspension flows as a function of flow conditions. Although the solid particles in the suspension come in different shapes and sizes, different fluids may exhibit different flow properties, and design parameters may vary widely between processes, there is still some basic physics common to all suspension flows. The goal of fundamental research in suspension fluid mechanics is to elucidate these common features.

From an abstract perspective, the study of suspension flow is a "many-body problem," which involves extracting essential information from a system with such a large number of particles that the system's complete dynamics are too difficult to compute. Although it is possible to know a lot of detailed information about the microscopic properties of the system, such as the trajectory of an individual particle, the quantities which are relevant to a human observer are the averaged, macroscopic properties of the flow. Statistical mechanics and other systematic averaging techniques can be used in order to translate incomplete information about the system into predictions about its large-scale average behavior. The rheological properties which distinguish a suspension from a familiar Newtonian fluid, such as water, arise because a suspension is a complex system of this type, where the microstructure affects the macroscopic properties.

The suspensions of interest in this research are concentrated collections of neutrally buoyant, monodisperse spherical particles in highly viscous Newtonian fluids. These suspensions are model systems in which the hydrodynamic interactions of identical, isotropic particles are isolated. Neutral buoyancy means that the densities of the particles and fluid are equal and thus settling of the particles due to gravity does not occur. Suspensions which are concentrated contain an average solid volume fraction $\phi = 0.4$ or larger, fairly close to the maximum hexagonal close-packing density for monodisperse spheres $\phi_{hcp} = 0.74$ (Phillips et al., 1992; Koh, 1991). Concentrated suspensions are also the type most frequently encountered in industry and biology. In addition, the discussion here is focused on particles that are large enough, with diameters on the order of 100 μm or larger, so that Brownian and colloidal interactions may be neglected. Brownian interactions arise from thermal fluctuations, and colloidal forces from intermolecular attraction. At the same time, the particles are small enough so that inertial effects may be neglected when these particles move in the surrounding viscous fluid phase. This assumption requires that the Reynolds number based on particle size is low.

Since the particles are relatively large and are in close contact, it is assumed that the main interactions experienced by the particles are binary interactions with other particles. A complication, though, is that the fluid squeezed between two particles during an inter-particle interaction affects the dynamics of the interaction. Microscopically, the fluid phase is made up of discrete molecules which collide with the large particles and with each other. However, since the particle length scale is large enough to allow the fluid to be treated as a continuum, the net effect of all collisions involving tiny fluid molecules in the gap between two large particles can be approximated as a lubrication hydrodynamic force on the particles, acting to separate them.

Successful understanding of a suspension requires the development of conservation equations and constitutive relations that describe the average velocities and densities of the fluid and solid phases and their coupling to process conditions. Suspensions of inertialess, neutrally buoyant, monodispersed, non-Brownian and non-colloidal spheres in a Newtonian fluid are the simplest imaginable and the starting point of this and most analyses. Complications caused by particle-particle interactions and by particle shape, which lead to internal degrees of freedom, can be added once a framework exists for the simple isotropic case.

1.2 Particle Migration

Particle migration is a phenomenon that plagues many industrial processes involving flows of concentrated suspensions in which the quality of the product depends on the uniformity of particle distribution in the material. For example, an initially well-mixed suspension flowing in a pipe typically reaches a steady state in which the particles have clustered, or migrated, into the center of the pipe. Such a rearrangement of the particles can be disastrous in a process where a homogeneous mixture is required at the end of the pipe, but often cannot be predicted or prevented due to the current lack of understanding of suspension dynamics. A better understanding of particle migration would have an impact on processing of concrete, ceramics and solid propellants, and transport of powders.

1.3 Experimental Observations of Particle Migration

Experimental observations of particle migration in the laboratory motivate modeling, in order to explain this counterintuitive de-mixing behavior. All these experiments were performed in simple flow geometries on model suspensions of non-colloidal, monodisperse spheres suspended in viscous Newtonian liquids. The shearing flow geometries discussed below include pressure-driven flow in a circular pipe, pressure-driven flow in a rectangular channel, narrow-gap annular Couette flow, and wide-gap annular Couette flow. In each case, the particles were initially uniformly distributed in the flow, but at a later time, when the flow reached a steady state, the particles had rearranged such that the resulting concentration profile was nonuniform.

The first quantitative experiments involving pressure-driven flow of concentrated suspensions through tubes at low Reynolds number were performed by Karnis, Goldsmith, and Mason (1966). These early researchers observed a velocity profile in the flow direction which was "blunted" in the center compared with the parabolic velocity profile obtained for a Newtonian fluid with the same average material properties, such as density and viscosity, and flow rate, resulting in plug flow for a core region of particles near the tube center. A set of velocity profiles measured by Karnis et al. is shown in figure 1.1 which contrasts the velocity profiles of dilute and concentrated suspensions.

These velocity profiles suggest that the particles had drifted into a nonuniform configuration in response to the inhomogeneous shear rate, or velocity gradient, in the flow. Specifically, particles moved away from regions near the tube wall where the local shear rate was high to regions near the tube center where the local shear rate was low. However, in their experiments, Karnis et al. did not observe any of the particle migration they suspected and eventually attributed the blunted velocity profiles they saw to wall effects. It was not until Leighton

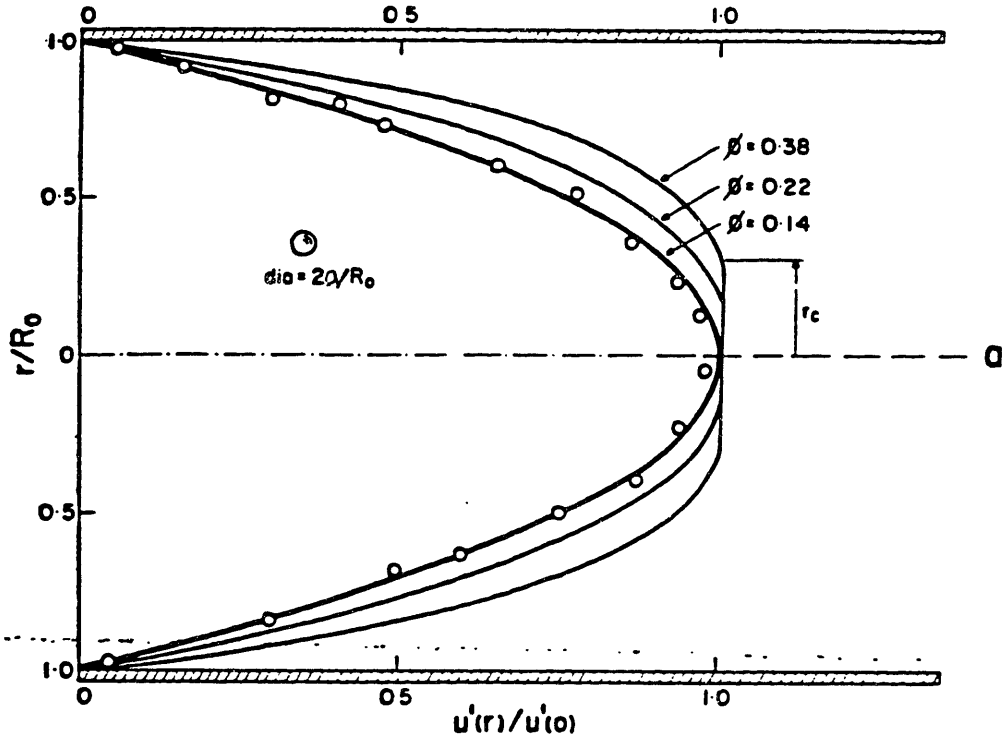

Figure 1.1 Dimensionless steady-state mean suspension velocity profiles measured by Karnis et al. (1966) for three values of particle concentration. The velocity profiles shown become increasingly blunted with increasing particle concentration. Other flow parameters are: the tube radius R_0=0.4 cm, the ratio of tube radius to particle radius R_0 / a = 36, and the volumetric flow rate Q=0.0356 cm^3/s. The solid lines are the best fit through the experimental points. The ϕ = 0.14 (open circles) curve is parabolic, and accordingly indicates the velocity profile for a Newtonian fluid in this geometry.

and Acrivos (1987b) that quantitative evidence supporting the idea of particle migration was presented, and a mechanism for shear-induced particle migration was proposed.

Later, Hampton et al. (1997) used NMR imaging to measure the velocity and concentration profiles of particles for pressure-driven flow in circular pipes. This work yielded direct observation of nonuniform concentration profiles and simultaneous blunted velocity profiles, for bulk particle volume fractions ranging from 0.1 to 0.45. Large peaks in particle concentration were observed at the center of the tube for particle volume fractions 0.2 to 0.45. This evidence, shown in figure 1.2, finally confirmed the idea that particle migration was what Karnis et al. (1966) observed.

Koh, Hookham, and Leal (1994) investigated pressure-driven flow in a rectangular channel by using laser Doppler velocimetry (LDV). These researchers adapted LDV so that they were able to measure concentration as well as velocity profiles, by recording the time between the Doppler scattering signals from individual particles as well as the frequency of the signals, which yielded the velocity. Like Hampton et al., (1997) they observed not only a blunted velocity profile, but also a nonuniform particle concentration profile in the cross-channel direction with a definite peak at the channel center indicating particle aggregation there. For the most concentrated suspensions, with average solid volume fraction of 0.3, the center-line velocities were as small as half the expected values of a Newtonian fluid moving at the same bulk flow rate, and the center-line concentrations were measured to be as large as six times the concentration values near the wall.

Lyon and Leal (1998) extended these LDV measurements of pressure-driven channel flow into the concentrated regime, from bulk particle volume fractions of 0.3 to 0.5. They observed similar particle aggregation at the center line and blunting of the velocity profile, displayed in figure 1.3, and compared their measurements with model predictions for the highly concentrated regime.

In the process of making viscosity measurements in a narrow-gap annular Couette cell, Gadala-Maria and Acrivos (1980) noticed a decrease in the effective viscosity of a concentrated suspension after long shearing times. Leighton and Acrivos (1987b) suggested that the apparent decrease in viscosity is due to the axial migration of particles out of the gap between the two rotating concentric cylinders and into a stagnant region of suspension below the shearing region of

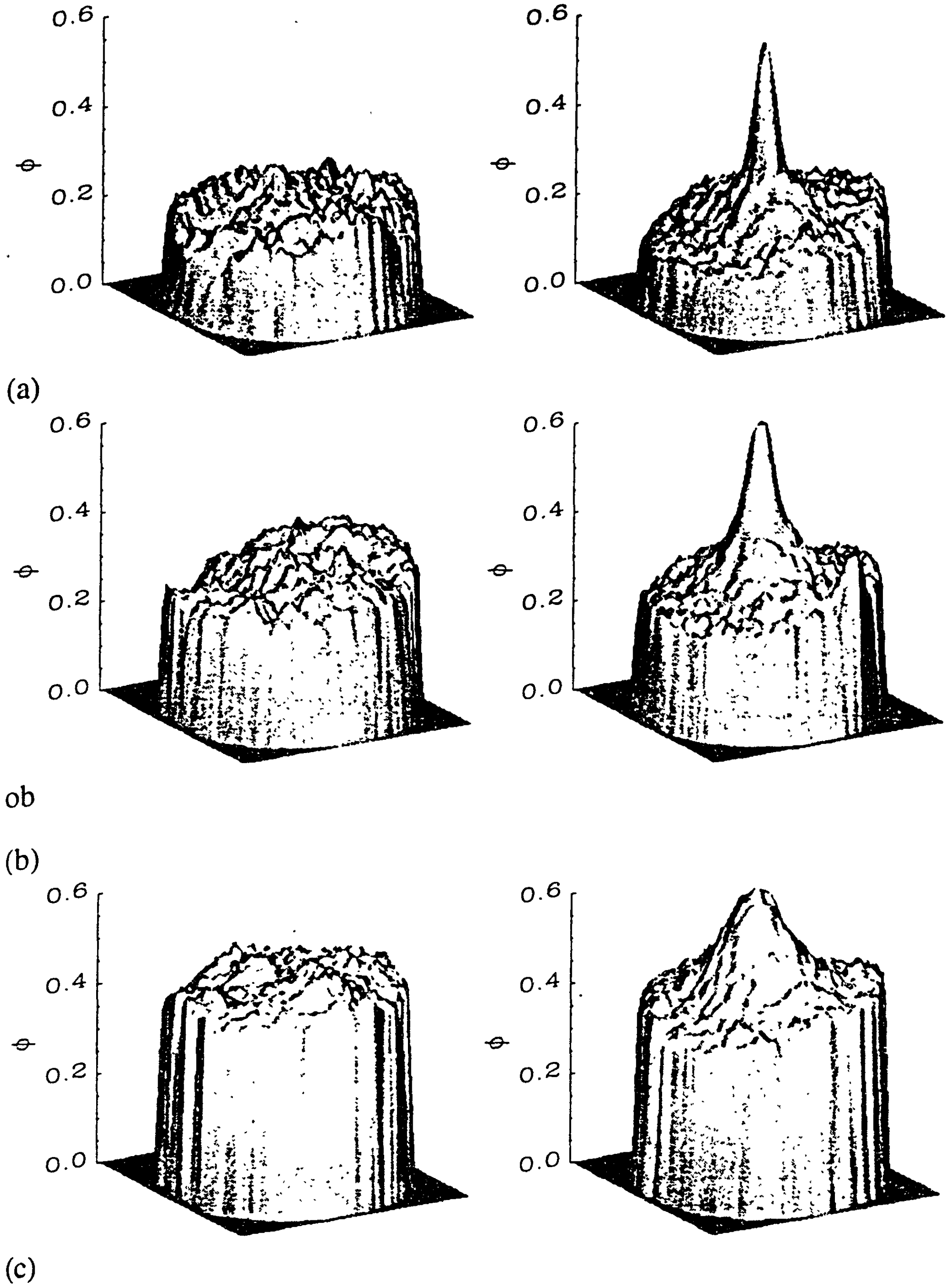

Figure 1.2 NMR images recorded by Hampton et al. (1997) of the particle volume fraction (ϕ) profile for pressure-driven suspension flow in a circular pipe. On the left are the initial profiles and on the right are the fully developed profiles. The pipe radius to particle radius ratio is 39. The bulk particle volume fraction is (a) 0.20, (b) 0.30, and (c) 0.45.

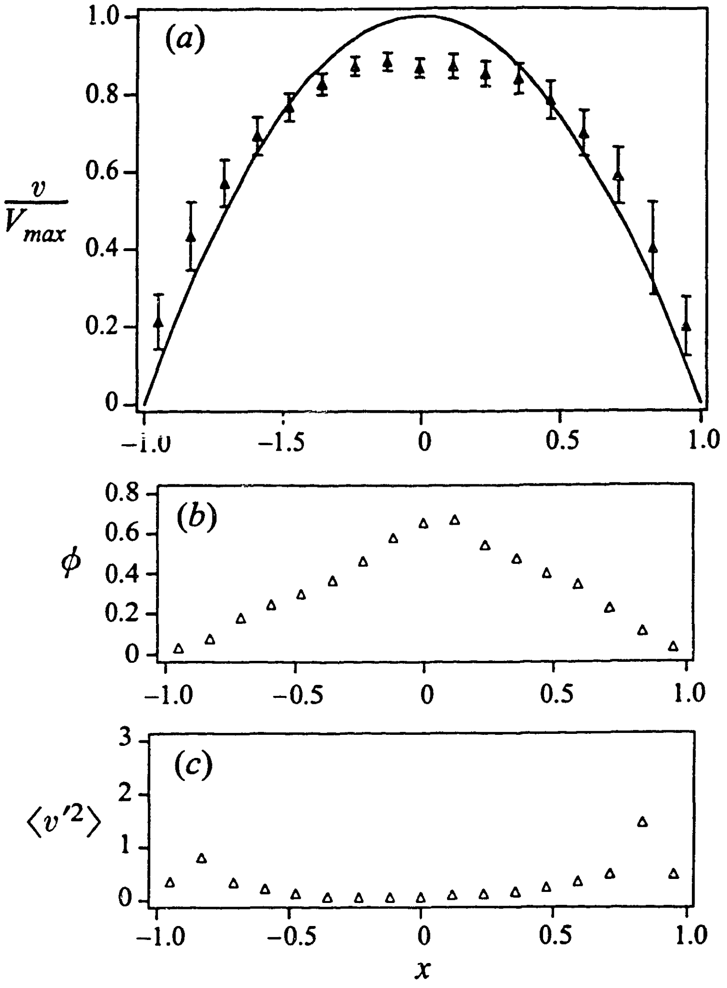

Figure 1.3 Mean velocity (a), particle volume fraction (b), and velocity fluctuation (flow direction) (c) profiles measured by Lyon and Leal (1998) with laser Doppler velocimetry, for a suspension with average particle volume fraction = 0.4, and the channel half width to particle radius ratio = 11. In (a), the mean velocity profile is compared with the mean velocity profile of a Newtonian fluid at the same flow rate.

the apparatus. They proposed a mechanism which explained the existence of particle migration in the direction normal to the shearing direction and also the rate of migration. The mechanism is particle diffusion in response to gradients in shear rate and in particle concentration acting through irreversible interactions between particles. Gradients in shear rate and concentration directly affect the frequency and dynamics of collisions between particles. Leighton and Acrivos used the transient shear flow experiments to measure diffusion coefficients for the particle fluxes.

Leighton and Acrivos developed their model of shear-induced axial particle migration by comparing analytical results with experimental measurements of the torque and shear rate in the Couette cell. Recent NMR experiments by Chow et al. (1994) in this geometry dramatically confirm Leighton and Acrivos' theoretical description. By means of NMR imaging, Chow et al. watch the nonuniform particle concentration profiles develop and show that although the stagnant region at the bottom of the Couette cell begins at the same particle concentration as the bulk suspension, after a prolonged period of shearing, the particles in the stagnant region are so closely packed that solid-like order is induced. Ordered packing allows the particles to reach a higher density than a random packing configuration.

Another striking example of particle migration is seen in wide-gap annular Couette flow. Abbott et al. (1991) used NMR imaging to show that particles in an initially homogeneous 50% solid suspension sheared between two concentric cylinders migrate radially to cluster at the wall of the outer, stationary cylinder. These researchers reported that the particle volume fraction near the outer cylinder wall at steady state reached a value near 0.6, close to 0.63, the maximum random packing fraction for monodisperse spheres. Abbott et al. (1991) also measured the suspension velocity profile and found that the flow in the densely packed region near the outer, stationary cylinder, is almost stagnant. Meanwhile, near the center, the particle concentration decreased by at least 30%. These results indicate that radial migration in the wide-gap annular geometry is a significant effect.

Abbott et al. also showed that migration is irreversible by switching the direction of shearing. In addition, the authors checked for the occurrence of axial migration, but found no significant evidence of it. This result was not inconsistent with the findings of Leighton and Acrivos (1987b), however, because the Couette apparatus Abbott et al. (1991) employed was constructed differently from that of Leighton and Acrivos (1987b), being closed at the bottom end of the shearing region. Another dramatic effect Abbott et al. observed visually and with NMR was the formation of distinct microstructures in both monodisperse and bidisperse suspensions. In both cases, larger spheres formed concentric hexagonal-close-packed circular sheets near the outer wall. A NMR image of this microstructure formation is shown in figure 1.4.

1.4 Direct simulations: Stokesian Dynamics

In principle, the fluid mechanics of a suspension of spherical particles in a Newtonian fluid at low Reynolds number can be exactly described. Here, momentum transport in the fluid surrounding the particles is described by the Stokes flow equations which must be solved subject to the no-slip boundary condition on the surface of each particle. The fluid mechanical problem is a many-body problem for the evolution of the particle positions and velocities as a function of time. These variables are influenced by the fluid through the force balance on each particle.

Stokesian Dynamics (Brady and Bossis, 1988) is the fluid mechanical equivalent of molecular dynamics for solving the averaged behavior of a collection of particles whose motion is described in the manner above. However, in practice, the simulation method is limited in its application because of its large computational cost, due to the long range interactions which result from the Stokes equations, the complexity of close-range binary particle interactions, and the large number of particles needed to properly approximate a real system. Consequently, the description of process flows using Stokesian Dynamics is impractical. As in other areas of non-Newtonian fluid mechanics (Bird et al., 1987), constitutive equations and conservation laws are needed that describe the average properties of the fluid during flow: this is the domain of constitutive modeling.

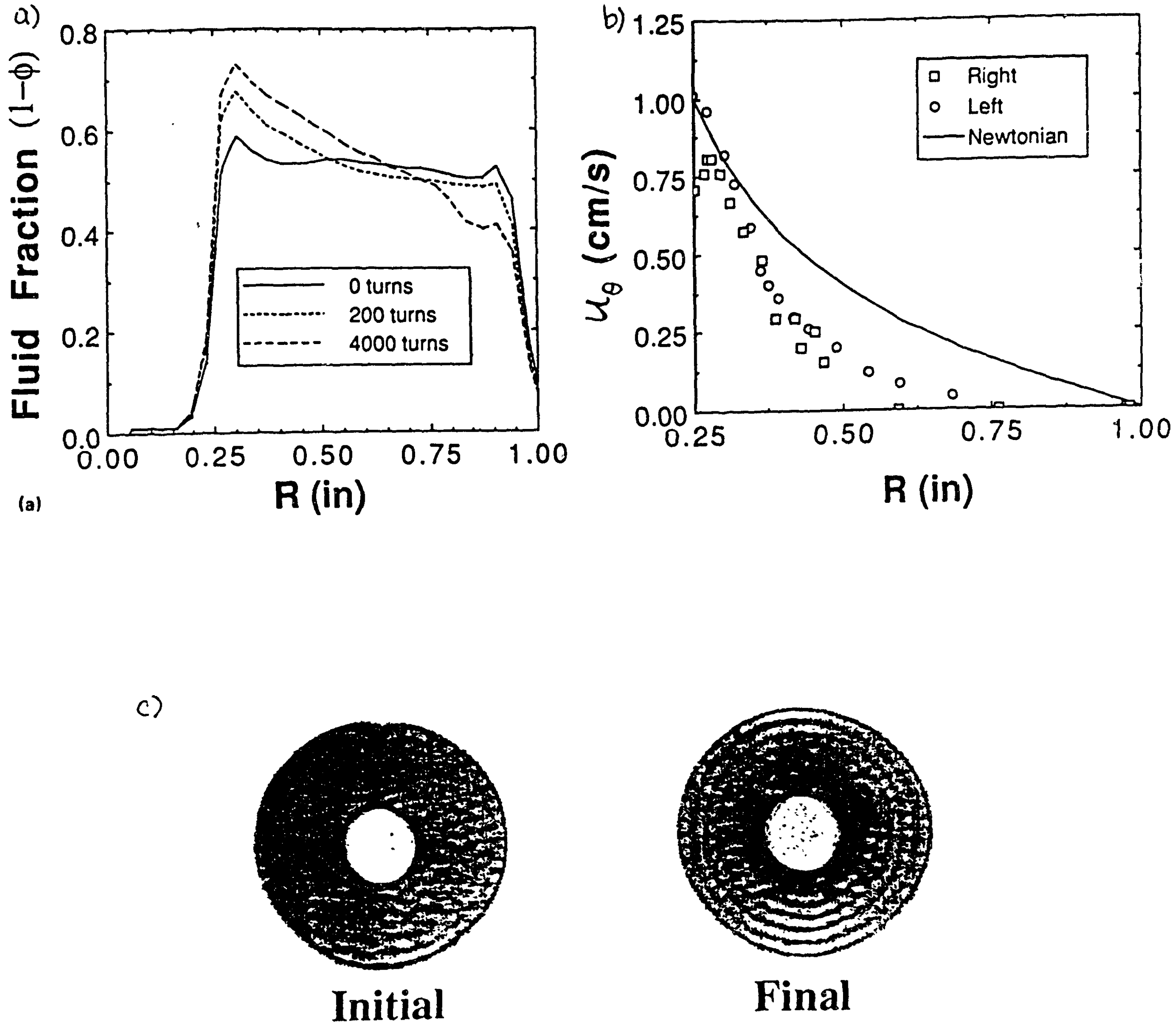

Figure 1.4 NMR imaging of wide-gap Couette flow by Abbott et al. (1991) for a 50% concentrated suspension of 675 μm diameter spheres.
(a) Evolution of particle volume fraction profile from initially uniform to nonuniform at steady state.
(b) Steady state velocity profile compared with that for a Newtonian fluid.
(c) NMR image of microstructure. The image on the left represents the initially well-dispersed state of the suspension. The image on the right was taken after rotating the inner cylinder until steady-state was achieved (4000 revolutions). The dark area near the inner cylinder represents a higher fluid fraction, indicating that the particles have migrated away from this region of higher shear rate. The shear-induced structure is easily seen in the steady-state image.

1.5 Constitutive Models

Currently, two major classes of models for particle migration in concentrated suspensions exist. The first type consists of phenomenological models, such as those of Leighton and Acrivos (1987) and Phillips et al. (1992). In these models, particle migration is driven by gradients in shear rate. The second type is granular flow-based models, such as those of McTigue and Jenkins (1992) and Nott and Brady (1994). In these models, migration is driven by gradients in "suspension temperature," defined as the average kinetic energy of particle velocity fluctuations due to inter-particle collisions.

The phenomenological models were developed to describe particle migration in inhomogeneous shear flow. The local shear rate, which plays a central role in these models, has proven difficult to generalize for other kinematics. We are focusing on "temperature" models because we think they are promising for studying complex flows, where both shearing and elongation are present. In these flows, the question of how to define the "shear rate" challenges the phenomenological models, but the "temperature" models may be able to avoid this problem by not defining the suspension temperature explicitly in terms of any deformation rate quantity.

The concept of granular "temperature" in particulate systems was introduced by Ogawa (1978), in analogy to the thermal vibration of molecules in a gas. An individual particle's velocity can be written as the sum of mean and fluctuating parts,

$$\underline{v} = \underset{\text{mean}}{\langle \underline{v} \rangle} + \underset{\text{fluctuating}}{\underline{v}'} \tag{1.1}$$

where the angle brackets represent an ensemble average. The ensemble average of a quantity is defined as the average over a large number of simultaneous realizations of the same system. In a system for which the driving conditions do not change in time, which we assume follows the ergodic hypothesis, the ensemble average is equivalent to a time average, computed on a time interval long compared to the rate of fluctuations, but short compared to any macroscopic variation in the system.

Then, the "temperature" is given specifically as

$$T \equiv \langle \underline{v}' \cdot \underline{v}' \rangle \tag{1.2}$$

The models express the temperature in this scalar form, which is isotropic, in analogy to molecular systems. A more general form for the suspension temperature would be a tensor,

$$\mathbf{T} \equiv \langle \underline{v}' \, \underline{v}' \rangle \tag{1.3}$$

which would allow for anisotropic velocity fluctuations. Although the kinetic energy of particle velocity fluctuations due to inter-particle collisions is presented as a particle migration mechanism in the McTigue and Jenkins and Nott and Brady models, a complete set of measurements of the properties of the these velocity fluctuations in a simple, homogeneous flow does not exist, but is necessary to ensure that the models incorporate a realistic migration mechanism.

1.6 Thesis Goals

The objectives of this thesis are twofold. The first goal is to assemble a set of physical observations of particle velocity fluctuations arising from inter-particle collisions for a concentrated suspension in homogeneous shear flow. The second aim is to assess the implications these observations have on suspension models. We focus our measurements on several properties, including the relative sizes of the collisional velocity fluctuation components, the dependence of the fluctuation components on particle volume fraction, the dependence of the fluctuation components on shear rate, and the variation of the fluctuation components with position.

The suspension temperature models contain the assumption that the suspension temperature is isotropic, even though anisotropic velocity fluctuations have been observed in suspension settling (Nicolai et al., 1995). Our goal is to measure all three fluctuating velocity components at constant shear rate and particle concentration, to determine whether the temperature is anisotropic.

Also, the models involve a particular assumed scaling of the suspension temperature with shear rate and particle volume fraction. Specifically, all the models considered here scale the collisional particle velocity fluctuations with the shear rate squared. Each model utilizes a different scaling for the suspension temperature with particle volume fraction. In this work, we measure the dependence of each temperature component with shear rate and particle volume fraction.

Finally, the suspension temperature models predict the variation of the suspension temperature with position in an inhomogeneous flow. Our goal is to measure the fluctuating velocity components as functions of position and compare the results to the models' predictions. Since the models only predict the behavior of the sum of the temperature components, we will add the observed temperature components and compare the sum to the models' predictions.

Our approach is to measure these properties in homogeneous shear flow to eliminate particle migration effects. We have chosen laser Doppler velocimetry (LDV) as the measurement method due to its fine spatial and temporal resolution, which is necessary for observation of fluctuations.

Chapter 2

Literature Review

This chapter contains a summary of observed properties of concentrated suspensions, principal methods of modeling concentrated suspensions, and major experimental techniques applied to these systems. The discussion at the end of the chapter places this study in context.

2.1 Bulk Rheological Properties of a Concentrated Suspension of Monodisperse Spheres

A homogeneous and monodisperse suspension of non-colloidal spheres in a viscous Newtonian liquid has several well-known macroscopic rheological properties: a viscosity that varies with bulk particle concentration, normal stress differences in steady shear flow that are linear in shear rate and also vary with bulk particle concentration, viscoelasticity, and apparent slip along solid surfaces.

Ever since Einstein's landmark publication (1906), researchers have tried to relate the viscosity of a suspension to the viscosity of the suspending liquid and the particle concentration. For suspensions of spheres, all models and measurements have reduced to the idea that the viscosity of the suspension is independent of shear rate and is enhanced over the viscosity of the suspending liquid by a factor that increases with particle volume fraction. (Frankel and Acrivos, 1967; Batchelor, 1970) The classic work of Krieger (1972) contains the standard empirical observations of the relative viscosity of concentrated suspensions. In this work, Krieger found that the suspension viscosity was not shear rate-dependent; the viscosity enhancement factor, or "relative viscosity," increased with particle volume fraction as

$$\eta(\phi) = \eta\left(1 - \frac{\phi}{\phi_{max}}\right)^{-2.5\,\phi_{max}} \tag{2.1}$$

where ϕ_{max} is the particle volume fraction at which the suspension viscosity becomes infinite.

Gadala-Maria (1979) measured nonzero normal stress differences in concentrated suspensions by using parallel-plate rheometry. Gadala-Maria found that the difference between the normal stress differences (N_1 - N_2) was positive and scaled approximately linearly with the shear rate in steady shear flow. The difference (N_1 - N_2) also increased with particle volume fraction, at fixed shear rate, for particle volume fractions of 30% to 50%, but Gadala-Maria did not quantify the dependence. Gadala-Maria's results concurred with those of Bagnold (1954), an early and innovative suspension experimentalist, who measured a gradient direction normal stress that scaled linearly with the shear rate in steady shear flow of viscous suspensions. Bagnold (1954), Leighton (1993) and Phan-Thien (1995) attributed the existence of normal stress differences to anisotropic local microstructure.

The constitutive model of Phan-Thien (1995) allows the average local suspension microstructure to be anisotropic and contains an expression for the stress tensor in terms of the average microstructure. In addition, the evolution of the average microstructure is coupled to the flow kinematics. Although this model assumes the suspension is homogeneous and does not account for particle migration, it predicts nonzero normal stress differences, in agreement with observations. Furthermore, the model is able to approximate qualitatively the experimental results of Gadala-Maria (1979) in steady shear flow, in that the difference between the predicted normal stress differences (N_1 - N_2) is positive, scales approximately linearly with the shear rate, and increases with particle volume fraction.

Viscoelastic behavior of a non-colloidal suspension was observed by Rigord et al. (1996) for 20% to 40% particle volume fraction suspensions in an oscillating pressure-driven flow through capillary tubes. The authors found thinning with increasing oscillation frequency in the viscous part of the complex viscosity, first appearing at 20% particle volume fraction and becoming quite noticeable at 40% particle volume fraction. Gondret et al. (1996) found similar thinning of the viscous response in 35% to 55% particle volume fraction suspensions sheared in parallel plate and cone and plate rheometers. In addition, Rigord et al. found that the 40% concentrated suspension had a nonzero storage modulus, indicating viscoelastic behavior, but they did not quantify the dependence of the storage modulus on particle volume fraction.

These data agree with the simulation results of Toivakka et al. (1995) for a rectangular monolayer sheared between planes, where the storage modulus was found to be larger than the loss modulus at moderate oscillation frequencies and small strains. Toivakka et al. claim that the cause of this viscoelastic behavior is energy storage in the suspension microstructure as the suspension is compressed and then decompressed, due to the imposed "hard sphere" repulsive force between any two particles at contact.

Energy storage in the suspension microstructure is a reasonable concept for small strains (strain < 1 unit), since energy could be stored in the compression of lubrication layers of fluid between neighboring particles. However, once particles in the suspension collide and pass each other in the flow, the stored energy is released and the suspension acts as a purely viscous material for further shearing in the same direction. If the direction of shearing is reversed, the suspension stores energy again at small strains until particle collisions mix the microstructure in the new direction. (Gadala-Maria and Acrivos, 1980). Hence, it is not surprising that viscoelasticity is observed in small-amplitude oscillatory shear flows and start-up of steady shear flows.

Apparent wall slip, defined as a relative velocity between the wall of a flow and the flowing material at the wall, is a phenomenon frequently observed in flowing suspensions of non-colloidal particles. The usual explanation for apparent wall slip is that spherical particles cannot pack as efficiently by a solid surface as in the bulk, and accordingly a lower effective particle volume fraction exists near the surface, which leads to a low resistance layer near the surface (Yilmazer and Kalyon, 1989; Jana et al., 1995). Wall slip is an observable phenomenon in standard rheometry and typically causes unexpectedly low viscosity readings and viscosity readings that are extremely sensitive to the roughness of the solid shearing surfaces. Kalyon and co-workers have used parallel plate and capillary rheometry to study wall slip extensively in highly loaded suspensions of many types. Yilmazer and Kalyon (1989) found that the apparent slip velocity in parallel plate and capillary rheometer flows was proportional to the wall shear stress. They were able to extract the apparent slip velocity by varying the gap widths and capillary diameters in the two rheometers.

Yoshimura and Prud'homme (1988) also used similar rheometry methods of studying wall slip. Aral and Kalyon (1994) used a flow visualization technique to observe wall slip, and showed that varying the roughness of the parallel plate surfaces alone could cause slip, no slip, or sample fracture.

Jana et al. (1995) applied laser Doppler velocimetry, a pointwise measurement method with fine spatial and temporal resolution, to the problem of apparent wall slip in Couette flow between rotating concentric cylinders. The authors measured the suspension velocity profile across the gap between the cylinders and extracted slip coefficients from the data by using the diffusive flux model to estimate the concentration profile and assuming a Navier slip law at the inner and outer cylinder walls. Jana et al. found that the slip coefficients scale with particle volume fraction as the relative viscosity function divided by 8.

An often-debated issue regarding apparent wall slip is whether the slipping occurs between the particles and the wall, or between neighboring layers of particles near the wall. Krishnan (1994) observed both phenomena occurring in a 50% concentrated suspension in rectilinear shear flow by video image analysis, another technique with high spatial resolution. According to Krishnan, the first particle layer adjacent to the wall was packed more efficiently than in the bulk, and the majority of the slipping took place between the first and second particle layers adjacent to the wall. These results challenge the traditional view of apparent wall slip and indicate that it is a more complex phenomenon than previously thought.

2.2 Fine Scale Effects in a Concentrated Suspension of Monodisperse Spheres

Since a concentrated suspension is characterized by a microstructure, meaning the instantaneous positions and velocities of all the particles, there are also fine scale properties of this microstructure that are not apparent from making macroscopic rheological measurements. Among the fine scale properties that have been quantified are the self-diffusivity of particles and the pair distribution function. Video imaging is the standard method used for visualizing and characterizing the microstructure.

The self-diffusivity relates to the random displacements a particle experiences about its mean motion in a homogeneous flow due to interactions with its neighbors. Although the displacements have a mean of zero, they have a nonzero variance. The self-diffusivity is defined as the amount of displacement (variance) experienced during a typical flow time scale.

Eckstein et al. (1977) and Leighton and Acrivos (1987a) measured the self-diffusivity in narrow-gap Couette flow and found that it scales with the product of the average shear rate and the square of the particle radius, as expected from dimensional analysis. Comparison of these studies with the more recent work of Phan and Leighton (1993) and Breedveld et al. (1999) reveals agreement among the experimental studies except for Eckstein et al. (1977) on the variation of the self-diffusion coefficient with particle volume fraction. The most recent work, Breedveld et al. (1999), indicates that the self-diffusivity in steady, narrow-gap Couette flow is anisotropic, since the component in the gradient direction is larger than that in the neutral direction. This result is supported by the simulation results of Phung (1996) and the theoretical work of Morris and Brady (1996). Also, Breedveld et al. (1999) found that neither of these self-diffusion components increases monotonically with particle volume fraction. Both components peak around 40% particle volume fraction and either decrease or plateau at higher concentrations.

In addition, Parsi and Gadala-Maria (1987) and Leighton and Rampall (1993) found that the pair orientation distribution function in concentrated suspensions is anisotropic in steady, rectilinear shear flow, namely that it is enhanced in the compression direction of the flow and reduced in the extension direction. The two groups studied suspensions with particle volume fractions of 40% and 45%, respectively. The pair distribution function is the key to understanding many of the macroscopic properties described above, because it weights the likelihood of each particle pair configuration when the averaged properties are calculated. An orientation pair distribution function enhanced in the compression direction of shear flow and reduced in the extension direction was suggested by Bagnold (1954), according to the reasoning that particles tend to slow down as they collide, and the mean shearing motion tends to cause collisions along the flow compression direction. As a result, on average, particle pairs statistically spend more time aligned in the flow compression direction.

The properties mentioned above which were observed in homogeneous suspensions also affect how an inhomogeneous suspension behaves. Any accurate particle migration model must contain these properties, or at least reduce to the observed homogeneous case in the absence of migration.

2.3 Direct simulations: Stokesian Dynamics and Related Methods

As mentioned in Chapter 1, Stokesian Dynamics (Brady and Bossis, 1988) is the fluid mechanical equivalent of molecular dynamics for solving the averaged behavior of a collection of particles whose motion is described in the manner above. Stokesian Dynamics simulations are especially useful in predicting the macroscopic consequences of microscopic effects, in visualizing the predicted suspension microstructure and separating the contributions of multiple effects, such as hydrodynamic and Brownian forces, to the total stress, as in the work of Phung (1996).

However, due to the long range interactions which result from the Stokes equations, Stokesian Dynamics simulations become unwieldy for even moderate numbers of particles in a periodic domain. This leads to the use of unrealistic geometries and too few particles in the simulations. Nott and Brady (1994) found that for 50 particles in a periodic cell, three-dimensional simulations were too computationally expensive to perform, and consequently restricted the motions of the simulated particles to a monolayer of two-dimensional disks. Phung (1996) extended Stokesian Dynamics to three dimensions for Brownian suspensions, but still used a small number of particles in the periodic cell (between 27 and 81 for a three-dimensional periodic cell), and did not reach a high enough ratio of viscous, hydrodynamic forces to Brownian effects to be able to compare the results with the experiments described above.

More recent simulation studies have utilized systems with larger numbers of particles by neglecting far-field hydrodynamic interactions and focusing on pairwise lubrication interactions. According to Silbert, Melrose and Ball (1999), at least 50 particles are needed to eliminate system size effects in a 3-D simulation. The authors use 200 or 700 particles in their recent simulations, almost a factor of 10 larger than the number Phung used. Ball and Melrose (1995) were able to study a three-dimensional, concentrated system of 3500 particles by eliminating all but the dominant binary squeeze flow interactions. Although this system size is much more realistic than the original cells of 27 or 50 particles, even so, the system is only nine particle diameters wide, significantly smaller than the 16 particle diameters width at which Hampton et al. (1997) experimentally observed finite size particle effects in circular tube flow. In simulations of suspensions with more complex particle interactions, such as colloidal suspensions (Dratler et al., 1997; Bilodeau and Bousfield, 1998), or suspensions of rough, non-colloidal particles (Haan and Steif, 1998), it is still standard practice to approximate the suspension as a monolayer in order to reduce computation load. Overall, the large number of particles needed to approximate a real system creates a heavy computational burden, especially for a three-dimensional simulation.

Ball and Melrose (1995) found, like Nott and Brady (1994) and Phung (1996), that the binary lubrication interactions between the particles are singular and very sensitive to the contact conditions between particles. Purely hydrodynamically interacting particles stick together and form clusters, but particles which experience a slight repulsive force when they collide do not cluster. It is not clear which version of the contact conditions provides a more accurate picture of real particle interactions, but the simulation results are very sensitive to the chosen conditions. In simulating the limit of a purely hydrodynamically interacting suspension, the particles form a cluster that spans the entire system and the simulations do not reach a steady state. It is this singularity which prevents the simulations from reaching farther into the hydrodynamic regime, to allow comparison with the experiments discussed earlier.

Although Stokesian Dynamics and related simulation methods provide information about microstructure and the macroscopic consequences of microscopic effects, the description of process flows using these simulations is impractical. As in other areas of non-Newtonian fluid mechanics (Bird et al., 1987), constitutive equations and conservation laws are needed that describe the average properties of the fluid during flow: this is the domain of constitutive modeling.

2.4 Constitutive Modeling

As mentioned in Chapter 1, the two main types of constitutive models for particle migration in concentrated suspensions are phenomenological models, such as that of Leighton and Acrivos (1987b) and Phillips et al. (1992), and granular flow-based models, such as those of McTigue and Jenkins (1992) and Nott and Brady (1994). A more detailed presentation of the models is given here.

2.4.1 Diffusive Flux Model

Concepts of the diffusive flux model of Leighton and Acrivos (1987b) are outlined below, followed by presentation of the equations of the model of Phillips et al. (1992). A comparison of the model with experimental data is then given.

2.4.1.1 Rationale for Diffusive Fluxes

First we discuss the phenomenological explanation by Leighton and Acrivos (1987b) of shear-induced particle migration, that is, formation of non-uniform particle concentration profiles in response to non-uniform shear rates in a flow. We then present the constitutive equation of Phillips et al. (1992), which places Leighton and Acrivos' explanation in a model for suspension flow. These models treat a suspension as a collection of discrete particles moving in an incompressible continuum fluid and contain no information about interactions between the particles and the fluid, since in the highly concentrated regime under consideration the only significant interactions in the material are assumed to be binary particle interactions. Leighton and Acrivos propose a mechanism for particle migration in a shear flow, representing migration as a balance between competing particle fluxes that arise in response to gradients in macroscopic quantities in the flow system.

According to Leighton and Acrivos, diffusive particle fluxes arise in shear flows in response to gradients in inter-particle collision frequency and to gradients in viscosity within the flow system. These fluxes appear because the gradients in collision frequency and gradients in viscosity cause any two particles to respond asymmetrically to a binary collision. The particle on the side with higher collision frequency or higher viscosity is hindered in recoil from the collision since it tends to interact with more particles or experience more drag from the surrounding continuum compared to the other particle. Therefore, the resultant of the final velocities of the two particles shows a net drift in the direction of lower collision frequency or higher viscosity. (Leighton and Acrivos, 1987b)

Whereas collision frequency is a function of shear rate, a measure of the relative velocity of particles on neighboring shearing surfaces, and particle concentration, viscosity depends on particle concentration only. As a result, gradients in particle concentration and shear rate drive particle diffusion, often in opposite directions, so that a steady state is reached when the collisional and viscosity driven fluxes balance.

Leighton and Acrivos derive the scaling for the particle flux in response to a gradient in suspension viscosity, since they expect this flux to dominate their experimental results. Previous experimental results of Leighton and Acrivos (1987a) show that the diffusion coefficient for shear-induced migration is proportional to the product of the shear rate and the particle radius squared. The researchers relate this result to the dynamics of particle interactions in a unidirectional shear flow by estimating that for each collision a diffusing particle moves a characteristic distance normal to the flow direction of a, the particle radius. Furthermore, the frequency of binary interactions a test particle experiences scales as the product of the local shear rate and the local particle concentration, since the particle concentration represents the probability of encountering a single particle and the local shear rate indicates the relative velocity per unit separation between neighboring shearing surfaces. They further estimate that the number of particles is proportional to the local particle concentration and that the fractional change in viscosity over the interaction length scale, the particle radius a, is roughly given by the product of the particle radius a and the local viscosity gradient, divided by the magnitude of the local viscosity. These scaling arguments result in the following form for the flux of particles due to a gradient in suspension viscosity in the flow:

$$\underline{N}_\eta = -K_\eta \dot{\gamma} \phi^2 \frac{a^2}{\eta} \underline{\nabla} \eta \qquad (2.2)$$

Since the viscosity is a function of particle concentration only, its gradient can be expanded as the product of the derivative of the viscosity with respect to particle concentration and the particle concentration gradient.

2.4.1.2 Equations of the Model of Phillips et al. (1992)

The Phillips model (Phillips et al., 1992) incorporates the ideas of Leighton and Acrivos regarding the mechanism for shear-induced particle migration into a simple model for suspension flow and shear-induced migration. The model for a suspension of spheres in an incompressible Newtonian fluid consists of a mass conservation equation for the mean suspension, which is treated as an incompressible continuum,

$$\underline{\nabla} \cdot \underline{u} = 0 \qquad (2.3)$$

the momentum equation, in which inertial terms are neglected,

$$\underline{0} = -\underline{\nabla} p + \underline{\nabla} \cdot \boldsymbol{\tau} \qquad (2.4)$$

and a Newtonian constitutive equation

$$\boldsymbol{\tau} = \eta_f \eta_s(\phi)\, \dot{\boldsymbol{\gamma}} \qquad (2.5)$$

In the stress tensor equation, the suspension viscosity $\eta_f \eta_s(\phi)$ is a function empirically obtained by Krieger (1972) of fluid phase viscosity and particle concentration, which equals the fluid phase viscosity in the limit of infinite dilution and becomes infinite near the limit of maximum hexagonal close-packing, at $\phi_m = 0.68$.

$$\eta_s(\phi) = \left(1 - \frac{\phi}{\phi_m}\right)^{-1.82} \qquad (2.6)$$

The mean total pressure in the suspension is p, the mean suspension continuum velocity is $\underline{u}$, and $\dot{\boldsymbol{\gamma}}$ is the mean suspension rate-of-strain tensor. The only nonzero components of the rate-of-strain tensor for steady, fully-developed, unidirectional shear flow ($u_1 = u_1(x_2)$; $u_2 = u_3 = 0$) describe the gradient in mean suspension velocity perpendicular to the flow direction:

$$\dot{\gamma}_{12} = \dot{\gamma}_{21} = \frac{\partial u_1}{\partial x_2} \qquad (2.7)$$

The equations (2.3-2.6) of the model are solved for three unknown variables, $\underline{u}$, p, and ϕ. As a result, the model requires an additional equation, a diffusion equation for the particle concentration:

$$\frac{D\phi}{Dt} = a^2 K_c \underline{\nabla} \cdot \left(\phi^2 \underline{\nabla} \gamma + \phi \gamma \underline{\nabla} \phi\right) + a^2 K_\eta \underline{\nabla} \cdot \left(\dot{\gamma} \phi^2 \frac{1}{\eta} \frac{d\eta}{d\phi} \underline{\nabla} \phi\right) . \qquad (2.8)$$

Equation (2.8) states that the rate of change of particle concentration seen by an observer moving with the mean suspension flow is due to the diffusion of particles in response to gradients in two quantities. The second term on the right side of the equation is the Leighton and Acrivos (1987b) expression for the particle flux in response to viscosity gradients, whereas the first term on the right side represents the particle flux in response to gradients in inter-particle collision frequency. Phillips et al. (1992) derive the scaling of the first term by using the approach of Leighton and Acrivos (1987b).

In a unidirectional shear flow, Phillips et al. (1992) estimate that the frequency of binary collisions a test particle experiences scales as the product of the local shear rate and the local particle concentration, since the particle concentration represents the probability of encountering a single particle and the local shear rate indicates the relative velocity per unit separation between neighboring shearing surfaces. Hence, the change in collision frequency over the collision length scale of the particle radius, *a*, is approximated by $\left[a \underline{\nabla}(\phi \dot{\gamma})\right]$. They also estimate that the number of particles is proportional to the local particle concentration, and that a diffusing particle moves a characteristic distance normal to the flow direction of *a*, the particle radius, as the result of a collision. The expression for the particle flux in response to gradients in inter-particle collision frequency is the product of all these factors and is given by

$$\underline{N}_c = -K_c a^2 \phi \; \underline{\nabla}(\phi \dot{\gamma}) \qquad (2.9)$$

The two coefficients K_c and K_η arising in equations (2.2) and (2.9) are proportionality constants of order unity which Phillips et al. (1992) find by matching the analytical predictions of the model with experimental measurements of particle concentration profiles from steady state and transient shear flows. Since the scaling of the flux terms is intended to account for all the dimensional and concentration dependence of the terms, the phenomenological constants are intended to be independent of the particle radius, the bulk particle concentration, and the average shear rate.

2.4.1.3 Comparison with Experimental Data

This model of shear-induced particle migration in a suspension seems to capture well the phenomena that are observed experimentally in unidirectional shear flow. In the work of Phillips et al. (1992), the predictions of the model were tested against measurements made by Abbott and Graham using NMR imaging. First, the two empirical constants, K_c and K_η, in the Phillips/Leighton/Acrivos model were fit to a set of concentration profiles measured by NMR imaging for wide-gap Couette flow, for a suspension of 675 μm particles with bulk particle volume fraction $\bar{\phi} = 0.55$. The values $K_c = 0.41$ and $K_\eta = 0.62$ were obtained, with the ratio K_c/K_η indicating the predicted difference between the steady state particle concentrations at the inner and outer cylinder walls. Then the model was compared to NMR measurements for wide-gap Couette flows of suspensions of particles of sizes 675 μm and 100 μm, and bulk particle volume fractions of 0.45, 0.50, and 0.55, all fairly close to the maximum random particle volume fraction of about 0.63. The model agrees very well with the transient and steady state experimental data, even for the smaller particle size and for bulk concentrations different from the fitting concentration.

However, it is necessary to consider other models because there are some effects observed in suspension flow that are not captured by the model of Phillips et al. First, the Phillips/Leighton/Acrivos model makes unrealistic predictions of particle concentration profiles for pressure-driven flow in a rectangular channel or a circular tube for values of the ratio $K_c / K_\eta \leq 0.66$. In these two rectilinear flows, due to the symmetry of the flow in the gradient direction, the velocity gradient at the center line must equal zero. Since two of the fluxes in the particle diffusion equation (2.8) are proportional to the local shear rate, these fluxes vanish at the flow center line where the shear rate is zero. Accordingly, there is no resistance to the migration of particles to the center line due to the third flux term in the equation. As a result of the extreme aggregation of particles at the exact center of the flow, a sharp cusp forms at the center line in the concentration profiles predicted by the Phillips/Leighton/Acrivos model. This feature of the concentration profile was not observed experimentally by Koh et al. (1994) and Lyon and Leal (1998), who measured concentration profiles by using LDV in rectangular channel flow. These studies found concentration profiles that were smoothly varying in the gradient direction and had a slope of zero at the center line.

Phillips et al. (1992) attributed the discrepancy between the theoretical predictions and the experimental measurements to the approximation that the collision frequency experienced by a particle is proportional to the local shear rate at the center of the particle. Actual particles sitting at the center line of a channel flow have finite size, and thus extend into regions of non-zero shear rate, where collisions do occur. Thus, the approximate Phillips/Leighton/Acrivos expression for the collision frequency neglects the finite size of the particles. The way to correct this omission is to allow for non-local effects, meaning that the properties of the flow at a point are determined by the properties of neighboring regions of the flow as well as at the point itself. One advantage of the suspension temperature models of Jenkins and McTigue (1990) and Nott and Brady (1994) is that such non-local effects arise naturally from fluctuation kinetic energy conservation in the form of a pseudo-thermal energy flux.

A three-dimensional flow that exhibits phenomena that contradict the predictions of the Phillips/Leighton/Acrivos model is torsional shear flow between parallel disks. In a paper reporting NMR measurements of particle concentration profiles in torsional shear flow between parallel disks, Chow et al. (1994) observed that particle migration does not occur even though shear rate gradients in the radial, or neutral, direction are present. Since the Phillips/Leighton/Acrivos model predicts particle migration in response to gradients in shear rate, the Phillips et al. (1992) model would predict a diffusive flux of particles radially inward, toward the centers of the disks. This disagreement between the Phillips/Leighton/Acrivos model predictions and experimental results for parallel disk flow implies that there may be an additional mechanism for particle migration missing from the model.

Krishnan et al. (1996) presented further results from torsional shearing flow between parallel disks. For a monodisperse suspension, these researchers also observed no particle migration. However, for a bidisperse suspension, Krishnan et al. observed segregation of the two sizes of particles, in the opposite configuration to what would have been predicted by the Phillips/Leighton/Acrivos model. Smaller particles migrated radially inward, and larger particles migrated radially outward. The data of Krishnan et al. imply that the steady state concentration profile in the neutral direction of parallel disk flow is determined by a balance of diffusive fluxes which depend differently on particle size, but which cancel exactly when the particles are identical. These results cannot be explained by the Phillips/Leighton/Acrivos model, since it lacks fluxes which scale differently in particle size, and suggest that particle migration occurs in the opposite direction to that observed.

In addition, the model of Phillips et al. (1992) assumes a Newtonian form of the stress tensor, which does not contain normal stress differences. This assumption contradicts the observation of Gadala-Maria (1979) that nonzero normal stress differences exist in torsional shearing flow of a concentrated suspension between parallel disks.

A final issue regarding the diffusive flux model is that it cannot be generalized easily to flows with mixed kinematics, that is, where both shearing and elongation are present. A generalized "shear rate" could be defined as a function of the second invariant of the rate-of-strain tensor, $\dot{\gamma} \equiv \sqrt{\frac{1}{2}\dot{\boldsymbol{\gamma}}:\dot{\boldsymbol{\gamma}}}$, but it is not clear whether this definition is a meaningful measure of the driving force for migration for non-shearing deformations.

2.4.2 The Suspension Temperature Statistical Mechanical Model: Jenkins and McTigue

The statistical mechanical foundation of the Jenkins and McTigue model (1990) is outlined below, and the equations of the model are presented. Subsequently, the Nott and Brady model (1994) is introduced, and, finally, the comparison of the models with experimental data is discussed.

2.4.2.1 Statistical Mechanics Applied to Granular Flows

The most recent model of a concentrated suspension to come out of the studies of granular flows, that of McTigue and Jenkins (1992), is based on the work of Jenkins and Savage (1983). Jenkins and Savage write balance equations for locally conserved quantities which are rigorous according to statistical mechanics. First, they choose a macroscopic property of the suspension, such as average particle concentration, and then identify a dynamical quantity which when ensemble averaged would produce the macroscopic property. Then, they write a time evolution equation for the microscopic quantity which is exactly valid in a volume element V about the position $\underline{r}$. Finally, this equation is ensemble averaged to yield the time evolution equation of the macroscopic property.

In order to calculate the transport coefficients which arise in these equations, Jenkins and Savage (1983) select a form for the single-particle distribution function and the pair distribution function. In principle, these two functions, which weight the averages used to compute macroscopic quantities by giving the probabilities of all the possible positions and velocities of one or two particles, respectively, can be found from equations governing their time evolution. In practice, finding the distribution functions is difficult, because solving the equation for each order distribution function requires knowledge of the form of the next order distribution function; the complexity of the functions increases with the number of particles involved in the interaction.

For these equations to be solvable, the infinite series of distribution functions must be truncated by the replacement of higher-order interaction terms with simpler, lower-order approximations of these interactions. As a result of these approximations, the exact distribution function giving the probabilities of the positions and velocities of any number of interacting particles cannot be found. However, in the correct length scale and time scale regimes, the simplifying approximations to higher order interactions often are justified. For example, the Boltzmann equation, in which the pair distribution function is approximated as the product of the single-particle distribution functions of two particles, reliably captures the behavior of dilute gases.

The assumption made in this equation that the motion of the particles is generally uncorrelated is reasonable for these gases.

Jenkins and Savage (1983) avoid the difficulties of solving for the single-particle and pair distribution functions entirely and instead propose plausible forms for these functions. This is a departure from the most rigorous treatment of averaging possible, which requires the solution of a time evolution equation containing a minimum of assumptions. They use a local equilibrium approximation for the single-particle distribution function, where the velocities of particles are distributed in a Maxwellian manner about the mean particle velocity at any point. This type of approximation means that the granular material can be considered a continuum made up of tiny elements, each containing a statistical number of particles for which averaged point properties constant over each entire element may be defined.

For the pair distribution function, needed to calculate the averages of quantities transferred through inter-particle collisions, Jenkins and Savage (1983) use a nearly local equilibrium approximation, but one which incorporates the effects of anisotropy in the mean flow at the microscopic level. The pair distribution function is written as the product of two single-particle local equilibrium distribution functions, the equilibrium radial distribution function for rigid spheres, which correlates the positions of the two particles in a dense gas, and a factor linear in the relative mean velocity at the positions of the two particles, which describes the tendency of the mean flow to move the two particles together or apart.

2.4.2.2 Jenkins and McTigue (1990): Suspension Flow

Jenkins and McTigue (1990b) first considered two-phase flow by turning to heuristic arguments inspired by Haff (1983) to derive forms for the transport coefficients in the balance equations. The experimental observations of particle migration mentioned in Chapter 1 lie in the "viscous" regime, where viscous forces from the interstitial fluid dominate particle inertial forces during inter-particle interactions. In this regime, the scalings of transport coefficients such as the suspension viscosity are different from those in a granular flow. The difference lies in the continuous, incompressible liquid phase, which changes the interactions between the particles from hard-sphere collisions to significantly more complicated interactions that involve the hydrodynamics generated by the particles' relative motion.

Jenkins and McTigue (1990) followed the heuristic scalings with calculations of the transport coefficients for the viscous regime by using the methods of Jenkins and Savage (1983). However, they treated the suspension as a one-phase system and completely neglected the fluid phase. Their resulting model consisted of conservation of mass, momentum, and fluctuation kinetic energy equations for the particle phase, which had to be solved for the particle volume fraction, average particle phase velocity, and suspension temperature.

The equations of Jenkins and McTigue (1990) are as follows:

conservation of mass,

$$\underline{\nabla} \cdot (\phi\, \underline{u}) = 0 \tag{2.10}$$

conservation of momentum,

$$\underline{\nabla} \cdot \left[-\pi\, \boldsymbol{\delta} + \eta_f\, \eta_s(\phi)\, \boldsymbol{\gamma} \right] = \underline{0} \tag{2.11}$$

and conservation of fluctuation kinetic energy,

$$0 = \left[-\pi\, \boldsymbol{\delta} + \eta_f\, \eta_p(\phi)\, \boldsymbol{\gamma} \right] : \boldsymbol{\gamma} - \eta_f\, \alpha(\phi)\, a^{-2}\, T + \eta_f\, \underline{\nabla} \cdot (\kappa(\phi)\, \underline{\nabla}\, T) \tag{2.12}$$

Here, ϕ is the particle concentration, $\underline{u}$ is the average particle phase velocity, T is the suspension temperature, and $\boldsymbol{\gamma}$ is the average particle phase rate-of-strain tensor. In addition, $\eta_s(\phi)$ is the effective suspension viscosity, $\eta_p(\phi)$ is the particle contribution to the suspension viscosity, $\kappa(\phi)$ is the pseudo-thermal conductivity, and $\alpha(\phi)$ is the dissipation coefficient. These variables and transport coefficients are defined precisely in Chapter 5.

In the momentum conservation equation, one of the forces which appears is the gradient of a "particle pressure," $\pi\,(\phi, T)$, or the isotropic stress. The "particle pressure" arises due to fluctuations in particle velocity and is expressed in terms of the granular temperature and particle concentration by an equation of state.

The terms on the right side of the fluctuation energy balance equation require identification. The first term indicates the rate of shear working from the mean flow, which is a fluctuation energy source, and the second term gives the rate of dissipation of fluctuation energy into heat due to fluid phase drag on the particles. The third term gives the fluctuation energy flux, and thus provides the equation with a non-local character. The dissipation of fluctuation energy term gives the effect of the fluid phase on the particle fluctuations and is proportional to the suspension temperature T.

As will be discussed later in chapter 5, the explicit absence of the fluid in the model is a problem in pressure-driven flows, such as pressure-driven channel flow, where the fluid provides the driving force for the particle motion. In response to this limitation, McTigue and Jenkins modified the model to include pressure-driven flow in a later version (McTigue and Jenkins, 1992), where the pressure in the suspension became the sum of the original particle contribution (a function of ϕ and T) and the fluid phase pressure. A different limitation of the 1992 version is that, due to the new fluid pressure variable, there are more unknowns than equations. The modified model can only be solved in simple geometries where the form of the fluid pressure gradient is known or can be assumed.

A final limitation of both the 1990 and 1992 versions of the Jenkins and McTigue model is that the stress tensor has a Newtonian form and does not include normal stress differences. As mentioned earlier regarding the diffusive flux model of Phillips et al. (1992), this form of the stress tensor cannot account for the experimental observations of Gadala-Maria (1979) of nonzero normal stress differences.

2.4.2.3 The Nott and Brady Model (1994): Statistical - Phenomenological Hybrid

Nott and Brady (1994) incorporate the ideas of Jenkins and McTigue (1990) of suspension temperature and a fluctuation energy balance into a two-phase model. It contains two mass conservation and two momentum conservation equations, one of each for the mean suspension continuum, and one of each for the particle phase only. Due to the presence of the two additional mean suspension equations, the Nott and Brady model is fully specified.

Nott and Brady's model contains the idea, inspired by Jenkins and McTigue, that suspension temperature, rather than shear rate, is the important quantity determining particle migration. Temperature directs migration implicitly, through the presence of the fluctuation energy conservation equation and the "particle pressure" gradient which appears in the particle phase momentum equation and depends on temperature and particle concentration. Nott and Brady also use the viscous scalings of Jenkins and McTigue (1990) for transport coefficients which appear in the conservation equations, since they concentrate on flows at low Reynolds number, calculated using the particle radius as a characteristic length scale.

However, the Nott and Brady model is much less microscopically rigorous than Jenkins and McTigue's kinetic theory model. The coefficients in the conservation equations contain dimensionless functions of particle concentration which Nott and Brady find phenomenologically rather than derive microscopically. The use of these phenomenological transport coefficients distinguishes the Nott and Brady model from the statistical constitutive model of Jenkins and McTigue (1990) and causes the Nott and Brady model to bear some resemblance to the Phillips/Leighton/ Acrivos phenomenological diffusive flux model.

Although Nott and Brady allow for the presence of normal stress differences in the stress tensor constitutive equation, they do not provide a constitutive relation describing the normal stresses. This incompleteness does not allow the predictions of the model to be compared to the observations of Gadala-Maria (1979) of normal stress differences in parallel-plates torsional flow.

2.4.2.4 Comparison with Experimental Data

We focus on these "temperature" models because we believe they are promising for studying complex flows, where both shearing and elongation are present. In these flows, the question of how to define the "shear rate" is a challenge for the phenomenological models, but the "temperature" models may be able to avoid this problem by not defining the suspension temperature explicitly in terms of any deformation rate quantity.

Although the kinetic energy of particle velocity fluctuations due to inter-particle collisions is presented as a particle migration mechanism in the McTigue and Jenkins and Nott and Brady models, a complete set of measurements of the properties of the these velocity fluctuations in a simple, homogeneous flow does not exist, but is necessary to ensure that the models incorporate a realistic migration mechanism.

To date, only the Nott and Brady model has been compared with experimental data in a single flow geometry. The data of Lyon and Leal (1998), which include measurements of the suspension temperature, were obtained for the same geometry as the only published solution (Nott and Brady, 1994) for the model, which was pressure-driven flow in a rectangular channel. In addition, in their original paper, Nott and Brady compared their model predictions with Stokesian Dynamics simulations, again for pressure-driven channel flow. Lyon and Leal (1998) found reasonable but not quantitative agreement between their data and the Nott and Brady model. Clearly, further experimental tests of the temperature models in different flow geometries would provide necessary information about their accuracy in predicting particle migration.

2.5 Experimental Techniques Used for Concentrated Non-Colloidal Suspensions

Each of the principal measurement techniques applied to concentrated suspension flows is optimally suited to measuring a specific quantity of interest. Nuclear Magnetic Resonance (NMR) imaging gives the best information about particle concentration profiles, since it can distinguish between the fluid and solid phases, even in optically opaque suspensions. NMR also provides simultaneous velocity profiles. NMR imaging has been utilized for measuring concentration and velocity profiles in many flow geometries, including circular pipe flow (Sinton and Chow, 1991; Altobelli et al., 1991; Arola et al., 1999; Hampton et al., 1997), wide-gap Couette flow (Abbott et al., 1991; Graham et al., 1991; Tetlow et al., 1998), narrow-gap Couette flow (Chow et al., 1994), parallel plates torsional flow (Chow et al., 1994), piston-driven contraction- expansion flow (Altobelli et al., 1997), single screw extruder flow (Corbett et al., 1995) and suspension settling (Abbott et al., 1993; Bobroff and Phillips, 1998)

The best method for visualizing particle microstructure geometry and quantifying statistics of particle interactions is video image analysis applied to a refractive index-matched suspension. Leighton and Rampall (1993) applied this method to measure the pair distribution function of particles in steady homogeneous shear flow. Breedveld et al. (1999) quantified the self-diffusion coefficients of particles and fluid tracers in the gradient and neutral directions of a narrow-gap Couette flow. Nicolai et al. (1995) used the technique to measure mean and fluctuating velocities of settling particles. In addition, video image analysis is uniquely suited to measuring properties of bidisperse suspensions, since it can easily distinguish the two particle sizes if they only have different colors. In the work of Krishnan et al. (1996) in parallel-plate flow and Lyon and Leal (1998b) in channel flow, colored tracer particles of different sizes were used to visualize and quantify particle size separation due to migration.

Finally, the technique best suited to accurate measurements of the mean and fluctuating velocity is laser Doppler velocimetry (LDV), also applied to a refractive index-matched suspension, due to its fine spatial and temporal resolution. Since LDV is a pointwise measurement method, it yields the most precise velocity observations at particular positions, but does not record snapshots of whole regions of the flow as do NMR and video imaging. Koh et al. (1994) applied the technique to flow in a rectangular channel, and adapted the method to record simultaneous concentration and mean velocity profiles. Lyon and Leal (1998) extended the technique for the same geometry to higher concentrations and measured particle velocity fluctuations as well. As mentioned above, Jana et al. utilized LDV in measuring apparent wall slip coefficients in the cylindrical Couette geometry. Kapoor and Acrivos (1994) measured the particle velocity profile and apparent wall slip coefficient in the highly concentrated sedimentation layer of an inclined settling flow.

2.6 Recent Experiments Involving LDV, Concentrated, Non-Colloidal Suspensions, and Particle Velocity Fluctuations

A subset of the LDV measurements of concentrated suspensions were focused on particle velocity fluctuations. Three recent and important contributions to the literature include those of

Averbakh et al. (1997), Lyon and Leal (1998), and Tripathi (1998).

Averbakh et al. (1997) were the first authors to publish LDV measurements of particle velocity fluctuations in a concentrated suspension. The authors studied pressure-driven flow in a rectangular duct and measured the velocity fluctuations in the flow and gradient directions on the duct center line. Both the flow and gradient components increased linearly with the maximum mean velocity. The authors were the first to realize that the velocity fluctuations they measured could have contributions from effects other than particle collisions, such as particle rotation and LDV system noise, but they did not attempt to separate these factors. However, their recognition of the necessity of separating the collisional fluctuations from other factors influenced all subsequent LDV measurements of particle velocity fluctuations in concentrated suspensions. Averbakh et al. also measured the drift velocities of migrating particles in the gradient direction of the duct flow and found that the diffusive flux models of Leighton and Acrivos (1987b) and Philllips et al. (1992) qualitatively predicted the observed profiles (Shauly et al., 1997).

The work of Lyon and Leal (1998) concerned pressure-driven flow in a rectangular channel. The authors measured the steady-state profile of collisional velocity fluctuations in the flow direction and found reasonable agreement between their data and the suspension temperature models of McTigue and Jenkins (1992), Nott and Brady (1994), and Morris and Brady (1998). Lyon and Leal also extended the measurements of Koh et al. (1994) to high concentrations (from 30% to 50% particle volume fraction) by measuring the particle volume fraction and mean velocity profiles as well.

In a contemporary study, Tripathi (1998) investigated narrow-gap Couette flow between differentially rotating concentric cylinders. He measured collisional velocity fluctuations in three directions at steady-state on the flow center line. Tripathi found that the velocity fluctuations were anisotropic, since the neutral direction component was the largest, followed by the gradient component, and the velocity fluctuations in the flow direction were negligible. Tripathi also observed that the velocity fluctuations in the gradient and neutral directions scaled with the average shear rate squared, which supports the assumptions of the constitutive models presented earlier.

2.7 Objectives of This Study

The main goal of this work is to determine experimentally the properties of particle velocity fluctuations originating from inter-particle collisions in a flowing concentrated suspension. Specifically, we wish to characterize the dependence of the particle velocity fluctuations on particle volume fraction, shear rate, and position. We aim to accumulate a consistent set of experimental data of collisional particle velocity fluctuations that is sufficient for evaluating the assumptions and resulting predictions of particle migration models. One particular question we wish to answer is whether the collisional particle velocity fluctuations are isotropic, meaning that components measured in all directions are equal. Consequently, this research has a different focus from that of the studies of Lyon and Leal and Tripathi. Our approach is to make quantitative LDV measurements in a homogeneous shear flow in order to eliminate particle migration effects, and to utilize qualitative video imaging of particle trajectories to aid in interpreting the LDV data.

A secondary goal is to assess the implications the data have for suspension models and simulations. This purpose involves the determination of whether the models contain the correct assumption that the suspension temperature is isotropic and hence can be represented by a scalar, whether the models contain the correct scaling of the temperature in particle volume fraction and shear rate, and whether the models accurately predict the observed shear rate and suspension temperature profiles.

Chapter 3

Experimental Method

This chapter describes the experimental system and measurement method. There were two main experimental challenges we faced in adapting the laser Doppler velocimetry (LDV) technique to measuring velocity fluctuations in a concentrated suspension. First, the use of LDV requires the material to be transparent, which compelled us to match the refractive index of the fluid to that of the particles, while also ensuring that the particles were neutrally buoyant in the fluid. In addition, the Couette flow cell design was intricate because the Couette had to meet many constraints. This chapter contains a description of how these two challenges were met, following a discussion of the basic principles of the LDV method, and concludes with a description of our measurement and data reduction procedures.

3.1 Laser Doppler Velocimetry

Laser Doppler velocimetry is an effective method for measuring particle velocity fluctuations in a flowing concentrated suspension because it is non-invasive; that is, it does not change the flow being measured, and possesses the fine spatial and temporal resolution required for resolving velocity fluctuations. This is not surprising, since LDV was originally developed for measuring turbulent flows, in which some of the important quantities, such as the Reynolds stress, are defined in terms of velocity fluctuations.

3.1.1 Basic principles

Drain (1980) provides a clear and thorough explanation of the basic principles of LDV, which are summarized here. Alternative classic references include Durst et al. (1981) and Adrian (in Goldstein (ed.), 1996). When a wave, such as a sound wave, is transmitted from a source to a receiver, relative motion between the source and the receiver may cause a change or apparent change in the frequency of the wave. This real or perceived frequency change is defined as the "Doppler shift," and it occurs because the spacing between consecutive wavefronts shrinks or expands, depending on the direction of relative motion. For low relative speeds v compared to the speed of light c, whether the source or the observer moves (while the other remains stationary) the change in the frequency ν is given as

$$\Delta \nu = \frac{\nu \, v \cos\theta}{c}, \tag{3.1}$$

where θ is the angle between the direction of the line connecting the source and observer and the direction of relative motion. For light waves, a more complicated relativistic formula applies, but at relative velocities between the source and the observer that are low compared to the speed of light, the relativistic Doppler shift reduces to this non-relativistic limit.

In LDV experiments, a stationary source emits light which is scattered by a moving object to a stationary detector. This is called a "double Doppler shift" because the moving object receives incident light at a different frequency from the source emission and then the detector receives scattered light from the object at a different frequency from the object's scattering frequency (in its reference frame). For velocities small compared to the speed of light, the expression for the total difference between the frequency the detector receives and the frequency the source emits can be expanded to first order in v/c as

$$\Delta \nu = \nu_{\text{detector}} - \nu_{\text{source}} = \frac{\nu \, v}{c}(\cos\theta_1 + \cos\theta_2), \tag{3.2}$$

where θ_1 is the angle between the line connecting the source and object and the object's direction of motion and θ_2 is the angle between the line connecting the object and detector and the object's direction of motion.

In the differential Doppler technique, which is employed in this system, there are two sources emitting light of the same frequency which are oriented at different angles, θ_1 and θ_1', to the object's direction of motion. Typically, the sources are two stationary incident laser beams which cross and the moving object scatters light from both beams as it crosses the intersection point. The scattered light is observed by the detector from another direction, which forms angle θ_2 with the object's direction of motion. Accordingly, the expressions for the double Doppler shift of each beam become

$$\Delta \nu = \nu_{detector} - \nu_{source} = \frac{v\,\nu}{c}\left(\cos\theta_1 + \cos\theta_2\right) \tag{3.3}$$

$$\Delta \nu' = \nu'_{detector} - \nu_{source} = \frac{v\,\nu}{c}\left(\cos\theta'_1 + \cos\theta_2\right) \tag{3.4}$$

At the detector, a phenomenon called "optical mixing" occurs. The two scattered light beams interfere with each other, meaning that the time-dependent electromagnetic fields, which are waveforms, add together, by the superposition principle. Accordingly,

$$E_{tot} = E + E' = E_0 \cos(2\pi\nu t + \phi) + E'_0 \cos(2\pi\nu' t + \phi') \tag{3.5}$$

Since the detector is a "square-law" device, its output i(t) is proportional to the intensity of the combined light waves, which is proportional to the square of the total electric field.

$$i(t) = (E + E')^2 = \left[E_0 \cos(2\pi\nu t + \phi) + E'_0 \cos(2\pi\nu' t + \phi')\right]^2 \tag{3.6}$$

Expanding the terms on the right side of equation (3.6) yields,

$$i(t) = E_0^2 \cos^2(2\pi\nu t + \phi) + E_0'^2 \cos^2(2\pi\nu' t + \phi') + 2\,E_0\,E'_0 \cos(2\pi\nu t + \phi)\cos(2\pi\nu' t + \phi') \tag{3.7}$$

Applying a trigonometric identity to the third term, $\cos A \cos B = \frac{1}{2}\left[\cos(A-B) + \cos(A+B)\right]$, yields

$$\begin{aligned} i(t) = {} & E_0^2 \cos^2(2\pi\nu t + \phi) + E_0'^2 \cos^2(2\pi\nu' t + \phi') \\ & + E_0\,E'_0\left[\cos(2\pi(\nu-\nu')t + (\phi-\phi')) + \cos(2\pi(\nu+\nu')t + (\phi+\phi'))\right] \end{aligned} \tag{3.8}$$

Because the detector cannot respond fast enough to capture the oscillations of the light waves, on the order of 10^{15} per second, it averages the signals on a time scale long compared to the period of oscillation (Benefi and Barrett, 1976). The only term that is not averaged is the part of the last term with frequency $(\nu-\nu')$, since typically the frequency difference $(\nu-\nu')$ is orders of magnitude lower, only in the kHz-MHz range, which the detector can easily resolve. The time dependent factors of the first two terms each average to 1/2, and the part of the last term with frequency $(\nu+\nu')$ has a mean value of zero, so it vanishes, resulting in the output signal

$$i(t) = \frac{1}{2}\left(E_0^2 + E_0'^2\right) + E_0\,E'_0 \cos(2\pi(\nu-\nu')t + (\phi-\phi')) \tag{3.9}$$

The first two terms are constant in time, and the only time-varying term involves the frequency difference $(\nu-\nu')$. By substituting the expressions for $\nu_{detector}$ and $\nu'_{detector}$ from above, the time varying signal at the detector from the two scattered beams has frequency

$$f_{\text{Doppler}} = \nu_{\text{detector}} - \nu'_{\text{detector}} = \Delta\nu - \Delta\nu' = \frac{v\,\nu}{c}\left(\cos\theta_1 - \cos\theta'_1\right) \qquad (3.10)$$

Since the two beams are generated by a single source, the phase angles ϕ and ϕ' are identical and the difference vanishes from i(t).

Then, by a similar trigonometric identity, $\cos A - \cos B = 2\sin\frac{1}{2}(B-A)\ \sin\frac{1}{2}(A+B)$,

and the resulting expression for the detected frequency is

$$f_{\text{Doppler}} = 2\,\frac{v}{\lambda}\sin\alpha\ \cos\beta\ , \qquad (3.11)$$

$$\text{where}\ \ \alpha = \frac{1}{2}\left(\theta'_1 - \theta_1\right)\ \ \text{and}\ \ \beta = \frac{1}{2}\left(\theta'_1 + \theta_1 - \pi\right)$$

More physically, α is half the intersection angle of the two incident beams, β is the angle the object's velocity forms with the normal to the bisector of the two beams, and λ is the wavelength of the incident light. The crucial feature to note here is that the observed Doppler frequency has no dependence on the angle θ_2 of the detector. This means there is no constraint on the positioning or aperture size of the detector.

An alternate picture of the differential Doppler technique is the "fringe model," which is valid only at low particle densities and small particle sizes, but is easier to visualize. In this picture, instead of considering the interference of the scattered light from the two beams at the detector, we look at interference of the two incident beams in the region where they cross.

The two incident beams are plane waves where they intersect, and accordingly form alternating bright and dark planes of constructive and destructive interference called "fringes" where they cross, as shown in figure 3.1. The spacing of these fringes is found to be

$$s = \frac{\lambda}{2\sin\alpha}\ , \qquad (3.12)$$

where, as in figure 3.1, α is half the intersection angle of the two beams and λ is the wavelength of the incident light. A particle moving perpendicular to the fringe planes moves through alternating bright and dark regions, and scatters light with the frequency of its velocity divided by the fringe spacing, or more precisely

$$f_{\text{Doppler}} = \frac{2\,v\ \cos\beta\ \sin\alpha}{\lambda} \qquad (3.13)$$

where β is the angle between the particle's velocity and the normal of the fringe planes. Here

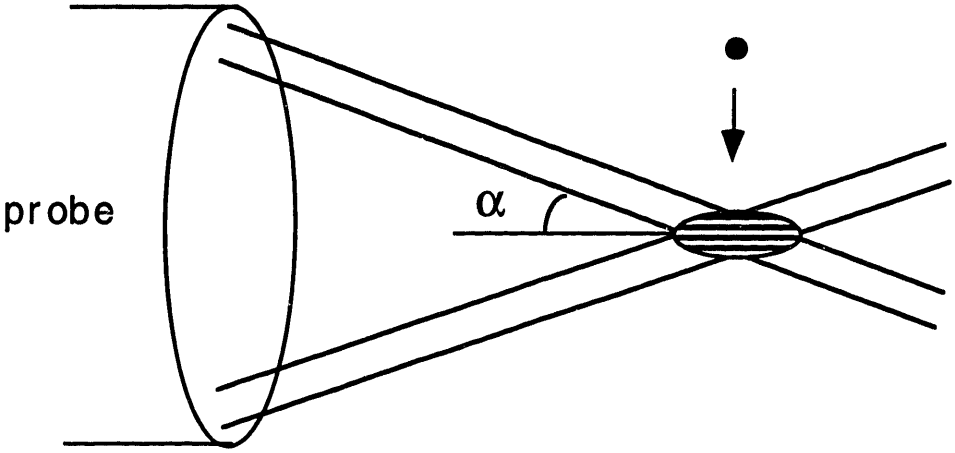

Figure 3.1 Particle crossing "fringe" planes of two intersecting beams

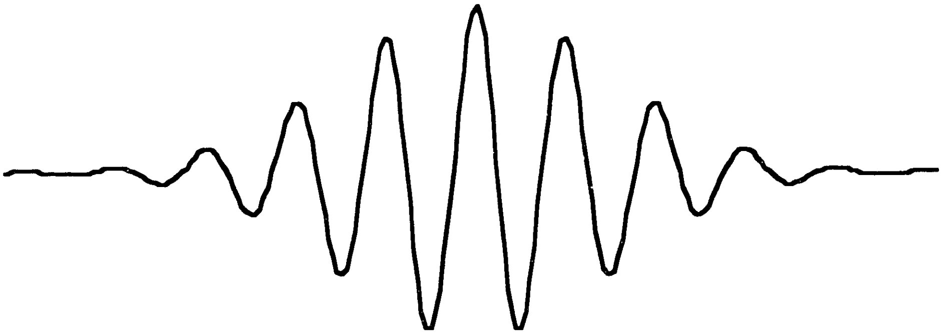

Figure 3.2 "Burst" Doppler signal: oscillates at Doppler frequency, amplitude modulated by Gaussian beam intensity profile

again, the observed Doppler frequency is independent of the direction of detection.

The fringe region where the beams intersect is called the "measuring volume" and is bounded by points where the light intensity is $1/e^2$ of the maximum intensity. For beams with a Gaussian intensity profile, the measuring volume is an ellipsoid with axes $2\,r_0$, $\frac{2\,r_0}{\sin\alpha}$, and $\frac{2\,r_0}{\cos\alpha}$, where r_0 is the beam radius measured from the beam center to the $1/e^2$ intensity points.

The scattered light signal obtained from a particle moving perpendicular to the fringe planes is called a "burst" and a representative sketch appears in figure 3.2. The signal amplitude is modulated by the Gaussian intensity profile of the intersection region, and the frequency is the Doppler frequency.

3.1.2 Dantec Fiberflow LDV System

The basic components of the Dantec Fiberflow system used here are the laser, beamsplitter and frequency shifter, fiber optic probe, photomultiplier, spectrum analyzer and computer, shown in a schematic diagram in figure 3.3. The light source is an Argon ion laser (Ion Laser Technology, Model 5500A-00, air-cooled, 300mW) which emits three main wavelengths, 514.5 nm (green), 488 nm (blue) and 476.5 nm (violet). The beam is directed into a series of optics where an acoustic Bragg cell splits the beam and shifts the frequency of one of the resultant beams. The 40 MHz frequency shift allows the LDV system to differentiate between velocity direction, by causing positive and negative velocities of the same magnitude to have different Doppler frequencies. The beams are separated into the three different wavelengths, and guided through a fiber optic cable to the fiber optic probe.

The probe greatly simplifies the apparatus, because it is a mobile, self-aligned unit. The probe is held in two rotating mounts attached to a set of translation stages, which allow control of three positions and two angles of the beams. Upon exiting the probe, the two parallel beams pass through an 80 mm focusing lens, which directs them to intersect at the focal point at a half-angle of 13.71° (0.239 rad), slightly larger than the specification value of 13.36° (0.233 rad). The probe also contains a photodetector which collects the light scattered backward and passes it back through

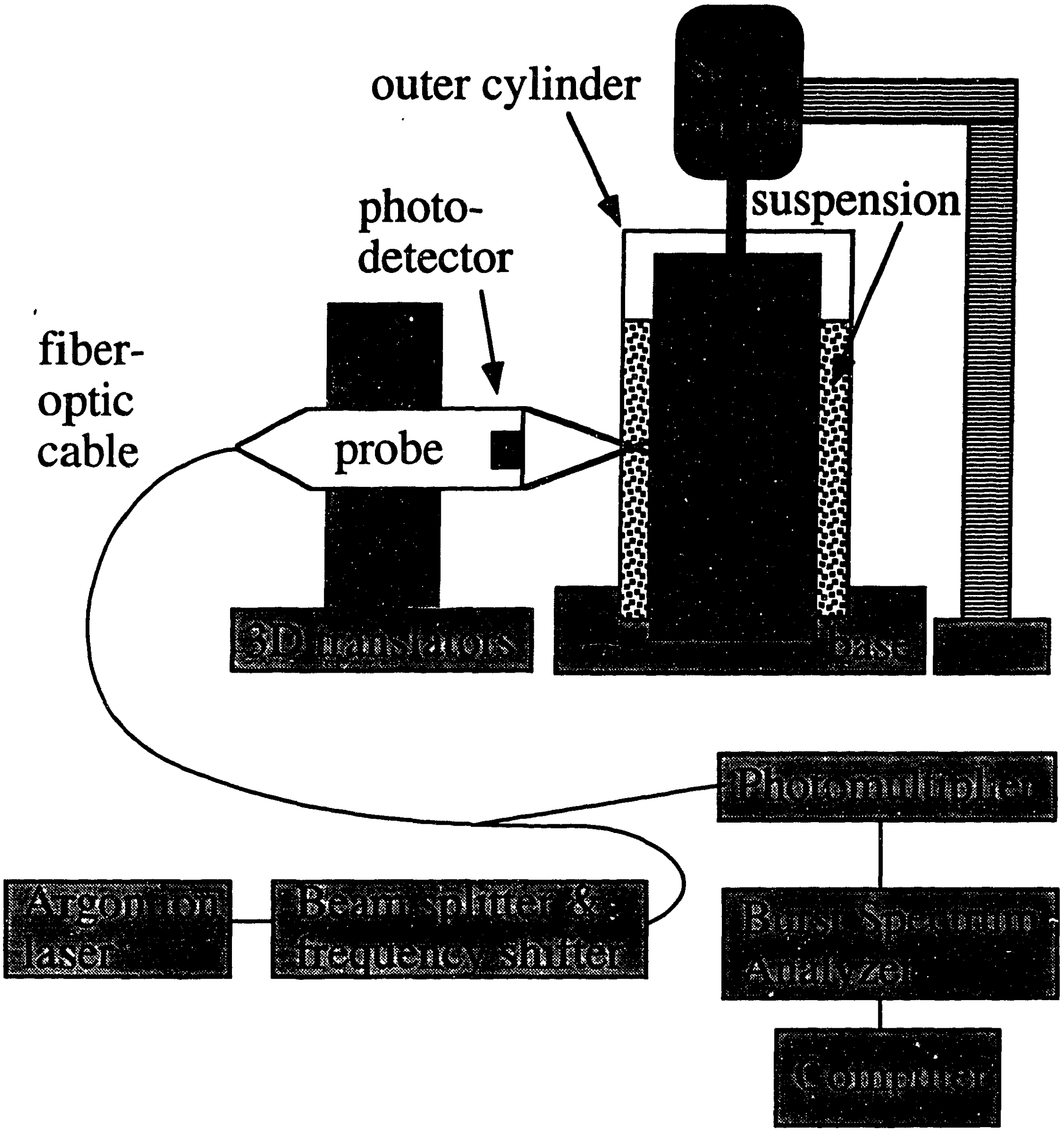

Figure 3.3 Schematic view of LDV system

the fiber optic cable to the photomultiplier.

According to Mie scattering theory, explained in Durst et al. (1981) and Drain (1980), particles scatter the greatest light intensity in the forward direction, that is, the direction of the incident beam. However, oblique backscattering at certain angles provides enough light intensity for a reasonable signal and is the easiest arrangement in the Couette geometry studied here, where the inner cylinder blocks forward scattering for most points in the flow. The arrangement in this study is oblique backscattering with the probe directing the beams perpendicular to the cylinder axis, through the outer cylinder wall.

The photomultiplier converts the scattered light signal to a voltage signal, amplifies the signal according to the user-selected gain and high voltage parameters, and feeds the voltage signal to the Burst Spectrum Analyzer (Dantec, Model 57N10), which filters each signal, takes the discrete Fourier transform, fits the peak frequency, and identifies that as the Doppler frequency. The computer (PC 486) acts as a post-processor (via IEEE 488 interface) by calculating the velocity from the fitted frequency and displaying a velocity distribution, typically containing the calculated velocities from at least 1000 Doppler burst signals.

3.1.3 Operation of the Burst Spectrum Analyzer (BSA)

The spectrum analyzer plays a very important role in the LDV system since it processes the Doppler signals extremely rapidly and uses superior fitting techniques that enable it to extract even faint signals from noise. The BSA has several main functions, including taking the discrete Fourier transform of the time-varying frequency signals, fitting the frequency spectrum, validating the spectrum, and timing the arrival and transit times of each signal. The superior fitting techniques include zooming in on the optimal frequency range, using the whole frequency spectrum in the fit, and zero filling.

The BSA calculates the discrete Fourier transform of a Doppler signal, or burst, as follows $f_k = \sum_{n=0}^{N-1} x_n \, e^{-i 2 \pi n k / N}$ where f_k is the value of the transform at the kth frequency value, and N is the number of samples in time of function x(t). Once the frequency spectrum is complete, the BSA fits the spectrum with a sinc function

$$\mathrm{sinc}\,(\pi\,(f-f_0)\,T) = \frac{\sin(\pi\,(f-f_0)\,T)}{\pi\,(f-f_0)\,T} \tag{3.14}$$

centered about the frequency f_0 where the global maximum of the spectrum is located. The sinc function is the frequency spectrum for a sinusoid of frequency f_0 sampled for only a limited "window" of time, T. Finally, the BSA validates the spectrum by comparing the heights of the two largest local maxima. If the ratio between their heights is greater than 4, the spectrum is accepted. Otherwise, it is rejected. The determining value of 4 was chosen empirically as a compromise between data quality and rate (Burst Spectrum Analyzer User's Guide). The validation process is designed to reject spectra where two or more particles with different velocities pass through the measuring volume at the same time.

Meanwhile, the BSA uses the time-varying burst signal to determine when to start sampling. When two filtered measures of the signal amplitude, the pedestal and envelope, shown in figure 3.4, exceed a threshold voltage value of 50mV, the BSA starts sampling and starts the timer. There are two further threshold values that the pedestal and envelope could surpass, and then the BSA would restart the timer and the sampling. The idea is to sample only from the center of the burst signal, where the signal amplitude is the largest (Burst Spectrum Analyzer User's Guide, 1993).

In the first step of taking the discrete Fourier transform, the resolution of the transform is limited by the sampling frequency. By the Nyquist criterion, the sampling frequency must be at least twice the upper frequency in the signal in order to get an accurate representation. This is a difficult constraint to meet since the frequency range of the BSA is limited to 80 MHz. The way the BSA gets around this constraint is by shifting the frequency spectrum so that the center frequency, which the user selects, is shifted to zero. Then, the maximum frequency is only half the selected bandwidth, and the BSA's programmed sampling rate of 1.5 times the bandwidth is more than sufficient (Burst Spectrum Analyzer User's Guide, 1993).

In the second step of fitting the spectrum, the BSA has two advantages over a counter processor. First, all the data in the spectrum is utilized in the fit, instead of only the data near the

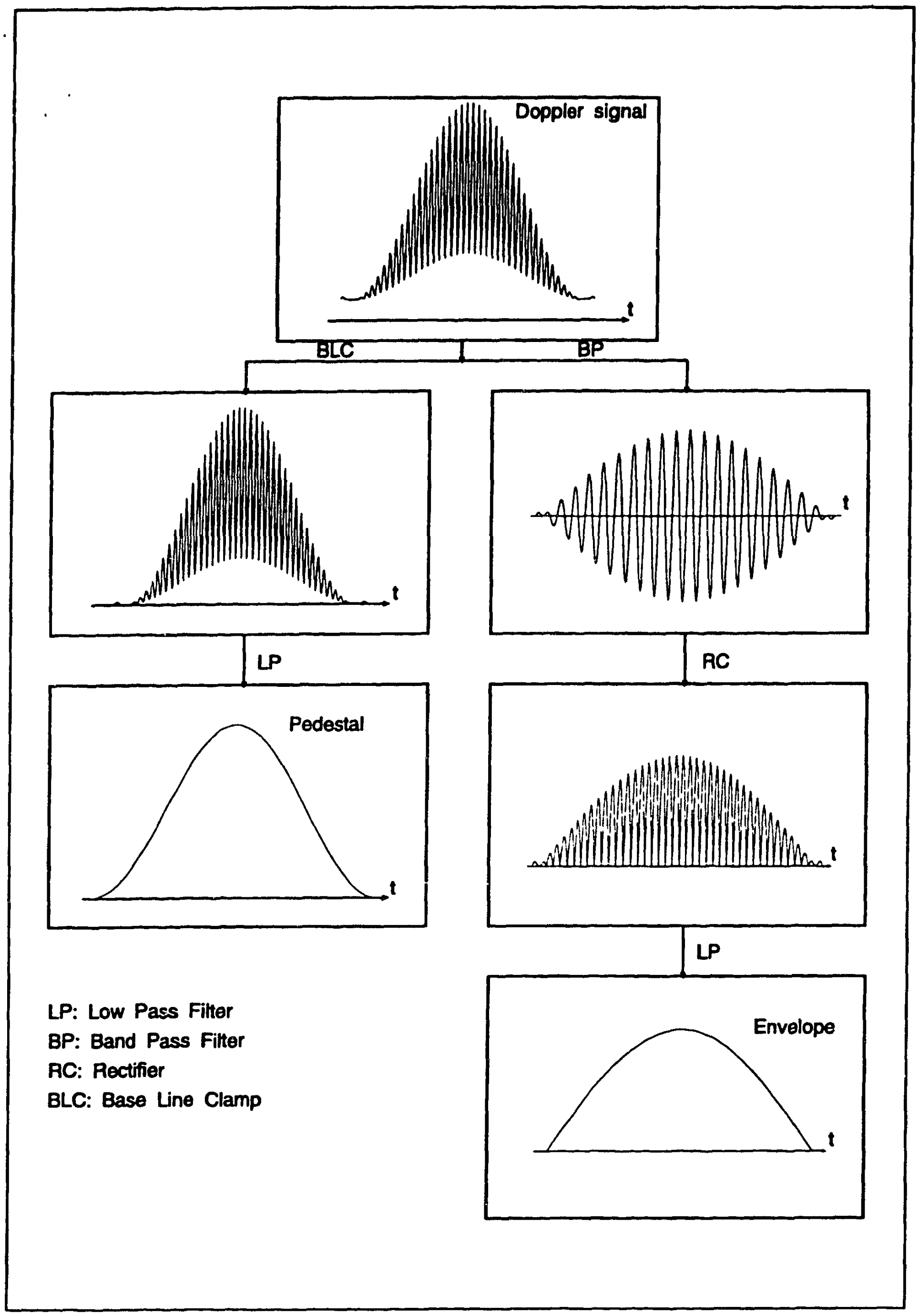

Figure 3.4 Filtering of the Doppler signal by the Burst Spectrum Analyzer into the envelope and pedestal (reproduced from Burst Spectrum Analyzer User's Guide, 1993).

zero crossings. Also, the BSA uses "zero-filling" to add an equal number of zeroes to the signal samples to aid in interpolation. This method does not affect the spectrum but doubles the number of frequency samples and accordingly improves the frequency spectrum fit (Burst Spectrum Analyzer User's Guide, 1993).

3.1.4 Assessment of the LDV System for Suspension Studies

The Dantec Fiberflow system we use has fine spatial resolution, with measuring volume dimensions of 168 x 35 x 35 μm^3 in air. Also, the system has fine temporal resolution, with data acquisition times ranging from 1.7 x 10^{-7} to 0.044 s, compared with an estimated collision interval of 0.2 s, for a suspension with ϕ=0.5 and $\dot{\gamma}$=10 s^{-1}. The fine temporal resolution made the LDV method look especially favorable at the beginning of this project, when the best time resolution available from alternative methods was 1/30 s for Digital Particle Imaging Velocimetry and 0.1 s for Nuclear Magnetic Resonance Imaging. Due to the advent of high speed cameras and stronger magnets these methods have increased in speed to resolution times of 2 x 10^{-4} - 2 x 10^{-3} (Kodak High Speed Camera Catalog, 1996) and 3 x 10^{-3} s (Iwamiya et al., 1994), respectively, to become competitive with LDV, but the errors involved in extracting fluctuating velocities from the recorded images are still large, and LDV still remains the measurement method that is best-suited to measuring fluctuations.

The LDV system utilizes one wavelength of light emitted from the Argon ion laser, the green beam with wavelength 514.5 nm. This allows us to measure one velocity component at a time. In order to measure multiple velocity components simultaneously, we would have to use different wavelengths for the different components in order to separate the signals, and a separate spectrum analyzer for each component.

A major limitation of the LDV method is that it requires the flow medium to be transparent. Otherwise, the scattered light signals are often attenuated until they vanish on the way back to the photodetector; in some cases, the incident beams cannot even penetrate into the flow far enough to intersect. This means that for a concentrated suspension, we must match the refractive index of the fluid to that of the particles, so that the incident beams pass through particles and fluid as if they are a single uniform medium, and the particles are "invisible." Since refractive index is a function of the wavelength of the incident light, the matching of the two phases should be done at the LDV wavelength. Also, since the refractive index of the fluid is a function of temperature, but the particle refractive index is not, the temperature of the system should be maintained near the refractive index matching temperature. Any mismatch in the refractive indices of the two phases causes attenuation of the LDV signal.

3.2 Materials

3.2.1 Particle and Fluid Description

The particles we selected were Lucite 47G, a copolymer of poly (methyl methacrylate (95%) - ethyl acrylate (5%)), manufactured by ICI Corp. In order to insure as monodisperse a suspension as possible, we used only the particles in the size range 180 to 212 μm diameter. We separated these particles from the others by dry-sieving the particles by hand three times through brass sieves (VWR) for each batch, with only the particles landing on the 80 mesh sieve (180-212 μm diameter) in the final round accepted. Nominally, these particles have average diameter 196 ± 16 μm. We chose particles in this size range for two reasons. First, these particles had the greatest clarity in the optical micrographs we took of various size ranges. They were also the particles closest in size to the spatial resolution of our LDV system, but that still were found in relative abundance in the Lucite 47G size distribution. The particles come from a single lot of Lucite 47G.

The particle density and refractive index were matched by a fluid mixture with mass fractions of 50.45% Triton X-100 (alkyl aryl polyether alcohol) (J.T. Baker), 27.9% 1,6 Dibromohexane (Aldrich), and 21.65% UCON lubricant 75-H-90,000 (polyalkylene glycol) (Union Carbide). Each of these components provides a different salient feature of the mixture. Triton X-100 has high refractive index, 1,6, Dibromohexane has high density, and UCON 75-H-90,000 has high viscosity. The mixture density is 1.183 ± 0.001 g/cm^3, the refractive index at 589 nm and 22° C is 1.4880 ± 0.0007, and the viscosity at 22° C is 0.84 Pa s.

The fluid mixture is based on a recipe suggested and subsequently fully characterized by Michael Lyon (1997; Lyon and Leal, 1998), adapted to match our specific particles. The mixture must have at least three components in order to allow the density and refractive index to be tuned independently. A small amount of Tinuvin 328 antioxidant was added to the mixture to prevent the Dibromohexane from degrading. (Abbott et al., 1991)

3.2.2 Density Matching Procedure

The most difficult part of matching the fluid and particle densities was measuring the particle density. We did not have a density gradient column available, so our matching method consisted of mixing many different fluids with a range of densities close to the Lucite 47G specification and observing the time it took for the particles to rise or sink. The mixtures where the particles remained suspended the longest bracketed the particle density. The densities of the fluid mixtures were known to be the average of the components' densities weighted by the volume fractions of the components in the mixture. The final density of the matching mixture was 1.183 ± 0.001 g/cm^3, where the uncertainty comes from the uncertainty in distinguishing between the suitability of different mixtures that are close to the particle density (and the uncertainty in the specified density of Triton X-100). We erred on the side of the particles sinking in the fluid, because it had been observed that they could be resuspended by shearing the suspension, which is not necessarily true for particles floating at a free surface. (Gadala-Maria and Acrivos, 1979; Leighton and Acrivos, 1986; Krishnan, 1994)

Before utilizing this method of measuring the particle density, we also attempted two other methods, but they were less accurate. We measured the liquid volume displaced by a known mass of particles, where measuring the exact change in volume was the limiting factor. Also, we timed the settling of individual particles in a long and wide tube of water, where the uncertainty in the exact size of each individual particle and the small number of reproducible trials compared to the number required for meaningful statistics caused the most inaccuracy.

3.2.3 Refractive Index Matching Procedure

We matched the particle and fluid refractive indices in a two step process. First, we measured the particle refractive index, and then found a fluid mixture with the same refractive index at the average lab temperature. Finding the fluid mixture with the desired refractive index was not as straightforward as in the case of the density. According to an index-matching technician at Cargille Optical Liquids Labs, the refractive index of a liquid mixture is the volume fraction weighted average of the refractive indices of the components, if the components are nonpolar. If any of the components is polar, the refractive index will be a nonlinear function of the composition. In this case, only 1,6 Dibromohexane was definitely nonpolar. We measured the refractive indices of the components as a function of temperature using a temperature-controlled Abbe refractometer (model 10450), and then used the volume fraction weighted average as an initial guess for the mixture refractive index. We mixed several fluids with the same, desired density, and refractive indices in a narrow range about the volume fraction average value. We measured the refractive indices of these various mixtures, and revised the composition until we found a mixture that matched the measured particle refractive index at the average lab temperature of 22 ± 2 ° C.

We measured the particle refractive index by making use of the temperature sensitivity of the fluid refractive index, using a technique very similar to that of Koh (1991), Koh et al. (1994), Kapoor (1994), and Lyon and Leal (1998). We placed a 2% particle volume fraction suspension of the sieved Lucite 47G particles in one of the test liquids with refractive index close to the particle specification value in a water-jacketed cylindrical glass cuvette with 50 mm path length (Starna Cells Inc.). We split a laser beam using a 50/50 plate beamsplitter (Melles Griot), directed one of the resulting beams through the cuvette and measured the transmitted light intensity that passed through the cuvette and through a 5 mm diameter pinhole to a photodetector placed behind the cuvette. The incident laser beam power was monitored simultaneously by a second photodetector, which was placed in the path of the other resulting beam. The photodetectors (Newport, model 815/818 SL) were connected through an A to D board to a Mac Quadra 800 computer, and the output voltages were read at set intervals by a LabVIEW program written by David Lee, and converted back to power measurements by a calibration of output voltage vs. power reading performed earlier. A schematic view of this apparatus appears in figure 3.5. We controlled the temperature in the cuvette by connecting the jacket to a temperature-controlled water bath (controller-VWR; cooler-Neslab). When we varied the cuvette temperature, the fluid refractive index changed, but the particle refractive index remained the same. We identified the best refractive index match with the temperature at which the suspension transmitted the most light intensity, relative to the current incident beam power. Then, we measured the refractive index of the test fluid at that optimal temperature to get the value of the particle refractive index.

Since refractive index is a function of the wavelength of the incident light, we used one of the beams from the LDV system as the incident beam (514.5 nm) to ensure we measured the relevant matching refractive index for our specific system. The Abbe refractometer could only measure the refractive index of the liquids at the wavelength of the sodium D line, or 589 nm, but we expected that two liquids that had the same refractive index at 589 nm would have nearly identical refractive indices at 514.5 nm, based on the data in the Cargille Specialty Optical Liquids catalog. Therefore, if the test liquid and the average lab temperature liquid have the same refractive index at 589 nm, in the Abbe refractometer, we expect them to have nearly identical refractive indices at 514.5 nm, in the LDV system.

In order to ensure our temperature measurements were accurate, we placed a thermometer in the water bath and checked that it agreed with the readings of a thermocouple (Omega, J-type) placed in the cuvette. From comparing the bath thermometer and cuvette thermocouple readings, we found it was necessary to wait 15 minutes for the cuvette to come to thermal equilibrium with the bath at each new temperature set by the bath controller and spaced our light intensity measurements accordingly.

We made measurements with three test fluids and used fresh particles each time. The results are shown in figure 3.6. We observed some variation in the optimal match refractive index among the three samples. We took the mean of the three values to be the measured particle refractive index and the standard deviation as the uncertainty, yielding a final value of 1.4880 ± 0.0007.

After completing this detailed process, in an ideal situation, we would be able to control the lab temperature in order that the refractive index match might be maintained. Unfortunately, the temperature in our lab does vary, but almost always keeps the fluid refractive index within the uncertainty range of the particle refractive index. Thermally isolating the flow cell is impractical due to the presence of the large aluminum inner cylinder which conducts heat efficiently and maintains the suspension at the current room temperature. We decided that it is sufficient to monitor the temperature in the fluid surrounding the concentric cylinders to indicate the current fluid refractive index.

3.2.4 Scattering Sites are Bubbles in Particles

With such an emphasis on refractive index matching in our system, an important question arises. How does LDV, which relies on scattering, collect any signals at all? If the refractive indices of the fluid and particles are perfectly matched, there is no scattering, since the light passes through both phases as if they are a single medium. The answer appears in the optical micrograph of the particles at 200x magnification in figure 3.7. The particles actually contain many tiny bubbles of monomer, trapped at the time of polymerization of the particles, which are in the size range 1 to 5 μm, about the right size for LDV scattering particles. These bubbles have a significantly different refractive index from the fluid and the bulk of the particles, and therefore are quite effective scatterers which provide the signals for LDV measurements. We made a rough visual estimate from optical micrographs that each particle contains about 125 scattering sites on average, which turned out to be an overestimate, and accordingly indicates an upper bound.

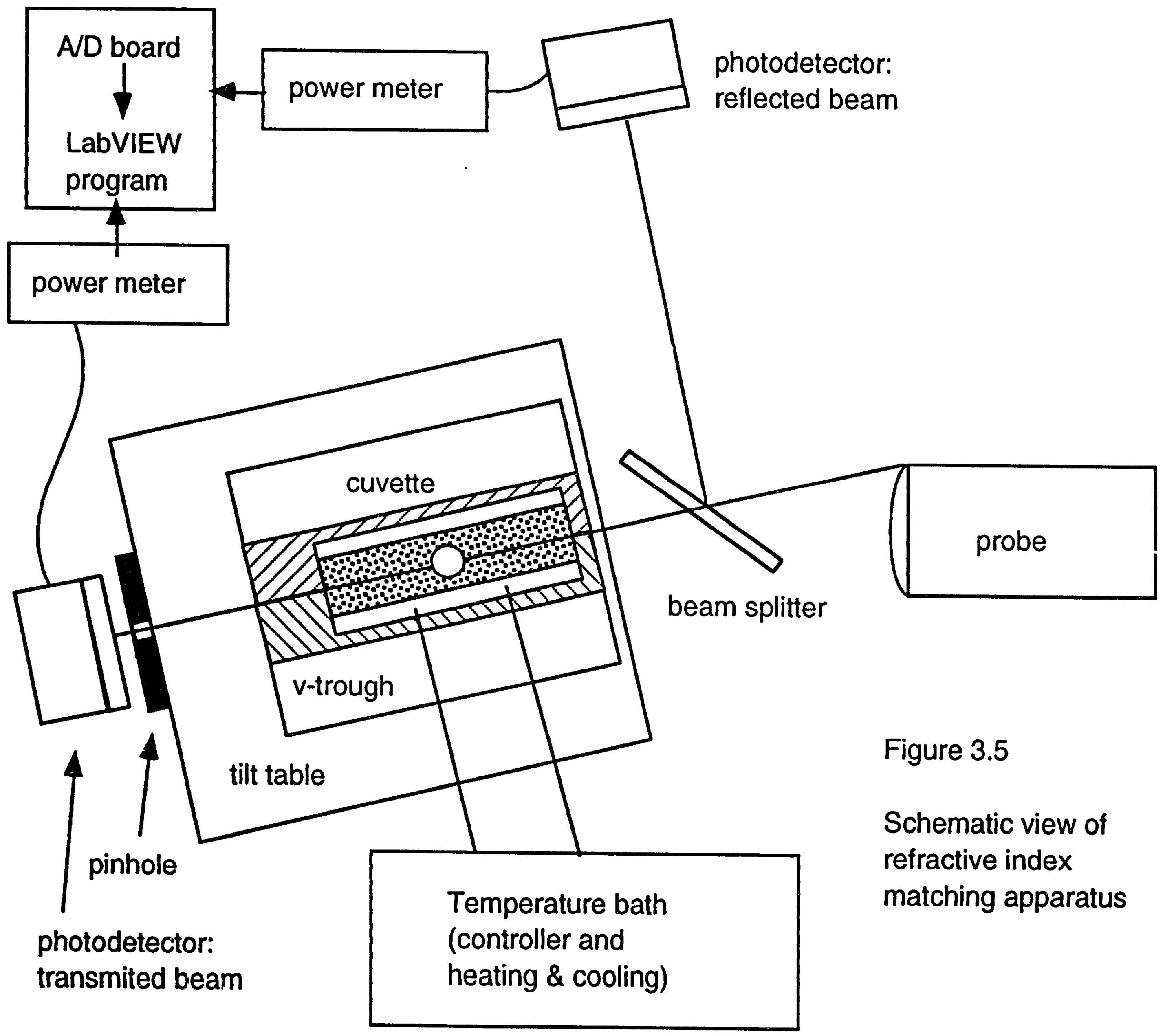

Figure 3.5

Schematic view of refractive index matching apparatus

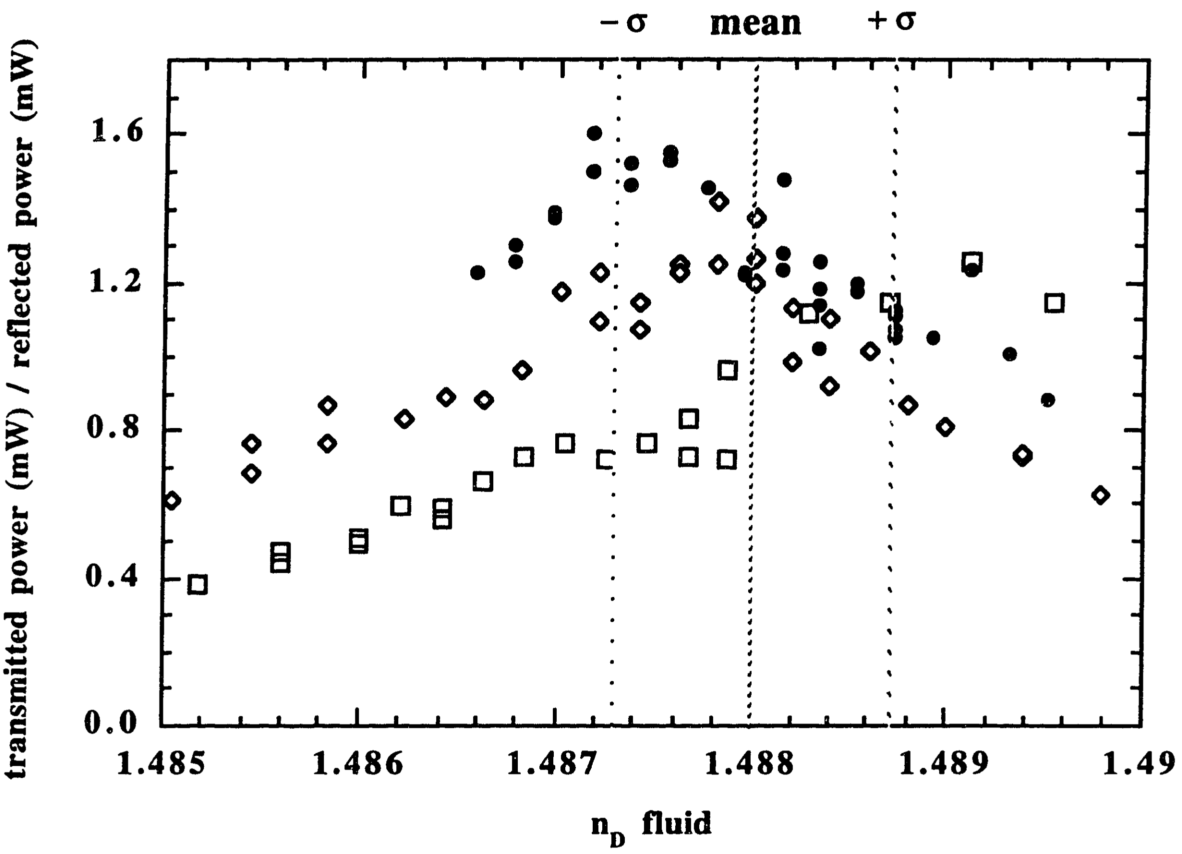

Figure 3.6 Plot of data sets from three refractive index matching runs, each with a different suspending liquid in the 2% concentrated test suspension. The average particle refractive index, computed from the average of the peak values, was 1.4880 ± 0.0007.

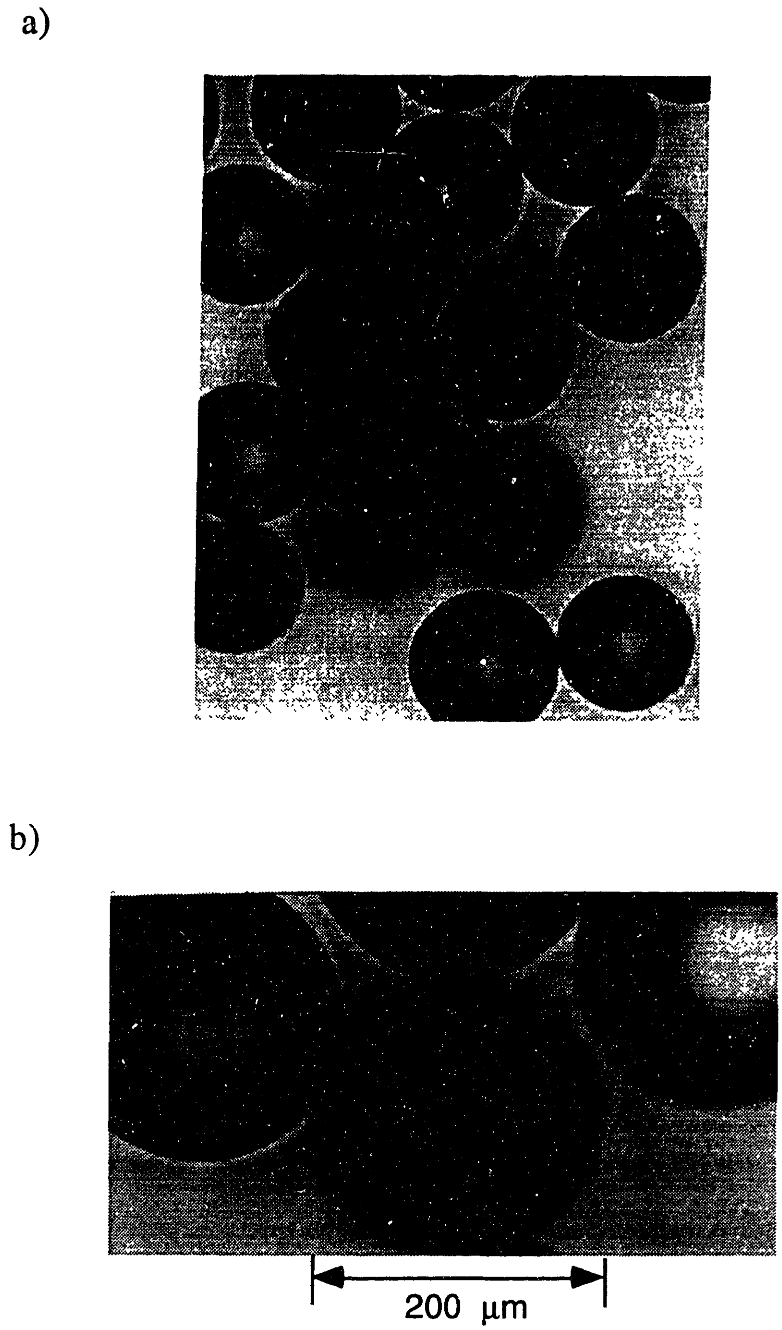

Figure 3.7 Optical micrographs of Lucite 47G particles, 180-212 μm diameter, revealing bubbles of monomer inside the particles which act as scattering sites.

a) 100x magnification ; b) 200x magnification.

3.3 Couette Flow Cell Design

The Couette cell is a device for generating simple shearing flow between concentric cylinders. The basic features of the design were modeled on an existing flow cell borrowed from Professor Howard Stone, in the Division of Engineering and Applied Sciences at Harvard University, which was built by Professor Sameer Madanshetty, Department of Mechanical and Aerospace Engineering Department, Boston University (Madanshetty et al., 1996), and used temporarily in our lab for some preliminary LDV experiments. Our design is shown in side view in figure 3.8(a) and in top view in figure 3.8(b).

The main common elements of the design are that the inner cylinder (1) is rotated by a motor (9) placed above the cylinder and connected to the cylinder by a shaft and coupling (10), and the outer cylinder (2) is stationary and transparent and acts as a window for a camera, or LDV. The top of the flow is open, which allows easy replacement of the suspension sample.

3.3.1 Dimensions

The main size constraints on the flow included making the gap wide enough to accomodate enough particles across so that the suspension properties would be independent of the gap width to particle diameter ratio, making the gap width to inner cylinder radius as small as possible to make the shear stress as uniform across the gap as possible, making the flow tall enough that vertical end effects would be negligible near the middle of the flow, and making the center to outer box wall perpendicular distance small enough that the incident LDV beams could intersect as far inside the flow as the cylinders' center, required for measuring the radial velocity fluctuations.

The key dimensions of the flow cell are as follows. The inner cylinder radius is 5.715 cm (2.25 in.), and cone angle at the bottom is about 6.4°. The outer cylinder inner radius is 6.31 cm, resulting in a gap width of 0.595 cm, which is 10.4% of the inner cylinder radius and about 30 particle diameters wide. This gap to inner cylinder radius ratio produces a nearly homogeneous shear flow with about 20% variation in the shear stress from the inner to the outer cylinder wall. The gap width of 30 particle diameters is above the minimum gap to diameter ratio of around 16-18 particle diameters (Koh et al., 1994; Hampton et al., 1997) at which the suspension flow can be considered a continuum. The average outer cylinder outer radius is 6.636 cm. The working height of the flow ranges from 19.6 to 19.8 cm, about 33 gap widths, which is tall enough that the flow near the midplane will be two-dimensional (Koh, 1991). The outer wall of the box (3) containing refractive index matching fluid is a minimum distance of 8.55 cm from the center of the inner cylinder. Typically, the annular gap is filled with about 530 ml of suspension and the box is filled slightly over halfway with 1100 ml matching fluid.

The dimensions of the flow cell resulted in the following values for several relevant dimensionles groups. The particle Reynolds number, given by

$$\mathrm{Re}_p = \frac{\rho \gamma a^2}{\eta_f} \simeq \left(1.4 \text{ x } 10^{-5} \text{ s}\right)\gamma \quad , \tag{3.15}$$

where γ ranges from about 0.8 to 15 s^{-1}, is small enough that the particles' inertia may be neglected. The Brownian Peclet number, given by

$$\mathrm{Pe}_B = \frac{6 \pi \eta_f a^3 \gamma}{k T} \simeq \left(3.8 \text{ x } 10^9 \text{ s}\right)\gamma \ , \tag{3.16}$$

has a very large value, which indicates unambiguously that Brownian and colloidal forces are negligible in this flow. The overall flow Reynolds number,

$$\mathrm{Re} = \frac{\rho U (R_{\text{outer}} - R_{\text{inner}})}{\eta} \quad , \tag{3.17}$$

ranges from a minimum of 0.009 for a 50% concentrated suspension at 2 rpm to a maximum of 0.725 for a 2% suspension at 15 rpm. The Taylor number, which indicates when a Couette inertial instability will occur, is given by

$$\mathrm{Ta} = 2 \left(\frac{V_{\text{inner}} (R_{\text{outer}} - R_{\text{inner}})\, \rho}{\eta}\right)^2 \frac{(R_{\text{outer}} - R_{\text{inner}})}{R_{\text{inner}}} \simeq \left(5.38 \text{ x } 10^{-4}\right) (\text{rpm speed})^2 \tag{3.18}$$

for the pure suspending liquid. For the maximum rotation speed of 15 rpm, Ta is approximately 0.12, which is much less than the critical value of 3416 for the first onset of unstable flow (Kundu, 1990). Consequently, the flow was never susceptible to the Couette inertial instability during any of these experiments.

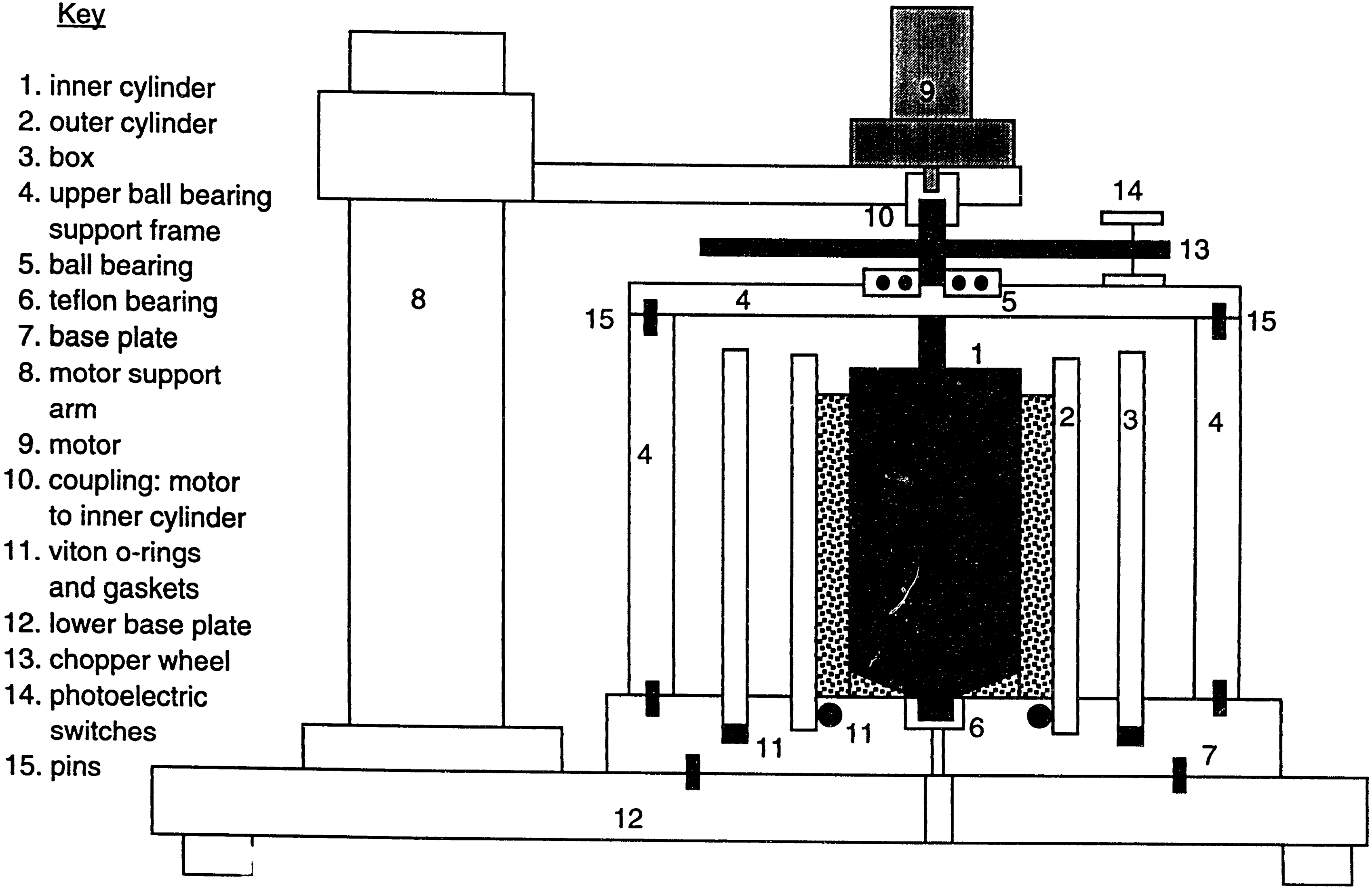

Figure 3.8. a) Schematic side view of Couette flow apparatus

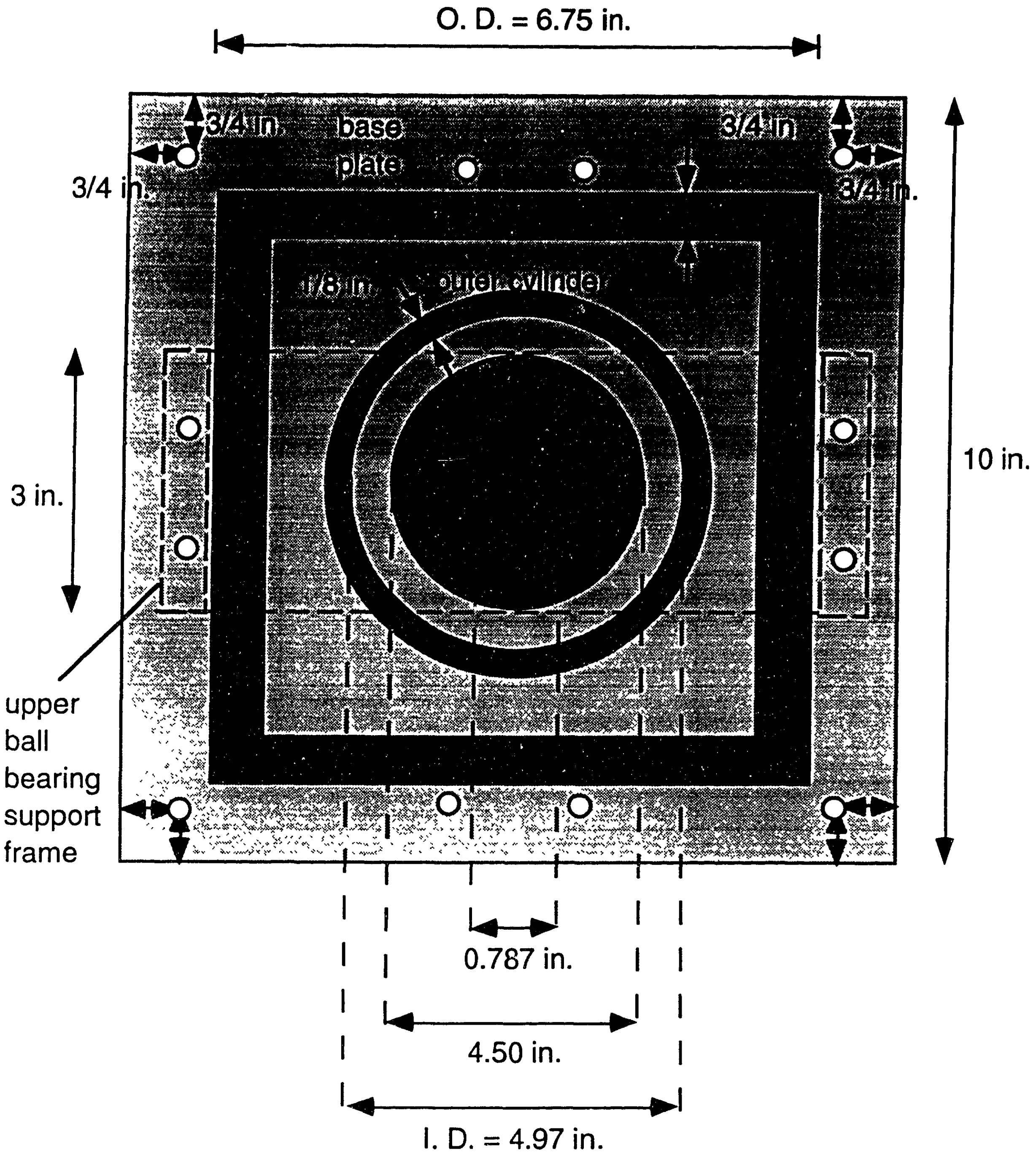

Figure 3.8. b) Top view of Couette flow cell

3.3.2 Parts and Materials

The parts of the apparatus that were purchased complete were the motor and controller (9) (Motomatic II Servo Amplifier with E286 matching gearmotor, with 50:1 gear reduction, Electro-Craft/Rockwell Automation),the ball bearing (5) (Hoover-NSK), and the photoelectric switches (14) (Idec Corp.). The motor was rated with maximum speed 100 rpm and maximum torque 55 lb-in. The MIT Central Machine Shop built all the metal parts, which were made of aluminum, including the inner cylinder (1), coupling connecting the shaft to the motor (10), base plate (7), lower base plate (12), motor support arm (8), upper ball bearing support frame (4), chopper wheel on shaft (13), and tilt table. The inner cylinder was black anodized to reduce reflections of the incident and scattered laser light. The teflon bearing (6) supporting the bottom of the rotating inner cylinder was machined by Dan-Kar Corporation, and all the other plastic parts, including the Lucite outer cylinder and the Lucite box, were built by Altec Plastics.

3.3.3 Important Design Features

The goal in designing the new Couette cell was to insure that the flow would be as spatially homogeneous as possible, in order to mimic a theoretical homogeneous shear flow, and that the mean flow velocity would not fluctuate in time once the flow reached a steady state, so that the observed velocity fluctuations would only come from inter-particle collisions. There are four important design features that made the Couette cell able to create as homogeneous and steady a flow as possible and to handle the suspension materials: fixed alignment of the inner cylinder and motor, concentricity of the cylinders, inner cylinder conical bottom, and proper sealing of the outer cylinder and box.

First, the inner cylinder is fixed at both ends, held at the top by the ball bearing, and at the bottom by the teflon bearing; the axis of the cylinder is very accurately aligned with the motor shaft axis by means of the coupling. Whereas the inner cylinder sits in the lower teflon bearing, the upper ball bearing is pressed on to the inner cylinder shaft and also into the bearing support frame, which is connected to the base plate. The arms of the bearing support frame are connected with pins as well as screws to prevent them from acting like hinges, lending the frame extra resistance to bending. The precise and rigid alignment of the inner cylinder and the motor limits runout, or horizontal displacement during rotation, of the inner cylinder to only 38 μm, or 0.6% of the gap width. When the annular gap is filled with suspension, runout can also lead to fluctuations in the suspension surface height, as one side of the gap becomes slightly narrower and the other side becomes slightly wider. For a 50% concentrated suspension at 15 rpm, the surface height variation over a revolution was about 1mm and at 10 rpm and lower speeds was 0.5 mm or less, basically undetectable, over a rest surface height of 19.6 cm, a fractional change of about 0.5% or less. Because these horizontal and vertical fluctuations due to inner cylinder displacement are negligible, we can claim that the inner cylinder is driving the flow in a steady and axisymmetric manner, and does not create mean flow fluctuations. This is important because it would be undesirable for mean flow velocity fluctuations to inflate the velocity fluctuations measured at a point in the flow.

Another feature is intended to make the flow as spatially homogeneous as possible. The inner radius of the outer cylinder is made concentric with the inner cylinder axis, according to the groove for the cylinder bottom cut into the base plate. This may seem like a trivial point, but actually the outer cylinder was cut from a single piece of Lucite tubing, in which the extrusion process often causes the inner and outer surfaces to be two cylinders which are not concentric. The variation in tube wall thickness around the tube circumference is visible to the eye. So, making the average radius or the outer radius concentric with the inner cylinder will yield an eccentric flow, which is undesirable in this case. The top of the outer cylinder is free to move and is aligned with the bottom by a set of adjustable viton rubber shims placed between the box inner wall and the outer wall of the outer cylinder. Even if the outer and inner cylinders are not perfectly concentric, that is a steady flow feature in the laboratory reference frame, not a fluctuation, and does not affect our fluctuation measurements. In our original measurements, the outer cylinder radius varied at most by ± 2% of the gap size (when the outer cylinder average radius was made concentric with the inner cylinder axis). After a later modification to improve the concentricity by shifting the outer cylinder groove, the variation in radius was even less, estimated at maximum ± 1% of the gap size.

In the worst case scenario, for the 50% concentrated suspension, we observed a steady surface height displacement from the rest height of 19.6 cm of 2, 4.5, and 6 mm for rotation speeds of 5, 10, and 15 rpm, respectively. That represents a fixed surface height displacement of only 1-3% of the rest height. For lower concentrations, we observed even less displacement.

An additional feature intended to make the flow as spatially homogeneous as possible is the conical bottom of the inner cylinder, modeled after the Couette design of Quinzani (1991). This is designed to make the shear rate more uniform throughout the flow. If the cylinder were straight along its entire length, the shear rate would be higher than average near the bottom of the flow, since there is an extra velocity gradient in the vertical direction due to the base of the flow cell, and the shear rate would be lower than average at the top, where the free surface lies. This shear rate gradient could produce an nonuniform particle concentration profile in the vertical direction, which we wish to avoid. For example, in the experiments of Leighton and Acrivos (1987b) and Chow et al. (1994), particles in narrow-gap Couette flow were observed to migrate axially into a stagnant region below the shearing apparatus and greatly enhance the local concentration there. Consequently, the bottom of the inner cylinder is machined into a conical shape, so that the bottom of the flow resembles a truncated cone and plate flow. The cone angle is chosen so that the average shear rate in the annular gap above equals the average cone and plate shear rate in the cone gap below. The cone and plate flow is truncated in order to avoid particles lodging in the narrowest part of the cone, so that the narrowest part of the cone is at least 1 mm, or 5 particle diameters, tall, at a radius of 1.27 cm. This results in a slightly lower shear rate in the cone and plate compared with the annular gap above, but the difference is at most about 7% of the average shear rate.

Finally, the method of sealing the flow cell was adapted to accomodate the unusual organic solvents in the refractive index matching fluid. 1,6 dibromohexane swells and weakens methyl chloride and silicone glue, which are the standard sealants for joining plexiglass parts or plexiglass and metal parts, respectively. In contrast, viton, a fluoropolymer, resists halogenated hydrocarbons like 1,6 Dibromohexane. Accordingly, the Lucite outer cylinder and box are sealed on the sides and bottom with viton o-rings and gaskets (11) (Greene Rubber Co.) .

One extra feature to note is that the design is modular, with the intent that multiple geometries can be studied without rebuilding the entire apparatus. Future experiments with wide gap Couette flow, eccentric cylinders, or Couette flow with an obstruction would require only a new or modified baseplate, new outer cylinder, and possibly a new box.

3.3.4 Alignment of the Couette Device

The whole Couette device is attached to the lower baseplate, which is clamped to the tilt table below. The tilt table allows the Couette flow cell to be leveled with respect to the optical table (Newport, model RP Reliance) it is secured to and can be used to adjust the height of the flow. The tilt table has a kinematic design, with three adjustable legs, and two extra legs to prevent toppling that retract during alignment. The tilt table may be the least rigid part of the apparatus, and may allow for undesired vibration of the entire Couette device as a rigid body. However, if there are vibrations, they should be consistent between suspension experiments, since the Couette cell remained tightly clamped in a fixed position on the tilt table, for nearly all the experiments presented here, and the tilt table legs remained locked in one position.

After the Couette device was assembled and the base plate leveled with respect to the optical table using the mobile tilt table and a spirit level indicator, the Couette cell and LDV probe were aligned. The idea was to align the probe and inner cylinder once while the flow device was empty, or only filled with a Newtonian fluid, and then subsequently to align the two cylinders each time the system was refilled with a new suspension. We assumed that the box and inner cylinder axes were parallel, since they both fit into carefully machined grooves in the base plate, and the box was tightly bolted to the plate. We aligned the probe with the box by taping a flat mirror firmly on the outer box wall, shining the LDV beams on to the mirror so that they met exactly on the mirror surface, and checking that each reflected beam overlapped with the other incident beam, which we determined by comparing the incident and reflected dots on a translucent surface. The probe could be rotated about its own axis (angle ϕ) to direct the two incident beams in a horizontal or a vertical plane. When there was a discrepancy between the incident and reflected beams in the vertical plane, we were able to make very fine adjustments by tilting the probe (angle θ) until the beams overlapped. The probe orientation in the horizontal plane was fixed, so we had to rotate the Couette cell and clamp it in a new position on the tilt table to align the incident and reflected beams.

Next, the edges of the inner cylinder were located by shining the beams in a vertical plane toward the inner cylinder when the annular gap was empty or filled with a dilute suspension. A piece of white paper was taped on the back wall of the box so that the spots created by the two beams passing through the device were clearly visible. The beams were translated from one edge to the other until the positions where the spots were equally bright on each side were found. Then, the midpoint between these positions was defined as the center of the inner cylinder.

Subsequently, the probe was moved to the center line and the beams were directed in a horizontal plane. The inner cylinder wall was located by moving the beams inward and outward until the far and near ends of the intersection volume were observed to touch the inner cylinder wall. The midpoint between these two recorded positions was identified as the middle of the intersection volume touching the inner cylinder wall.

Finally, we checked the alignment of angle ϕ. The beams were moved to the center line and directed in an approximately horizontal plane. We measured the tangential velocity while slightly varying the angle about the approximate horizontal value. We identified the proper angle, in which the beams were directed in a horizontal plane relative to the flow, with the maximum mean velocity value we measured. Once these alignment steps were completed, the Couette device remained clamped to the tilt table in fixed position and the LDV probe angles were never reset.

3.3.5 Measuring the Inner Cylinder Rotation Rate

We time the rotation rate of the inner cylinder independently for each run. A chopper wheel with four blades made of black delrin (13) is fixed on the shaft of the inner cylinder. A pair of photoelectric switches (14) (Idec Corp.) is fixed at one radial position so that the chopper wheel blades pass between them. One photoelectric switch sends out a beam, and the other receives it. When the unobstructed beam strikes the receiver, it produces a constant positive DC voltage. When the beam is obstructed, the receiver produces zero voltage. Consequently, when the blades chop the beam, the receiver signal looks like a series of step functions.

The photoelectric switches are connected to our Mac Quadra 800 computer through an A/D board (National Instruments) where the original analog voltage signal is digitized and read by LabVIEW (version 3.0). A LabVIEW program written by David Lee uses the step function signal to time the period of one full revolution. The first step change in voltage zeroes the timer. The next step change in voltage triggers the timer to start, and then the timer runs for eight more step changes, and finally displays the total time recorded for all four blades to pass the beam. A driver program also written by David Lee runs the timer program for a selected time interval and records the timed period of each revolution in a text file.

Because the inner cylinder rotation speed is measured with a method completely independent of LDV, the inner cylinder can be used to test the accuracy of LDV (i.e. how different is the mean LDV velocity we measure from the true velocity?). Since the rotation period and inner cylinder radius are known accurately, the velocity at the surface of the inner cylinder is known precisely, and can be compared with the mean LDV velocity we measure. We tested a range of speeds (0.3 to 60 rpm/ 0.16 to 36.6 cm/s) without fluid and (0.7 to 10 rpm/ 0.42 to 6 cm/s) with fluid in the Couette gap, and found that LDV has an overall accuracy of ± 2.5%. This is typical for LDV (Genieser, 1997; Liu, 1997).

3.4 Measurement Procedures

3.4.1 Suspension Loading Procedure

First, the three component fluid with mass fractions specified above was thoroughly mixed, and the particles were sieved. Since the fluid and particles have almost identical densities, particle mass fraction and particle volume fraction of the suspension are the same, so the desired particle volume fraction was attained for each suspension by putting together fluid and particles in corresponding mass fractions. The fluid and particles were vigorously stirred by hand and degassed in a vacuum oven (VWR) for up to 4 hours, with the very viscous concentrated suspensions requiring the most time to degas. It was important to get the bubbles out of the suspension so that they did not affect the suspension rheology and so that the LDV did not mistake scattering coming from tiny bubbles in the fluid for scattering coming from suspended particles. The suspension was poured down the walls of the cylinders into the gap, in a further attempt to avoid bubble formation, and a bleed valve screw underneath the lower teflon bearing prevented air from being trapped during pouring or from being drawn into the flow during rotation.

After the suspension was poured into the annular gap of the Couette cell, the outer cylinder was realigned with the inner cylinder to produce minimum suspension surface height variations around the cylinder. Whereas the bottom of the outer cylinder was fixed in a groove and sealed with an o-ring, the top was free to move. We fixed the position of the top of the outer cylinder by fitting shims in between the outer wall of the outer cylinder and the inner wall of the box.

3.4.2 Steady State Measurements

All the measurements presented here were made when the velocity and particle concentration profiles had reached steady state. Nott and Brady (1994) estimate the time required for the coupled particle concentration and velocity profiles to reach steady state as follows,

$$t_{ss} \sim \left(\frac{H}{a}\right)^2 \frac{1}{4\, d(\phi)\, \gamma_{avg}} \sim \left(\frac{H}{a}\right)^2 \frac{3}{\gamma_{avg}} \qquad (3.19)$$

where H is the gap width, γ_{avg} is the average suspension shear rate in the gap, and $d(\phi)$ indicates the dependence of the particle self-diffusivity on particle volume fraction. Based on the experimental results of Leighton and Acrivos (1987a), Phung (1993) and Phan and Leighton (1994), Nott and Brady approximate the value of 12 $d(\phi)$ as 1 for concentrated suspensions. For the dimensions of our flow, the time to reach steady state was approximately 18 minutes for a 30%, 40% or 50% concentrated suspension at 10 rpm. We always ran the Couette device at the speed of interest for at least 50 minutes before starting the velocity measurements, usually starting with the high speeds (5-15 rpm). The velocity fluctuation measurements typically lasted 16 minutes each, with some series of measurements lasting several hours. A useful feature of non-colloidal suspensions is that since Brownian motion is absent, once the flow is stopped, the particles are "frozen" in place, and remain distributed in the steady state arrangement. The only phenomenon that can disturb this arrangement is settling of the particles.

Because the particles are slightly negatively buoyant in the fluid, we observed slight settling overnight. To resuspend the particles, we ran the Couette flow at 10 rpm for an hour before almost every series of measurements, and ran the Couette at 10 rpm or higher speeds for several hours on days when experiments were not performed (Gadala-Maria and Acrivos, 1979; Leighton and Acrivos, 1986; Krishnan, 1994). During the course of an experiment, the shearing flow counteracted settling, and no detectable negative mean vertical velocity was observed at any point.

The reason steady state measurements are attractive is that they are the most easily reproducible. In Chapter 4, we verify reproducibility of these measurements. In a concentrated non-colloidal suspension, the initial condition of a homogeneous mixture of fluid and particles is needed for well-defined transient experiments, but is extremely difficult to duplicate, for several reasons. First, once the steady state concentration profile has formed, it remains, which means that starting from a homogenous suspension again involves removing the suspension, mixing, degassing, and pouring it into the Couette again. Also, there is no opportunity for realignment of the outer cylinder, since that involves shearing as well, so the flow may not be exactly the same. Finally, during pouring, some particle migration occurs, which may be different from run to run, and has been observed to result in an initially non uniform concentration profile (Chow et al., 1994). For all these reasons, steady-state measurements are more reliable than transient measurements.

3.4.3 Measurement of Three Velocity Components

We measure the mean and fluctuating velocities in two locations in the flow, as shown in figure 3.9. We measure the tangential and vertical velocity at the place closest to the probe, labeled 0°, and scan across the gap forward and backward. We measure the radial and vertical velocity at a location on the side of the flow, labeled 90°, and we scan across the gap left to right. The whole

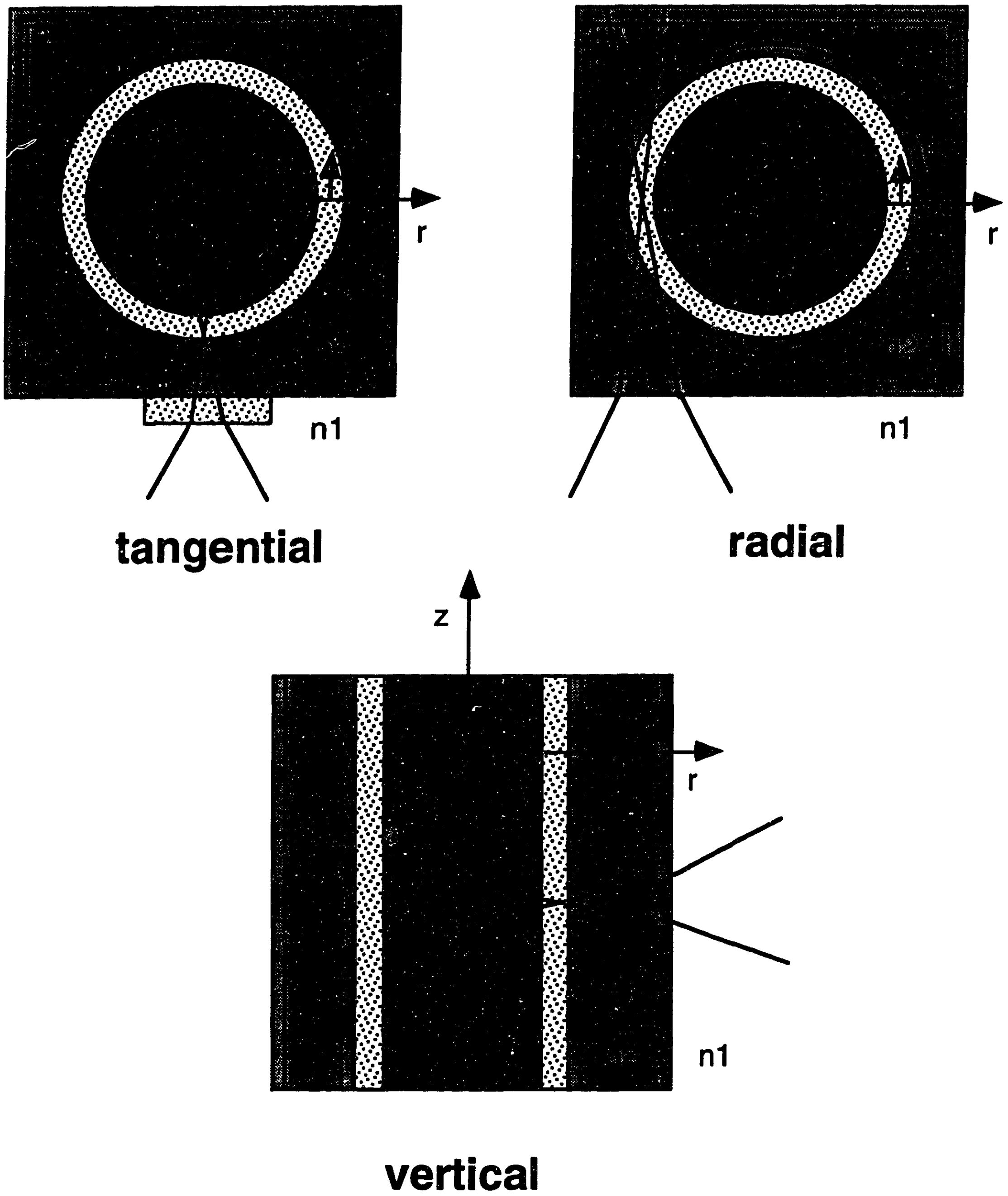

Figure 3.9 Orientation of the LDV beams for measuring each velocity component in Couette flow

flow is enclosed in a square Lucite box, filled with a fluid that matches the refractive index of the Lucite walls so that velocities can be measured at points off of the 0° axis.

The refractive index matching fluid was a mixture of Triton X-100 and 1,6 dibromohexane, since those components were already known to match PMMA closely, and were compatible with the suspending fluid in case any leaks occurred. The walls of the box and outer cylinder actually have a slightly different refractive index from the particles, even though the materials are nominally the same. This is likely due to orientation of the PMMA molecules during extrusion of the Lucite tubing and sheets or slight differences in composition. The proper refractive index for the box fluid was found through a less exact method than that used for the suspending fluid. The method involved tuning a test fluid by adding small amounts of dibromohexane in order to make a piece of Lucite sitting in the fluid appear the least visible to the eye in ambient daylight. The composition of the optimal test fluid consisted of mass fractions: 97.4% Triton X-100 and 2.6% 1,6 dibromohexane. Later, the refractive index of the mixture was measured and found to be 1.491 at the average laboratory temperature of 22° C.

Another important point is that the beams become attenuated as they pass through the suspension, due to scattering by imperfections in the particles, some of which are on the order of the particle size. This limits the region of points we can access in the 90° position, since the beams must pass through a much longer path through the suspension there than at the 0° position. The most accessible 90° points are on the outer edge. All the measurements, aside from a few vertical scans, were taken at a height of 9.5 cm above the base plate surface, about 0.5 cm below the midpoint of the suspension height.

3.4.4 Verification that the Number of Bursts Collected is Statistically Significant

In order to check that we were collecting a statistically significant number of bursts for calculating the mean and standard deviation of the velocity distribution, we repeated measurements of the same point in a 50% concentrated suspension, collecting varying numbers of bursts. Since the 50% concentrated suspension has the most frequent collisions at a given shear rate, it has the largest amount of random motion, and is therefore the suspension for which the statistics question is the most relevant. We measured the tangential velocity at the 0° location and in the center of the gap, where we could collect arbitrary numbers of bursts in a reasonable amount of time. We made three measurements collecting 5000 bursts each, and used this as an ideal value of the mean and standard deviation. We found, from the data shown in figure 3.10, that the mean velocity approached the ideal value for runs where at least 1000 bursts were collected, and that the standard deviation approached the ideal value for runs where at least 1000 bursts were collected, but was much closer where 3000 bursts were collected.

For all the 30%-50% concentrated suspension runs, we tried to collect as many bursts as possible in the measuring time limit of 1000 seconds. When there were runs with fewer than 1000 bursts collected, we grouped all the data from several of these runs and found the mean and standard deviation of this combined distribution. The combined distribution almost always had at least 1000 bursts. We added an extra term to the uncertainty in the average standard deviation, which was the standard deviation of the set of standard deviations from the original runs. This procedure typically applied to the radial velocity, where we often measured very few signals during each run. When there were multiple runs at the same speed and location with more than 1000 bursts each, we considered each an independent run, and averaged the set of mean and standard deviation values only. In this case we did not give the runs with more points greater weight in the average, because we considered them all equally valid. This procedure typically applied to the vertical and tangential velocities.

3.4.5 Handling Irregularities in the LDV Velocity Distributions

Some of the velocity distributions we collected contained outliers, single points or groups of points that were far from the main Gaussian-like peak in the histogram, shown schematically in figure 3.11. We believe these outliers are spurious signals, since many of them indicate highly improbable velocities that correspond to the limits of the LDV frequency bandwidth, which a)

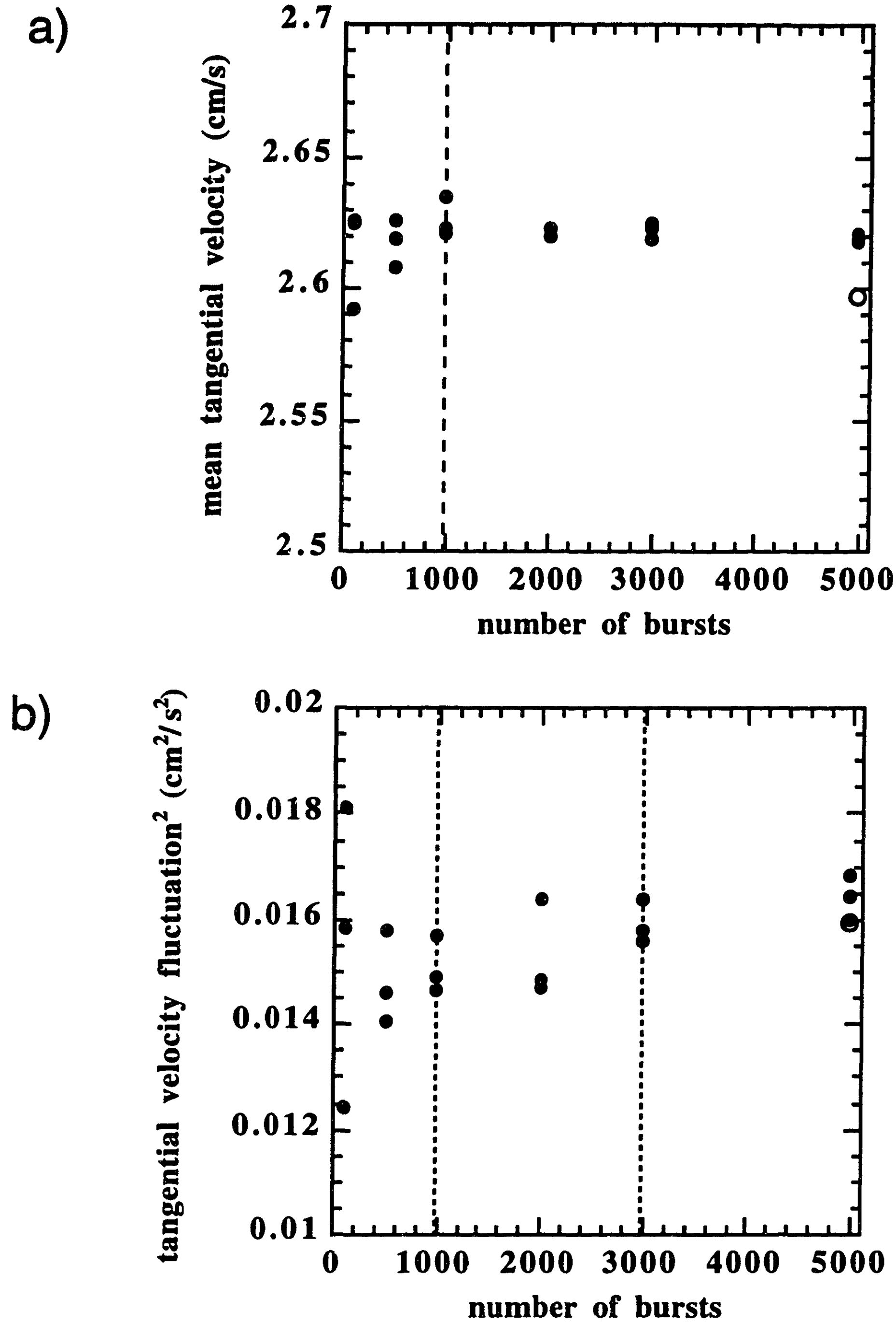

has

Figure 3.10 Repeated measurements in a 50% concentrated suspension at the 0° location, $r/R_o = 0.954$, average shear rate = 10 s^{-1}. The solid circles represent repeated measurements with varying numbers of bursts collected. The hollow circles represent a measurement from another day where 5000 bursts were collected.
a) Mean tangential velocity plotted against number of bursts
b) (Tangential velocity fluctuation)^2 plotted against number of bursts

a) outlier

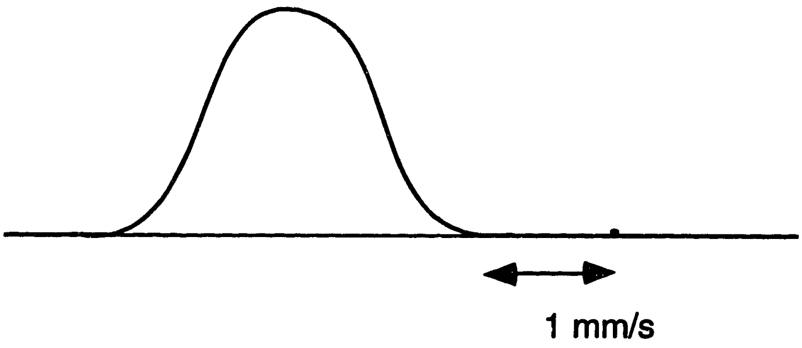

b) tail

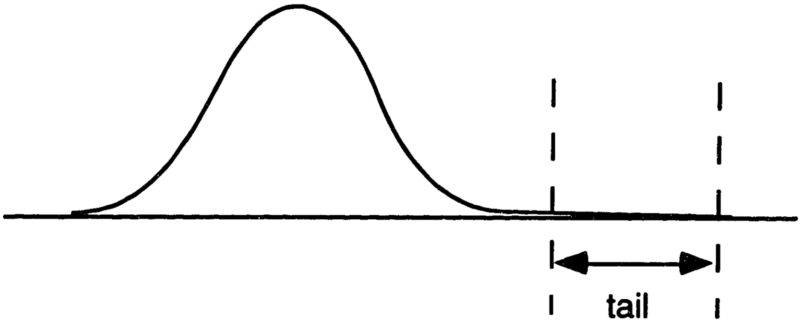

c) bimodal

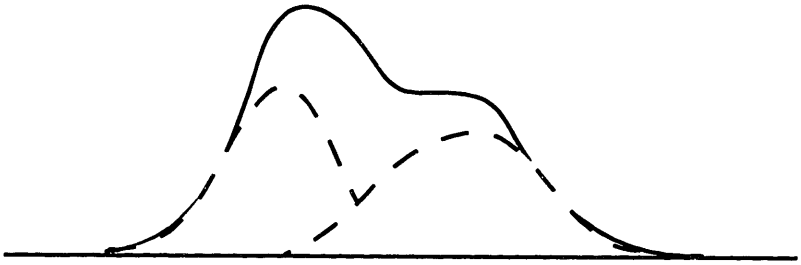

Figure 3.11 Sketch of irregularities found in LDV velocity distributions

nothing to do with the flow we are measuring. The rule that we applied consistently to all the data files was that we removed any velocity points that were separated from the majority of the distribution by a gap in velocity of 1 mm/s or more. We chose 1 mm/s as the cutoff interval because it was greater than or equal to almost all of the standard deviation values we measured. Effectively, we were removing points that were separated from the edge of the main curve by at least one standard deviation.

In the dilute 2% suspension, some of the velocity distributions measured at the 90° location had long tails on one side of the histogram. Not all the points in the tails were outliers, because they were not separated from the rest of the peak by as much as 1 mm/s. We also believed that the tails were spurious data, because they were clearly associated with noisy LDV signals, usually at points that were close to the outer edge of the flow, where the highly amplified BSA parameters we were using were not optimal. This was especially a problem for radial velocities of points at the +90° location in the flow. Here, our goal was to make the distributions as symmetrical as possible. We only removed points from the tail that were farther away from the mean than the farthest points on the other side of the peak, and that were separated from the main peak by a significant gap (~0.3 mm/s) in velocity between points in the tail.

The final irregularity we encountered in the velocity distributions was the presence of zero peaks in the tangential velocity data we collected from the 30%, 40% and 50% concentrated suspensions. Each velocity distibution contained a peak about zero, and about a nonzero value, yielding a bimodal velocity distribution. We suspect the zero peaks are detected because the measuring volume is touching the outer cylinder wall, or a layer of particles or fluid immediately adjacent to it. A further discussion of the source of the zero peaks continues in section 3.5.3.7.

In order to separate the zero and nonzero peaks, which often overlapped, we binned the data into the smoothest histogram attainable and fit each resulting bimodal distribution with the sum of two Gaussian curves, where the means, standard deviations, and peak heights were adjustable parameters. The fitting routine was a least-squares fit in Kaleidagraph 3.0 on the Mac Quadra 800. First, we made an initial guess of the mean and standard deviation values and found the best fit peak heights. Then, we optimized all the parameters together starting from the initial guess. We identified the mean and standard deviation of the nonzero velocity peak as the correct values associated with that run. We also incorporated the error in the double Gaussian fit into the uncertainty estimate for runs with zero peaks.

3.5 Data Reduction Method

3.5.1 Shear Rate

We calculate the shear rate as a function of radial position for the 30%, 40%, and 50% concentrated suspensions in three steps. First, we measure the mean tangential velocity profile with 20-30 points across the gap. Then, we divide the flow in half into an inner and outer region, and define a third, middle region that overlaps with about half of each of the inner and outer regions. We find a quadratic fit of the mean velocity profile $u_\theta(r) = A + B\,r + C\,r^2$ in each of the regions, with typical R^2 values ranging from 0.995 to 0.9998. We differentiate the fits in r, and then use the relation: $|\dot{\gamma}| = \left| r \frac{d}{dr}\left(\frac{u_\theta}{r}\right) \right| = \frac{A}{r} - C\,r$ to calculate the shear rate profile in each region. We join the three shear rate profiles at the points where they intersect with each other into a single piecewise continuous profile that covers the whole gap.

For the seeded Newtonian liquid, dilute 2% concentrated suspension and semi-dilute 10% concentrated suspension, the most accurate fits of the velocity profile (based on R^2 values) that we could find actually were global fits involving all the points across the entire gap together. In these cases, we followed the same steps as above, except that we did not divide the flow into regions.

3.5.2 Concentration

We estimate the relative particle concentration profile from the calculated shear rate profile. Mathematically, the shear stress must decrease as $\frac{1}{r^2}$ across the gap, according to the tangential component of the momentum equation. The ratio of the local shear stress to the local shear rate yields a profile of the local suspension viscosity. If we assume that the Krieger viscosity function

(Krieger, 1972), given as

$$\eta(\phi) = \left(1 - \frac{\phi}{\phi_m}\right)^{-1.82} \tag{3.20}$$

describes the relation between the particle concentration and the suspension viscosity, then from the local viscosity profile we can calculate a local concentration profile. This is only a relative concentration profile, however, because we don't measure the absolute magnitude of the stress. We normalize the relative concentration profile so that the average concentration is the bulk concentration.

We can compare the results from this method to the method of Lyon and Leal (1998) of measuring concentration by timing the separation between adjacent LDV bursts. They estimate the average separation between consecutive particles crossing the measuring volume as the average product of the time between the consecutive particles crossing the measuring volume and the velocity of the latter particle.

$$\bar{r}(r) \sim \frac{1}{N-1} \sum_{i=2}^{N} v_{p_i} t_{bd_i} = \overline{v_p(r) t_{bd}(r)} \tag{3.21}$$

Since the average particle volume fraction $\bar{\phi}(r)$ at point x is inversely proportional to the local average particle separation distance,

$$\bar{\phi}(r) = \frac{k}{\overline{v_p(r)\, t_{bd}(r)}} \tag{3.22}$$

The value of k is found by normalization of the concentration profile so that the total volume flux of particles matches the known value. In our case, we normalize by setting the average value of $\bar{\phi}(x)$ to the bulk particle volume fraction value.

$$\phi_{bulk} = \frac{1}{\pi \left(R_{outer}^2 - R_{inner}^2\right)} \int_{R_{inner}}^{R_{outer}} \bar{\phi}(r)\, 2\, \pi\, r\, dr \tag{3.23}$$

We find that their method does not agree with the stress-shear rate method mentioned above. The discrepancy lies in the interpretation of the time between bursts. We find this depends strongly on the choice of LDV parameters. Since we only use one set of parameters when measuring the tangential velocity profile, it is an optimal setting for some radii but not others. For example, in a run with a 50% concentrated suspension, the data rate near the inner cylinder wall was low, because the beams had to pass through a lot of scattering material. The data rate in the middle of the gap was higher, with the amplification being just right for those bursts. For points near the edge, the bursts were over-amplified, leading to some of the noisy ones being rejected and causing the data rate to be lower. If we use the LDV timing method to measure the concentration here, we find it is highest in the center and lower at the walls. This contradicts the NMR measurements of Abbott (1991) and Graham (1991), so we believe it is incorrect.

In constrast, Koh et al. (1994) and Lyon and Leal (1998) were satisfied with the concentration profile predictions of this method for channel flow. We believe that the difference in flow geometries caused us to have different evaluations of the method. Their channel gap widths were 1.0 and 1.7 mm (11 to 24 particle diameters wide), compared with our 6.31 mm (30 particle diameters wide), so for their flow the same LDV parameters may have been optimal all the way across the gap, and the time intervals between adjacent bursts they measured truly reflected the spacing between adjacent particles.

3.5.3 Particle Velocity Fluctuations

The velocity fluctuation we measure, which is the standard deviation of the measured velocity distribution, includes contributions from particle rotation, LDV noise, and equipment vibration in addition to the suspension temperature, which is the velocity fluctuation caused by inter-particle collisions. Particle rotation results from the vorticity in the flow and contributes to the velocity fluctuation due to the presence of off-center scattering sites within the particles. The LDV noise contribution comes from two sources. The first is noise in the photomultiplier, which is affected by the user-selected signal amplification and bandwidth parameters. The second source of LDV noise is gradients in the mean velocity within the finite-sized measuring volume. This source is most significant for the tangential velocity. The equipment vibration contribution appears because the Couette apparatus is not completely rigid and moves slightly horizontally and vertically as the motor turns. Hence, we must distinguish the collisional velocity fluctuations (the suspension temperature) from the other terms.

3.5.3.1 Fluctuations Arising from Mean Particle Rotation

The mean particle rotation contribution has the same shear rate scaling as the collision contribution, so we cannot eliminate it by a choice of the shear rate regime. However, we believe that particle rotation is a weak function of particle concentration, because its origin is the vorticity of the flow.

We estimate the rotational contribution to the velocity fluctuation by assuming that scattering sites are distributed uniformly throughout a particle which is rotating with the mean flow vorticity, with angular velocity $\omega = 1/2\,\dot\gamma$. The density of scattering sites is n per unit volume, in a particle of radius a.

$$\langle v_\theta'^2 \rangle_{rot} = \frac{1}{N} \sum_i (\underline{v}_{i\,rot} \cdot \underline{\delta}_\theta)^2 \tag{3.24}$$

$$\langle v_\theta'^2 \rangle_{rot} = \frac{1}{nV} \int_V n\, dV\, (\underline{v}_{rot} \cdot \underline{\delta}_\theta)^2 \tag{3.25}$$

Expanding the velocity and unit vector in the spherical coordinates of the particle yields

$$\langle v_\theta'^2 \rangle_{rot} = \frac{1}{V} \int_V dV\, [\, (\omega\, r \sin\Theta\, \underline{\delta}_\Phi) \cdot (\sin\Theta \sin\Phi\, \underline{\delta}_r + \cos\Theta \sin\Phi\, \underline{\delta}_\Theta + \cos\Phi\, \underline{\delta}_\Phi)\,]^2 \tag{3.26}$$

where the polar axis is aligned along the cylinder axis (z). Since the unit vectors are orthogonal, only one term survives.

$$\langle v_\theta'^2 \rangle_{rot} = \frac{1}{V} \int_V r^2 \sin\Theta\, dr\, d\Theta\, d\Phi\, [\omega\, r \sin\Theta \cos\Phi\,]^2 \tag{3.27}$$

$$\langle v_\theta'^2 \rangle_{rot} = \frac{\omega^2}{4/3\,\pi\, a^3} \int_{r=0}^{a} r^4\, dr \int_{\Theta=0}^{\pi} \sin^3\Theta\, d\Theta \int_{\Phi=0}^{2\pi} \cos^2\Phi\, d\Phi \tag{3.28}$$

After integration, this expression yields

$$\langle v_\theta'^2 \rangle_{rot} = \frac{1}{10}\, a^2 \omega^2 = \frac{1}{40}\, a^2 \dot\gamma^2 = \langle v_r'^2 \rangle_{rot} \quad . \tag{3.29}$$

This result is an order of magnitude smaller than the collisional fluctuations we expect, which should be $O(\, a^2 \dot\gamma^2\,)$. Lyon and Leal (1998) arrived at the same conclusion, and subsequently concluded that fluctuations due to mean rotation were insignificant. The mean vorticity does not cause a rotational contribution to the total fluctuating velocity in the z direction, and the particles do not rotate significantly on average about the flow and gradient axes, so we estimate that there is no rotational contribution to the total velocity fluctuation in the z direction.

3.5.3.2 Particle Rotational Fluctuations are Negligible

We neglect the contribution from rotational fluctuations, because it is over an order of magnitude smaller than the mean rotation contribution. Rotational fluctuations come from neighboring particles exchanging angular momentum when they collide. In this nearly homogeneous shear flow, the local vorticity is proportional to the local shear rate, which is slowly varying over the gap, so neighboring particles have nearly identical vorticity and therefore hardly exchange any angular momentum when they collide, accordingly causing the rotational fluctuations to be negligible.

We estimate the size of the contribution of rotational fluctuations to the measured total velocity fluctuation based on the expression for the mean rotation contribution above.

$$\Delta\left(\langle v_\theta'^2\rangle_{rot}\right) = \frac{1}{5}\, a^2\, \omega\, (\Delta\, \omega) \tag{3.30}$$

Then, the ratio between rotational fluctuations and the mean rotation contribution becomes,

$$\frac{\Delta\left(\langle v_\theta'^2\rangle_{rot}\right)}{\langle v_\theta'^2\rangle_{rot}} \simeq \frac{\frac{1}{5}\, a^2\, \frac{a}{H}\, \omega\, (\Delta\, \omega)}{\frac{1}{10}\, a^2\, \omega^2} \simeq 2\,\frac{\Delta\, \omega}{\omega} \quad . \tag{3.31}$$

Substituting for ω yields,

$$\frac{\Delta\left(\langle v_\theta'^2\rangle_{rot}\right)}{\langle v_\theta'^2\rangle_{rot}} \simeq 2\,\frac{\frac{1}{2}\, a\, (\nabla\, \gamma)}{\frac{1}{2}\, \gamma} \simeq 2\,\frac{a\, (\nabla\, \gamma)}{\gamma} \tag{3.32}$$

Nondimensionalizing the shear rate gradient results in $(\nabla\, \gamma) \sim \frac{\Omega}{H}\left(\nabla^*\, \gamma^*\right)$, where H is the gap half-width and Ω is the angular velocity of the rotating inner cylinder. Then, substitution into equation (3.32) yields

$$\frac{\Delta\left(\langle v_\theta'^2\rangle_{rot}\right)}{\langle v_\theta'^2\rangle_{rot}} \simeq 2\, a\, \frac{\Omega}{H}\, \frac{\left(\nabla^*\, \gamma^*\right)}{\Omega\, \gamma^*} \simeq 2\left(\frac{a}{H}\right) \frac{\left(\nabla^*\, \gamma^*\right)}{\gamma^*} \tag{3.33}$$

Because $\frac{(\nabla^* \gamma^*)}{\gamma^*}$ is an O(1) factor, the ratio scales with 2 (a/H), which equals 2(1/30) = 1/15 for our flow. Accordingly, we have shown that the rotational fluctuation contribution is an order of magnitude smaller than the mean rotation contribution to velocity fluctuations, and is therefore negligible.

3.5.3.3 Fluctuations Arising from LDV Noise

The LDV noise contribution comes from two main sources. The first is noise in the photomultiplier, which is affected by the user-selected signal parameters, especially the signal amplification and bandwidth. The main cause of this is shot noise, which occurs because electrons are emitted discretely from the photoelectric plates in a process that follows Poisson statistics, rather than a one-to-one correspondence between the number of photons hitting the photocathode and the number of electrons emitted that get attracted to the next photoelectrode (Fingerson et al., 1993).

The second source of LDV noise is gradients in the mean velocity within the measuring volume, since it has a finite size (Drain, 1980). This source is most significant when we measure the tangential velocity. In that case, the long axis of the measuring volume points in the direction of the velocity gradient.

Because the velocity gradient is nearly constant over a small region of the flow such as the LDV measuring volume, we can estimate the mean velocity gradient contribution to the fluctuating velocity in the tangential velocity as

$$v'_{grad} = \frac{L}{2}\,\gamma_{local} \tag{3.34}$$

In the other directions, the mean velocity gradients are zero, so we do not expect contributions in those directions. However, we must measure L/2 empirically, because the spectrum analyzer has a threshold voltage of 50 mV below which it will reject signals. Only if the voltage threshold is set to zero would the measuring volume have the expected optical size. (Lyon and Leal, 1998)

We approximated the size of L/2 in the concentrated suspensions from the data shown in

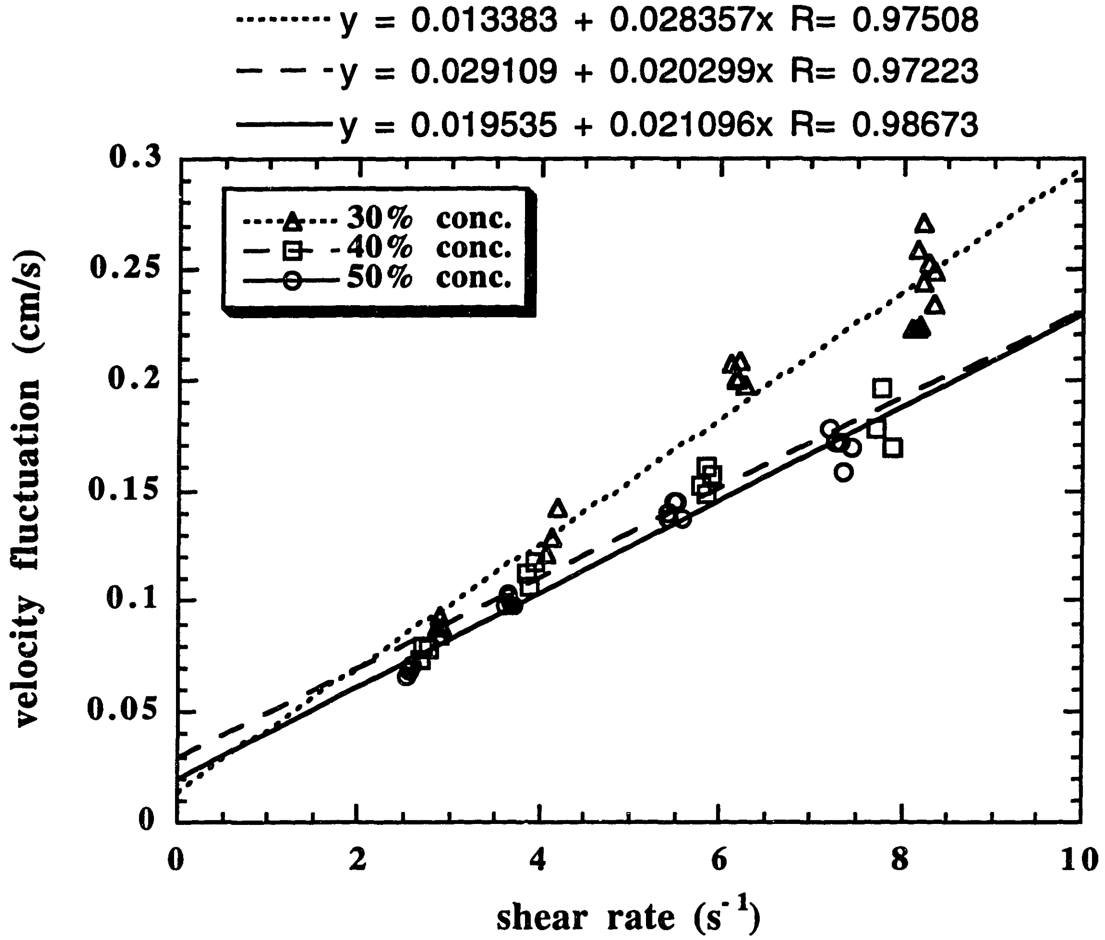

Figure 3.12 Baseline measurement for the tangential velocity fluctuation from a 2% concentrated suspension. Beams pass through a 3mm path length cuvette filled with 30%, 40% or 50% concentrated suspension. The suspension-filled cuvette was intended to produce the same large measuring volume size in the dilute suspension as in the actual concentrated suspensions. The observed velocity fluctuation was measured at four different rotation speeds and plotted against local shear rate. The linear curve fits shown on the plot for the three concentrations are average fits including velocity fluctuations measured at four radial positions. The slope of each line approximately equals the effective measuring volume half-length for that concentration, in centimeters.

figure 3.12. The data points indicate tangential velocity fluctuations measured in a dilute 2% particle volume fraction suspension. In each measurement, the LDV beams passed through a 3 mm path length cuvette filled with a concentrated suspension. Each plotted symbol corresponds to a different particle volume fraction suspension in the cuvette. The function of the cuvette was to scatter the beams so that the resulting measuring volume was the same size as in the actual concentrated suspensions. Since the flowing suspension was dilute, the only source of the measured velocity fluctuations was LDV noise, not inter-particle collisions. If we assume that the contribution from LDV shot noise and equipment vibration is relatively constant in shear rate, then the increase in the fluctuation with shear rate is due to the velocity gradient contribution. When we match the curves of the velocity fluctuation plotted against the local shear rate by using a linear least-squares fit, the slope of the line yields L/2. L/2 ranges from 290 to 330 μm for the 30% concentrated suspension, from 170 to 230 μm for the 40% concentrated suspension, and from 190 to 220 μm for the 50% concentrated suspension, depending on the radial position. These values represent a significant enhancement over the value of L/2 ~ 120 μm measured in the same way in the 2% particle volume fraction suspension alone, which actually matches the expected optical size in the fluid.

3.5.3.4 Fluctuations Arising from Couette Apparatus Vibrations

The Couette apparatus vibrations were measured by pointing the LDV beams at an optical glass cuvette which was taped on the outer wall of the box and filled with additional suspension, while the motor rotated at various speeds. We found that the velocity fluctuation contribution from the equipment vibration was insensitive to rotation rate between 5 and 15 rpm, and also to the concentration of the suspension in the Couette flow. Fluctuation values from 2% and 50% particle volume fraction suspensions are indistinguishable, when the cuvette was filled with 50% particle volume fraction suspension both times and nearly identical LDV parameters were selected.

3.5.3.5 Separating Dilute and Concentrated Suspension Effects

We measured velocity fluctuations in a dilute suspension at a given shear rate, to give a baseline for the LDV noise, particle rotation, and Couette vibration contributions. Then, we varied the particle concentration at constant shear rate. The suspension temperature is the most sensitive function of particle concentration, so it changes the most when the concentration changes.

We use a dilute suspension of 2% particle volume fraction. This volume fraction lies in the linear Einstein regime, according to Acrivos (1993), so that the particles do not interact and therefore have a minimal effect on the suspension rheology (the viscosity increases by 5% over the pure fluid value) but still provide a suitable number of LDV signals in a reasonable amount of measurement time.

When we plot measured velocity fluctuation against particle volume fraction, we expect to see a fairly constant velocity fluctuation at low concentrations, and then to see an increase at higher concentrations where the inter-particle collisions become significant, as shown in figure 3.13. We can write the measured particle velocity as the sum of the mean and the various fluctuations.

$$v_{\text{measured}} = \left(\bar{v} + v'_{\text{collisions}} + v'_{\text{rot}} + v'_{\text{LDV}} + v'_{\text{vib}} \right) \qquad (3.35)$$

Since the fluctuations come from different sources, it is reasonable to assume they are independent, and then the total variance is just the sum of the squares of each fluctuation.

$$\left\langle {v'_{\text{measured}}}^2 \right\rangle = T + \left\langle {v'_{\text{rot}}}^2 \right\rangle + \left\langle {v'_{\text{LDV}}}^2 \right\rangle + \left\langle {v'_{\text{vib}}}^2 \right\rangle \qquad (3.36)$$

So, by subtracting the dilute concentration baseline from the concentrated velocity fluctuation, we can get a reasonable measure of the size of the suspension temperature.

To test for anisotropy in the suspension temperature, we are measuring the tangential, radial, and vertical velocity fluctuations independently, figuring out the amount of each that is due to inter-particle collisions, and then comparing the relative sizes of these terms.

3.5.3.6 Measurement of the Three Fluctuation Components

We found that the LDV parameters, the path length the beams travelled inside the suspension, and laser beam power affected the observed values of the LDV noise, so we hold these factors constant for every measurement, in order to compare the runs on an equal basis.

In order to be able to compare accurately all three velocity fluctuation components, we use a single set of LDV amplification and bandwidth parameters and cause the beams to pass through approximately equal path lengths of the suspension. For points on the same radius, but different tangential angles around the flow, this is accomplished by placing additional suspension in front of the shorter beam paths.

We chose the set of parameters we used to accommodate the most concentrated suspension. We received the optimal signals in the 50% concentrated suspension with these parameters for points at the 90° location. We used a value of 50 dB for the gain and 1232 V for the high voltage. For lower values of the amplification parameters, we collected fewer than 100 bursts over an interval of 1000 seconds, which is an unacceptably low data rate. For higher values of the amplification parameters, there was no improvement in the signal, and only more noise was added. We always collected the maximum number of samples (64), since points we tried recording with fewer samples always gave us unrealistically large standard deviations. We kept the same large frequency bandwidth (139.1 mm/s) all the time, which meant that we only sampled each burst for a short time interval of 341.3 μs. This allowed many bursts to be validated, because they only had to have a clear signal with one dominant frequency over a short time interval, but it may have led to some of the bursts at low rotation speeds being counted more than once.

The additional suspension placed in the beam path was contained in an optical glass cuvette which was taped on the outer wall of the box. The longest beam paths were always found for points at the 90° position, so the cuvette was placed in the beam paths at the 0° position. For the tangential velocity measurements, always made at the 0° position, a large contribution to the velocity fluctuation comes from mean velocity gradients within the measuring volume, and so the size of the measuring volume must be kept constant when comparing the concentrated suspension and the dilute suspension baseline. For that reason, for each concentrated suspension and for the corresponding 2% concentrated suspension baseline, the beams measuring the tangential velocity passed through a cuvette filled with the concentrated suspension, so that the measuring volume size

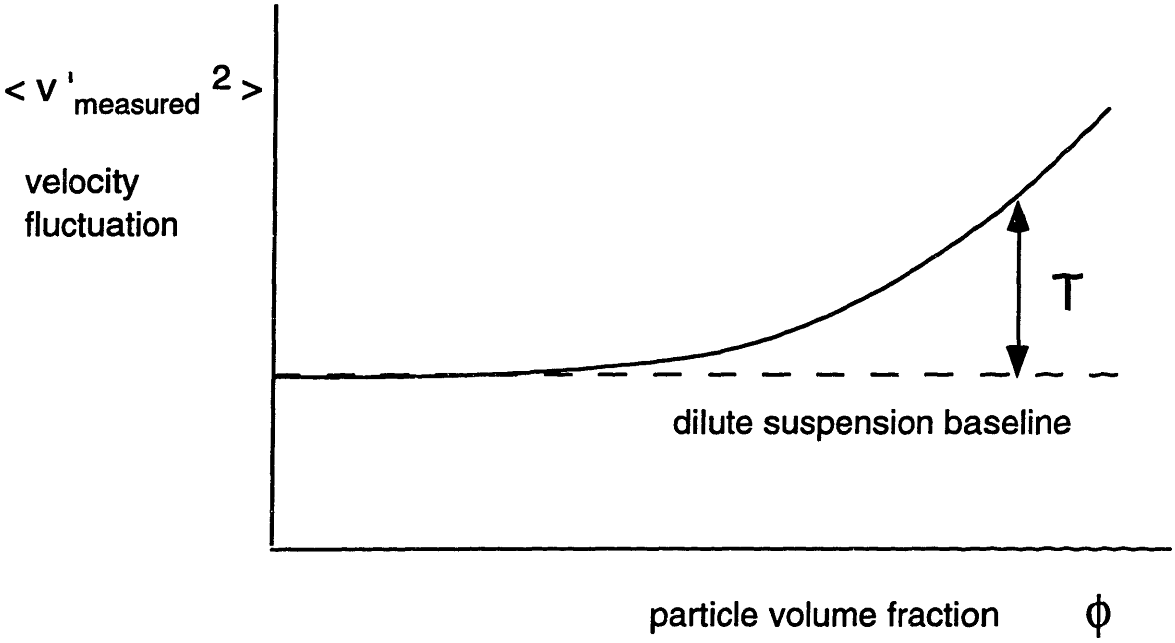

Figure 3.13 Expected trend of the variation of the measured particle velocity fluctuation with particle volume fraction, at constant shear rate. This schematic plot demonstrates how the collisional velocity fluctuation (T), a concentrated suspension effect, can be separated from dilute suspension effects.

in the flow would be very similar in both cases, since the cuvette accounts for the majority of the beam path inside the suspension.

3.5.3.7 Zero Peaks in Tangential Velocity Measurements

We encountered the presence of zero peaks in the tangential velocity distributions we collected from the 30%, 40% and 50% concentrated suspensions when an extra suspension-filled 3mm path length cuvette was placed in the beam path. We suspect the zero peaks are detected because the measuring volume is touching the outer cylinder wall, or a layer of particles or fluid immediately adjacent to it.

We believe we observe these zero peaks in the concentrated suspensions and not in the 2% concentrated suspension for two reasons. First, in the concentrated suspensions, there is a high concentration of particles slowly rolling and sliding along the wall, whereas in the 2% suspension, this slow region tends to have sparser signals because the particles remain uniformly distributed and the fluid does not slip at the walls. Alternatively, the zero peak could result from equipment vibration, which we have observed in another way. In the 30%, 40% and 50% concentrated suspensions, there is a high concentration of particles near the outer cylinder wall, and the suspensions are almost continually scattering the light, especially at low rotation speeds. If there is any pause in the velocity signals from the particles in the center of the measuring volume, the probe picks up the low frequency vibration of the Couette cell from the nearly stationary scatterers.

These signals coming from a distance from the center of the measuring volumes are visible to LDV because the measuring volume size is enhanced by scattering of the incident beams inside the 3mm path length cuvette filled with 30%, 40% or 50% concentrated suspension, with the measuring volume length being as large as 660, 460 or 440 μm, respectively, compared with the theoretical length of the measuring volume in the fluid of 250 μm. As mentioned earlier, the theoretical figure of 250 μm agrees with the effective measuring volume length extracted from measurements of the tangential velocity fluctuation in a 2% concentrated suspension with the beams passing through a 2mm pathlength cuvette.

3.5.3.8 Minimizing Wall Effects

We tried to eliminate wall effects by measuring points at the most interior radii that the beam attenuation at the 90° location would allow. We wish to avoid wall effects for two reasons. First, when we look at the suspension on a very small length scale close to a wall, we cannot call it a continuum any more, and comparisons of data to continuum models are invalid. Also, the LDV signals we collect near walls are noisier than those from the flow interior. The vertical fluctuating velocity values we measure vary noticeably with fine changes in position and are less consistent between repeated runs and in general are higher than fluctuating velocities in the bulk, due to a larger LDV shot noise contribution. This can be seen from the results in figure 3.14. We believe the higher and noisier values are an LDV effect, because we see the same trend in the $\langle v_z'^2 \rangle$ profile for the 2% concentrated suspension. We did not see this jump in v' near the wall for the radial velocity fluctuation component, presumably because one of the beams hardly passes through the flow and therefore produces signals of approximately the same light intensity, so the LDV noise contribution is relatively constant.

For the 50% concentrated suspension, the most concentrated one we measured, and therefore the one for which the wall effects pose the most serious issue, we believe we were able to reach far enough into the flow to escape wall effects. The average measurements between three neighboring interior radial positions were nearly identical, and we could see where the jumps in $\langle v_z'^2 \rangle$ began at higher radii. The most interior positions were 4-5 particle diameters away from the wall, out of 30 particle diameters filling the whole gap width. For the lower concentrations studied, more interior positions were accessible, up to about 6.5 particle diameters for the 30% concentrated suspension and 7.5 particle diameters for the 10% concentrated suspension.

3.5.3.9 Uncertainty in the Suspension Temperature

In estimating the precision of our velocity fluctuation measurements, we found that the uncertainty in the velocity fluctuation could be expressed as the sum of two terms. The first term represented the uncertainty due to factors which changed within a run, but not on average from run

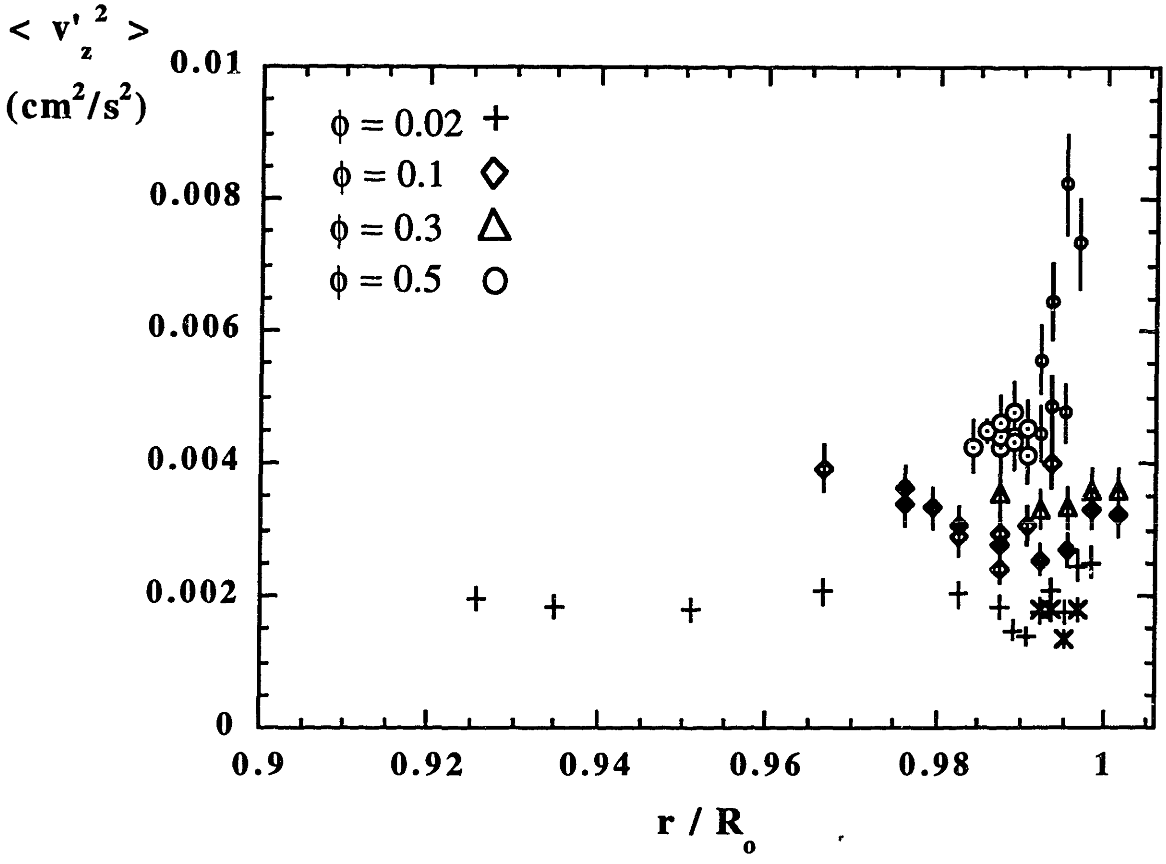

Figure 3.14 Measured vertical velocity fluctuation plotted against dimensionless radial position. These data demonstrate the wall effects on the measured vertical velocity fluctuation at bulk particle concentrations of ϕ = 0.02, 0.1, 0.3 and 0.5, and an average shear rate = 10 s^{-1} (10 rpm).

to run, and the second term represented factors which changed between runs. The first term was the "standard deviation of the standard deviation," meaning, the uncertainty in the velocity fluctuation due to the uncertainty in each individual velocity measurement from which it was calculated, and is given by

$$\Delta\left(v'_1\right) = \frac{v'}{\sqrt{N-1}} \ , \tag{3.37}$$

where N is the number of values in the distribution. The uncertainty of each individual measurement was a combination of the following effects: fluctuations in the inner cylinder rotation speed, particle rotational fluctuations, LDV photomultiplier shot noise variation, and incident beam intersection angle fluctuations, in addition to the varying particle collisions we were trying to measure. We expect these factors on average not to change from run to run--only within a run. In the velocity distributions we measured, the number of bursts in the distribution ranged from about 1000 to 5000, leading to $\Delta v'_1$ values of 0.014 v' to 0.032 v', and accordingly to $\Delta\left(v'^2_1\right)$ values of 0.028 v'^2 to 0.064 v'^2.

The second term estimates the effect of laser power fluctuations and imperfect reproducibility of probe positioning with the LDV traverse. We estimated the effects of these factors by taking repeated measurements in the seeded Newtonian suspending liquid, in order to eliminate the effects of particle interactions. In one case, we reinitialized the traverse between each repetition, and in the other case simply repeated the same measurement several times without changing anything. Taking the larger of the two uncertainties to be the uncertainty due to laser power fluctuations and imperfect reproducibility of probe positioning yielded $\Delta\left(v'^2_2\right) = \pm 5.2\% \left\langle v'^2_r \right\rangle_{avg}$ in the radial direction and $\pm 9.1\% \left\langle v'^2_z \right\rangle_{avg}$ in the vertical direction, at the 90° location. Our corresponding measurements in the tangential direction were not made with an equal pathlength of fluid and the same LDV parameters, and so we believe they are not relevant to the uncertainties we encountered in our subsequent cuvette measurements. Instead, we apply the vertical velocity uncertainty to the tangential direction as well, since the vertical and tangential (with cuvette) signals look the most alike.

For the concentrated suspensions, varying particle interactions add to the uncertainty in each measurement, but the only way for us to quantify this total uncertainty is to repeat measurements in the concentrated suspensions several times. For measurements that we repeated, we used the scatter in the multiple repetitions to represent the uncertainty in the average measurement. However, it was impractical for us to repeat every measurement multiple times, so we used the percent error we found in the Newtonian liquid as the between-runs uncertainty for measurements at all concentrations that were not repeated.

We also found that LDV measured the mean velocity to an accuracy of ± 2.5%, which we measured by comparing LDV readings of the velocity of the rotating inner cylinder (with and without the seeded suspending liquid in the gap) with the inner cylinder rotation speed independently measured by the chopper wheel, photoelectric switches, and LabVIEW timer program.

The overall error bar is the root mean square sum of the two precision terms.

$$\Delta\left(v'^2_{\text{total}}\right) = \sqrt{\left[\Delta\left(v'^2_1\right)\right]^2 + \left[\Delta\left(v'^2_2\right)\right]^2} \qquad (3.38)$$

3.6 Testing the Limits of the Measurements

In addition to the procedures detailed above, there were several other measurement techniques we tried which eventually turned out to be unsuccessful, including high laser power measurements, tilted probe measurements, and measuring the covariance $\langle v'_\theta \, v'_r \rangle$.

For several months during the experiments, the laser was able to run at higher power than before (up to 450 mW). We thought that this extra power would allow us to access points farther into the interior of the flow for concentrated suspensions, but it turned out that for the 50% concentrated suspension it only allowed us to make measurements an extra 0.1 mm into the flow, which was not a significant change. Accordingly, we kept the laser power fixed at 300 mW.

Also, when we measured the tangential velocity fluctuation, the long axis of the measuring volume pointed in the direction of the velocity gradient, causing a large contribution to the velocity fluctuation from mean velocity gradients within the measuring volume. We wanted to keep this contribution as small as possible. The method we tried for doing this was tilting the LDV probe in the x-z plane, so that the profile width of the measuring volume in the velocity gradient direction would be smaller. Unfortunately, we were unable to tilt the probe enough to distinguish the tilted fluctuation values from the original normal values we measured. The limiting factor was how far our traverse could travel in the vertical direction compared with the height of the Couette cell platform. In addition, the data rate and quality decreased dramatically as the tilt angle increased.

Finally, since we are evaluating the description of the suspension temperature as a second order symmetric tensor, we should be able to measure 6 independent components, namely, three diagonal and three off-diagonal, in the shear flow coordinate system. We present results only for the three diagonal components. Also, we expect two of the off-diagonal terms, $\langle v_r' v_z' \rangle$ and $\langle v_\theta' v_z' \rangle$, to be zero, because we do not see a correlation of the particle's z velocity fluctuation with anything else. A faster-moving particle could be above or below a slower- moving particle when they collide. So, in general, for every positive correlation $v_\theta' (v_z')$, there is a corresponding anti-correlation $v_\theta' (- v_z')$, and on average the covariance $\langle v_\theta' v_z' \rangle$ is zero. The last component, $\langle v_\theta' v_r' \rangle$, could be nonzero, because we would expect that particle collisions involve moving to the side and slowing down or speeding up, and that these two changes are related because smaller radii correspond to higher average speeds.

Unfortunately, the $\langle v_\theta' v_r' \rangle$ component is very difficult to measure in our current apparatus, because with a single wavelength beam, we can measure only one velocity component at a time. However, we can extract $\langle v_\theta' v_r' \rangle$ from oblique measurements of the horizontal velocity. The best way to measure $\langle v_\theta' v_r' \rangle$ by this indirect method would be from above or below, but we have a free surface at the top, no window on the bottom, and the flow is too tall to allow the beams to pass from above into the middle region where end effects are negligible. Hence, measuring from above or below is not possible. Measuring $\langle v_\theta' v_r' \rangle$ from the side involves comparing three fluctuation measurements, all with different path lengths that the beam must pass through in the suspension and different effective measuring volume sizes, with corresponding baselines in the 2% concentrated suspension. Accounting for all these factors is beyond the scope of this project.

In addition, we want to relate our measurements of an anisotropic temperature to model predictions of how the anisotropy affects the macroscopic flow properties, and in the model we are starting with, the temperature tensor is diagonal, in the flow, gradient, and neutral direction coordinate system, for simplicity. In that case, the temperature components ($T_{\theta\theta}$, T_{rr}, T_{zz}) are the eigenvalues and are invariants of the tensor. If we include off-diagonal terms, the invariants become more complicated. For all these reasons, it was not feasible for us to measure $\langle v_\theta' v_r' \rangle$, the last possible nonzero component of the suspension temperature tensor.

3.7 Video Imaging Apparatus and Procedures

Qualitative flow visualization was performed with video imaging, on 2%, 30%, 40% and 50% concentrated suspensions. We recorded the videos using a CCD camera (Cohu, model 4915), with a 55 mm length barrel attached for magnification, and a Panasonic VHS VCR. The camera was focused on the 0° location in the flow, at a height of about 6.5 cm from the base of the flow, and the lens was approximately 6.2 cm from the box outer wall. The camera was aligned perpendicular to the flow in the vertical direction, but was tilted in the horizontal direction at an angle of no more than 10°. The field of view was 5.75 mm x 4.25 mm and the depth of field was 1.6 mm. We used ambient lighting to illuminate the bubbles of monomer inside the particles, which appeared as white dots against the black background of the inner cylinder. The viewer sees particles crossing the field of view from left to right at different speeds, since several shearing surfaces are in focus. A schematic view is shown in figure 3.15.

We were able to collect, store and manipulate images from the video tape using the Mac program NIH Image 1.55 on a Mac Quadra 800 connected to an LG-3 frame grabber board (Scion Corp.). We used this capability to take snapshots of pairs of particles before, after, and during a collision, and to track individual particle trajectories by averaging sequential frames.

In summary, this chapter contains a complete description of the experimental method employed in this work, from the basic principles of LDV to the data reduction method. In addition, the last section contains a description of the video imaging apparatus, which was utilized to aid in interpreting the LDV measurements. The next chapter consists of a presentation of qualitative results obtained from video imaging and quantitative velocity fluctuation measurements obtained from LDV.

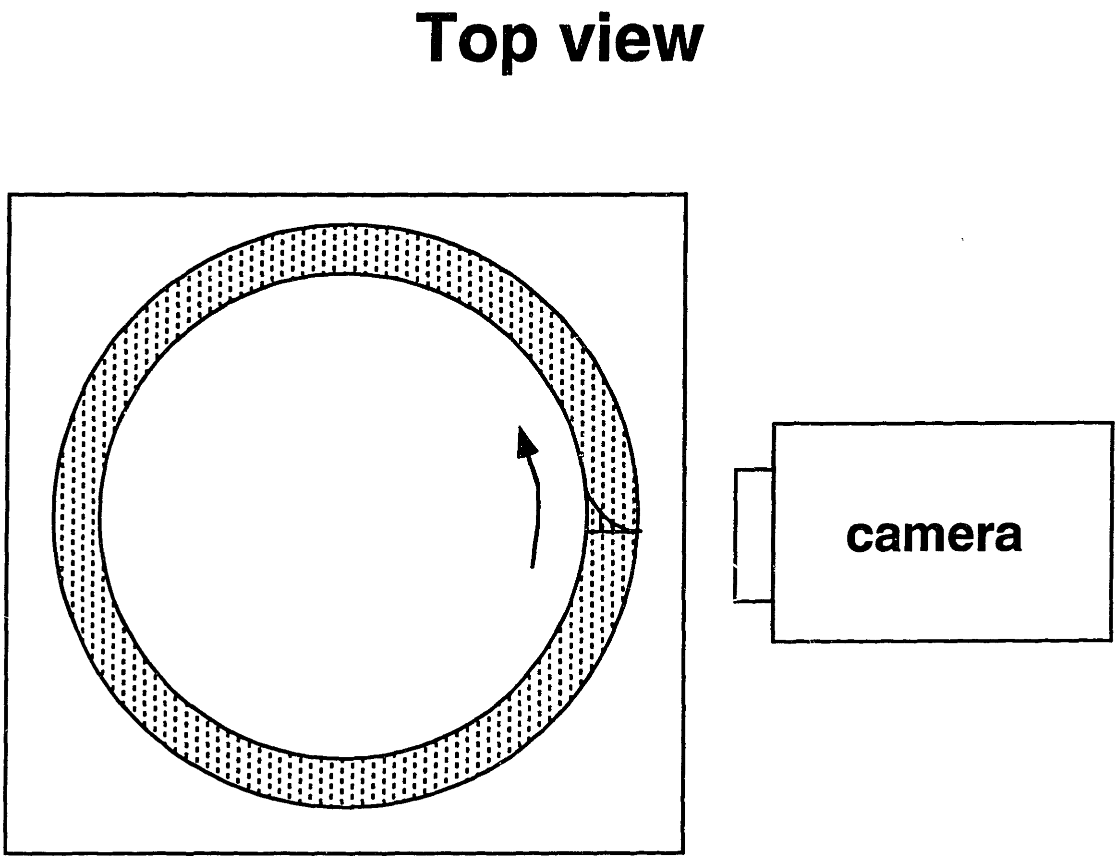

Figure 3.15 Schematic view of video imaging apparatus

Chapter 4

Data

The first part of this chapter describes qualitatively the particle trajectories obtained from video imaging of the Couette flow. The second section describes laser Doppler velocimetry (LDV) experiments we performed to verify that the Couette cell we built was creating the intended nearly homogeneous steady shear flow. The third section describes our physical observations obtained using LDV of the macroscopic quantities of interest, including the mean velocity, shear rate and particle concentration, and particle velocity fluctuations resulting from inter-particle collisions.

4.1 Particle Trajectories from Video Imaging

Qualitative flow visualization by video imaging provides a convenient introduction to the quantitative LDV data presented in the rest of this chapter. Before following the painstaking measurement method and data analysis procedures described in sections 3.4 and 3.5, we may want to know the answers to some basic questions, such as whether we actually can see particle velocity fluctuations and what an inter-particle interaction looks like. It is difficult to answer these two questions by using LDV, because it is a pointwise, Eulerian measurement method (i.e. fixed in the laboratory reference frame). Although our video imaging apparatus, described in section 3.7, is not as precise as LDV for quantitative measurements, it is well suited to answering these qualitative questions.

We recorded several video tapes of flowing 2%, 10%, 30%, 40%, and 50% concentrated suspensions at average shear rates ranging from 1 s^{-1} (1 rpm) to 15 s^{-1} (15 rpm). As described in section 3.7, the camera's field of view was a tangential-vertical plane at the 0° location. Particle trajectories in the tangential (flow) and vertical (neutral) directions were visible to the camera.

Figure 4.1 compares the trajectories of particles in a dilute 2% particle volume fraction suspension with that of a particle in a concentrated 50% particle volume fraction suspension. Both the trajectory images were produced by averaging the pixel intensity values from frames equally spaced in time. The average shear rate in both flows was 5 s^{-1}. It is clear that the dilute suspension trajectories are straight lines and that the spacing between successive particle images is equal for every time interval, indicating that the particles move in straight paths at constant speed. In contrast, the particle in the concentrated suspension traces a bumpy path, and the successive particle images are not evenly spaced, even though the images were evenly spaced in time. This image indicates that the particle in the concentrated suspension demonstrates velocity fluctuations in the flow direction and the neutral (vertical) direction. (Motion in the radial direction is not visible in these images.) Consequently, particle velocity fluctuations are indeed visible to the camera in the concentrated suspension that are not observed in the dilute suspension at identical flow conditions. In the 50% concentrated suspension, the video tape displays especially large fluctuations in the flow direction.

In the 50% concentrated suspension, pairwise particle interactions are clearly visible to the camera. Two examples are displayed as sets of snapshots in figures 4.2 and 4.3. In figure 4.2, two particles at the same vertical position are interacting, in an "in-plane" collision. The particles approach each other, stick together, rotate as a doublet in the <u>same</u> vertical plane, and then separate. In figure 4.3, another type of collision is captured. Two particles at different vertical positions interact, in an "out-of-plane" collision. The particles approach each other, stick together, rotate as a doublet about an axis that is <u>oblique</u> to the horizontal plane, and then separate. The velocity fluctuations we detect as a bumpy trajectory can be considered a rapid series of very brief collisions of the types shown in these figures. It appears in the video recordings of the 50% concentrated suspension at various shear rates that in-plane collisions may be more likely at low shear rates and out-of-plane collisions at high shear rates, but this has not been quantified with statistics.

a)

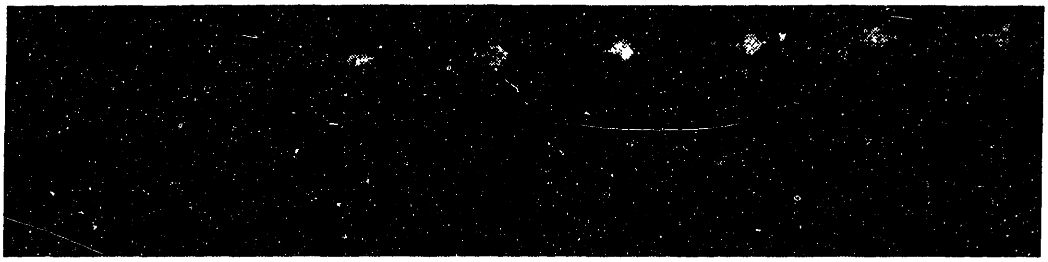

$\phi = 0.02$ dilute suspension, average shear rate = 5 s^{-1}

b)

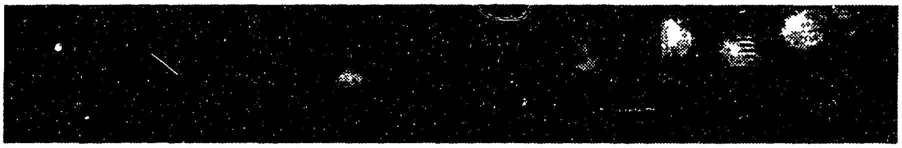

$\phi = 0.5$ concentrated suspension, average shear rate = 5 s^{-1}

Figure 4.1 Video images of particle trajectories in a dilute 0.02 particle volume fraction suspension (a) and in a concentrated 0.5 particle volume fraction suspension (b). Both the trajectory images were produced by averaging the pixel intensity values from frames equally spaced in time, and the average shear rate in both flows was 5 s^{-1}.

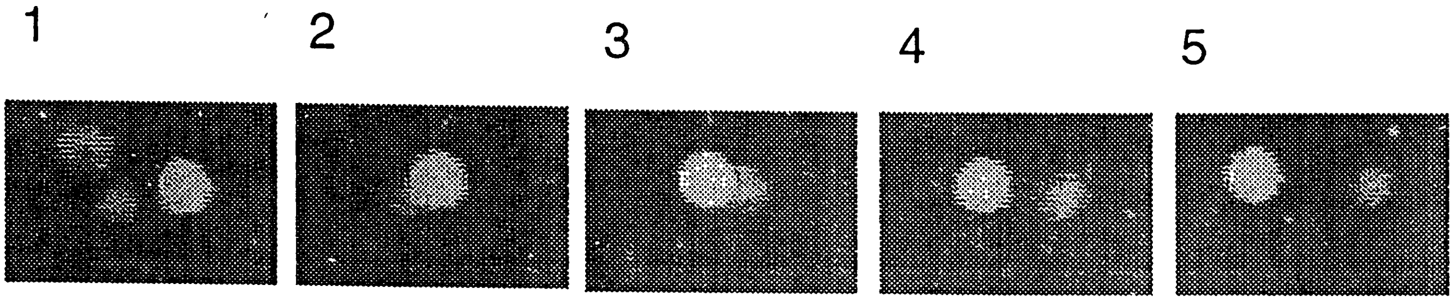

Figure 4.2 Video images of an "in-plane" collision between two particles in a 50% concentrated suspension. In these snapshots of a collision, arranged as a cartoon, progressing from left to right and spaced evenly in time, we see the particles approach each other, stick together, rotate as a doublet in the same vertical plane, and then separate.

The average shear rate is 2 s^{-1}.

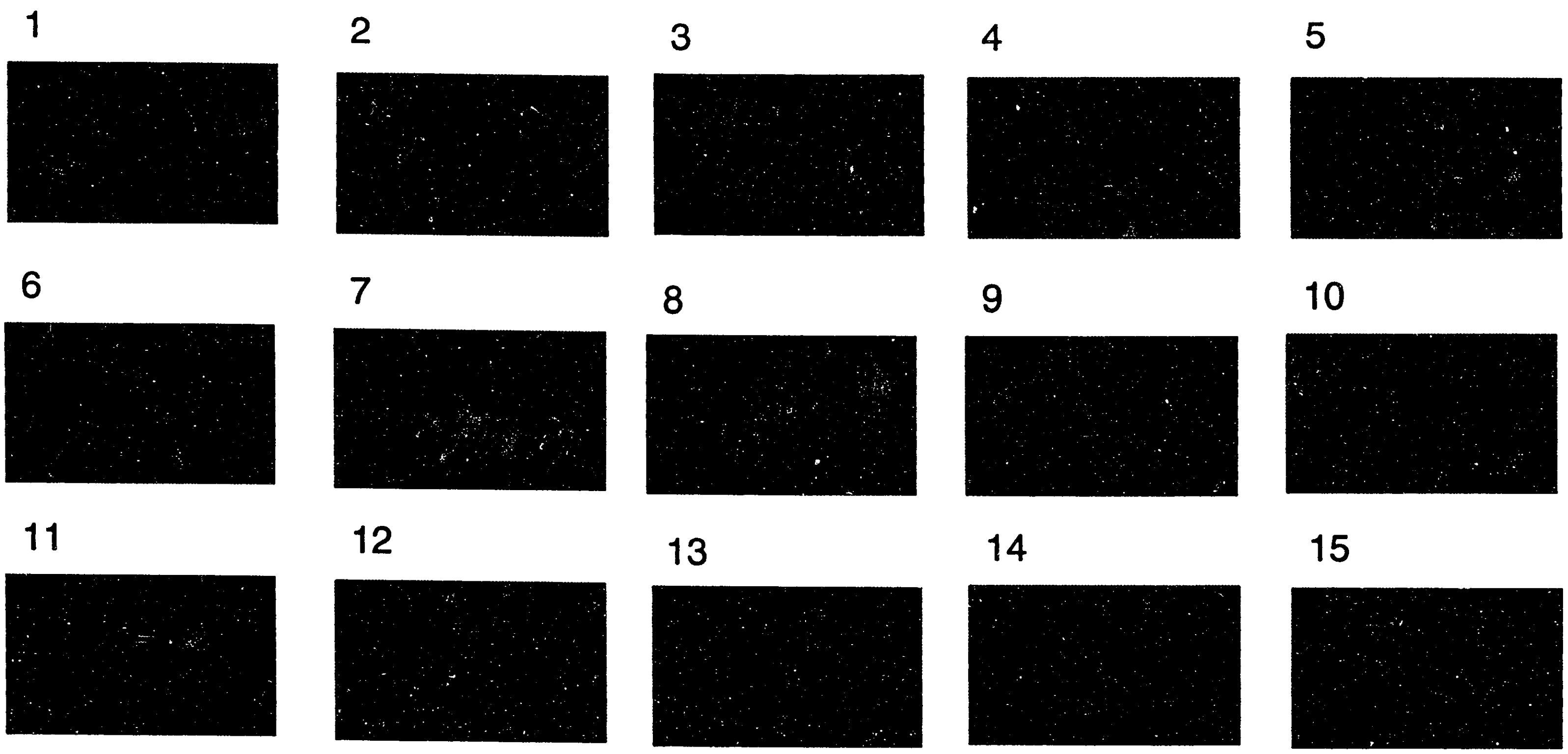

Figure 4.3 Video images of an "out-of-plane" collision between two particles in a 50% concentrated suspension. In these snapshots of a collision, arranged as a cartoon, progressing from left to right and spaced evenly in time, we see the particles approach each other, stick together, rotate as a doublet about an axis that is oblique to the horizontal plane, and then separate. The average shear rate is 5 s^{-1}.

4.2 LDV Experiments: Validation of Couette Flow

4.2.1 Validation of Couette Flow with Seeded Newtonian Fluid

Before making measurements in concentrated suspensions in the Couette flow cell (described in section 3.3) we filled the flow cell with a pure Newtonian fluid and tested the flow to ensure that it produced the correct behavior. The Newtonian fluid was the suspending liquid described in section 3.2 seeded with tiny silicon carbide seeding particles (TSI Inc.), of average diameter 0.75 μm, and at a volume fraction of 9×10^{-7}. Since the seeding particles occupied such a minute fraction of the flow, their presence did not disturb the flow from that of a pure liquid. Their only impact was to act as scattering sites for LDV.

First, we determined that the mean tangential velocity profile we measured was reproducible and matched the theoretical prediction for any Newtonian fluid (Kundu, 1990)

$$u_{\text{Newtonian}} = \frac{\Omega_i R_i}{1-k^2}\left[\frac{R_i}{r} - k\frac{r}{R_o}\right] \tag{4.1}$$

where $k \equiv \frac{R_i}{R_o}$ and R_i and R_o are the inner and outer cylinder radii, respectively, and Ω_i is the inner cylinder angular frequency of rotation. In figure 4.4, two measured mean velocity profiles are shown to agree with each other and with the theoretical profile within experimental error, which is indicated by the standard deviation of the velocity distribution obtained at each point.

Next, we verified that vertical end effects and secondary flows are negligible near the vertical (axial) midplane of the flow. First, we established that the mean and fluctuating velocities observed in the vertical direction are independent of vertical position. In figure 4.5, it is demonstrated that the mean vertical velocity, measured at a constant radial position in the middle of the Couette gap, does not change with vertical position within the uncertainty of the measurements, again given by the standard deviation of each velocity distribution. While the fluctuating velocities at varying vertical positions show some scatter, there is no recognizable trend.

Also, we confirmed that the mean and fluctuating vertical velocities, measured at a fixed radial position, are independent of azimuthal position around the flow (see figure 4.6). In addition, we found that the mean vertical velocity is zero at all azimuthal positions, within experimental error.

Finally, we verified that the mean vertical and radial velocity profiles, measured at the 0° and 90° locations, respectively, are zero compared with the experimental uncertainty (standard deviation) of the measurements. The negligible mean velocities are shown in figure 4.7

The results of these tests confirm that the flow cell we built does produce the desired Couette flow betwen concentric cylinders. The resulting flow of a Newtonian fluid can be described as one-dimensional, where there is variation in the velocity and pressure fields (aside from the hydrostatic pressure) only in the radial direction.

4.2.2 2% Concentration Suspension

The next test involved comparing measurements from the 2% concentrated suspension of large Lucite 47G particles with those from the seeded Newtonian liquid to verify that the 2% concentrated suspension also exhibited Newtonian behavior. This was a requirement for using the 2% concentrated suspension as a suitable baseline for the concentrated suspensions.

First, we established that the mean tangential velocity profile for the 2% concentrated suspension is identical to the measured Newtonian mean tangential velocity profile, within experimental uncertainty, as shown in figure 4.8. Also, in figure 4.9, it is apparent that the mean vertical velocity, measured at the ± 90° positions, is zero at all points measured across the gap, compared with experimental error. According to these plots, the 2% concentrated suspension acts as a Newtonian fluid that does not experience secondary flows or end effects.

In addition, we confirmed that, for the 2% concentrated suspension, the mean normalized tangential velocity profile measured is independent of the inner cylinder rotation speed. This can be seen in figure 4.10, where the points measured in a flow where the inner cylinder rotated at 5 rpm overlap with the velocity profile measured at 10 rpm, where the mean velocities were normalized.

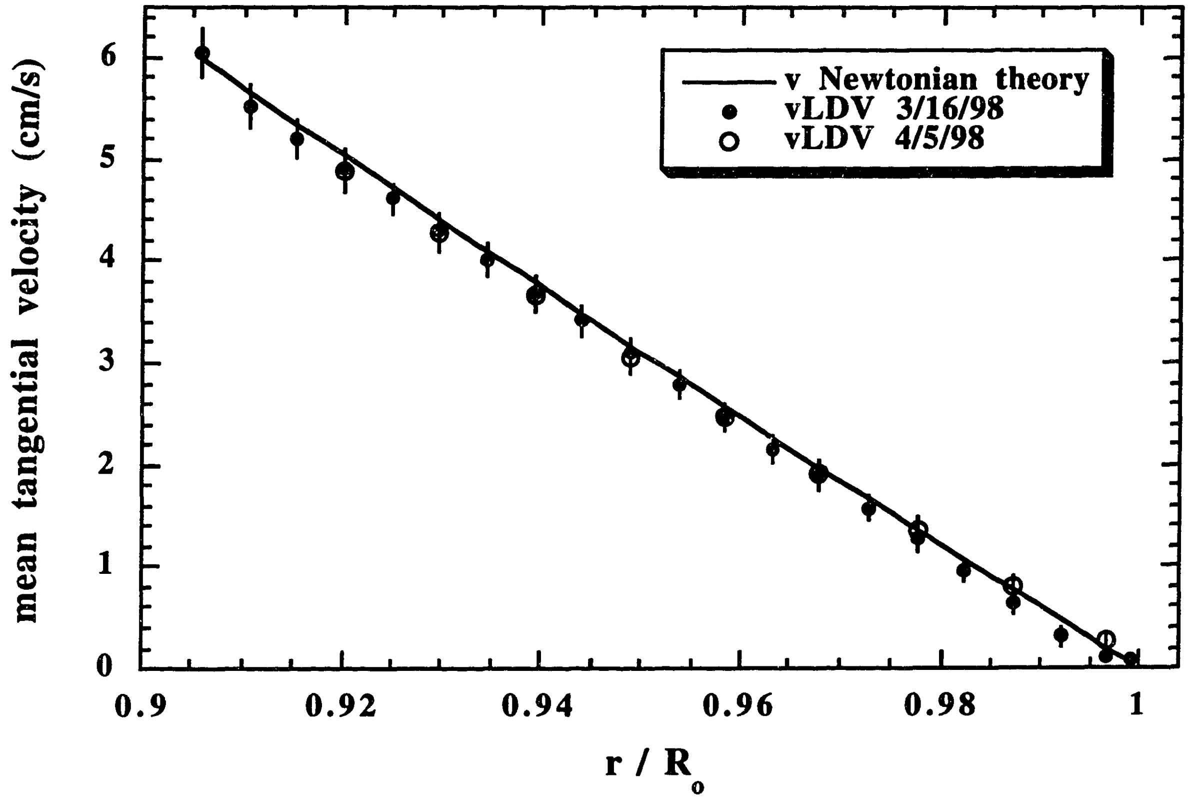

Figure 4.4 Two measurements of the mean tangential velocity profile for the Newtonian suspending liquid seeded with silicon carbide 0.75 μm diameter seeding particles, at an average shear rate = 10 s^{-1} (10 rpm). The measured results are compared with the theoretical velocity profile for a Newtonian fluid. As mentioned in Chapter 3, the inner and outer cylinder radii are given as R_i = 5.715 cm, and R_o = 6.31 cm.

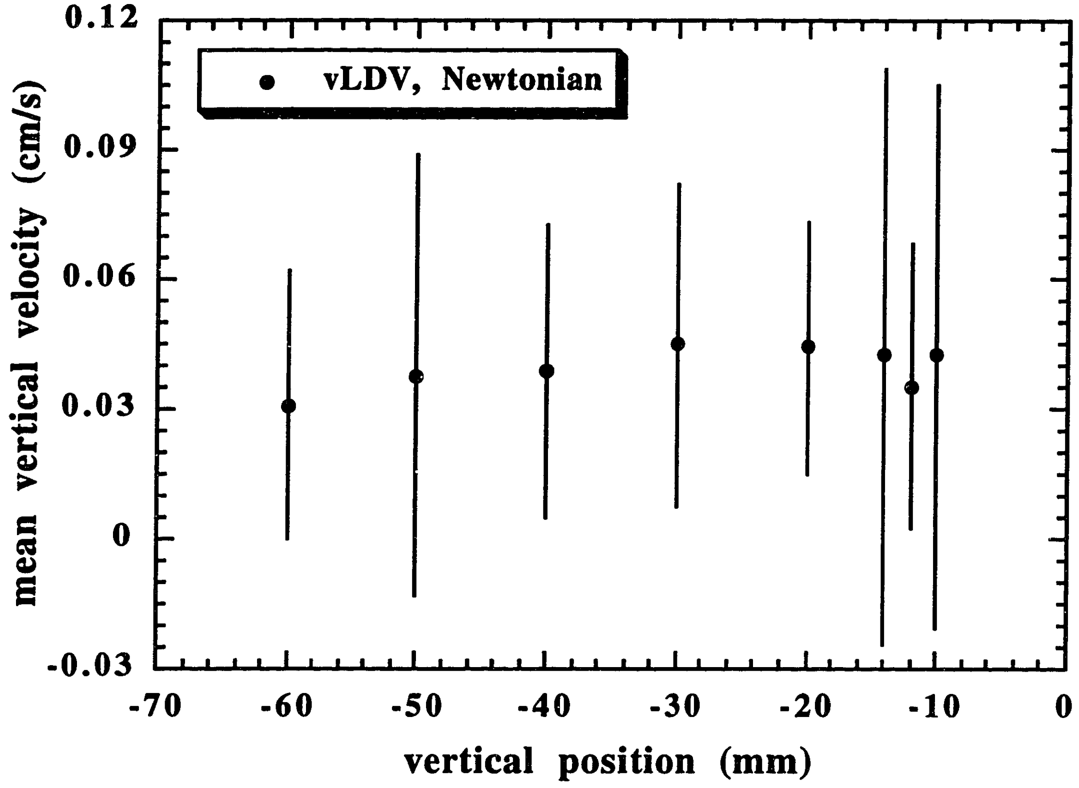

Figure 4.5 Mean vertical velocity measured at the 0° location as a function of vertical (axial) position, an average shear rate = 10 s^{-1} (10 rpm), and constant radius r / Ro = 0.954. Results are for the Newtonian suspending liquid seeded with 0.75 μm diameter silicon carbide particles.

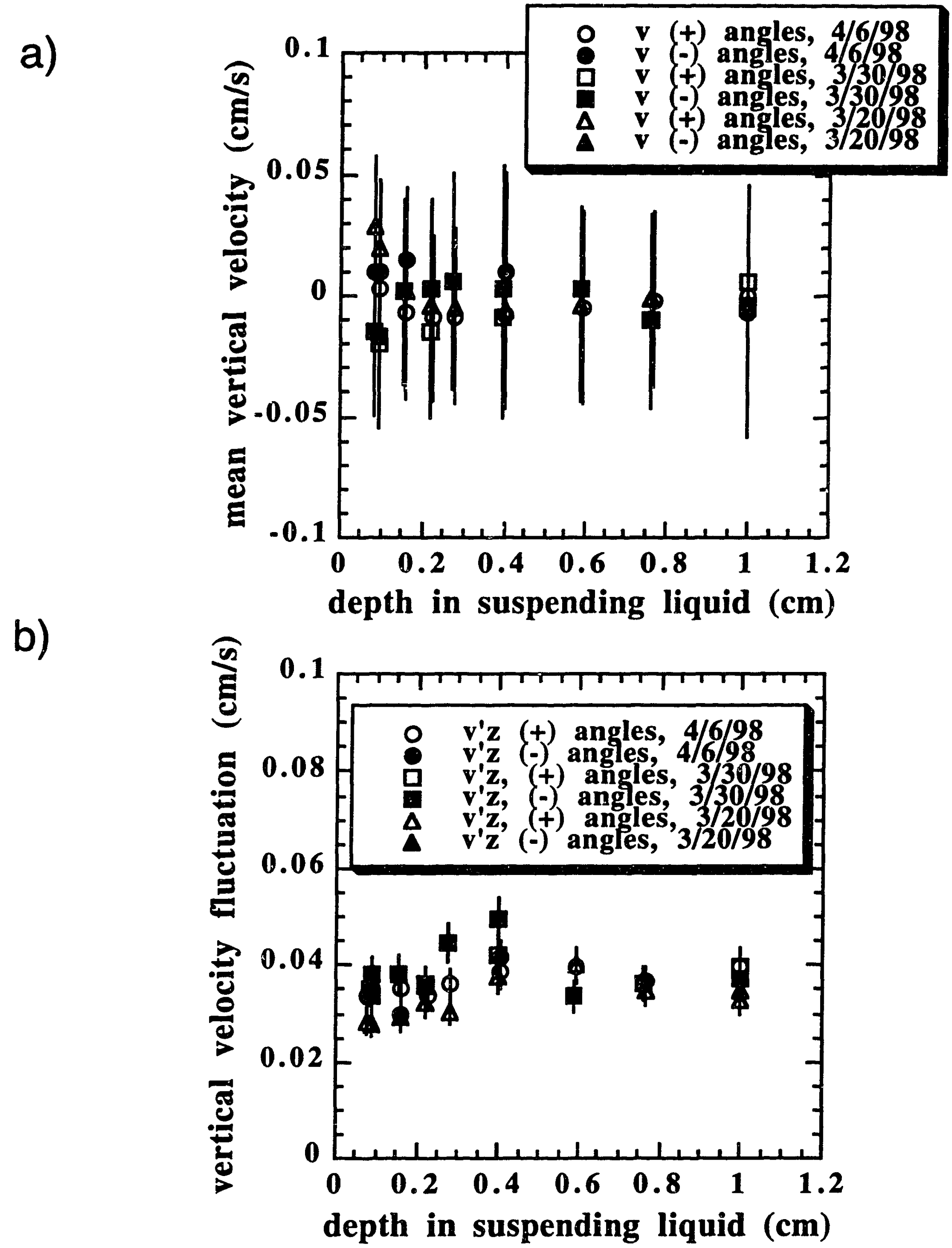

Figure 4.6 Mean (a) and fluctuating (b) vertical velocity in the Newtonian suspending liquid seeded with 0.75 μm diameter silicon carbide particles, at an average shear rate = 10 s^{-1} (10 rpm), at constant radius r / R_o = 0.987, measured at different azimuthal positions around the flow (corresponding to different depths the beams cross in the suspending liquid).

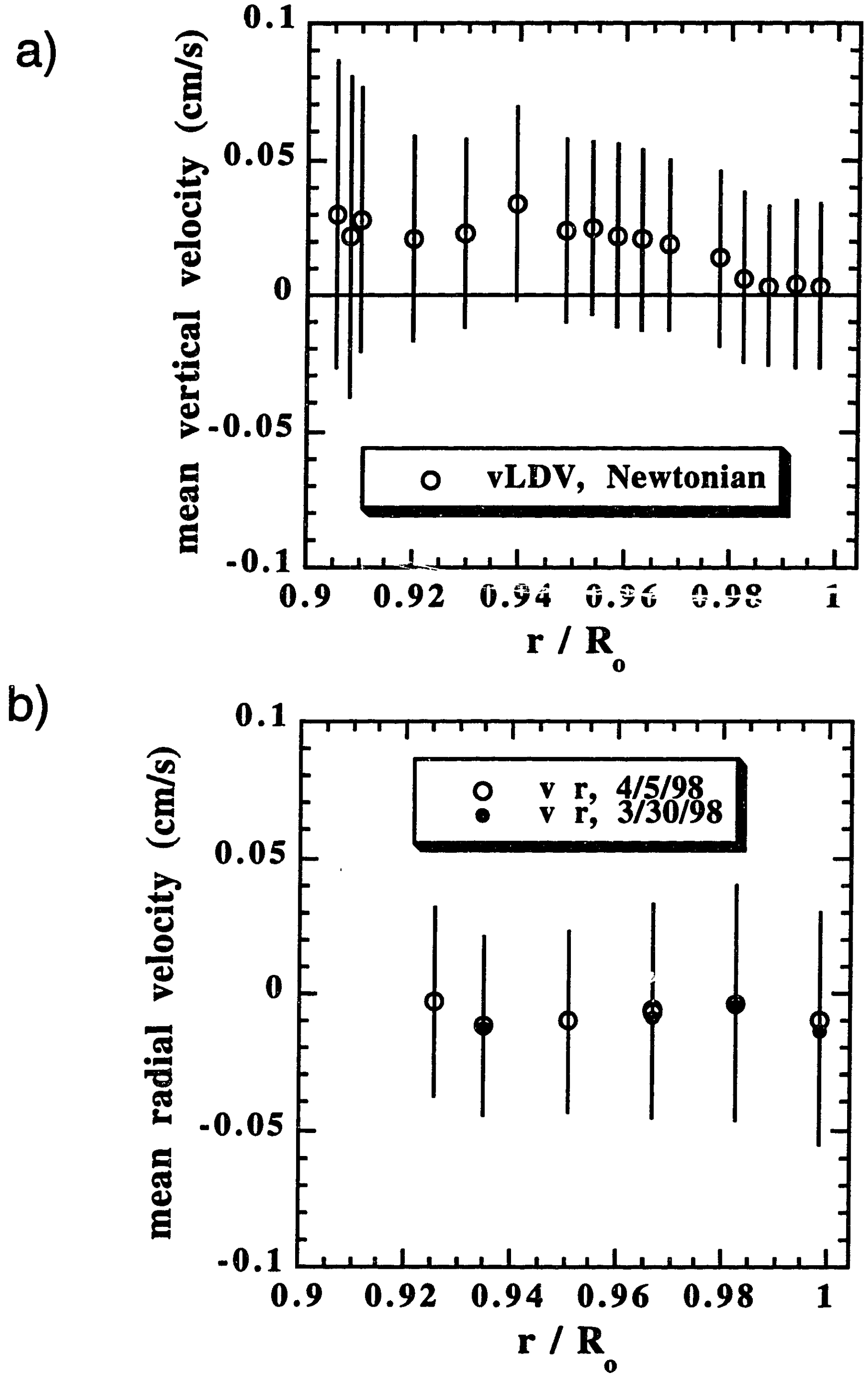

Figure 4.7 Mean velocities measured in Newtonian suspending liquid seeded with 0.75 μm silicon carbide particles, average shear rate = 10 s^{-1} (10 rpm).

a) Mean vertical velocity measured profile at the 0° location, height = -24 mm, constant LDV parameters
b) Mean radial velocity measured at the 90° location, constant LDV parameters, two independent runs.

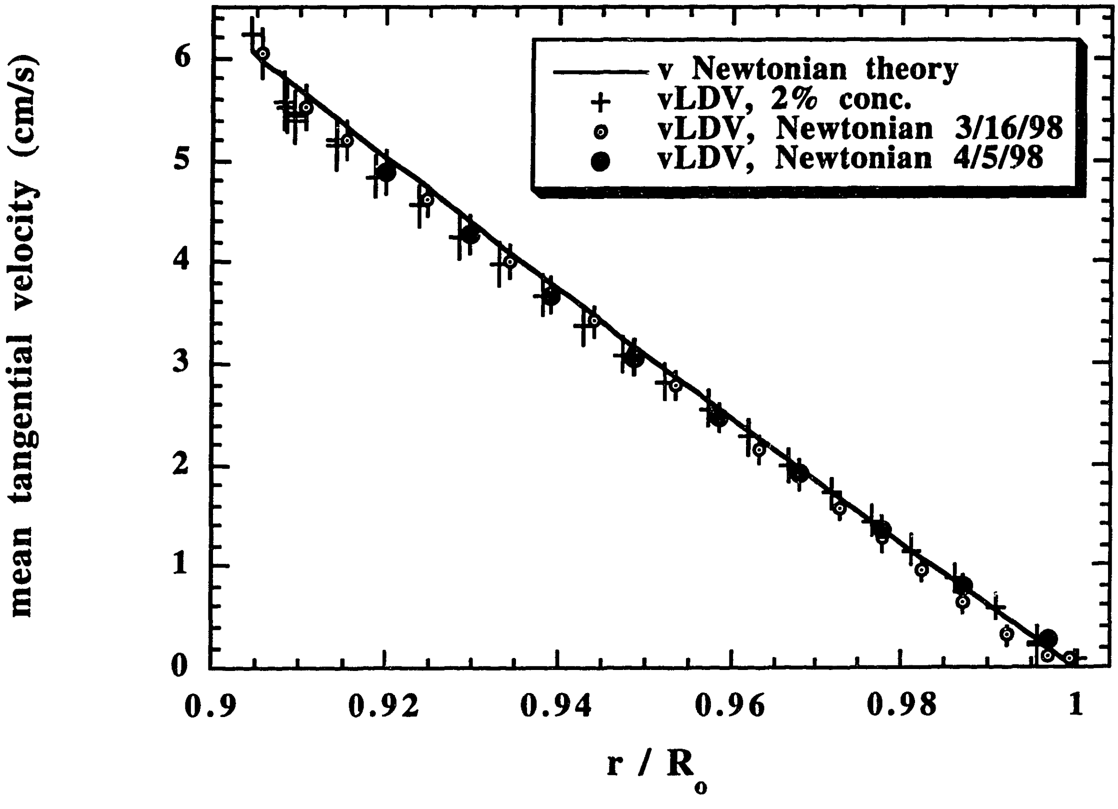

Figure 4.8 Mean tangential velocity profile for the 2% concentrated suspension of Lucite 47G particles compared with the Newtonian suspending liquid seeded with silicon carbide particles and measured twice. Constant LDV parameters are used within each series of runs; the average shear rate = 10 s^{-1} (10 rpm).

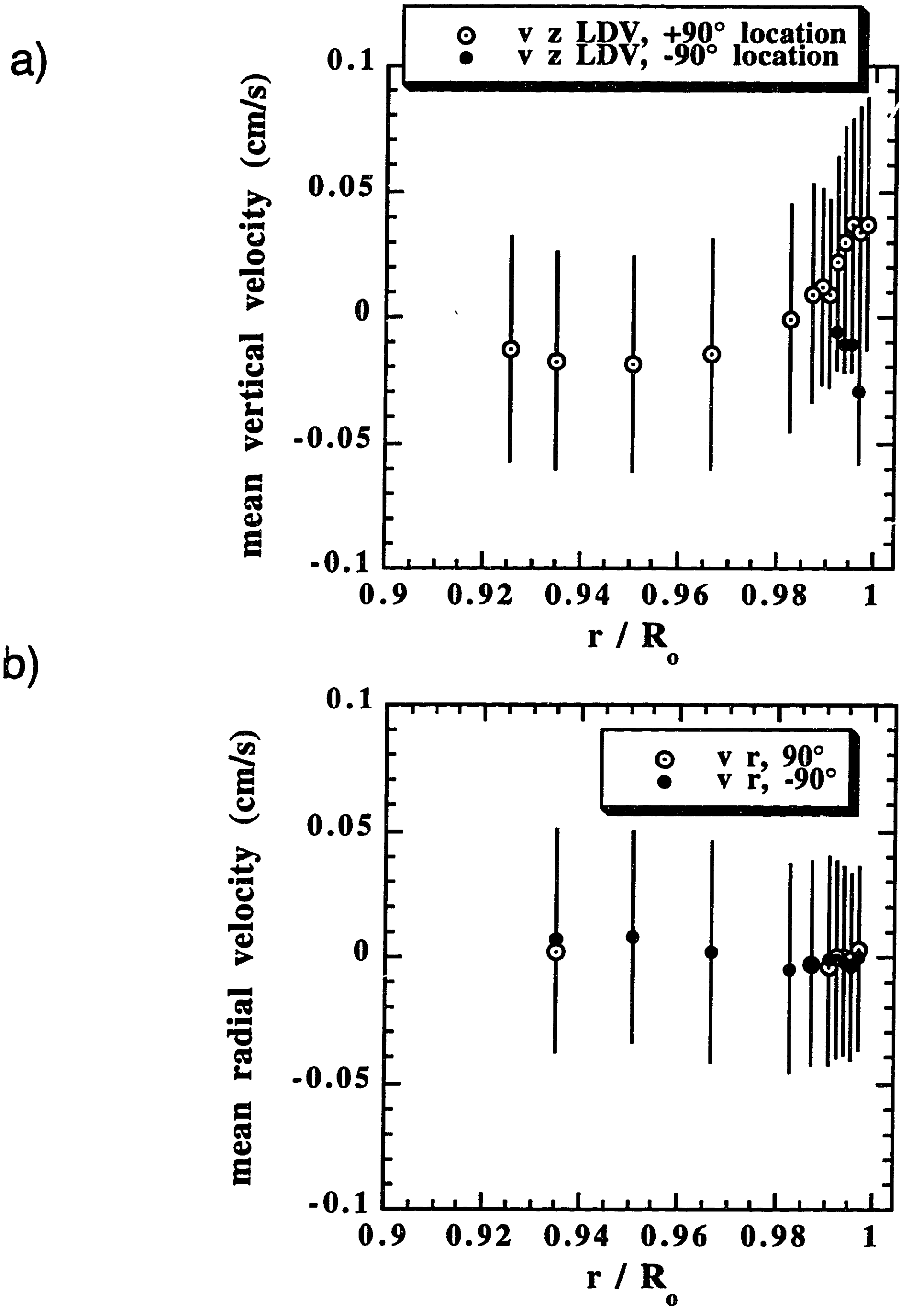

Figure 4.9 Mean vertical (a) and radial (b) velocity profiles measured at the ± 90° locations in a 2% concentrated suspension of Lucite 47G particles in the suspending liquid, at an average shear rate = 10 s^{-1} (10 rpm). The error bars have the value of the standard deviation of the measured velocity distribution at each point.

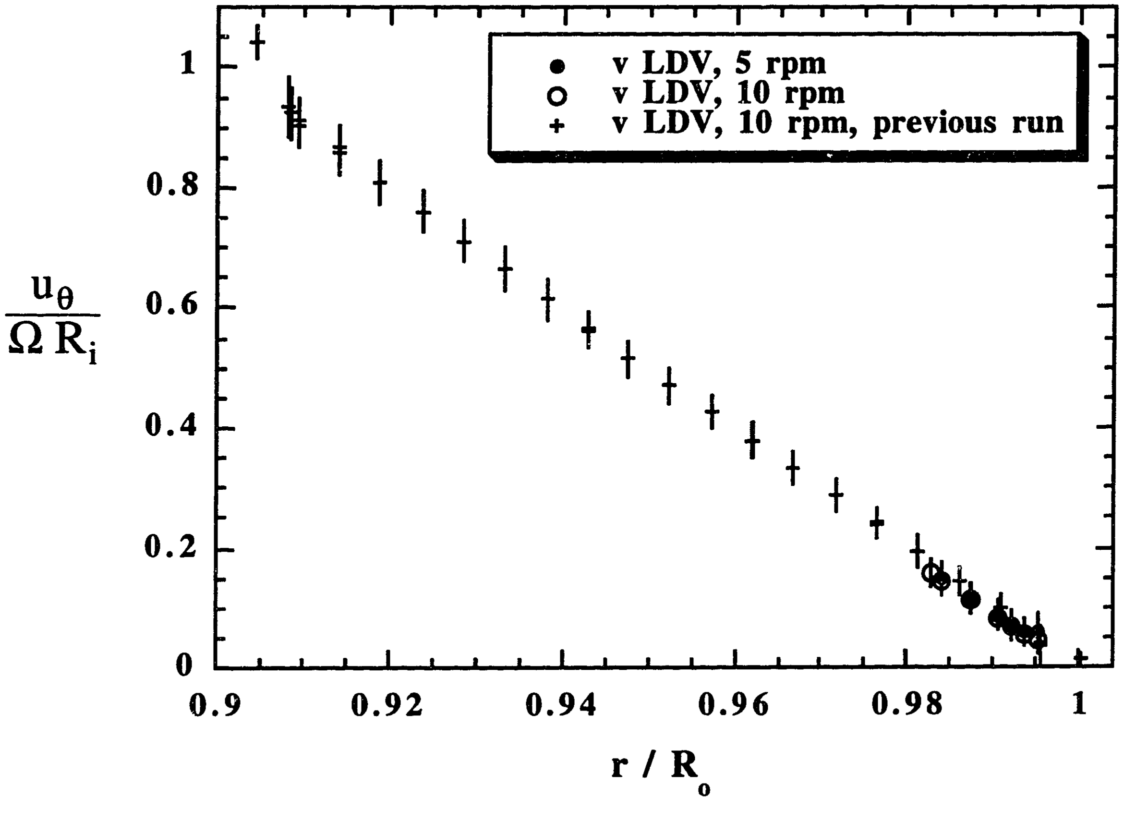

Figure 4.10 Comparing dimensionless mean tangential velocity profiles for average shear rates = 5 s^{-1} (5 rpm) and 10 s^{-1} (10 rpm) for a 2% concentrated suspension. Here, points from the 5 s^{-1} profile overlap with the 10 s^{-1} profile, where each profile is scaled by the velocity of the inner cylinder wall.

Finally, in figure 4.11, we validate the method of equalizing measurement conditions by placing a suspension-filled cuvette in front of the flow at the 0° location. We compare measurements made at the ± 90° locations in the 2% concentrated suspension with measurements made at the 0° position, with a cuvette filled with the same 2% concentrated suspension attached to the outer wall of the enclosing box. In figure 4.11, the vertical velocity fluctuation, measured with different path length cuvettes, matches with that obtained at the 90° position when the path length the beams travel in the suspension is nearly equal in both locations. Accordingly, this test supports the use of the cuvette equalizing method.

4.2.3 One-Dimensional Flow for Concentrated Suspensions

The last test involved verifying that the concentrated suspensions also produced unidirectional shear flow when placed in the Couette device. First, we checked that the mean tangential velocity profile is reproducible for the 50% concentrated suspension, the most concentrated susension we studied. In figure 4.12, three measurements of the mean tangential velocity profile that were widely separated in time are displayed. The fact that the points overlap almost exactly indicated that the flow is extremely reproducible, even over intervals as long as a year and a half.

Also, we confirmed that the flow is one-dimensional in the 50% concentrated suspension. In figure 4.13, it is clear that the mean vertical and radial velocities, measured at the ± 90° locations, are zero compared with experimental uncertainty. We also confirmed that the 40% and 30% concentrated suspensions yielded one-dimensional flows, as shown in figures 4.14 and 4.15, respectively.

A final verification of one-dimensional flow for the 50% concentrated suspension is that no variation is observed in the mean vertical velocity with varying vertical (axial) position, near the midplane of the flow. This is shown in figure 4.16. Overall, the results of the last test establish that the concentrated suspensions produced reproducible unidirectional shear flow in the Couette flow cell.

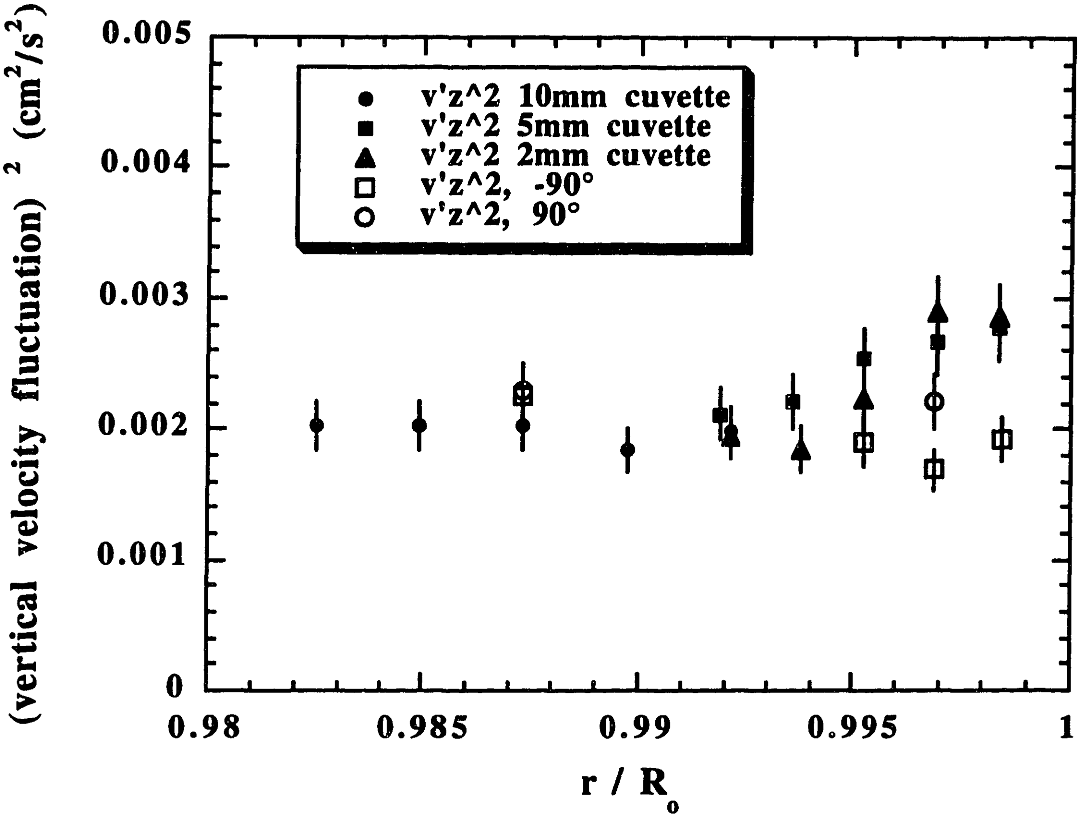

Figure 4.11 Vertical velocity fluctuation measured at 90° and -90° locations, and at 0° location with varying path length cuvettes, average shear rate = 10 s^{-1} (10 rpm), constant LDV parameters.

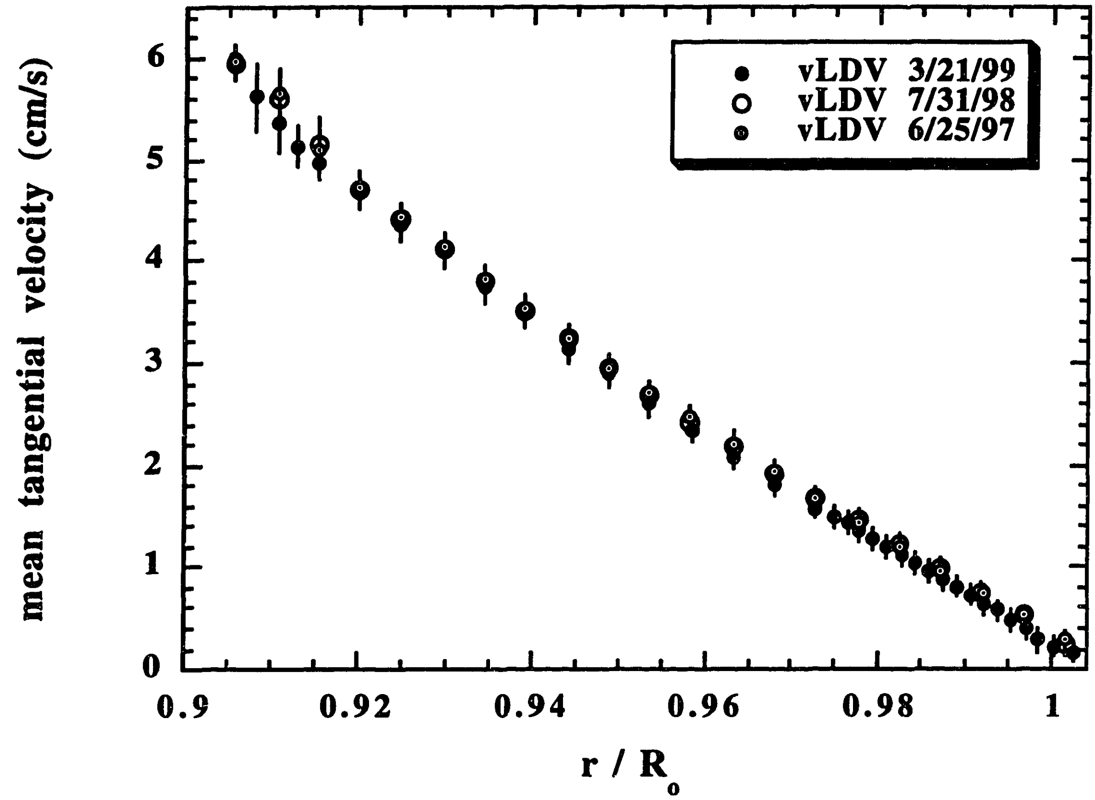

Figure 4.12 Three measurements of the mean tangential velocity profile at the 0° location in a 50% concentrated suspension, average shear rate = 10 s^{-1} (10 rpm). These results demonstrate the reproducibility of the measurements, even after long intervals.

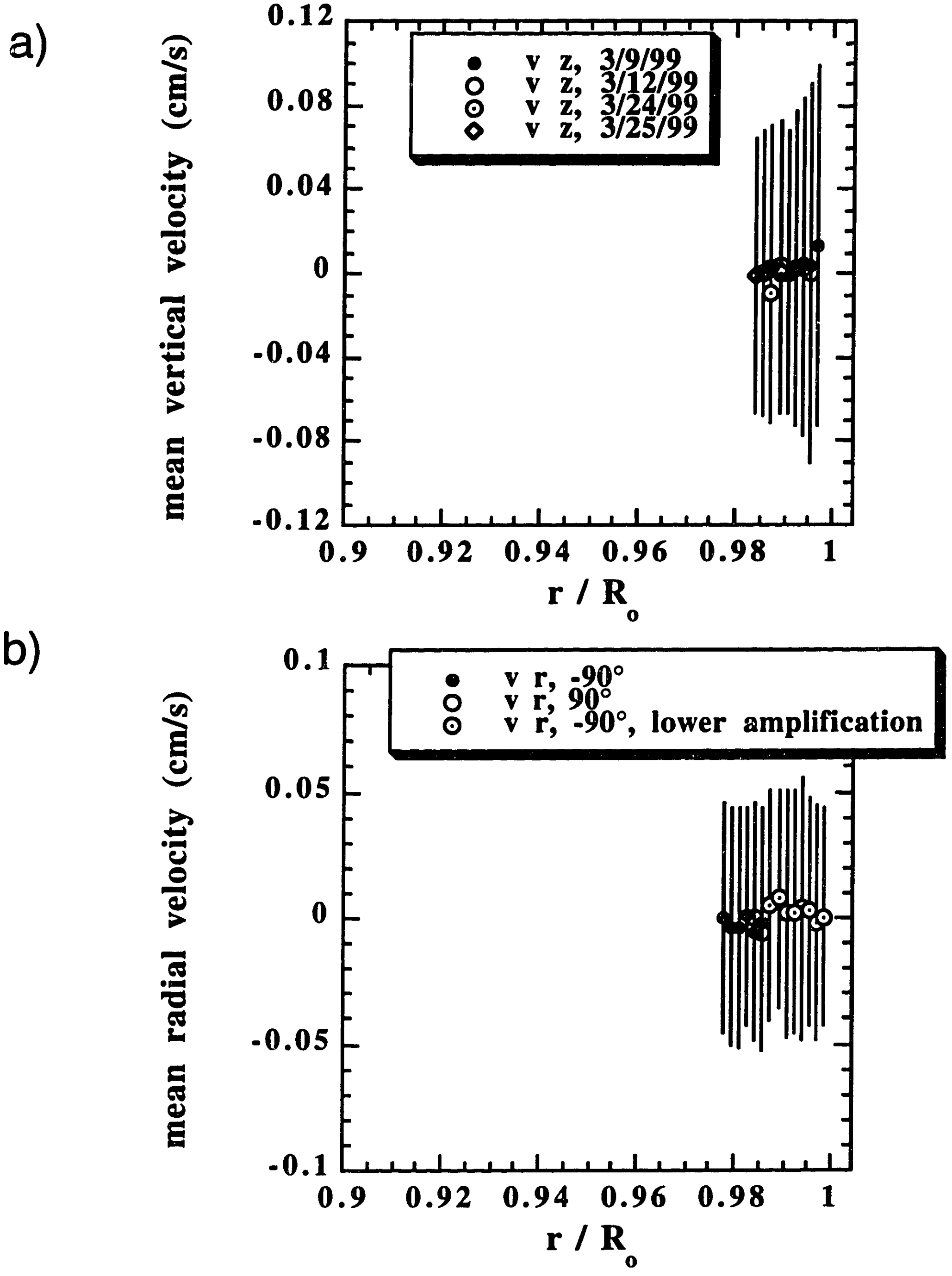

Figure 4.13 Mean vertical (a) and radial (b) velocities measured at the ± 90° locations in the 50% concentrated suspension, at an average shear rate = 10 s^{-1} (10 rpm).

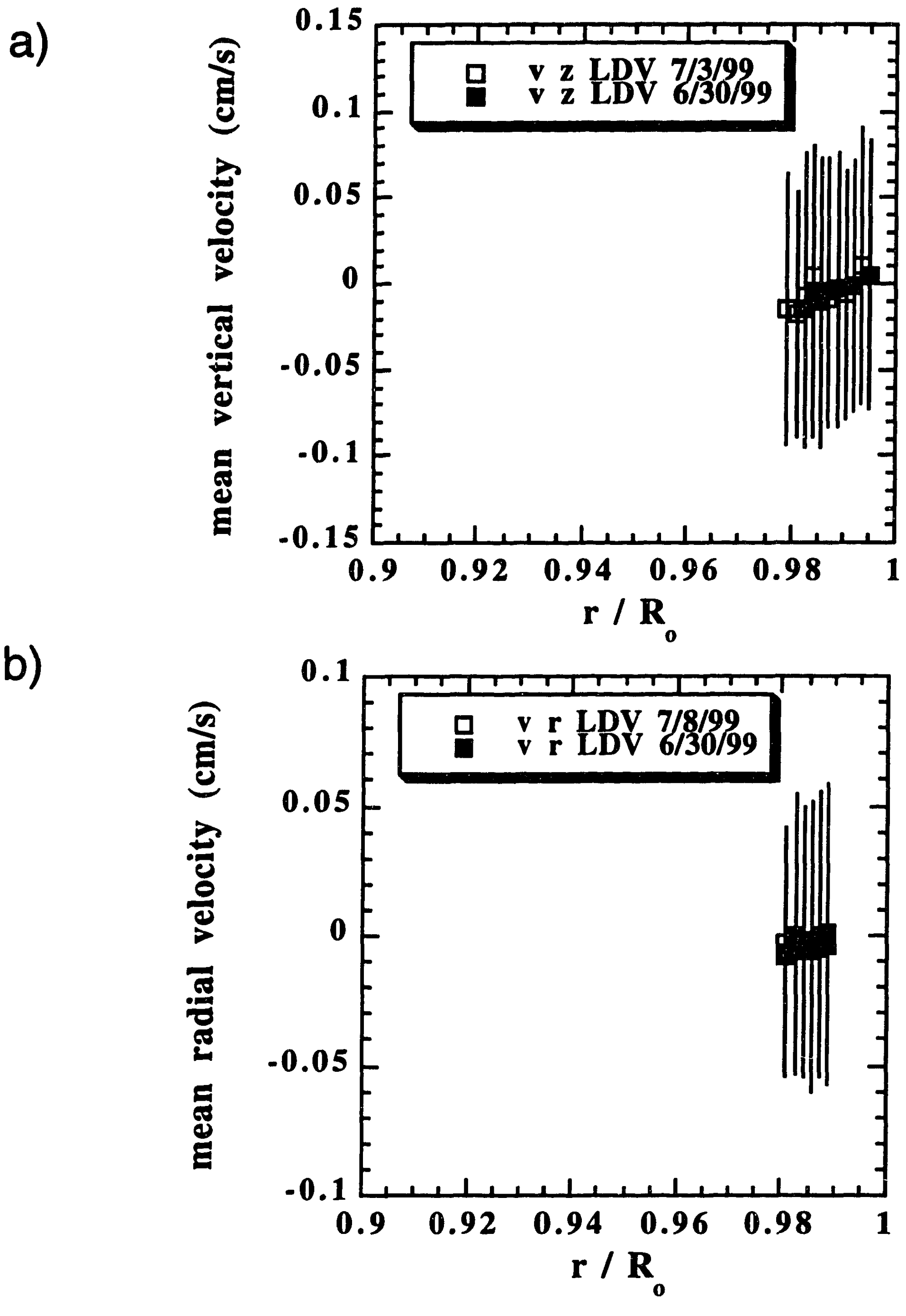

Figure 4.14 Mean vertical (a) and radial (b) velocities measured at the ± 90° locations in the 40% concentrated suspension, average shear rate = 10 s^{-1} (10 rpm).

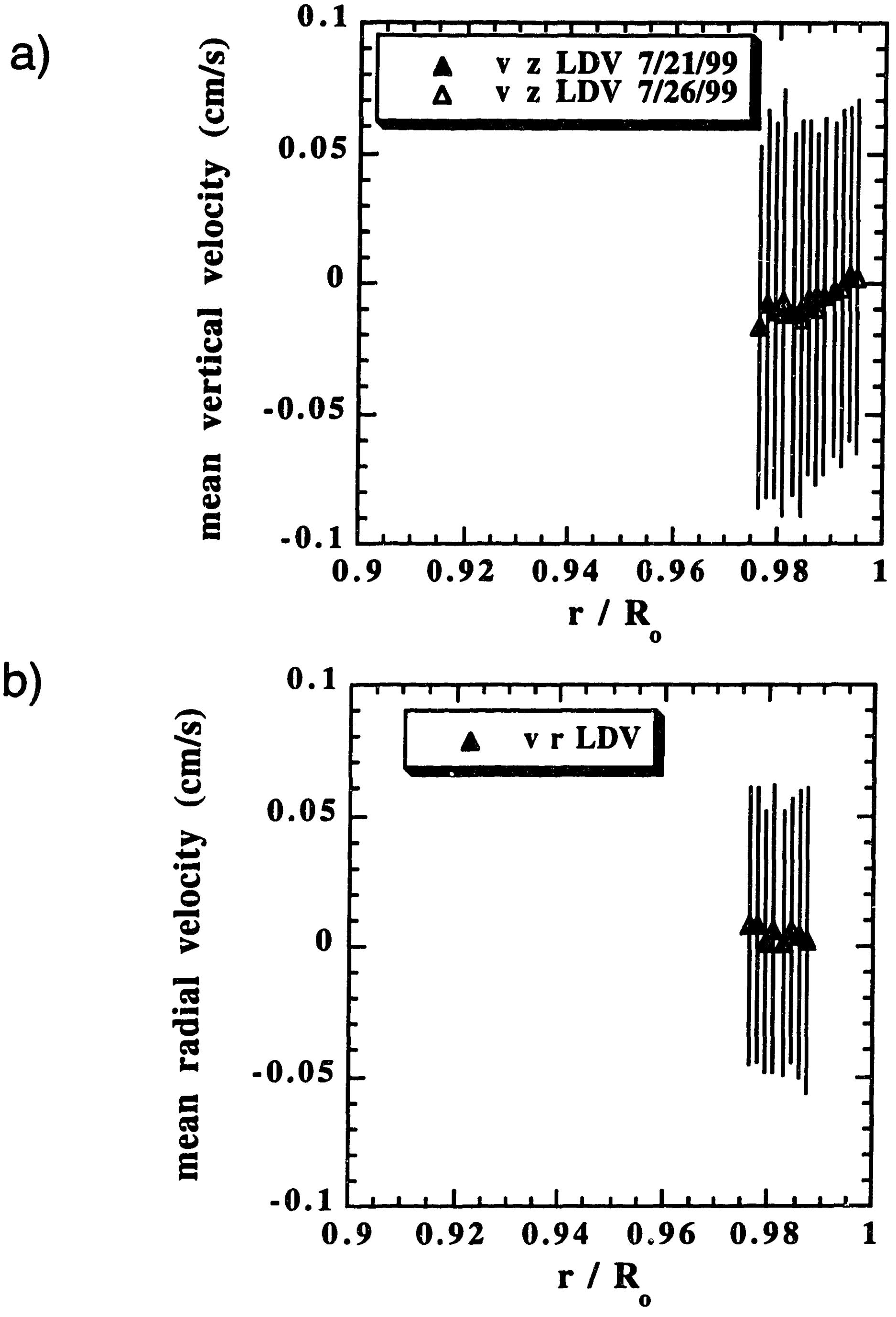

Figure 4.15 Mean vertical (a) and radial (b) velocities measured at the ± 90° locations in the 30% concentrated suspension, average shear rate = 10 s^{-1} (10 rpm).

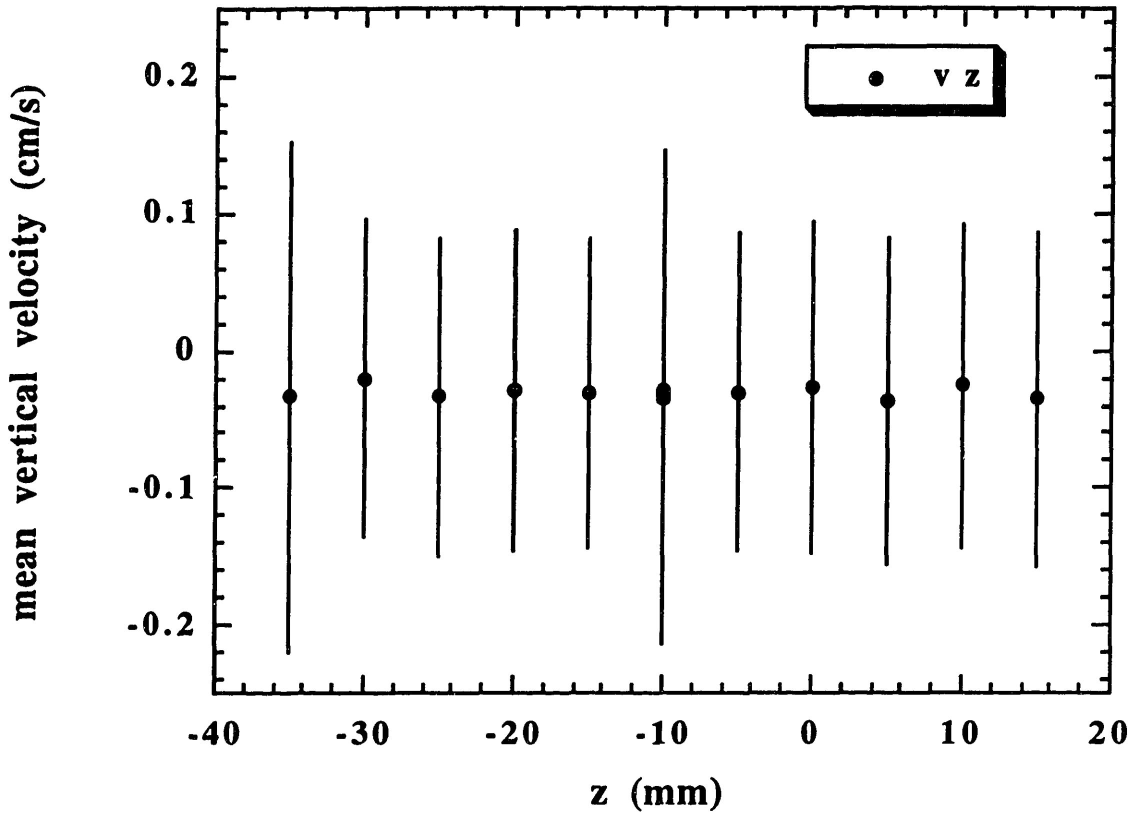

Figure 4.16 Mean vertical velocity as a function of height (z) in the 50% concentrated suspension, average shear rate = 20 s^{-1} (20 rpm), fixed radial position $r/R_o = 0.964$, constant LDV parameters.

ϕ	mean velocity & $\dot{\gamma}$ profiles	$<v'_r{}^2>$ & $<v'_z{}^2>$ profiles, $\dot{\gamma} = 10\ s^{-1}$	$<v'_\theta{}^2>$ profile, $\dot{\gamma} = 10\ s^{-1}$	$<v'_r{}^2>$, $<v'_z{}^2>$ & $<v'_\theta{}^2>$ $(\dot{\gamma})$
0.02	X	X	X	X
0.1	X	X		
0.3	X	X	X	X
0.4	X	X	X	X
0.5	X	X	X	X

Table 4.1 The set of experiments performed on suspensions in this study.

4.3 Physical Observations of the Mean and Fluctuating Velocity from LDV

This section contains a discussion of the physical observations made in our LDV experiments on suspensions. We display the set of experiments performed in table 4.1. We measured the mean velocity and three fluctuating velocity components for three suspensions of 30%, 40% and 50% particle volume fraction. For the 10% concentrated suspension, all the same measurements were made except the tangential fluctuating velocity component. For all the measurements in the concentrated suspensions, measurements from the 2% particle volume fraction suspension were used as a baseline.

4.3.1 Mean Velocity Profile: Calculations of the Shear Rate and Concentration Profiles

First, we present the measurements of mean quantities and follow that with a discussion of velocity fluctuation measurements. This section contains a series of physical observations of the mean velocity profile and resulting calculations of the shear rate and concentration profiles.

We recorded the mean tangential velocity profiles for each suspension at the 0° location. For almost all the runs (except the 10% concentrated suspension) we used a constant set of LDV parameters for measuring all the points across the Couette gap, in order to provide uniformity of measuring conditions for all the points. The mean tangential velocity profiles for 10%, 30%, 40% and 50% concentrated suspensions are displayed in figures 4.17-4.20, respectively. A comparison of the mean tangential velocity profiles from 30%, 40% and 50% concentrated suspensions is presented in figure 4.21.

The shear rate and particle concentration profiles were calculated from the mean velocity profile according to the methods described in section 3.5.1 and 3.5.2, respectively. A comparison of shear rate profiles from the Newtonian suspending liquid and 2%, 10%, 30%, 40% and 50% concentrated suspensions is presented in figure 4.22. In this plot, the dilute suspensions match the Newtonian shear rate profiles, whereas, for the concentrated suspensions, the shear rate profiles

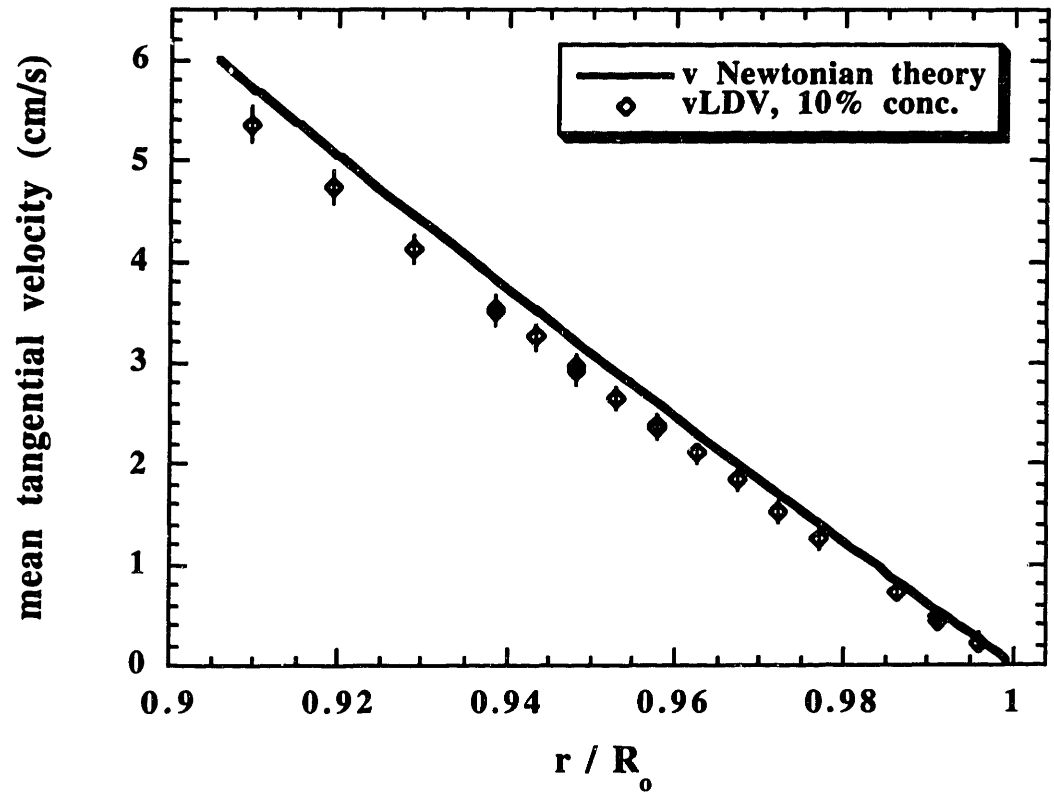

Figure 4.17 Mean tangential velocity profile for the 10% concentrated suspension compared with Newtonian theory at an average shear rate = 10 s^{-1} (10 rpm).

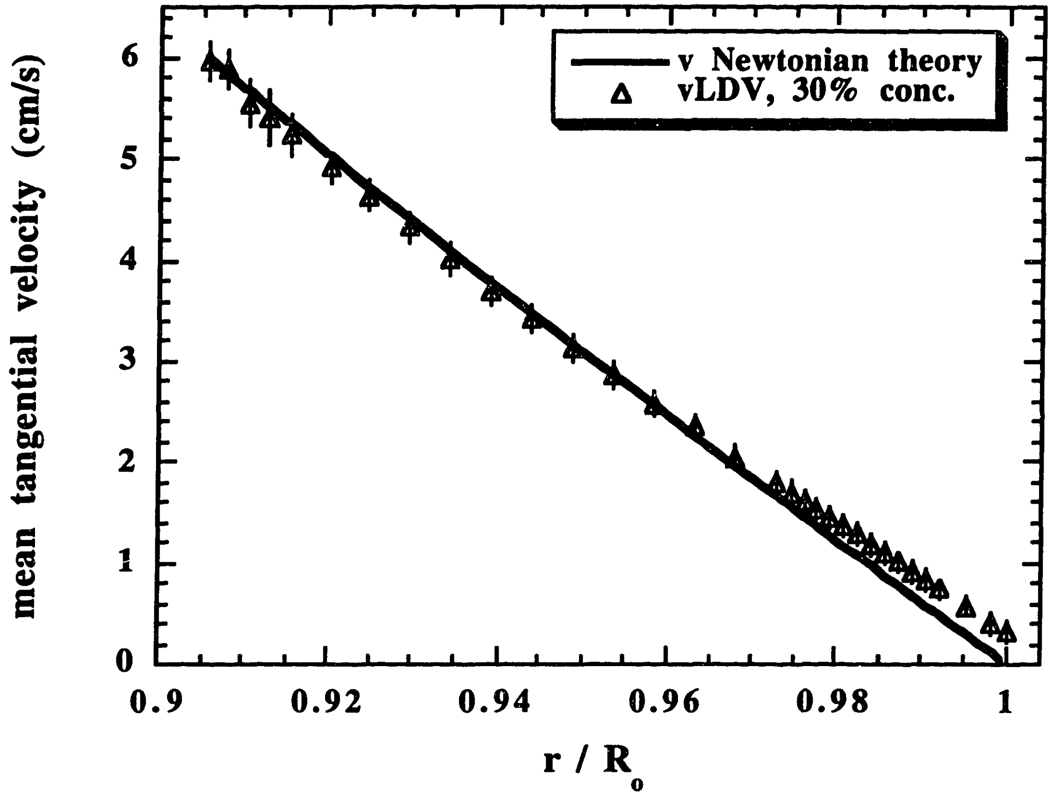

Figure 4.18 Mean tangential velocity profile for the 30% concentrated suspension compared with Newtonian theory at an average shear rate = 10 s^{-1} (10 rpm).

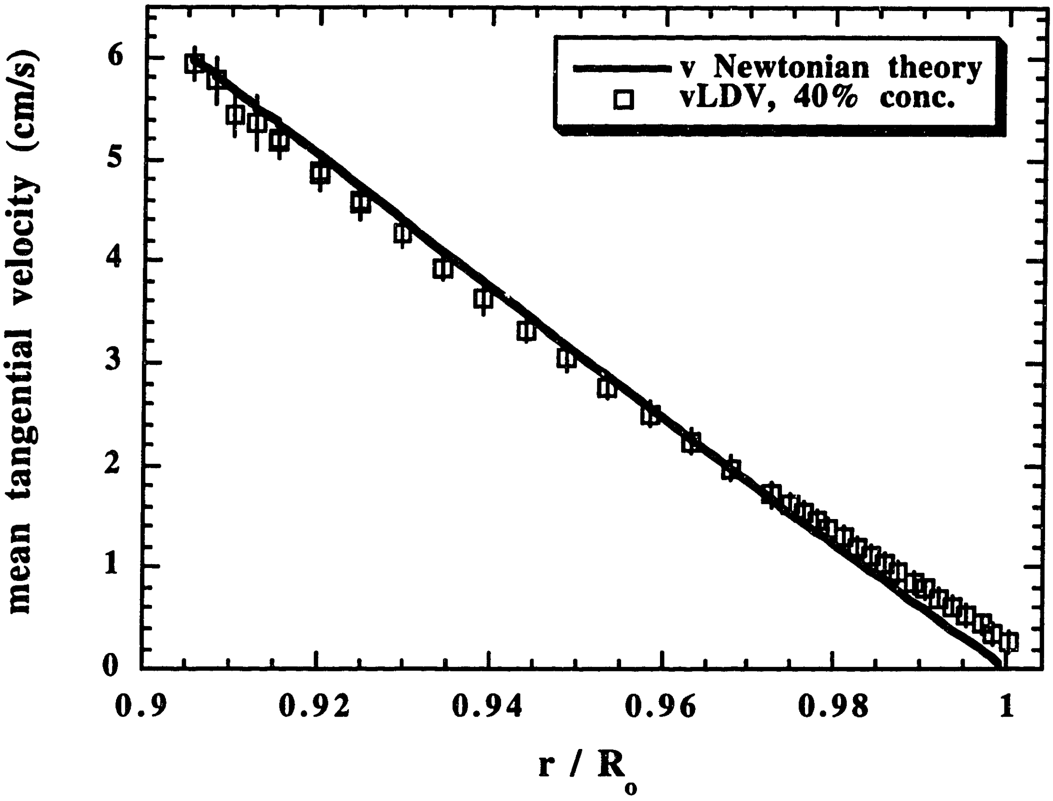

Figure 4.19 Mean tangential velocity profile for the 40% concentrated suspension compared with Newtonian theory at an average shear rate = 10 s^{-1} (10 rpm).

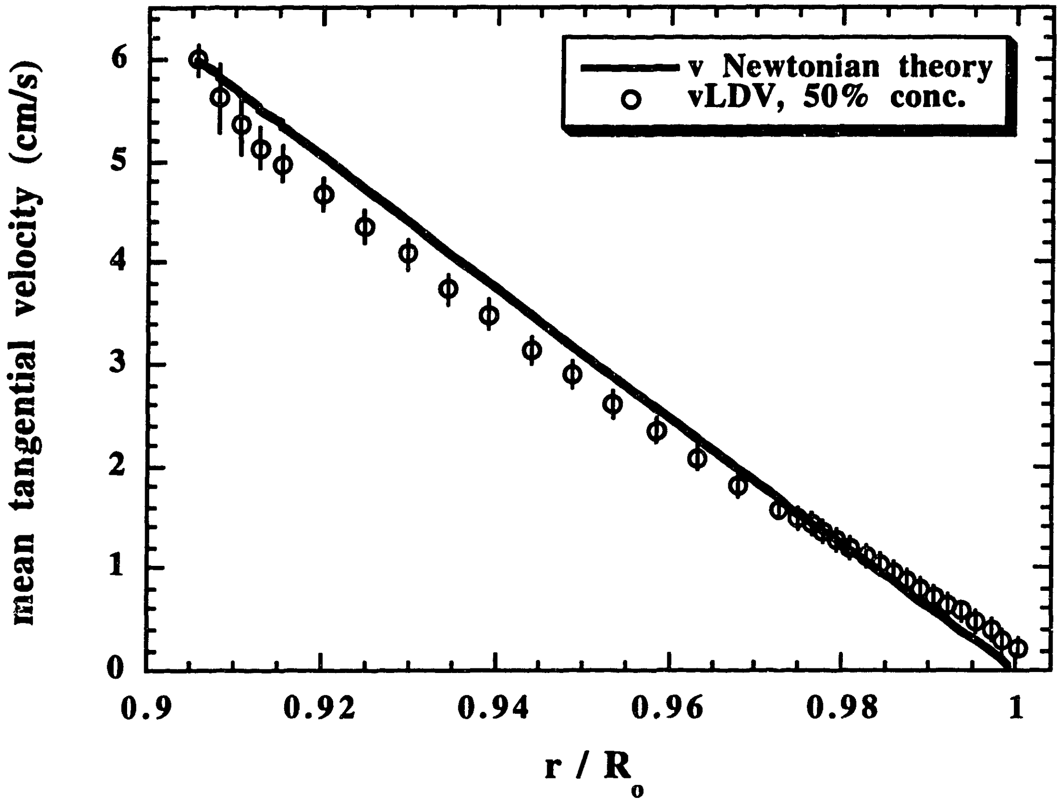

Figure 4.20 Mean tangential velocity profile for the 50% concentrated suspension compared with Newtonian theory at an average shear rate = 10 s^{-1} (10 rpm).

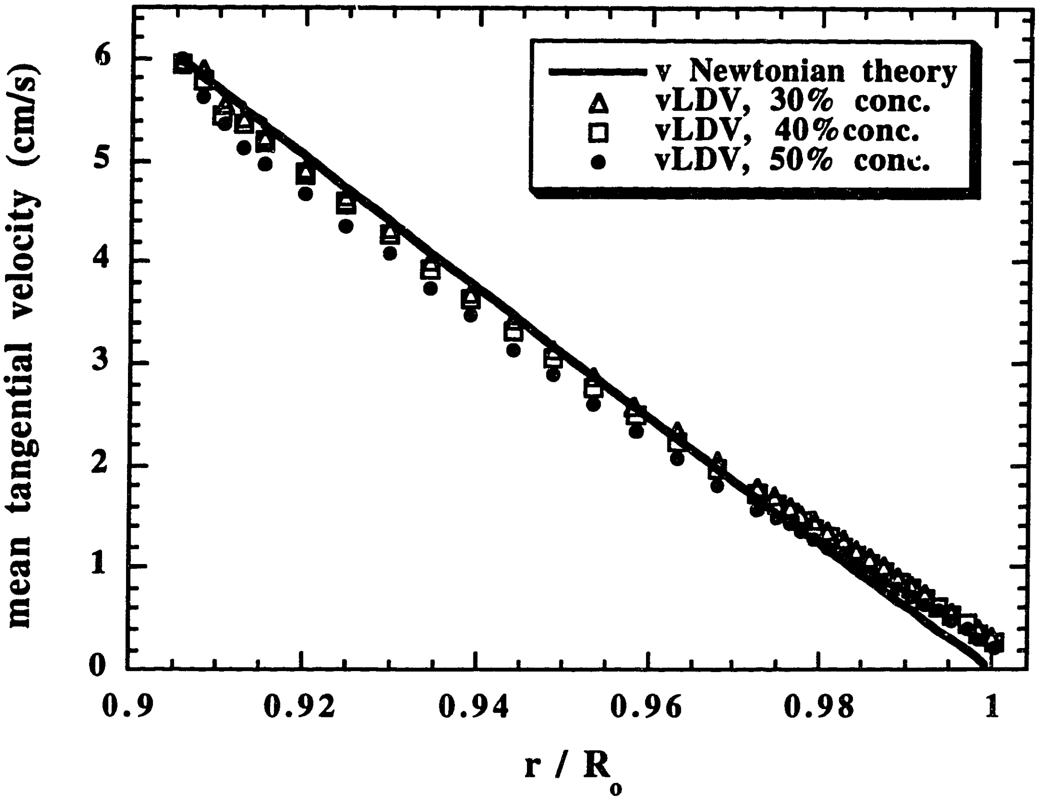

Figure 4.21 Comparison of the mean tangential velocity profiles for 30%, 40% and 50% concentrated suspensions with Newtonian theory, at an average shear rate = 10 s^{-1} (10 rpm).

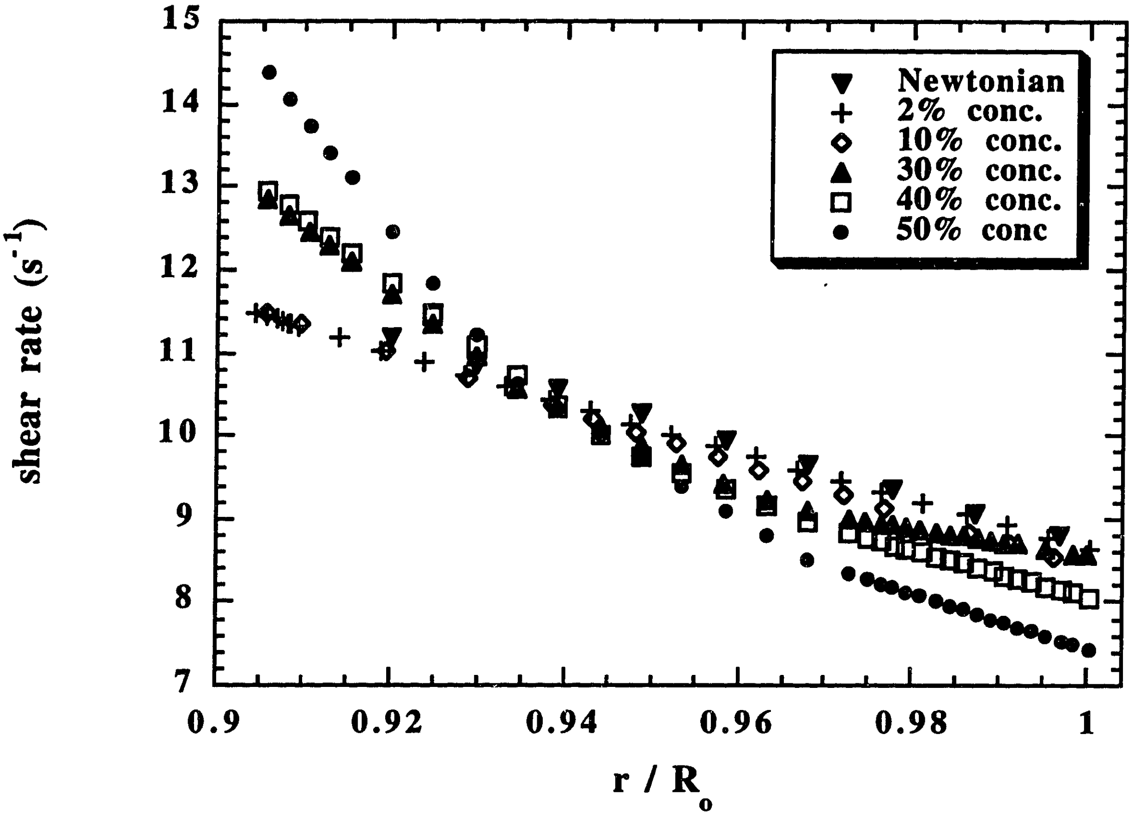

Figure 4.22 Shear rate profiles calculated from global (Newtonian and 2%,10% concentrated suspensions) or three-region (30%, 40%, 50% concentrated suspensions) fits of tangential velocity profile, average shear rate = 10 s^{-1} (10 rpm).

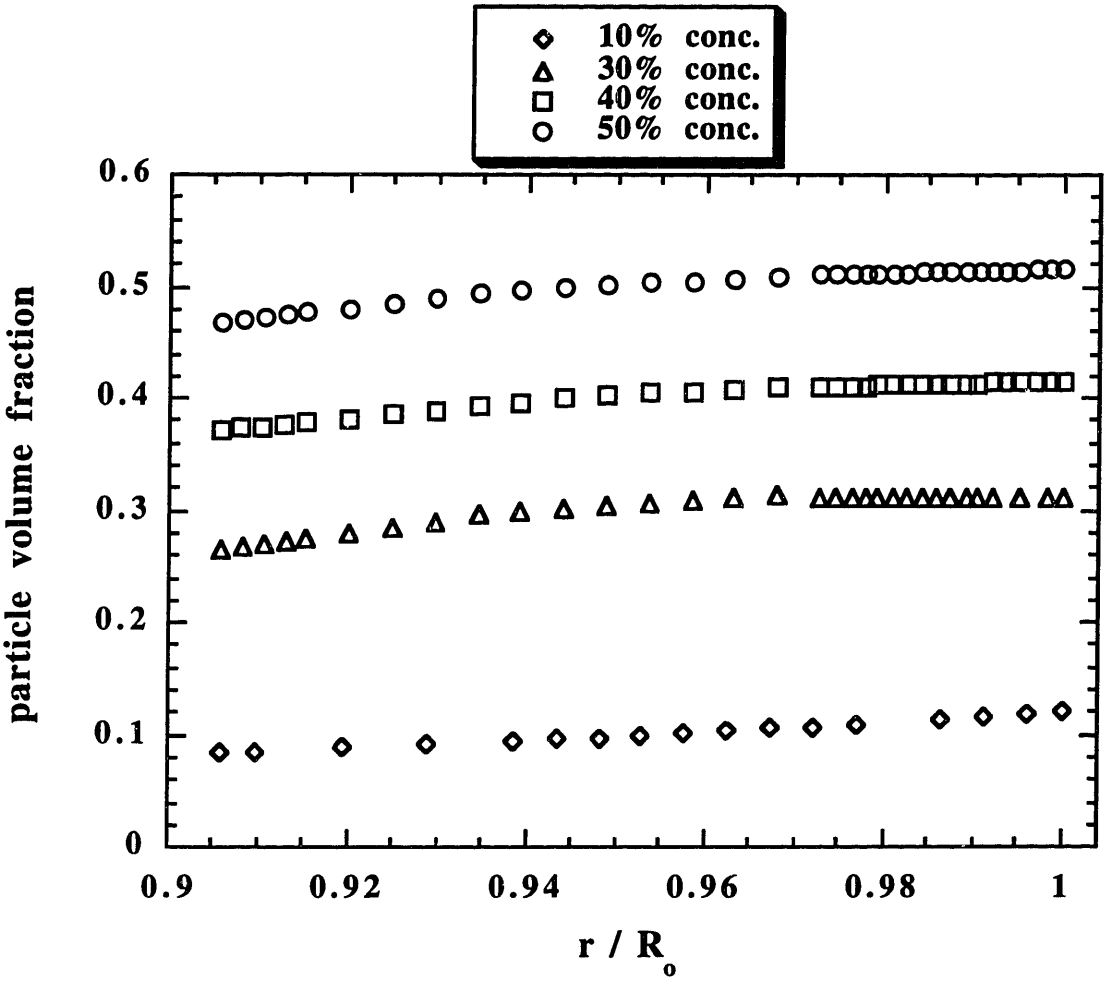

Figure 4.23 Concentration profiles for 10, 30, 40, 50% concentrated suspensions, calculated from shear rate profiles (figure 4.22) and Krieger relative viscosity function.

become increasingly curved and cover a wider range of values, with the 50% concentrated suspension profile deviating the most from the Newtonian profile.

The particle concentration profiles calculated from these shear rate profiles are displayed in figure 4.23. As described earlier in section 3.5.2, the local suspension viscosity is obtained from the ratio of the shear stress, which decreases as $\frac{1}{r^2}$ across the gap, and the local shear rate. If we assume that the Krieger viscosity function (Krieger, 1972), given as

$$\eta(\phi) = \left(1 - \frac{\phi}{\phi}\right)^{-1.82} \tag{4.2}$$

describes the relation between the particle concentration and the suspension viscosity, we can invert the function to calculate a local concentration profile from the local viscosity profile. This procedure yields only a relative concentration profile, however, because we do not measure the absolute magnitude of the stress. We normalize the relative concentration profile so that the average concentration is the bulk concentration.

For all the concentrations observed, a similar shape is evident in the profiles, with the lowest concentration lying near the inner cylinder wall and the highest near the outer cylinder wall. Although the slope of these concentration profiles is slight, at the higher concentrations the variation can have a large impact because the viscosity is a strong function of the concentration.

4.3.2 Particle Velocity Fluctuations

This section contains a report of physical observations of the particle velocity fluctuations caused by inter-particle collisions. We measured three components of the velocity fluctuations, in the tangential (flow, or 1), radial (gradient, or 2) and vertical (neutral, or 3) directions. Following the measurement and data reduction procedures described in sections 3.4 and 3.5, we identified the measured velocity fluctuation at a point with the standard deviation of the observed velocity distribution. To find the part of the total velocity fluctuation arising only from inter-particle collisions, we subtract off the dilute (2%) suspension baseline. We focus on four features of the physical observations: the relative sizes of the three fluctuation components at a given shear rate and rotation speed, and then the dependence of each collisional velocity fluctuation component on particle volume fraction, radial position, and shear rate.

4.3.2.1 Velocity Fluctuation Components at Fixed Rotation Speed

The differences in the size of the three velocity fluctuation components are illustrated in figures 4.24-4.26. All the components were measured at a constant rotation speed of 10 rpm (average shear rate = 10 s^{-1}), and plotted against the local shear rate at each point for each suspension. The radial and vertical velocity fluctuation components were measured at the ± 90° locations, and the tangential component was measured at the 0° location, with an extra suspension-filled cuvette placed in the beam path. Each symbol shape represents a different bulk concentration, and the points marked by + and x indicate the dilute 2% particle volume fraction suspension baseline.

In comparing the collisional velocity fluctuation components derived from these three graphs, it is clear that the tangential component is overwhelmingly the largest at every concentration, followed by the vertical and then the radial components. It is also apparent from these plots that the three components each vary differently with particle concentration.

4.3.2.2 Dependence of Velocity Fluctuation Components on Radial Position

A different presentation of the velocity fluctuation components shown in figures 4.24-4.26 in section 4.3.2.1 is a set of plots of the velocity fluctuations from each concentration against radial position. This yields the figures 4.27-4.29, for the same constant rotation rate of 10 rpm (average shear rate = 10 s^{-1}). It is immediately apparent from these plots that most of our data comes from the region near the outer cylinder wall, since the region of the flow we can measure at the ± 90° positions is limited by the beam attenuation resulting from the bubbles inside the particles.

For most of these velocity fluctuation profiles, within experimental uncertainty, there is little or no variation with radial position over the accessible measurement region. In the accessible region, the most interior points for the concentrated suspensions were located about seven particle

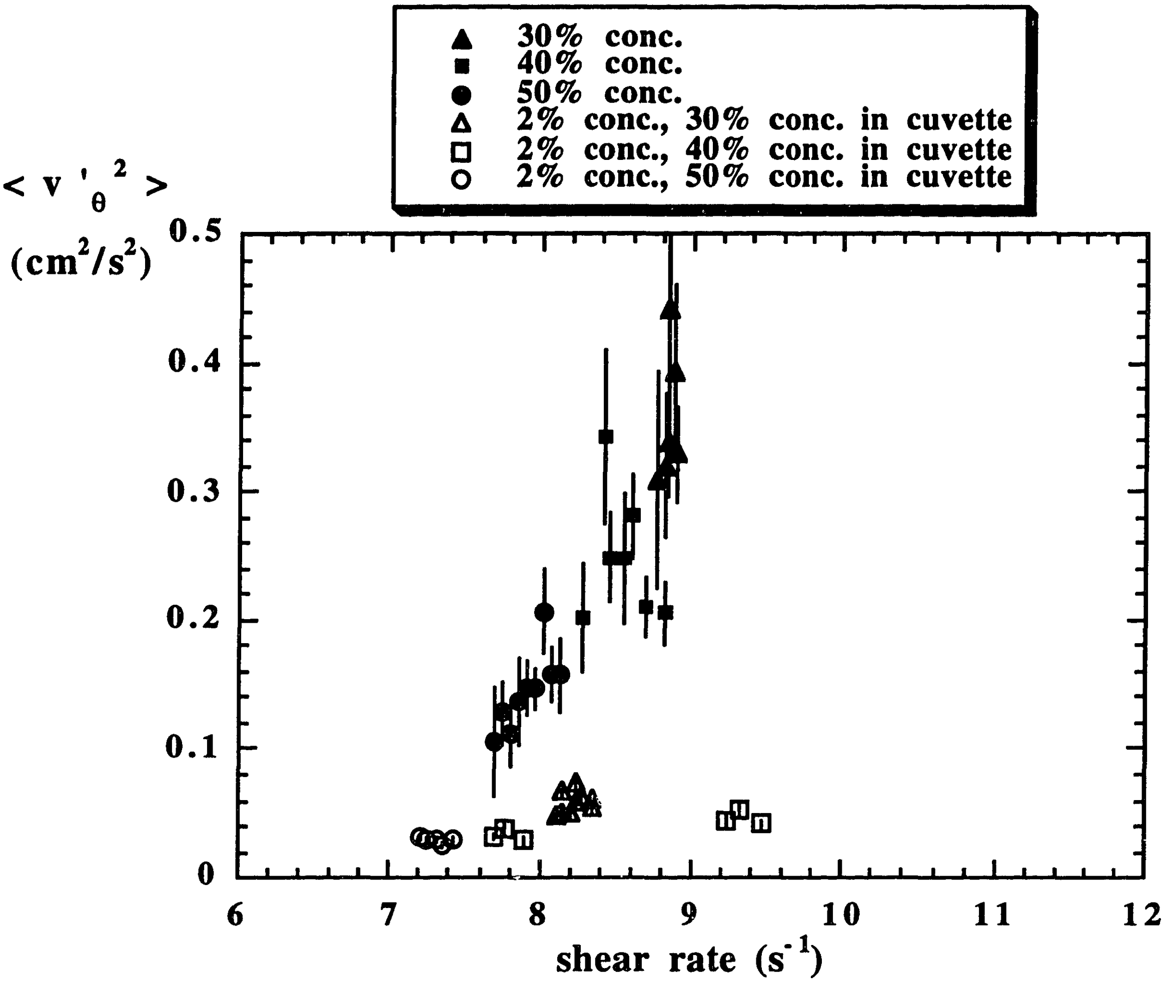

Figure 4.24 Tangential velocity fluctuation measured at the 0° location for the 30%, 40% and 50% concentrated suspensions compared with the 2% concentrated suspension baseline, plotted against local shear rate. The average shear rate = 10 s^{-1} (10 rpm), and the LDV beams pass through a suspension-filled 3 mm path length cuvette.

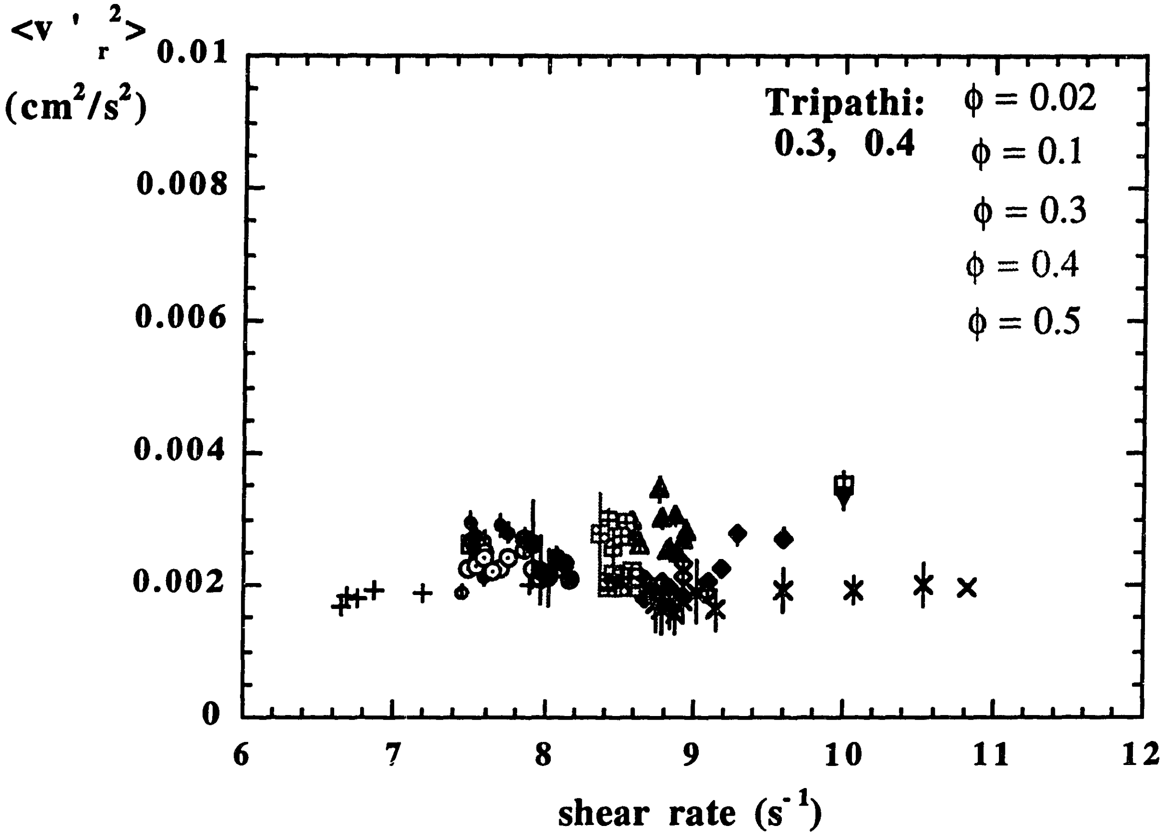

Figure 4.25 Radial velocity fluctuation, for various particle volume fractions (ϕ = 0.02, 0.1, 0.3, 0.4 and 0.5), measured at the ± 90° locations, plotted against local shear rate. Constant average shear rate = 10 s^{-1} (10 rpm).

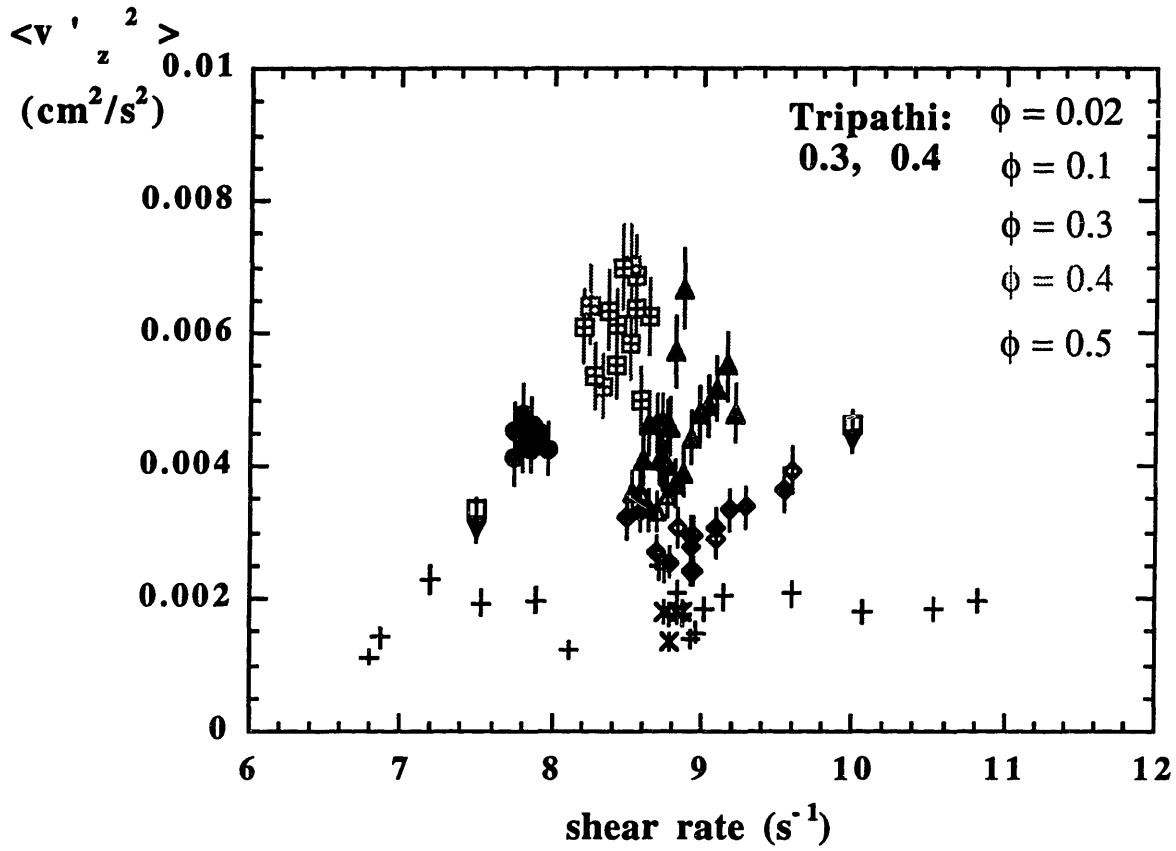

Figure 4.26 Vertical velocity fluctuation, for various particle volume fractions (ϕ = 0.02, 0.1, 0.3, 0.4 and 0.5), measured at the ± 90° locations, plotted against local shear rate. Constant average shear rate = 10 s^{-1} (10 rpm).

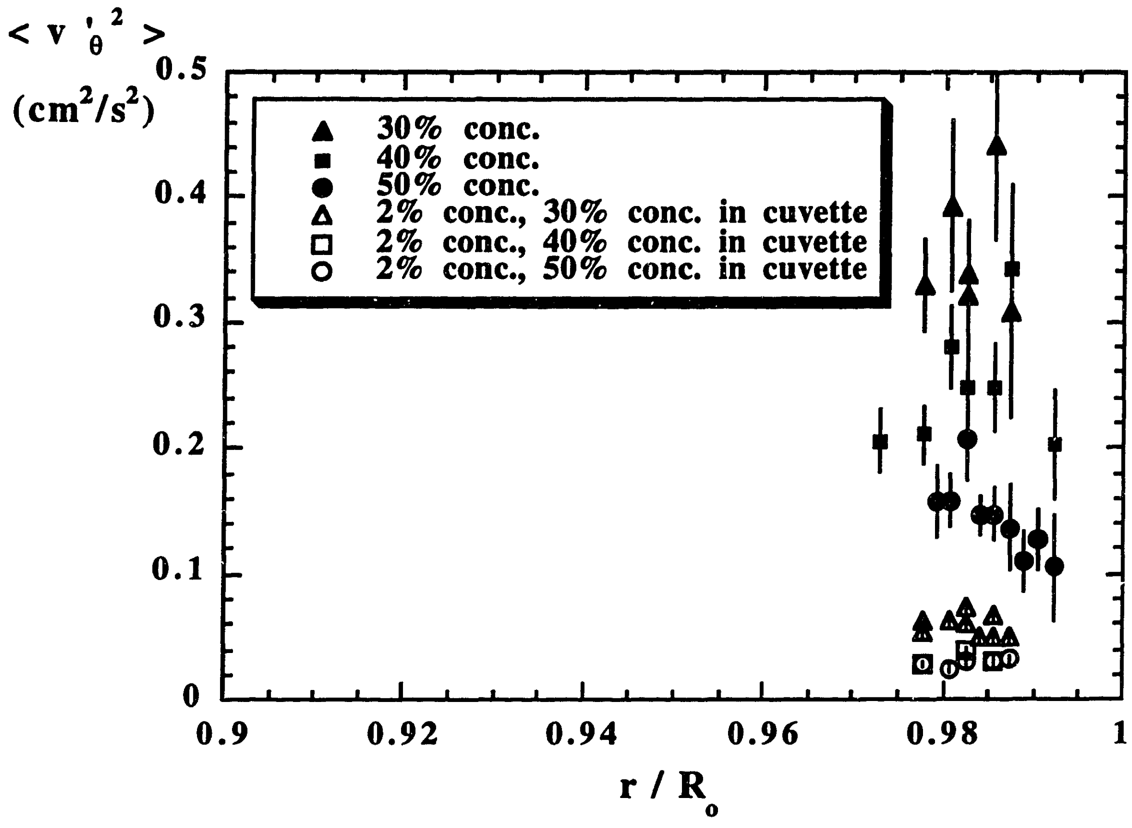

Figure 4.27 Tangential velocity fluctuation for the 30%, 40% and 50% concentrated suspensions compared with the 2% concentrated suspension baseline, plotted against dimensionless radial position. The average shear rate = 10 s^{-1} (10 rpm), and the LDV beams pass through a suspension-filled 3 mm path length cuvette.

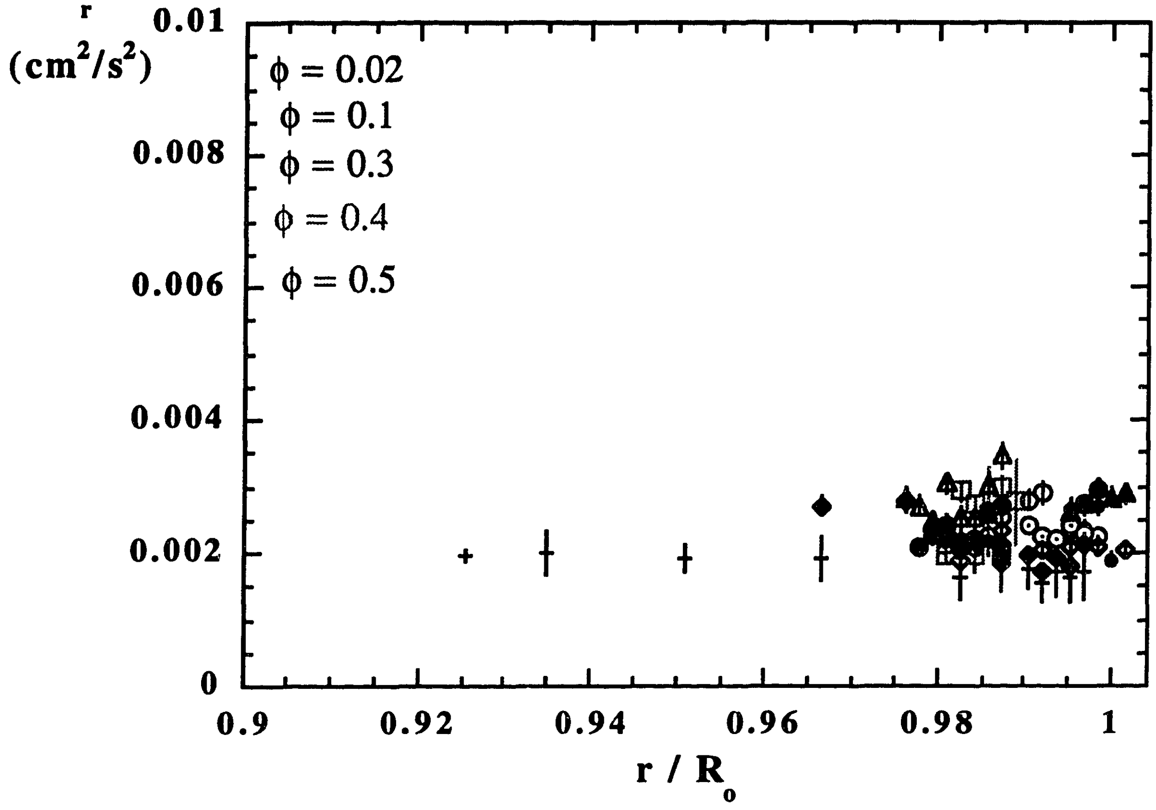

Figure 4.28 Radial velocity fluctuation, for various particle volume fractions (2%, 10%, 30%, 40% and 50% concentrated suspensions), measured at the ± 90° locations, plotted against dimensionless radial position. Constant average shear rate = 10 s^{-1} (10 rpm).

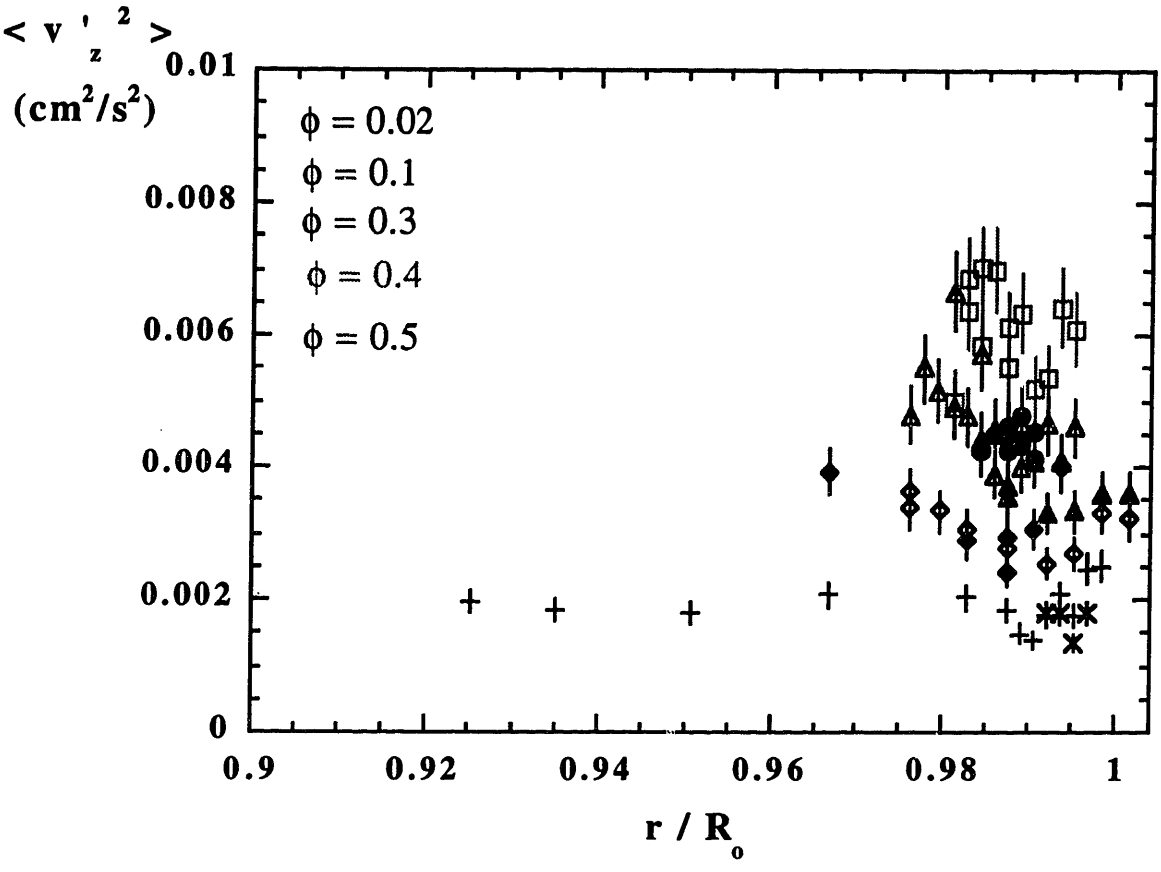

Figure 4.29 Vertical velocity fluctuation, for various particle volume fractions (2%, 10%, 30%, 40% and 50% concentrated suspensions), measured at the ± 90° locations, plotted against dimensionless radial position. Constant average shear rate = 10 s^{-1} (10 rpm).

diameters away from the outer cylinder wall, out of 30 particle diameters in total across the Couette gap. We believe these points are in the bulk flow, where wall effects are insignificant. Because we observed little variation between measurements at these interior points and at the other points, we are convinced our measurements are representative of the bulk flow and are not taken only from a wall boundary layer.

The exception to this argument is the vertical velocity fluctuation component, where a large high tail, due to LDV noise, in the 50% particle volume fraction profile is noticeable at the outer cylinder wall. As discussed in section 3.5, there is a radial position ($r/R_o = 0.99$) in the vertical component plot where the LDV noise becomes quite large. Since we only report measurements from radial positions beyond this noise region, we believe these observations are representative of the bulk flow.

4.3.2.3 Dependence of Collisional Velocity Fluctuation Components on ϕ, Particle Volume Fraction

In figures 4.30-4.32 we present the dependence of the collisional velocity fluctuation components on particle volume fraction, at constant rotation speed of 10 rpm (average shear rate = 10 s^{-1}) and constant local shear rate of 8.7 s^{-1}. We plot the average value of the collisional velocity fluctuation measured at each concentration against the local concentration that corresponds to a local shear rate of 8.7 s^{-1} at the 10 rpm rotation speed.

Indeed, as indicated in section 4.3.2.1, each component behaves in a distinct manner. The radial component (figure 4.31) hardly varies with particle concentration. It appears to increase slightly and then plateau. The tangential component (figure 4.30) monotonically decreases between concentrations of 30% and 50%. The vertical component (figure 4.32) increases from 10% to 40% particle volume fraction, and then decreases at higher concentration.

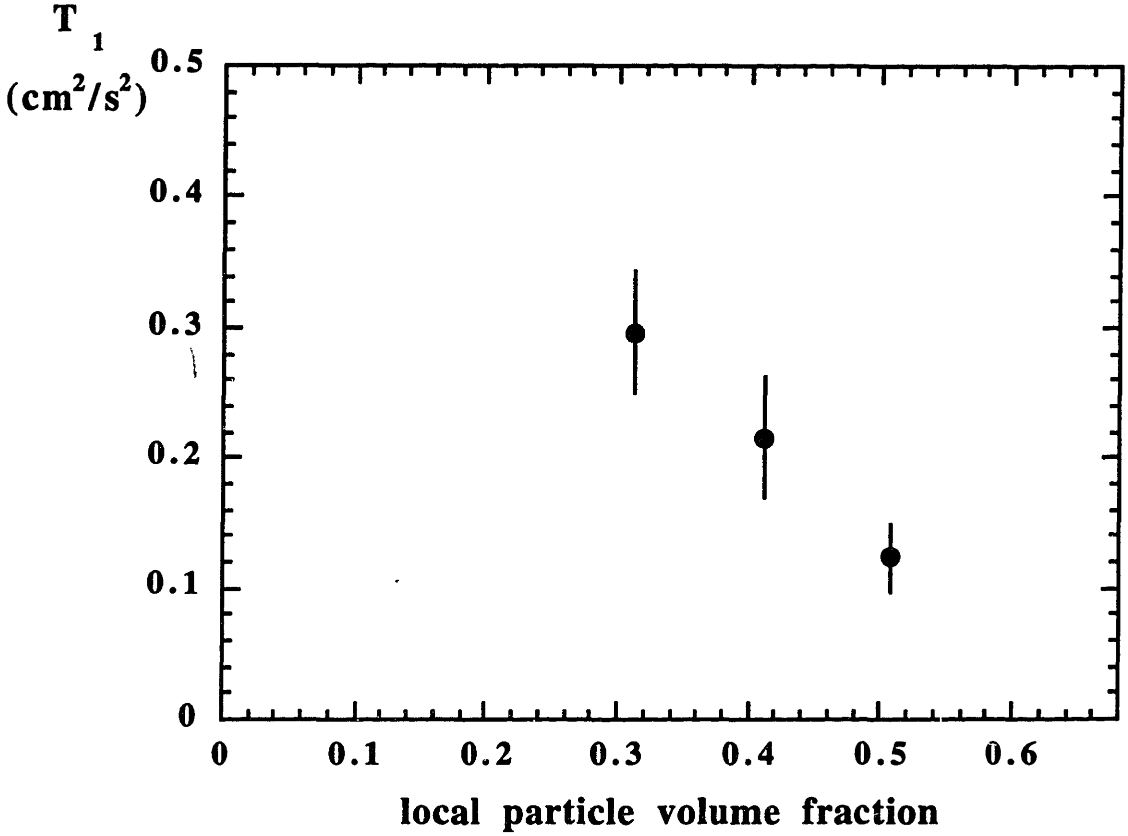

Figure 4.30 Tangential collisional velocity fluctuation, for various particle volume fractions (30%, 40% and 50% concentrated suspensions), measured at the 0° location, with the LDV beams passing through a suspension-filled 3 mm path length cuvette, at a constant local shear rate of 8.7 s^{-1} and constant average shear rate of 10 s^{-1} (10 rpm).

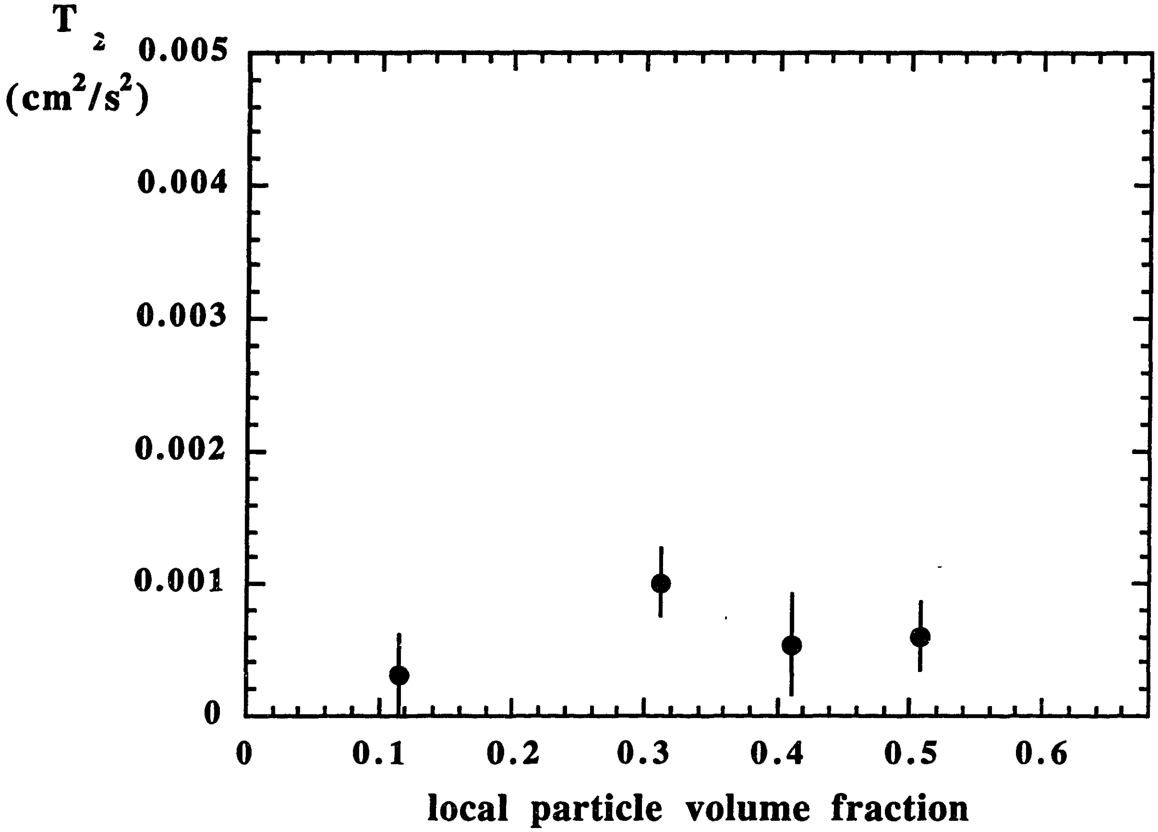

Figure 4.31 Radial collisional velocity fluctuation, for various particle volume fractions (10%, 30%, 40% and 50% concentrated suspensions), measured at the ± 90° locations, at a constant local shear rate of 8.7 s^{-1} and constant average shear rate of 10 s^{-1} (10 rpm).

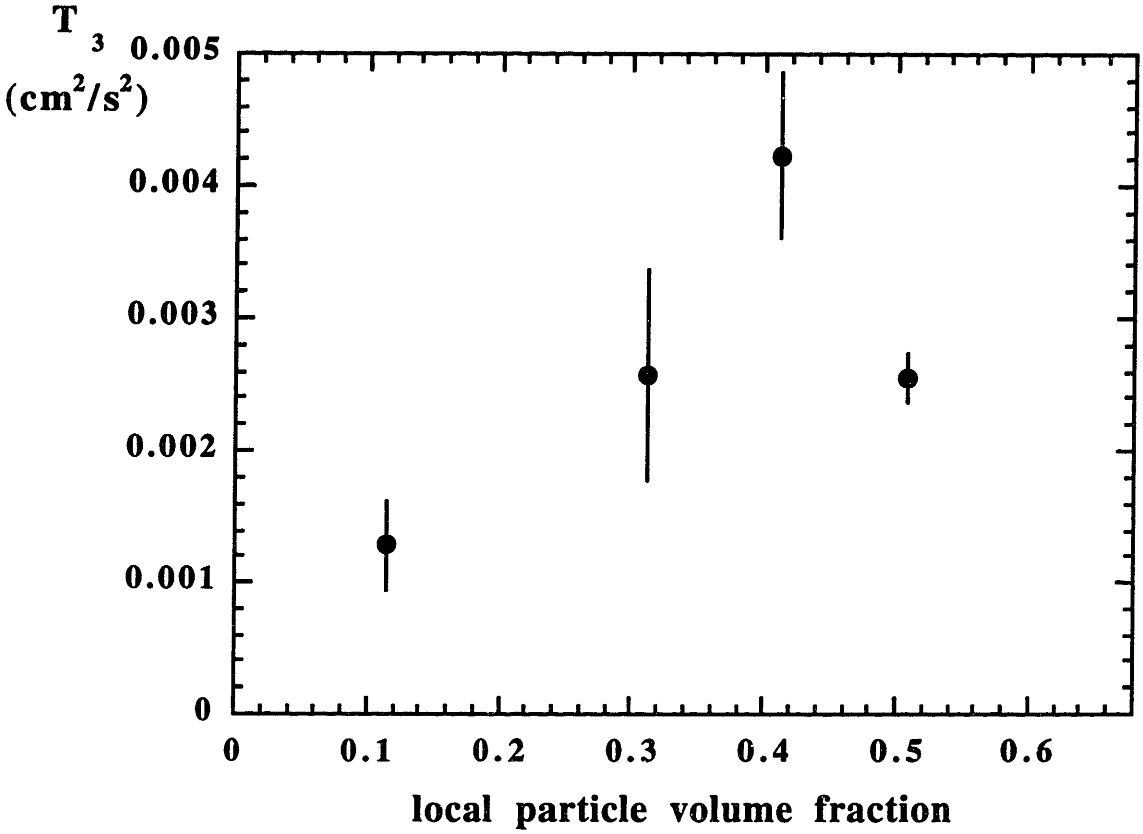

Figure 4.32 Vertical collisional velocity fluctuation, for various particle volume fractions (10%, 30%, 40% and 50% concentrated suspensions), measured at the ± 90° locations, at a constant local shear rate of 8.7 s^{-1} and constant average shear rate of 10 s^{-1} (10 rpm).

4.3.2.4 Dependence of Collisional Velocity Fluctuation Components on Shear Rate

Finally, we present the variation of each of the collisional velocity fluctuation components with shear rate, shown in figures 4.33-4.35. These data were obtained by measuring the collisional velocity fluctuation components at a small number of adjacent radial positions and varying the local shear rate by changing the inner cylinder rotation speed. The maximum range of average shear rates was 1 to 12 s^{-1}, for the 40% concentrated suspension. For each of the components, at most of the shear rates, the difference between the measurements at different positions is insignificant compared with the difference between measurements at different rotation speeds.

It is apparent from these figures that the three collisional velocity fluctuation components each vary differently with shear rate. The tangential component appears to scale quadratically with shear rate for the 30% and 40% concentrations. If we fit the curves with a least-squares quadratic fit in Kaleidagraph, we find

$$T_1(\phi = 0.3) = 40\ a^2\ \gamma^2 \tag{4.3}$$

$$T_1(\phi = 0.4) = 27.5\ a^2\ \gamma^2 \tag{4.4}$$

The 50% concentrated suspension varies more slowly with shear rate, and has a close to quadratic dependence as well, but it has a more complicated shape. The curve appears to rise, plateau, and then rise sharply again. If we neglect the details of this shape and fit the 50% concentrated suspension curve with a quadratic as well, we find

$$T_1(\phi = 0.5) = 17.3\ a^2\ \gamma^2 \tag{4.5}$$

Individual plots of the tangential component for each concentration appear in figures 4.36-4.38. Another point we notice is that all the curves on the tangential and vertical component plots approach zero at zero shear rate, as expected. This supports our assertion that we subtracted off the proper amount of non-collisional fluctuations.

The vertical component has a complex variation with shear rate, for the 30%, 40%, and

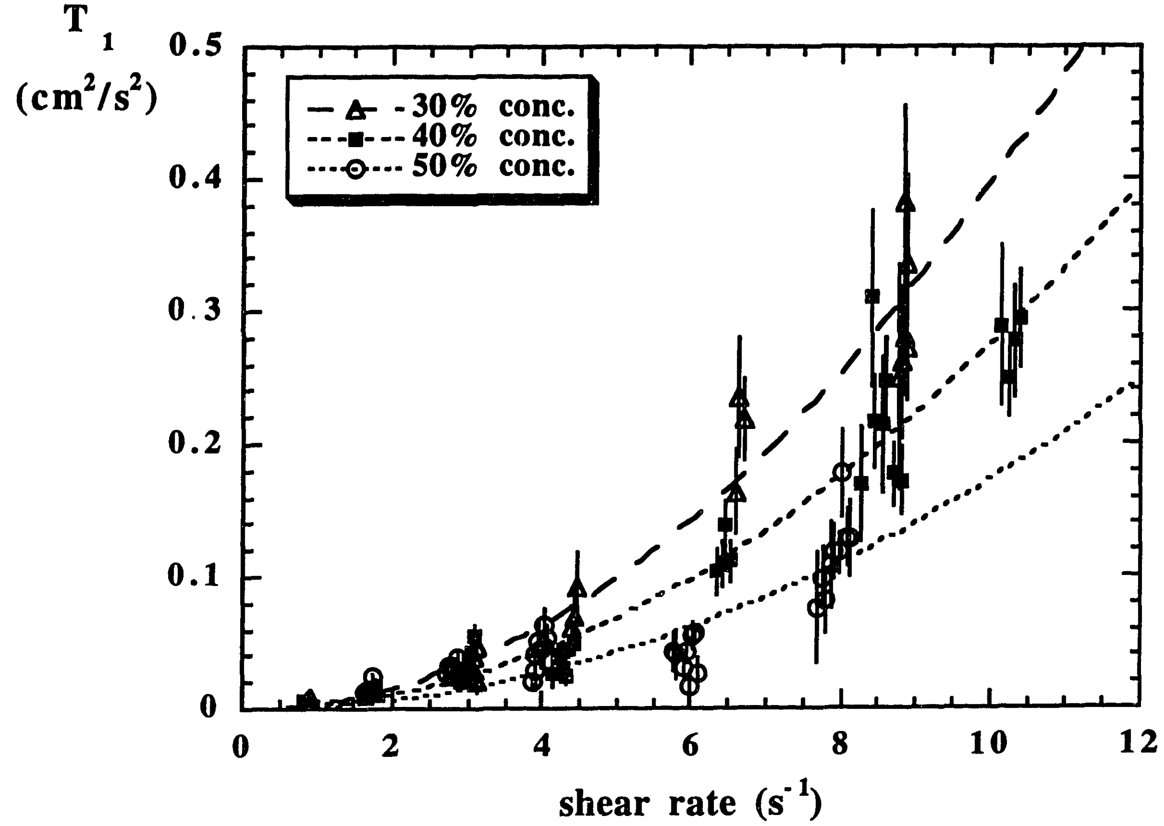

Figure 4.33 Tangential collisional velocity fluctuation for the 30%, 40% and 50% concentrated suspensions, plotted against local shear rate. The LDV beams passed through a suspension-filled 3 mm path length cuvette. These data were obtained at a small number of adjacent radial positions while the local shear rate was varied by changing the inner cylinder rotation speed.

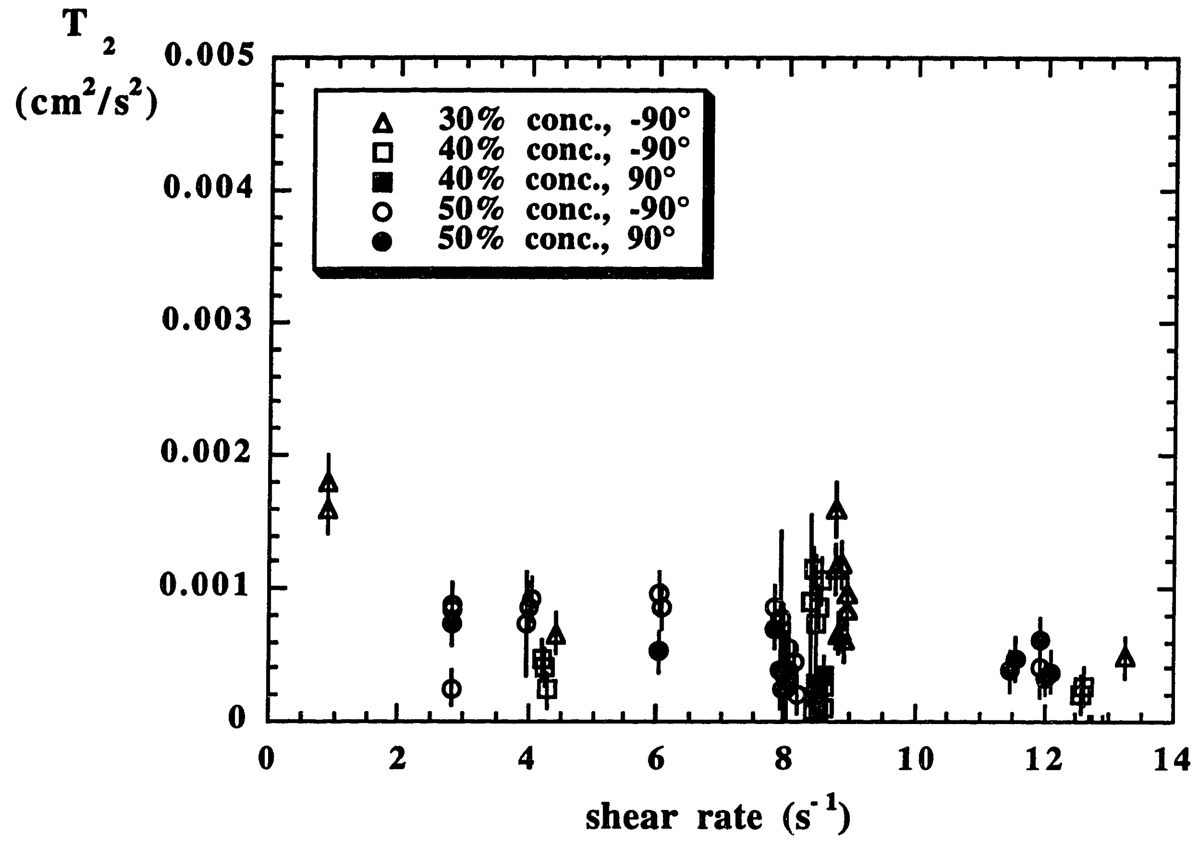

Figure 4.34 Radial collisional velocity fluctuation for the 30%, 40% and 50% concentrated suspensions, measured at the ± 90° locations, plotted against local shear rate. These data were obtained at a small number of adjacent radial positions while the local shear rate was varied by changing the inner cylinder rotation speed.

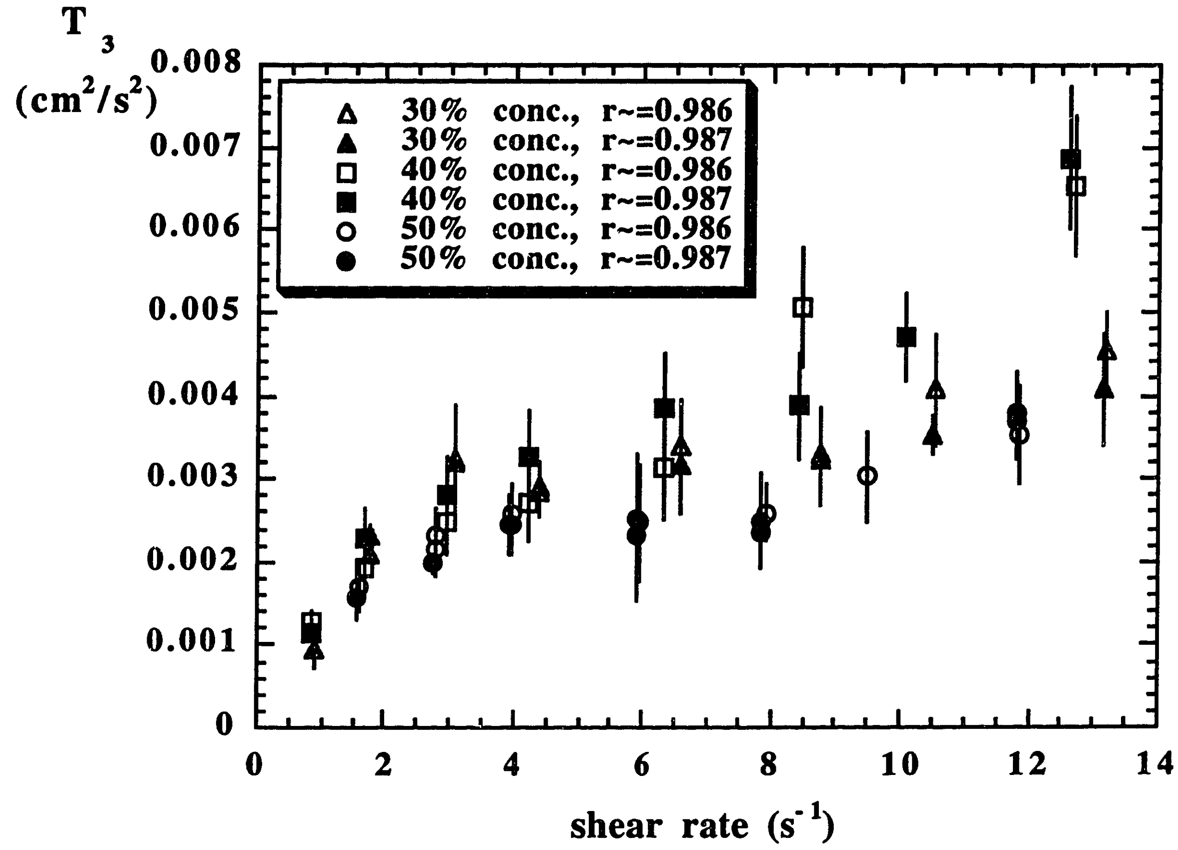

Figure 4.35 Vertical collisional velocity fluctuation for the 30%, 40% and 50% concentrated suspensions, measured at the ± 90° locations, plotted against local shear rate. These data were obtained at two adjacent radial positions (r/R_O = 0.986 and 0.987) while the local shear rate was varied by changing the inner cylinder rotation speed.

50% concentrated suspensions. It increases sharply at low shear rates, then plateaus and rises again slowly, in a shape similar to a quadratic. Averaging over the complex shape makes the curves appear to have a linear or square root dependence on the shear rate, depending on the bulk concentration value. Meanwhile, the radial component hardly changes with shear rate, and indeed slightly decreases at higher shear rates, at around the rates where the vertical component increases. The only concentration for which we were able to measure the radial component at a very low shear rate was the 30% concentrated suspension. This component does not appear to approach zero at zero shear rate, contrary to expectations. This could indicate that there is another source of noise mixing with the radial component that we did not account for, or that the radial component is small enough to be considered "zero" at all shear rates.

In summary, this chapter contains a discussion of the experimental results obtained from qualitative video image analysis and quantitative LDV measurements of the narrow gap Couette flow described in Chapter 3. The major observations we made based on video image analysis were that particle velocity fluctuations originating from inter-particle collisions are visible in a concentrated 50% particle volume fraction suspension but not in a dilute 2% particle volume fraction suspension, and that collision dynamics often closely involve the neutral direction. The principal observations we made based on the quantitative LDV data were that the collisional particle velocity fluctuations are anisotropic, for all concentrations studied, and that each velocity fluctuation component varies only slightly with radial position, over the region of accessible positions. Furthermore, each collisional particle velocity fluctuation component has a distinct scaling in particle volume fraction and shear rate. In the next chapter, a comparison of the predictions of several particle migration models is presented, and Chapter 6 contains a comparison of the predictions of the models with the data described here, and subsequent evaluation of the models.

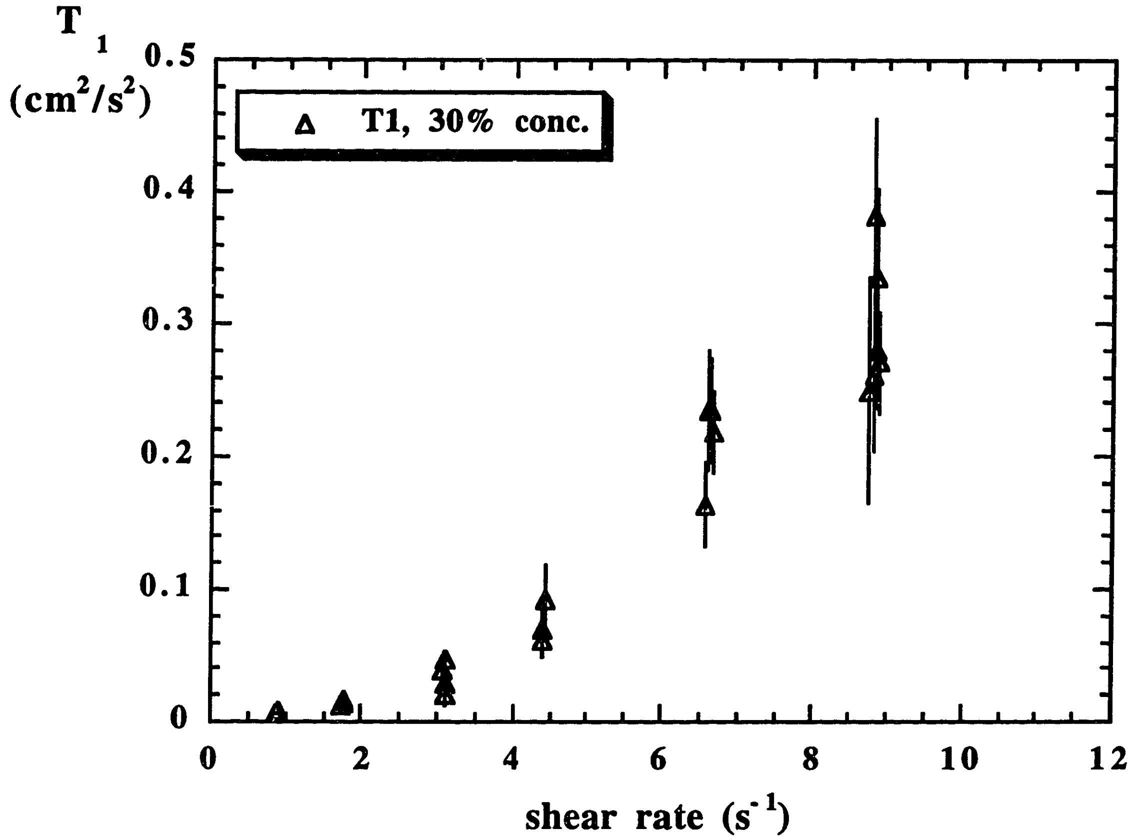

Figure 4.36 Tangential collisional velocity fluctuation for the 30% concentrated suspension, plotted against local shear rate. The LDV beams passed through a suspension-filled 3 mm path length cuvette. These data were obtained at a small number of adjacent radial positions while the local shear rate was varied by changing the inner cylinder rotation speed.

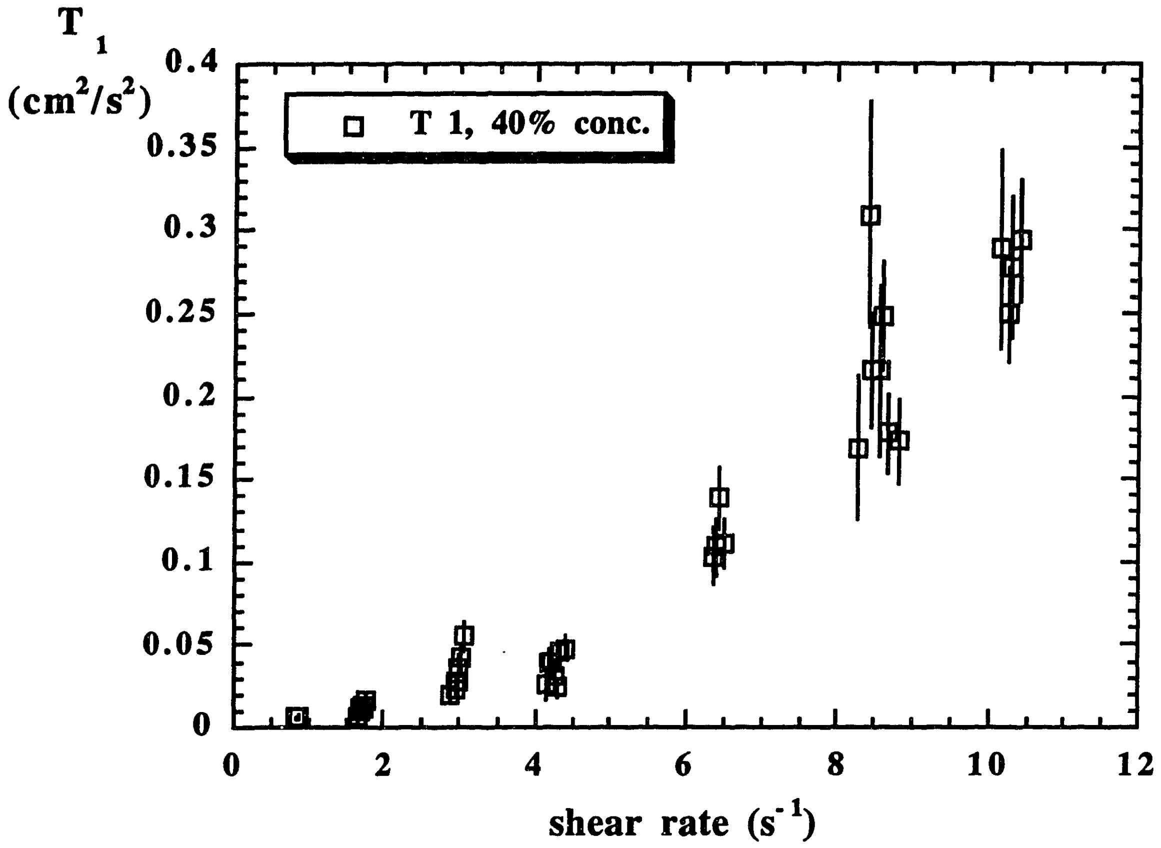

Figure 4.37 Tangential collisional velocity fluctuation for the 40% concentrated suspension, plotted against local shear rate. The LDV beams passed through a suspension-filled 3 mm path length cuvette. These data were obtained at a small number of adjacent radial positions while the local shear rate was varied by changing the inner cylinder rotation speed.

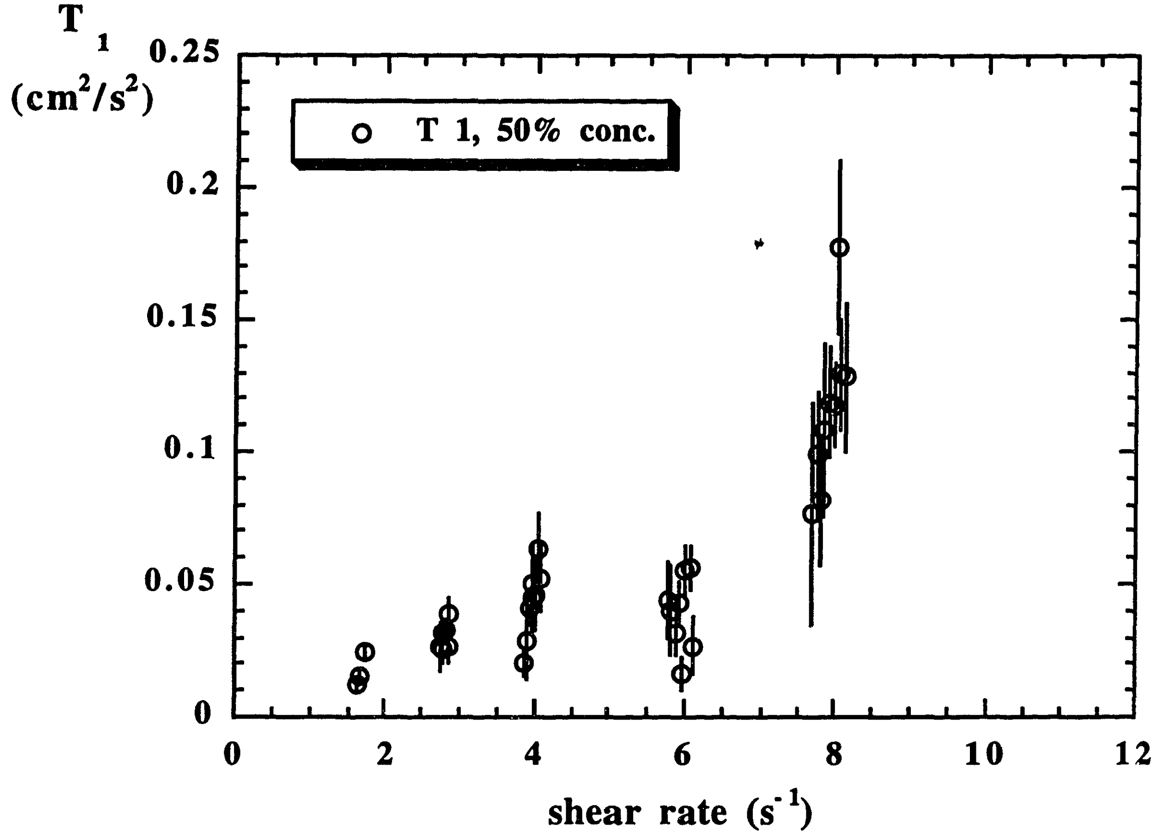

Figure 4.38 Tangential collisional velocity fluctuation for the 50% concentrated suspension, plotted against local shear rate. The LDV beams passed through a suspension-filled 3 mm path length cuvette. These data were obtained at a small number of adjacent radial positions while the local shear rate was varied by changing the inner cylinder rotation speed.

Chapter 5

Modeling

5.1 Catalog of Models: Similarities and Differences

The focus of this chapter is the application of existing suspension particle migration models to Couette flow between rotating concentric cylinders. Here, we consider the Jenkins and McTigue (1990), Nott and Brady (1994), Morris and Brady (1998), Phillips (1992), and Buyevich (1996) models. The first three models are all variations of the McTigue & Jenkins temperature model. The Phillips model is a phenomenological shear rate model, and the Buyevich model lies in between. In table 5.1, the correspondence of the models' nomenclature is presented.

The models are alike in that they all assume incompressibility, and a Newtonian stress tensor equation, with equations of state for the pressure and viscosity. The models differ from each other in that the equation of state for each stress tensor has a different dependence on particle concentration and suspension temperature. The models also have different auxiliary equations, either a diffusive flux balance, or a fluctuation kinetic energy balance.

We solve the equations of each model for steady shear flow in the Couette geometry (shear flow between rotating concentric cylinders) in order to compare model predictions with our experimental results. In this idealized flow, as in the experiment, the flow is directed in the tangential direction, the velocity gradient lies in the radial direction, and the neutral direction is the vertical direction. We solve the equations of mass and momentum conservation and an auxiliary equation (conservation of fluctuation kinetic energy or particle diffusion) for the spatial variation of several field variables: the particle volume fraction, the mean velocity, the scalar suspension temperature, and the pressure. We assume that at steady state these variables do not vary in the tangential direction, because the flow is axisymmetric, or in the vertical direction, because near the mid-plane of the Couette flow, the cylinders appear to be infinitely long. These assumptions are borne out by experimental data, as shown in section 4.2. Hence, the variables are considered only

Model	Phillips (1992)	Nott & Brady (1994)	Buyevich (1996)	Morris & Brady (1998)	Jenkins & McTigue (1990)	This Work
Mean velocity	$\underline{v}$	$<\underline{u}>$	$\underline{c}_f$ (fluid)	$<\underline{u}>$	$\underline{v}$	$\underline{u}$
Mean velocity, particle phase	-	$<\underline{u}>_p$	$\underline{c}_p$	$<\underline{u}>_p$	$\underline{v}$	$\underline{u}_p$
Fluctuating velocity of an individual particle	-	$\underline{u}'$	$\underline{w}'$	$\underline{u}'$	$\underline{C}$	$\underline{v}'$
total stress tensor (pressure tensor)	$[-p\,\delta + \tau]$	$<\Sigma>$, $<\Sigma>_p$	$[-p\,\delta + \tau]$ (fluid), Π (particles)	$<\Sigma>$, $<\Sigma>_p$	$\mathbf{t}$	Σ, Σ_p
particle pressure	-	Π	Π	Π	$\mathbf{p}$	Π
rate of strain tensor	$\boldsymbol{\gamma}$	$2<\mathbf{e}>$	$\mathbf{E}_p$	$2<\mathbf{e}>$	$2\mathbf{D}$	$\boldsymbol{\gamma}$
particle volume fraction	ϕ	ϕ	ϕ	ϕ	ν	ϕ
relative viscosity function	$\eta_r(\phi)$	$\eta_s(\phi)$	$M(\phi)$	$\eta_s(\phi)$	$\bar{\mu}(\nu)$	$\eta_s(\phi)$
particle pressure function	-	$p(\phi)$	$\phi\,(G(\phi)$ $+G_E(\phi)-1)$	$p(\phi)$	$\bar{p}(\nu)$	$p(\phi)$
function relating T to $a^2\gamma^2$ in homogeneous shear flow	ϕ^2 Note: defined in eq. (5.24)	$\frac{\eta_p(\phi)}{\alpha(\phi)}$	$\phi^2\,\chi^2(\phi)$	$\frac{\eta_p(\phi)}{\alpha(\phi)}$	$\frac{\bar{\mu}(\nu)}{\bar{\gamma}(\nu)}$	$\frac{\eta_p(\phi)}{\alpha(\phi)}$

Table 5.1 Correspondence of the models' nomenclature.

to vary in the radial direction, causing the problem to be classified as one-dimensional.

5.2 The Diffusive Flux Model: Phillips et al. (1992)

Phillips et al. (1992) solve the Couette problem for their model. We use an analytical solution given in their paper for steady state Couette flow between concentric cylinders with the value of a single coefficient fit from NMR measurements of steady state particle concentration profiles in wide gap Couette flow.

The suspension is treated as a single-phase continuum whose local viscosity depends on the local particle volume fraction. There are three field variables: the particle volume fraction ϕ, the mean suspension velocity $\underline{u}$, and the mean suspension pressure p.

5.2.1 General Form of the Equations

The equations of the diffusive flux model for a creeping flow are:

conservation of mass (incompressibility)

$$\underline{\nabla} \cdot \underline{u} = 0 \tag{5.1}$$

conservation of momentum

$$\underline{\nabla} \cdot \Sigma = \underline{0} \tag{5.2}$$

with the additional constitutive relation for the stress tensor,

$$\Sigma = -p\,\delta + \eta_f \eta_s(\phi)\,\gamma \tag{5.3}$$

where γ is the rate-of-strain tensor, given by

$$\gamma \equiv (\underline{\nabla u} + (\underline{\nabla u})^t) \tag{5.4}$$

ηf is the pure fluid viscosity, and $\eta_s(\phi)$ is the relative viscosity correlation, such as the Krieger function (Krieger, 1972), given as

$$\eta_s(\phi) = \left(1 - \frac{\phi}{\phi_m}\right)^{-1.82} \tag{5.5}$$

where ϕ_m is the maximum packing fraction, given as 0.68 by Phillips et al.,

and finally the auxiliary particle diffusion equation,

$$\frac{D\phi}{Dt} = a^2 K_c \underline{\nabla} \cdot \left(\phi^2 \underline{\nabla}\dot{\gamma} + \phi\dot{\gamma}\underline{\nabla}\phi\right) + a^2 K_\eta \underline{\nabla} \cdot \left(\dot{\gamma}\phi^2 \frac{1}{\eta}\frac{d\eta}{d\phi}\underline{\nabla}\phi\right) \tag{5.6}$$

where K_c and K_η are phenomenological constants that account for the flux of particles due to concentration and viscosity nonhomogeneities, respectively. These constants are found by fitting the model predictions to NMR data.

5.2.2 One-Dimensional, Steady Flow

For a one-dimensional, steady Couette flow, in cylindrical coordinates, the diffusive flux equations take the following form.

For overall mass conservation, we find

$$\frac{1}{r}\frac{d}{dr}(r\,u_r) = 0 \tag{5.7}$$

Integration yields

$$u_r = \frac{\text{constant}}{r} \tag{5.8}$$

At the outer cylinder wall, $u_r = 0$, because the mean suspension cannot flow into or out of the stationary wall. As a result, the constant is zero, and $u_r = 0$ everywhere in the flow.

Turning to the mean suspension momentum equation in the tangential direction we have

$$0 = \frac{1}{r^2}\frac{\partial}{\partial r}\{r^2\Sigma_{r\theta}\} + \frac{1}{r}\frac{\partial}{\partial\theta}\{\Sigma_{\theta\theta}\} + \frac{\partial}{\partial z}\{\Sigma_{\theta z}\} + \frac{\Sigma_{r\theta} - \Sigma_{\theta r}}{r} \tag{5.9}$$

Replacing the stress components by means of the constitutive equation (5.3) yields,

$$0 = \frac{1}{r^2}\frac{\partial}{\partial r}\left\{r^2\left[\eta_f\eta_s(\phi)\left(\frac{\partial u_\theta}{\partial r} + \frac{1}{r}\frac{\partial u_r}{\partial\theta} - \frac{u_\theta}{r}\right)\right]\right\} + \frac{1}{r}\frac{\partial}{\partial\theta}\left\{-p + \eta_f\eta_s(\phi)\left(\frac{1}{r}\frac{\partial u_\theta}{\partial\theta} + \frac{u_r}{r}\right)\right\}$$
$$+ \frac{\partial}{\partial z}\left\{\eta_f\eta_s(\phi)\left(\frac{1}{r}\frac{\partial u_z}{\partial\theta} + \frac{\partial u_\theta}{\partial z}\right)\right\} + \frac{\Sigma_{r\theta} - \Sigma_{\theta r}}{r}$$

(5.10)

Eliminating terms which contain derivatives with respect to θ or z or factors of u_r, or are antisymmetric in the stress, we reduce the equation to

$$0 = \frac{1}{r^2}\frac{\partial}{\partial r}\left\{r^2\left[\eta_f\eta_s(\phi)\left(\frac{\partial u_\theta}{\partial r} - \frac{u_\theta}{r}\right)\right]\right\} \tag{5.11}$$

Integration results in

$$\frac{\text{constant}}{r^2} = \eta_f\eta_s(\phi)\left(\frac{\partial u_\theta}{\partial r} - \frac{u_\theta}{r}\right) = \Sigma_{r\theta} = \eta_f\eta_s(\phi)\,r\frac{\partial}{\partial r}\left(\frac{u_\theta}{r}\right) \tag{5.12}$$

Given the boundary conditions $u_\theta(R_i) = R_i\,\Omega$ and $u_\theta(R_o) = 0$, the constant of integration can be evaluated to yield

$$\dot{\gamma} = \dot{\gamma}_{r\theta} = r\frac{\partial}{\partial r}\left(\frac{u_\theta}{r}\right) = \frac{-\Omega}{\left(\displaystyle\int_{R_i}^{R_o} \frac{1}{r^3\,\eta_f\,\eta_s(\phi)}\,d\,r\right)}\,\frac{1}{\eta_f\,\eta_s\,r^2} \tag{5.13}$$

Finally, integration yields the tangential velocity

$$\frac{u_\theta}{r} = \left[\frac{u_\theta}{r}\right]_{R_i} - \Omega\frac{\left(\displaystyle\int_{R_i}^{r}\frac{d\,r}{r^3\,\eta_f\,\eta_s(\phi)}\right)}{\left(\displaystyle\int_{R_i}^{R_o}\frac{d\,r}{r^3\,\eta_f\,\eta_s(\phi)}\right)} = \Omega\left\{1 - \frac{\left(\displaystyle\int_{R_i}^{r}\frac{d\,r}{r^3\,\eta_f\,\eta_s(\phi)}\right)}{\left(\displaystyle\int_{R_i}^{R_o}\frac{d\,r}{r^3\,\eta_f\,\eta_s(\phi)}\right)}\right\} \tag{5.14}$$

The pressure distribution is found from the mean suspension momentum equation in the radial direction,

$$0 = \frac{1}{r}\frac{\partial}{\partial r}\{r\,\Sigma_{rr}\} + \frac{1}{r}\frac{\partial}{\partial \theta}\{\Sigma_{\theta r}\} + \frac{\partial}{\partial z}\{\Sigma_{zr}\} - \frac{\Sigma_{\theta\theta}}{r} \tag{5.15}$$

Expanding the stress components yields,

$$\begin{aligned} 0 = {} & \frac{1}{r}\frac{\partial}{\partial r}\left\{r\left[-p + \eta_f\,\eta_s(\phi)\frac{\partial u_r}{\partial r}\right]\right\} + \frac{1}{r}\frac{\partial}{\partial \theta}\left\{\eta_f\,\eta_s(\phi)\left(\frac{\partial u_\theta}{\partial r} + \frac{1}{r}\frac{\partial u_r}{\partial \theta} - \frac{u_\theta}{r}\right)\right\} \\ & + \frac{\partial}{\partial z}\left\{\eta_f\,\eta_s(\phi)\left(\frac{\partial u_z}{\partial r} + \frac{\partial u_r}{\partial z}\right)\right\} - \frac{1}{r}\left[-p + \eta_f\,\eta_s(\phi)\left(\frac{1}{r}\frac{\partial u_\theta}{\partial \theta} + \frac{u_r}{r}\right)\right] \end{aligned} \tag{5.16}$$

Again, eliminating terms which contain derivatives with respect to θ or z or factors of u_r, we reduce the equation to

$$0 = \frac{1}{r}\frac{\partial}{\partial r}\{-r\,p\} + \frac{p}{r} \tag{5.17}$$

Expanding the derivative term leads to

$$\frac{dp}{dr} = 0 \tag{5.18}$$

Hence the pressure is independent of position, apart from a hydrostatic head, in this flow.

Next, we focus on the particle diffusion equation. For a one-dimensional shear flow, at steady state, the particle diffusion equation reduces to

$$\frac{\dot{\gamma}\,\phi}{\dot{\gamma}_w\,\phi_w} = \left(\frac{\eta_s(\phi_w)}{\eta_s(\phi)}\right)^{\frac{K_\eta}{K_c}} \tag{5.19}$$

Where ϕ_w and $\dot{\gamma}_w$ are the values of the concentration and shear rate at the flow boundary, or wall. Substituting in the shear rate expression above and the Krieger viscosity function yields

$$\frac{\phi}{\phi_w} = \frac{r}{R_i}\left(\frac{1-\phi_w/\phi_m}{1-\phi/\phi_m}\right)^{1.82(1-K_\eta/K_c)} \tag{5.20}$$

Note that at steady state only the ratio of flux coefficients K_η / K_c appears.

5.2.3 Analytical Solution

For the value $\frac{K_c}{K_\eta} = 0.66$, which provided the best fit to the experimental steady state particle concentration profiles presented in Phillips et al. (1992), an analytical solution is possible, where

$$\phi = \phi_m \frac{r^2}{\left(r^2 + \alpha R_i^2\right)} \tag{5.21}$$

and $\alpha \equiv \frac{\phi_m - \phi_w}{\phi_w}$. The integral of the concentration equation gives an expression for the average concentration

$$\bar{\phi} = \frac{2\,\phi_m}{R_o^2 - R_i^2}\left(\frac{R_o^2 - R_i^2}{2} - \frac{\alpha R_i^2}{2}\ln\frac{R_o^2 + \alpha R_i^2}{R_i^2(1+\alpha)}\right) \tag{5.22}$$

The concentration profile is solved by choosing a value for ϕ_w and evaluating the equation for $\bar{\phi}$. When the proper value of ϕ_w is found, it is substituted into the equation for $\phi(r)$. The velocity profile is found by substituting $\phi(r)$ into equation (5.14) above.

The Phillips diffusive flux model does not explicitly contain the suspension temperature T as an unknown. However, following the scaling argument used by Phillips et al. (1992) in deriving the particle diffusion equation, we can calculate T from the predicted concentration and shear rate profiles. We estimate that the fluctuating velocity v' is proportional to the mean free path between inter-particle collisions multiplied by the inter-particle collision frequency.

$$v' \sim (\text{mean free path})\,(\text{collision frequency}) \sim (a)\,(\phi\,\dot{\gamma}) \tag{5.23}$$

$$T \sim (v')^2 \sim \phi^2\, a^2\, \dot{\gamma}^2 \tag{5.24}$$

This result gives the dependence of temperature in the Phillips model on particle size, concentration, and shear rate.

5.3 Suspension Temperature Models: Solving the Equations of the Nott and Brady Model (1994)

The Nott and Brady model (1994) treats the suspension as a two-phase fluid. The model contains two mass conservation and two momentum conservation equations, one of each for the mean suspension continuum, and one of each for the particle phase only. These equations are obtained by ensemble averaging the mass and momentum conservation equations that apply at any material point, over all the suspension material or only over the particles. We solve for five field variables: the particle volume fraction ϕ, the mean suspension velocity $\underline{u}$, the mean particle phase velocity $\underline{u}_p$, the scalar suspension temperature T, and the fluid phase pressure p_f. In addition, the Nott and Brady model contains a different auxiliary equation from the Phillips model, replacing the particle diffusion equation with a conservation of fluctuation kinetic energy equation.

5.3.1 General Form of the Equations

In general, the five conservation equations are given as:

conservation of mass for the particle phase,

$$\frac{\partial \phi}{\partial t} + \underline{\nabla} \cdot (\phi\, \underline{u}_p) = 0 \tag{5.25}$$

conservation of momentum for the particle phase,

$$\rho_p\, \phi\, \frac{D_p \underline{u}_p}{D t} = \underline{b}_p + \underline{F}_p + \underline{\nabla} \cdot \Sigma_p \tag{5.26}$$

conservation of fluctuation kinetic energy,

$$c(\phi)\, \frac{D\, \langle 1/2\, (\rho\, \underline{u}^2)' \rangle}{D t} = \beta(\phi)\, \langle \underline{b}' \cdot\, \underline{u}' \rangle + \Sigma_p : \boldsymbol{\gamma} - \eta\, \alpha(\phi)\, a^{-2}\, T - \underline{\nabla} \cdot\, \underline{q} \tag{5.27}$$

conservation of mass for the mean suspension (incompressibility),

$$\underline{\nabla} \cdot\, \underline{u} = 0 \tag{5.28}$$

and conservation of momentum for the mean suspension,

$$\frac{D(\rho \underline{u})}{Dt} = \underline{b} + \underline{\nabla} \cdot \boldsymbol{\Sigma} \tag{5.29}$$

In the momentum equations, $\boldsymbol{\Sigma}$ and $\boldsymbol{\Sigma}_p$ are the stress tensors, averaged over the mean suspension and the particle phase, respectively, $\underline{b}$ represents an external force, such as gravity, and $\underline{F}_p$ is the internal force between the fluid and particle phases. In the fluctuation kinetic energy conservation equation, the right side reflects the competition among several factors, including the rate of working of a fluctuating external force, the rate of energy dissipation from the mean flow as a source of fluctuation energy, the rate of fluctuation energy dissipation into heat as a sink due to the friction between the particle and fluid phases, and the spatial conduction of fluctuation kinetic energy. In this equation, $\underline{q}$ is the fluctuation kinetic energy flux, $\alpha(\phi)$, $\beta(\phi)$ and $c(\phi)$ are unspecified functions of particle volume fraction, and the angle brackets signify an ensemble (or equivalent volume and time) average.

5.3.2 Steady Flow

Following the development given in Nott and Brady (1994), we simplify the equations for our problem. At steady state, all the explicit time derivatives are zero. In addition, our flow takes place at low Reynolds number, so we can neglect the inertia terms compared with viscous terms in the momentum equations. Also, there are no external forces $\underline{b}$ acting on the particles or fluid. Incorporating these restrictions leads to:

conservation of mass for the particle phase,

$$\underline{\nabla} \cdot (\phi\, \underline{u}_p) = 0 \tag{5.30}$$

conservation of momentum for the particle phase,

$$\underline{F}_p + \underline{\nabla} \cdot \boldsymbol{\Sigma}_p = \underline{0} \tag{5.31}$$

conservation of fluctuation kinetic energy,

$$\boldsymbol{\Sigma}_p : \boldsymbol{\gamma} - \eta\, \alpha(\phi)\, a^{-2}\, T - \underline{\nabla} \cdot \underline{q} = 0 \tag{5.32}$$

conservation of mass for the mean suspension (incompressibility),

$$\underline{\nabla} \cdot \underline{u} = 0 \tag{5.33}$$

and conservation of momentum for the mean suspension,

$$\underline{\nabla}\cdot\boldsymbol{\Sigma} = \underline{0} \tag{5.34}$$

We note that the last two equations are identical to the conservation equations in the Phillips model, so we calculate the same mean suspension velocity and stress profiles as for the Phillips model, subject to the variation in the particle concentration profile.

Now, we write out the constitutive relations Nott and Brady define for the internal force, fluctuation kinetic energy flux, particle stress tensor, and mean suspension stress tensor. The internal force is written as

$$\underline{F}_p = -6\,\pi\,\eta_f\, n\, f(\phi)^{-1}\,(\underline{u}_p - \underline{u}) \tag{5.35}$$

where n is the local number density of particles and f(ϕ) is the hindered settling function. The expression for the fluctuation kinetic energy flux is

$$\underline{q} = -\eta_f\,\kappa(\phi)\,\underline{\nabla}\,T \tag{5.36}$$

The particle phase contribution to the stress tensor is written as

$$\boldsymbol{\Sigma}_p = -\pi\,\boldsymbol{\delta} + \eta_f\,\eta_p(\phi)\,\boldsymbol{\gamma} + \eta_f\,\boldsymbol{\chi} \tag{5.37}$$

where π is the particle contribution to the pressure, which is given by

$$\pi = \pi_0 + \eta_f\, a^{-1}\, p(\phi)\, T^{1/2} \tag{5.38}$$

and $\boldsymbol{\gamma}$ is the rate-of-strain tensor, defined as

$$\boldsymbol{\gamma} \equiv (\underline{\nabla u} + (\underline{\nabla u})^{t}) \tag{5.39}$$

The expression for the mean suspension stress tensor is

$$\boldsymbol{\Sigma} = -p\,\boldsymbol{\delta} + \eta_f\,\eta_s(\phi)\,\boldsymbol{\gamma} + \eta_f\,\boldsymbol{\chi} \tag{5.40}$$

where p is the total pressure in the suspension and is given by

$$p = p_f + \pi \tag{5.41}$$

and χ is the normal stress difference tensor. Since Nott and Brady do not define its constitutive relation explicitly, we omit it from the following analysis.

In addition, $\eta_s(\phi)$ is the relative viscosity correlation, such as the Krieger function, given above for the Phillips model. In terms of η_s, the effective particle contribution to the viscosity is defined as

$$\eta_p(\phi) \equiv \eta_s(\phi) - 1 \tag{5.42}$$

In the set of constitutive equations, $\kappa(\phi)$, $p(\phi)$, $\alpha(\phi)$ are all functions of ϕ that must be defined.

Substituting these relations into the conservation equations yields the following set of equations:

conservation of mass for the particle phase,

$$\underline{\nabla} \cdot (\phi\, \underline{u}_p) = 0 \tag{5.43}$$

conservation of momentum for the particle phase,

$$\underline{0} = \frac{9}{2}\eta_f\, a^{-2} f(\phi)^{-1} (\underline{u}_p - \underline{u}) + \underline{\nabla} \cdot [-\pi\, \boldsymbol{\delta} + \eta_f\, \eta_p(\phi)\, \boldsymbol{\gamma}] \tag{5.44}$$

conservation of fluctuation kinetic energy,

$$0 = [-\pi\, \boldsymbol{\delta} + \eta_f\, \eta_p(\phi)\, \boldsymbol{\gamma}] : \boldsymbol{\gamma} - \eta_f\, \alpha(\phi)\, a^{-2}\, T + \eta_f\, \underline{\nabla} \cdot (\kappa(\phi)\, \underline{\nabla}\, T) \tag{5.45}$$

conservation of mass for the mean suspension (incompressibility),

$$\underline{\nabla} \cdot \underline{u} = 0 \tag{5.46}$$

and conservation of momentum for the mean suspension,

$$\underline{\nabla} \cdot [-(p_f + \pi)\, \boldsymbol{\delta} + \eta_f\, \eta_s(\phi)\, \boldsymbol{\gamma}] = \underline{0} \tag{5.47}$$

5.3.3 One-Dimensional, Steady Flow

Now, we express these equations in cylindrical coordinates and apply them to a one-dimensional steady state flow, in which the field variables ϕ, $\underline{u}$, $\underline{u}_p$, T, and p_f do not depend on coordinates θ and z and only depend on r. As discussed at the beginning of the chapter, in Couette flow between concentric cylinders, the relevant problem, there is no dependence on θ because the flow is axisymmetric. Also, there is no z dependence if the flow is tall enough so that end effects are negligible.

Starting with the mass conservation equations, for the particle phase, we find

$$\frac{1}{r}\frac{d}{dr}(r\, \phi\, u_{p_r}) = 0 \tag{5.48}$$

Integration of the equation results in

$$(\phi\, u_{p_r}) = \frac{\text{constant}}{r} \tag{5.49}$$

At the outer cylinder wall, $u_{pr} = 0$, because the particles cannot flow into or out of the stationary wall. As a result, the integration constant is zero, and $u_{pr} = 0$ everywhere in the flow.

For mass conservation of the mean suspension, we find

$$\frac{1}{r}\frac{d}{dr}(r\,u_r) = 0 \tag{5.50}$$

This equation and the corresponding boundary conditions are identical to equation (5.7), and we find $u_r = 0$ everywhere in the flow.

The mean suspension momentum equation in the tangential direction is written as

$$0 = \frac{1}{r^2}\frac{\partial}{\partial r}\{r^2\Sigma_{r\theta}\} + \frac{1}{r}\frac{\partial}{\partial \theta}\{\Sigma_{\theta\theta}\} + \frac{\partial}{\partial z}\{\Sigma_{\theta z}\} + \frac{\Sigma_{r\theta} - \Sigma_{\theta r}}{r} \tag{5.51}$$

This equation and the mean stress constitutive equation are identical to the equations (5.3 and 5.9) solved above in the Phillips paper for the shear rate. Following the same procedure, the solution is, given $u(R_i) = R_i\,\Omega$ and $u(R_o) = 0$,

$$\gamma = \gamma_{r\theta} = r\frac{d}{dr}\left(\frac{u_\theta}{r}\right) = \frac{-\Omega}{\left(\displaystyle\int_{R_i}^{R_o} \frac{1}{r^3\,\eta_f\,\eta_s(\phi)}\,dr\right)}\,\frac{1}{\eta_f\,\eta_s\,r^2} \tag{5.52}$$

and, integration yields,

$$\frac{u_\theta}{r} = \left[\frac{u_\theta}{r}\right]_{R_i} - \Omega\frac{\left(\displaystyle\int_{R_i}^{r}\frac{dr}{r^3\,\eta_f\,\eta_s(\phi)}\right)}{\left(\displaystyle\int_{R_i}^{R_o}\frac{dr}{r^3\,\eta_f\,\eta_s(\phi)}\right)} = \Omega\left\{1 - \frac{\left(\displaystyle\int_{R_i}^{r}\frac{dr}{r^3\,\eta_f\,\eta_s(\phi)}\right)}{\left(\displaystyle\int_{R_i}^{R_o}\frac{dr}{r^3\,\eta_f\,\eta_s(\phi)}\right)}\right\} \tag{5.53}$$

These are identical to equations (5.13) and (5.14), respectively.

For the mean suspension momentum equation in the radial direction, we obtain

$$0 = \frac{1}{r}\frac{\partial}{\partial r}\{r\,\Sigma_{rr}\} + \frac{1}{r}\frac{\partial}{\partial \theta}\{\Sigma_{\theta r}\} + \frac{\partial}{\partial z}\{\Sigma_{zr}\} - \frac{\Sigma_{\theta\theta}}{r} \tag{5.54}$$

This equation and the mean stress constitutive equation are identical to the equations (5.3 and 5.15) solved for the Phillips model for the total mean suspension pressure. Following the same procedure, the solution is

$$\frac{dp}{dr} = 0 \tag{5.55}$$

Hence the pressure is independent of position, apart from a hydrostatic head, in this flow.

The particle phase momentum equations are very similar to the mean suspension momentum equations. In the tangential direction, we find,

$$0 = \frac{9}{2}\eta_f a^{-2} f(\phi)^{-1}\left(u_{p\theta} - u_\theta\right) + \frac{1}{r^2}\frac{\partial}{\partial r}\left\{ r^2 \Sigma_{r\theta p} \right\} + \frac{1}{r}\frac{\partial}{\partial \theta}\left\{\Sigma_{\theta\theta p}\right\} + \frac{\partial}{\partial z}\left\{\Sigma_{\theta z p}\right\} + \frac{\Sigma_{r\theta p} - \Sigma_{\theta r p}}{r} \tag{5.56}$$

Expanding the stress components yields,

$$\begin{aligned} 0 = {} & \frac{9}{2}\eta_f a^{-2} f(\phi)^{-1}\left(u_{p\theta} - u_\theta\right) + \frac{1}{r^2}\frac{\partial}{\partial r}\left\{ r^2\left[\eta_f \eta_p(\phi)\left(\frac{\partial u_\theta}{\partial r} + \frac{1}{r}\frac{\partial u_r}{\partial \theta} - \frac{u_\theta}{r}\right)\right]\right\} \\ & + \frac{1}{r}\frac{\partial}{\partial \theta}\left\{-p + \eta_f \eta_p(\phi)\left(\frac{1}{r}\frac{\partial u_\theta}{\partial \theta} + \frac{u_r}{r}\right)\right\} + \frac{\partial}{\partial z}\left\{\eta_f \eta_p(\phi)\left(\frac{1}{r}\frac{\partial u_z}{\partial \theta} + \frac{\partial u_\theta}{\partial z}\right)\right\} + \frac{\Sigma_{r\theta} - \Sigma_{\theta r}}{r} \end{aligned} \tag{5.57}$$

Again, eliminating terms with derivatives or velocity components that vanish results in,

$$0 = \frac{9}{2}\eta_f a^{-2} f(\phi)^{-1}\left(u_{p\theta} - u_\theta\right) + \frac{1}{r^2}\frac{\partial}{\partial r}\left\{ r^2\left[\eta_f \eta_p(\phi)\left(\frac{\partial u_\theta}{\partial r} - \frac{u_\theta}{r}\right)\right]\right\} \tag{5.58}$$

Substituting for the shear rate $\left(\frac{\partial u_\theta}{\partial r} - \frac{u_\theta}{r}\right)$ from the mean suspension tangential momentum equation (5.52), we find

$$0 = \frac{9}{2}\eta_f a^{-2} f(\phi)^{-1}\left(u_{p\theta} - u_\theta\right) + \frac{-\Omega}{\left(\displaystyle\int_{R_i}^{R_o} \frac{1}{r^3 \eta_f \eta_s(\phi)}\, dr\right)} \frac{1}{r^2}\frac{d}{dr}\left(\frac{\eta_p(\phi)}{\eta_s(\phi)}\right) \tag{5.59}$$

This equation determines $u_{p\theta}$ once the other unknowns are solved. Since $u_{p\theta}$ is uncoupled from the rest of the problem, we can return to this equation at the end. By comparing this equation to equations (5.51-5.53) above, it is apparent that for both the mean suspension and the particle phase, the tangential momentum conservation equation sets the velocity profile.

For the particle phase momentum equation in the radial direction, we find,

$$0 = \frac{9}{2}\eta_f a^{-2} f(\phi)^{-1}\left(u_{pr} - u_r\right) + \frac{1}{r}\frac{\partial}{\partial r}\left\{ r\, \Sigma_{rrp} \right\} + \frac{1}{r}\frac{\partial}{\partial \theta}\left\{\Sigma_{\theta r p}\right\} + \frac{\partial}{\partial z}\left\{\Sigma_{zrp}\right\} - \frac{\Sigma_{\theta\theta p}}{r} \tag{5.60}$$

From the mass conservation equations above (5.48 and 5.50), we found that both u_{pr} and u_r are zero. Therefore, the first term vanishes. Expanding the stress components yields,

$$0 = \frac{1}{r}\frac{\partial}{\partial r}\left\{r\left[-\pi+\eta_f\eta_p(\phi)\frac{\partial u_r}{\partial r}\right]\right\}+\frac{1}{r}\frac{\partial}{\partial \theta}\left\{\eta_f\eta_p(\phi)\left(\frac{\partial u_\theta}{\partial r}+\frac{1}{r}\frac{\partial u_r}{\partial \theta}-\frac{u_\theta}{r}\right)\right\}$$
$$+\frac{\partial}{\partial z}\left\{\eta_f\eta_p(\phi)\left(\frac{\partial u_z}{\partial r}+\frac{\partial u_r}{\partial z}\right)\right\}-\frac{1}{r}\left[-\pi+\eta_f\eta_p(\phi)\left(\frac{1}{r}\frac{\partial u_\theta}{\partial \theta}+\frac{u_r}{r}\right)\right] \tag{5.61}$$

Eliminating the terms with derivatives or velocity components that vanish, in the manner of the mean suspension radial momentum equation above (5.54), we find,

$$0 = \frac{1}{r}\frac{\partial}{\partial r}\{-r\pi\}+\frac{\pi}{r} \tag{5.62}$$

In analogy to equation 5.17, this leads to

$$\frac{d\pi}{dr} = 0 \tag{5.63}$$

Hence the particle contribution to the pressure is independent of position in this flow. This equation sets a relation between ϕ and T, through the constitutive equation for $\pi(\phi,T)$.

Also, comparing equations (5.55) and (5.63), and recalling the definition $p = p_f+\pi$, we find it follows that

$$pf = \text{constant} \tag{5.64}$$

In summary, for the mean suspension and for the individual particle and fluid phases, the radial momentum conservation equations set the pressure across the gap.

Turning to the fluctuation kinetic energy conservation equation,

$$0 = \left[-\pi\boldsymbol{\delta}+\eta_f\eta_p(\phi)\boldsymbol{\gamma}\right]:\boldsymbol{\gamma}-\eta_f\alpha(\phi)a^{-2}T+\eta_f\underline{\nabla}\cdot(\kappa(\phi)\underline{\nabla}T) \tag{5.65}$$

expanding the rate of strain tensor terms yields first

$$0 = -\pi\,\mathrm{tr}(\boldsymbol{\gamma})+\eta_f\eta_p(\phi)\boldsymbol{\gamma}:\boldsymbol{\gamma}-\eta_f\alpha(\phi)a^{-2}T+\eta_f\underline{\nabla}\cdot(\kappa(\phi)\underline{\nabla}T) \tag{5.66}$$

and further yields

$$0 = -\pi\left(\frac{\partial u_r}{\partial r}+\frac{1}{r}\frac{\partial u_\theta}{\partial \theta}+\frac{u_r}{r}+\frac{\partial u_z}{\partial z}\right)$$
$$+\eta_f\eta_p(\phi)\left\{\begin{array}{c}\left(\frac{\partial u_r}{\partial r}\right)^2+\left(\frac{1}{r}\frac{\partial u_\theta}{\partial \theta}+\frac{u_r}{r}\right)^2+\left(\frac{\partial u_z}{\partial z}\right)^2\\ +\left(\frac{\partial u_\theta}{\partial r}+\frac{1}{r}\frac{\partial u_r}{\partial \theta}-\frac{u_\theta}{r}\right)^2+\left(\frac{\partial u_z}{\partial r}+\frac{\partial u_r}{\partial z}\right)^2+\left(\frac{1}{r}\frac{\partial u_z}{\partial \theta}+\frac{\partial u_\theta}{\partial z}\right)^2\end{array}\right\}$$
$$-\eta_f\alpha(\phi)a^{-2}T+\eta_f\underline{\nabla}\cdot(\kappa(\phi)\underline{\nabla}T) \tag{5.67}$$

Eliminating the terms with derivatives or velocity components that vanish,

$$0 = \eta_f \eta_p(\phi)\left(\frac{\partial u_\theta}{\partial r} - \frac{u_\theta}{r}\right)^2 - \eta_f\, \alpha(\phi)\, a^{-2}\, T + \eta_f\, \underline{\nabla}\cdot\left(\kappa(\phi)\, \underline{\nabla}\, T\right) \tag{5.68}$$

Substituting into the first term from the mean suspension tangential momentum equation (5.52),

$$0 = \eta_f \eta_p(\phi)\left\{\left(\frac{-\Omega}{\displaystyle\int_{R_i}^{R_o} \frac{1}{r^3\, \eta_f\, \eta_s(\phi)}\, d\,r}\right)\frac{1}{\eta_f\, \eta_s(\phi)\, r^2}\right\}^2 - \eta_f\, \alpha(\phi)\, a^{-2}\, T + \eta_f\, \underline{\nabla}\cdot\left(\kappa(\phi)\, \underline{\nabla}\, T\right) \tag{5.69}$$

5.3.4 Combining the Equations

Now, we combine the constitutive equation for π (5.38) with the fluctuation kinetic energy conservation equation (5.69) to solve for ϕ and T. The constitutive equation is given by

$$\pi = \pi_0 + \eta_f\, a^{-1}\, p(\phi)\, T^{1/2} \tag{5.70}$$

Since π_0 is an arbitrary constant, we set it to zero.

Before combining the two equations, we rewrite them in nondimensional form. The characteristic scalings we use for this include

$$r = R_o\, \tilde{r} \tag{5.71}$$

$$u_\theta = \Omega\, R_o\, \tilde{u}_\theta \tag{5.72}$$

$$\gamma = \Omega\, \tilde{\gamma} \tag{5.73}$$

$$T = a^2 \tilde{\gamma}^2\, \tilde{T} = a^2\, \Omega^2\, \tilde{T} \tag{5.74}$$

$$\pi = \eta_f\, \Omega\ p_1\ p(\phi)\, \tilde{T}^{1/2} \tag{5.75}$$

, where p_1 is an unknown constant.

$$\nabla = \frac{1}{R_o}\, \tilde{\nabla} \tag{5.76}$$

where ~ is used to denote a dimensionless quantity. In addition,

$$\frac{R_i}{R_o} \equiv k \tag{5.77}$$

Nondimensionalizing the constitutive equation for π first results in

$$p(\phi)\, \tilde{T}^{1/2} = p_1, \tag{5.78}$$

which can be rearranged as

$$\tilde{T} = \frac{p_1^2}{[p(\phi)]^2} \tag{5.79}$$

Nondimensionalizing the fluctuation kinetic energy equation yields

$$0 = \eta_p(\phi) \frac{1}{\left(\int_k^1 \frac{1}{\tilde{r}^3 \eta_s(\phi)} d\tilde{r} \right)^2} \left(\frac{1}{\eta_s(\phi)\, \tilde{r}^2} \right)^2 - \alpha(\phi)\tilde{T} + \varepsilon^2 (1-k)^2\, \underline{\tilde{\nabla}} \cdot (\kappa(\phi)\, \underline{\tilde{\nabla}}\, \tilde{T}) \tag{5.80}$$

where $\varepsilon \equiv \frac{a}{H}$ is the ratio between the particle diameter and gap width. Since $\varepsilon \equiv \frac{1}{30}$ for our flow, $\varepsilon^2 = \frac{1}{900}$. Also, k = 0.906 for our flow geometry, resulting in $(1 - k)^2 = 0.009$. Consequently, the last term in the fluctuation energy equation is negligible compared to the other two O(1) terms in the bulk of the flow, where $(R_o - R_i)$ is the appropriate length scale for the spatial derivatives. Only in a boundary layer about 1 or 2 particle diameters away from either wall, where the gap width is rescaled, would the three terms be of comparable size. We are not concerned with this region because our LDV data this close to the outer cylinder wall are not reliable. In the bulk of the flow, which is where our better quality measurements are, the conduction term in the energy equation is insignificant.

Accordingly, the fluctuation energy equation reduces to

$$0 = \eta_p(\phi) \left[\frac{1}{\left(\int_k^1 \frac{1}{\tilde{r}^3 \eta_s(\phi)} d\tilde{r} \right)} \right]^2 \left(\frac{1}{\eta_s(\phi)\, \tilde{r}^2} \right)^2 - \alpha(\phi)\tilde{T} \tag{5.81}$$

Substituting for $\tilde{T}$ from the particle pressure constitutive equation results in

$$\alpha(\phi) \frac{p_1^2}{p^2(\phi)} = \eta_p(\phi) \left[\frac{1}{\left(\int_k^1 \frac{1}{\tilde{r}^3 \eta_s(\phi)} d\tilde{r} \right)} \right]^2 \left(\frac{1}{\eta_s^2(\phi)\, \tilde{r}^4} \right) \tag{5.82}$$

Rearranging the equation yields

$$\tilde{r}^4 = \frac{1}{p_l^2\left(\int_k^1 \frac{1}{\tilde{r}^3\eta_s(\phi)}\,d\tilde{r}\right)^2}\frac{\eta_p(\phi)}{\alpha(\phi)}\frac{p^2(\phi)}{\eta_s^2(\phi)} \tag{5.83}$$

Combining the two constants p_l and the definite integral into one unknown constant p_l' results in,

$$\tilde{r}^4 = \frac{1}{p_l'^2}\frac{\eta_p(\phi)}{\alpha(\phi)}\frac{p^2(\phi)}{\eta_s^2(\phi)} \tag{5.84}$$

where $p_l' = p_l\left(\int_k^1 \frac{1}{\tilde{r}^3\eta_s(\phi)}\,d\tilde{r}\right)$

We can solve this equation implicitly for $\phi(\tilde{r})$. We guess the value of ϕ at the inner cylinder wall and find the value of the unknown constant p_l (defined as the value of the constant particle pressure) that gives us $\tilde{r}(\phi_{guess}) = k$. We then calculate $\tilde{r}(\phi)$ for points across the Couette gap. We find the average concentration by integrating over these points. We check that this average concentration matches the desired value. If not, we iterate by changing ϕ_{guess} and repeating the process.

Once the concentration profile $\phi(\tilde{r})$ is established, and the corresponding value of p_l known, we solve for the suspension temperature

$$T = a^2\Omega^2\frac{p_l^2}{[p(\phi)]^2} \tag{5.85}$$

and mean suspension velocity profile

$$\frac{u_\theta}{r} = \Omega\left[1 - \frac{\left(\int_k^{\tilde{r}} \frac{d\tilde{r}}{\tilde{r}^3\eta_s(\phi)}\right)}{\left(\int_k^1 \frac{d\tilde{r}}{\tilde{r}^3\eta_s(\phi)}\right)}\right] \tag{5.86}$$

Returning to the equation for the particle phase average tangential velocity (5.59), written now in nondimensional form,

$$0 = \frac{9}{2}\varepsilon^{-2}(1-k)^{-2} f(\phi)^{-1}\left(\tilde{u}_{p\theta} - \tilde{u}_{\theta}\right) + \frac{-1}{\left(\int_k^1 \frac{1}{\tilde{r}^3 \eta_s(\phi)}\, d\tilde{r}\right)} \frac{1}{\tilde{r}^2}\frac{\partial}{\partial \tilde{r}}\left(\frac{\eta_p(\phi)}{\eta_s(\phi)}\right) \qquad (5.87)$$

we see that in order for the two terms to balance, $\left(\tilde{u}_{p\theta} - \tilde{u}_{\theta}\right)$ must scale with $\varepsilon^2 (1 - k)^2$, which is negligible for our flow. Accordingly, we consider u_θ to be the mean velocity for the mean suspension and the particle and fluid phases individually.

An important feature of this solution is that all the variables are linked to the particle concentration profile, which in the bulk of the flow is fully determined by the functions $\eta_s(\phi)$, $\eta_p(\phi)$, $p(\phi)$ and $\alpha(\phi)$. Of these functions, only $\eta_s(\phi)$ has been determined empirically. The others are arbitrarily chosen by Nott and Brady (1994). For inhomogeneous flow problems where conduction of fluctuation kinetic energy is a significant effect, $\kappa(\phi)$ is an additional unknown function of ϕ.

5.4 Suspension Temperature Models: The Morris and Brady Model

The Morris and Brady (1998) model is identical to the Nott and Brady (1994) model, but with different functions of particle volume fraction, $\eta_s(\phi)$, $\eta_p(\phi)$, $p(\phi)$ and $\alpha(\phi)$, as the coefficients in the equations. Although the solution to the steady Couette problem in the bulk of the flow is given by equations (5.84-5.87), the choices of these coefficient functions make a significant difference in the models' predictions of the shear rate and suspension temperature profiles, and the agreement of the profiles with experimental data. The Morris and Brady and Nott and Brady models also have different boundary conditions for the suspension temperature T at the inner and outer cylinder walls, but since we make an approximation that turns the differential equation involving the suspension temperature into an algebraic equation, these boundary conditions do not enter the problem.

5.5 Suspension Temperature Models: The Jenkins and McTigue Model

The McTigue and Jenkins (1990,1992) model is the original temperature model on which the others are based. It was the first model of this type of suspension to contain a fluctuation kinetic energy conservation equation, in addition to the same mass and momentum conservation equations found in the Nott and Brady model (1994). For the steady Couette flow problem, the solution of Jenkins and McTigue's model in the bulk of the flow is also given by equations (5.84-5.87). Here also, Jenkins and McTigue choose different functions of particle volume fraction, $\eta_s(\phi)$, $p(\phi)$ and $\alpha(\phi)$, as the coefficients in the equations. Another important difference between this model and the Nott and Brady (1994) model is that the Jenkins and McTigue model considers the suspension to consist of a single phase, the particle phase, as a result of the model's origins in the granular flow literature. The suspension is treated as a dense gas of solid spheres, where the interaction force between a pair of particles arises from the fluid squeezed between them. The three field variables of interest are the particle volume fraction ϕ, the mean suspension velocity $\underline{u}$, and the scalar suspension temperature T.

In the 1990 version of the model, the fluid viscosity is the only fluid property that explicitly enters the equations through these particle-particle interactions. This version of the model makes sense for boundary-driven shear flows like shearing between concentric cylinders, but does not explain how the particles are in motion at all for flows like pressure-driven channel flow, where the fluid provides the driving force. McTigue and Jenkins modified the model to include pressure-driven flow in the subsequent 1992 version, where the pressure in the suspension is now the sum of the original particle contribution (a function of ϕ and T) and the fluid phase pressure. One difficulty in the 1992 version is that, due to the new fluid pressure variable, there are more unknowns than equations, and so it can only be solved in simple geometries where the form of the fluid pressure gradient is known or can be assumed. For the problem considered here, a boundary-driven shear flow, we use the earlier 1990 version of the model, which is strictly a one-phase model and completely specified.

5.6 The Buyevich Model: Phenomenological Temperature Model

The Buyevich model is very similar to the temperature models described above, except that it has a different auxiliary equation. Like the Nott and Brady model (1994), the Buyevich model is a two phase model, but the Buyevich equations characterize the particle and fluid phases separately, instead of the particle phase and mean suspension. The equations contain five field variables: the particle volume fraction ϕ, the mean particle phase velocity $\underline{u}_p$, the mean fluid phase velocity $\underline{u}_f$, the scalar suspension temperature T, and the fluid phase pressure p_f. In the Buyevich model auxiliary equation, the suspension temperature is related to the shear rate and particle concentration by a constitutive equation instead of a conservation equation. For a non-colloidal suspension, Buyevich's constitutive equation has exactly the same form as the simplified fluctuation kinetic energy conservation equation we generated from the Nott and Brady model, namely

$$T \sim \text{function}(\phi)\ a^2\ \gamma^2 \tag{5.88}$$

A new and unique feature of Buyevich's model is that it allows the suspension temperature to be an anisotropic tensor and a quadratic function of the rate-of-strain tensor, instead of only the scalar shear rate. We discuss this new feature in more detail in section 6.2.5 and chapter 7. However, in the Couette flow problem we solve here, the anisotropy of the suspension temperature has a minimal impact on the coupled velocity and concentration profiles, and the profile of the sum of the temperature components, so for the most part the Buyevich model predicts similar behavior to the other temperature models.

Buyevich writes the suspension temperature tensor as the sum of two tensors that are quadratic in the rate of strain tensor,

$$\mathbf{T} = A\,(\boldsymbol{\gamma}:\boldsymbol{\gamma})\,\boldsymbol{\delta} + C\,[\boldsymbol{\gamma}\cdot\boldsymbol{\gamma}] \tag{5.89}$$

where A and C are dimensionless constants. For unidirectional shear flow, this results in a diagonal tensor where $T_{zz} \equiv \langle v'_z\, v'_z \rangle$ is smaller than the other two identical elements $T_{rr} \equiv \langle v'_r\, v'_r \rangle$ and $T_{\theta\theta} \equiv \langle v'_\theta\, v'_\theta \rangle$.

5.7 Summary

In the steady-state, one-dimensional Couette flow problem, where external forces are absent, all the models yield the same conclusions from the momentum equation. From the component of the momentum equation in the flow direction, they all predict the same velocity profile, given the same concentration profile. From the momentum equation component in the radial direction, they all predict the pressure is constant across the gap, even though they have different constitutive relations for the pressure. For each model, the velocity specified by the tangential momentum equation component could belong to either of the two phases or to the overall suspension. However, we showed earlier, in the process of solving the Nott and Brady model (equation 5.87), that the particle phase and mean suspension velocities only differ by a negligible amount, $O(\varepsilon^2)$, so that for this particular problem we are not concerned with velocity differences between the two phases. We consider the velocity profile which satisfies this equation to be the mean velocity of the whole suspension and of each of the individual phases. For this simple problem, the subtleties of how the models divide the flow into phases and how exactly the volume averages are taken are invisible. Consequently, what we are really testing when we compare the models in Couette flow is the coupling between the concentration and temperature profiles, through the constitutive relation for the particle contribution to the pressure and the auxiliary equation.

In addition, for a homogeneous shear flow, all the models' expressions for the suspension temperature reduce to the form

$$T \sim \text{function}(\phi)\ a^2\ \gamma^2 \tag{5.90}$$

where the function of concentration is different for each model. In figure 5.1 we display a plot comparing the variation of the suspension temperature with particle concentration in a homogeneous shear flow for each model. For the Jenkins and McTigue model, the temperature is nearly independent of concentration. The Nott and Brady and Morris and Brady models give a linear dependence of the temperature on concentration. The Phillips model scaling yields a quadratic dependence of the temperature on concentration. For the Buyevich model, the suspension temperature is a quadratic function of the concentration, multiplied by the Enskog factor for a dense system. Even this one difference, in the functional dependence on concentration, has a substantial impact on the model predictions for macroscopic properties such as the shear rate profile.

In chapter 6, we present plots of model predictions of shear rate, particle volume fraction, and suspension temperature profiles compared with each other and with experimental data at different bulk particle concentrations. Table 5.2 contains a list of the actual coefficients that are functions of particle concentration used in computing the predictions of each model.

When the models' shear rate profile predictions were compared to data, all the models' results were multiplied by the apparent wall slip correction factor of Jana et al. (1995). For each bulk concentration, all the shear rates across the gap were multiplied by a factor

$$\gamma_{\text{with slip}} = \gamma\left[1-\left(\frac{u_{s,i}}{\Omega R_i}+\frac{u_{s,o}}{\Omega R_o}\right)\right] \tag{5.91}$$

where the values of $\frac{u_{s,i}}{\Omega R_i}$ and $\frac{u_{s,o}}{\Omega R_i}$ for a 50% concentrated suspension were those reported in Jana et al. (1995) and normalized for each additional bulk concentration used here. The slip factor effectively reduces all the shear rates across the gap, in order to capture the reduced amount of shearing the bulk suspension experiences due to the enhanced shearing in thin, low viscosity layers by the boundaries.

We utilized this apparent wall slip correction factor for two reasons. First, we measured nonzero tangential velocities of approximately 0.2 to 0.3 cm/s at the outer cylinder wall by using LDV, for the 30%, 40%, and 50% concentrated suspensions, at an average shear rate of 10 s^{-1} (10 rpm). This observed slip velocity agrees closely with the value 0.22 cm/s Jana et al. (1995) obtain for the flow of a 50% concentrated suspension under similar conditions, in a nearly identical flow geometry. Since the slip correction factor was extracted from measurements of a flow extremely similar to ours, we believe it should yield an accurate correction to our flow.

In addition, when we initially compared the models' predicted shear rate profiles to the observed profiles, all the models' profiles were displaced upward from the observed profiles by an apparently fixed amount for each bulk particle concentration. The displacement increased with particle volume fraction. Once we multiplied the models' profiles by the factor in equation (5.91), all the models' shear rate profiles intersected with the observed profile approximately at the observed average shear rate. The apparent wall slip correction model of Jana et al. (1995) gave a reasonable explanation for the initial discrepancies. Due to this agreement between the apparent wall slip correction to the models and our observations, we conclude that apparent wall slip should be included in order to obtain a realistic representation of the experimental system.

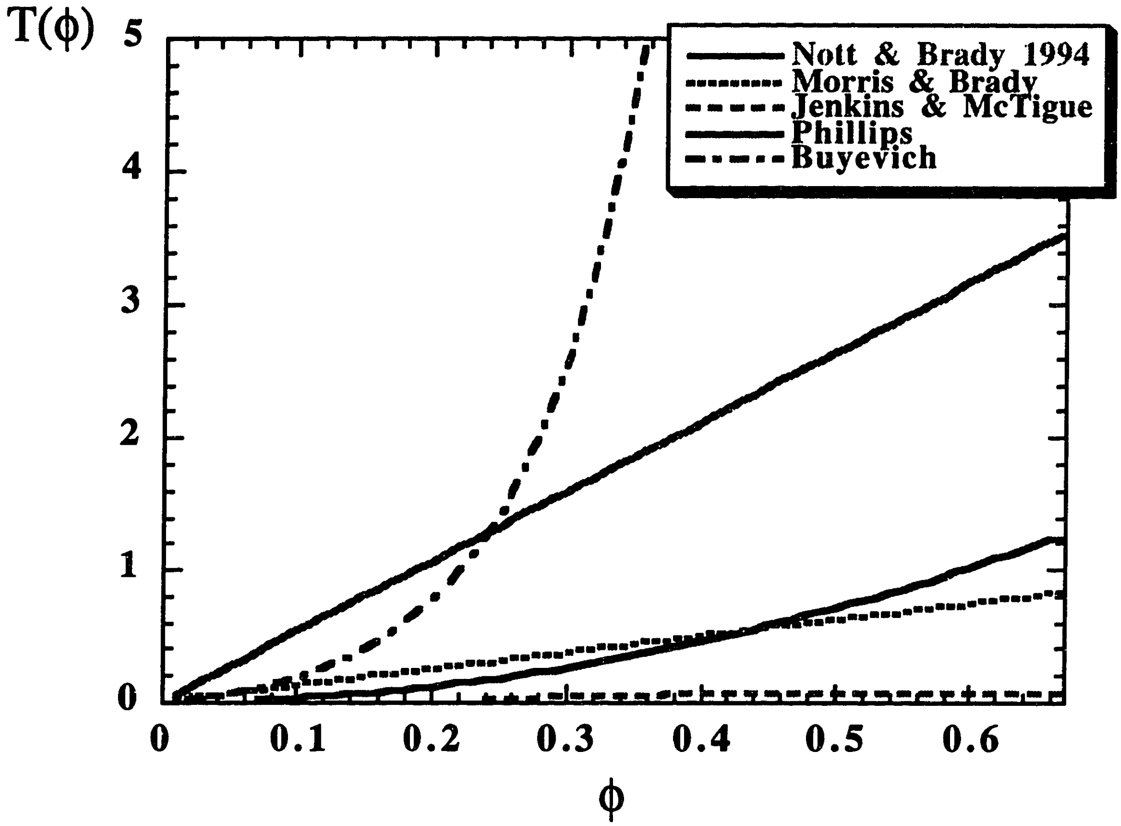

Figure 5.1 Comparison of the variation of the suspension temperature with particle concentration in a homogeneous shear flow for the suspension models considered in this thesis.

Model	Coefficients that are Functions of Particle Volume Fraction
Phillips et al. (1992)	$\eta_r(\phi) = \left(1 - \frac{\phi}{\phi_m}\right)^{-1.82} \quad ; \quad \phi_m = 0.68$ $\frac{K_c}{K_\eta} = 0.66$
Nott and Brady (1994)	$\eta_s(\phi) = \left(1 - \frac{\phi}{\phi_m}\right)^{-1.82} \quad ; \quad \eta_p(\phi) \equiv \eta_s(\phi) - 1$ $p(\phi) = \phi^{\frac{1}{2}}\,\eta_p(\phi) \quad ; \quad \alpha(\phi) = 0.19\,\frac{\eta_p(\phi)}{\phi} \quad ; \quad \phi_m = 0.68$
Morris and Brady (1998)	$\eta_s(\phi) = \left(1 - \frac{\phi}{\phi_m}\right)^{-1.82} \quad ; \quad \eta_p(\phi) \equiv \eta_s(\phi) - 1$ $p(\phi) = \eta_p(\phi) \quad ; \quad \alpha(\phi) = 0.815\,\frac{\eta_p(\phi)}{\phi} \quad ; \quad \phi_m = 0.68$
Jenkins and McTigue (1990)	$s(\nu) = \frac{(1-\nu)^3}{12\,\nu\,(2-\nu)} \quad ; \quad \alpha_1(\nu) = \frac{1}{4}\left(\frac{3}{2\,s(\nu)} + \frac{7}{10}\ln\left(\frac{1}{2\,s(\nu)}\right)\right)$ $\alpha_2(\nu) = \frac{1}{2}\ln\left(\frac{1}{2\,s(\nu)}\right) \quad ; \quad \bar{\mu}(\nu) = \frac{1}{5}\,6\,\nu\,\alpha_1(\nu) + \frac{1}{2}\,6\,\nu\,\alpha_2(\nu)$ $\bar{p}(\nu) = \frac{6}{\sqrt{\pi}}\,\nu\,(\alpha_1(\nu) + \alpha_2(\nu)) \quad ; \bar{\gamma}(\nu) = 3\,\nu\,6\,(\alpha_1(\nu) + 5\,\alpha_2(\nu))$
Buyevich (1996)	$M(\phi) = (1-\phi)^{-\frac{5}{2}} \quad ; \quad G(\phi) = \frac{(1+\phi+\phi^2-\phi^3)}{(1-\phi)^3}$ $G_E(\phi) = \left(1 - \left(\frac{\phi}{\phi_m}\right)^{\frac{1}{3}}\right)^{-1} \quad ; \quad \phi_m = 0.65$ $\chi(\phi) = \frac{G(\phi) - 1}{4\,\phi} + \frac{G_E(\phi) - 1}{4\,\phi}$

Table 5.2 Model coefficients that are functions of particle volume fraction. These are used in computing model predictions to compare with experimental data in Chapter 6.

Chapter 6

Discussion

The implications of the physical observations described in Chapter 4 on suspension models are discussed here. We compare directly model predictions of Couette flow between rotating concentric cylinders to LDV measurements of the real experimental system. First, we consider macroscopic properties, including the shear rate and particle volume fraction profiles, and then focus on the collisional particle velocity fluctuations, otherwise known as the suspension temperature. We compare the model predictions and the collisional fluctuation data in several ways, including the relative sizes of the collisional fluctuation components, the profiles of the fluctuation components across the Couette gap, the dependence of the fluctuation components on particle volume fraction, and the dependence of the fluctuation components on shear rate. As in Chapter 5, we have chosen the Phillips (1992), McTigue and Jenkins (1992), Nott and Brady (1994), Morris and Brady (1998), and Buyevich (1996) models for comparison with the data. The model predictions evaluated here are derived in sections 5.2-5.4.

6.1 Macroscopic properties

6.1.1 Comparison Between Observed Shear Rate Profiles and Model Predictions

The macroscopic property that provides the most direct comparison between experimental data and model predictions was the shear rate profile. Because the flow geometry is simple, the models predict the same shear rate profile, although subject to variation through the particle concentration profile. Meanwhile, we could extract the shear rate profile from the well-reproducible LDV mean tangential velocity data without introducing a large amount of error into the calculation, as described in section 3.5.1. The shear rate profile comparison is accordingly a meaningful test of each model's chosen functions of concentration, which couple together the concentration, shear rate, and suspension temperature profiles.

The shear rate profile comparisons are shown in figures 6.1-6.3, for three concentrated suspensions of 30%, 40% and 50% particle volume fraction, and an average shear rate of 10 s^{-1} (10 rpm). In each plot, the lines represent the model predictions and the points indicate the data calculated from the velocity profiles displayed in figures 4.18-4.20. The plot for the 30% concentrated suspension includes a second set of data, which is a local 5-point fit of an earlier measurement of the 30% concentrated suspension velocity profile. All the model predictions were multiplied by the apparent wall slip correction factor of Jana et al. (1995).

It is apparent in each of the three graphs that the Phillips, Nott & Brady, and Buyevich models capture qualitatively the approximate range and average slope of the shear rate profiles. However, none of the models captures the slightly curved shape of the three-region-fit shear rate profiles. This is especially noticeable for the 50% concentrated suspension, which has the largest slope and the most curvature in the shear rate profile. It is also noticeable that the model predictions diverge from each other increasingly with particle concentration, since the differences in their coefficients which are functions of concentration become significant there.

Since the Jenkins and McTigue model is the most rigorously derived model, we expect it to match the data at least as well as the other, more phenomenological models. Contrary to these expectations, the shear rate profiles predicted by Jenkins and McTigue match worst with the data. This mismatch can be attributed to one of the approximations that Jenkins and McTigue make. The authors relate the average inter-particle spacing to the local particle volume fraction by a function based on the Carnahan-Starling approximation of the pair radial distribution function. Although the Carnahan-Starling approximation has been traditionally applied to dense gas systems, it is not valid in the highly concentrated regime of interest here because it does not become singular in the limit of maximum packing (Buyevich, 1996). Consequently, the Jenkins and McTigue model significantly underpredicts the relative suspension viscosity compared to the experimentally observed Krieger (1972) function that all the other models use. If the inter-particle spacing in the Jenkins and McTigue model were adjusted so that the predicted relative viscosity matched the Krieger correlation, then it is likely that the predictions of the model would be quite similar to those of the other models.

6.1.2 Comparison Between Corresponding Concentration Profiles and Model Predictions

If we analyze the data one step further, as described in section 3.5.2, we can calculate the particle concentration profiles from the shear rate profiles in the figures. In figures 6.4-6.6, the model predictions and reduced data from the shear rate profiles in figures 6.1-6.3 are presented together, for the 30%, 40% and 50% concentrated suspensions. It has been well-documented experimentally, for a non colloidal suspension with a viscous Newtonian suspending liquid (Abbott at al., 1991; Hampton et al., 1997; Lyon and Leal, 1998), that the steady state concentration profile is not a function of the rate at which the flow is driven, such as the volume flow rate in pipe flow or the inner cylinder rotation speed in Couette flow. Even though we use the same data here as above, gathered from the 10 rpm experiment, the concentration profiles shown in the plots would be the same at any rotation speed once the flow reached steady state. In figure 6.4, the model predictions for the 30% concentrated suspension concentration profile match both sets of data well.

Although the three-region-fit profile is slightly curved, almost all the models capture the average slope. As the concentration increases to 40% and 50% in figures 6.5 and 6.6, the model predictions scatter and agree poorly with the data, especially in the case to the 50% concentrated suspension profile, which has the most curvature, like the shear rate profile. Among the models, as before, the Phillips, Nott & Brady, and Buyevich models best capture the approximate size and slope of the shear rate profiles. Overall, the trend we observe is that the models tend to capture the behavior of moderately concentrated suspensions like the 30% concentrated suspension better than that of highly concentrated suspensions like the 50% concentrated suspension.

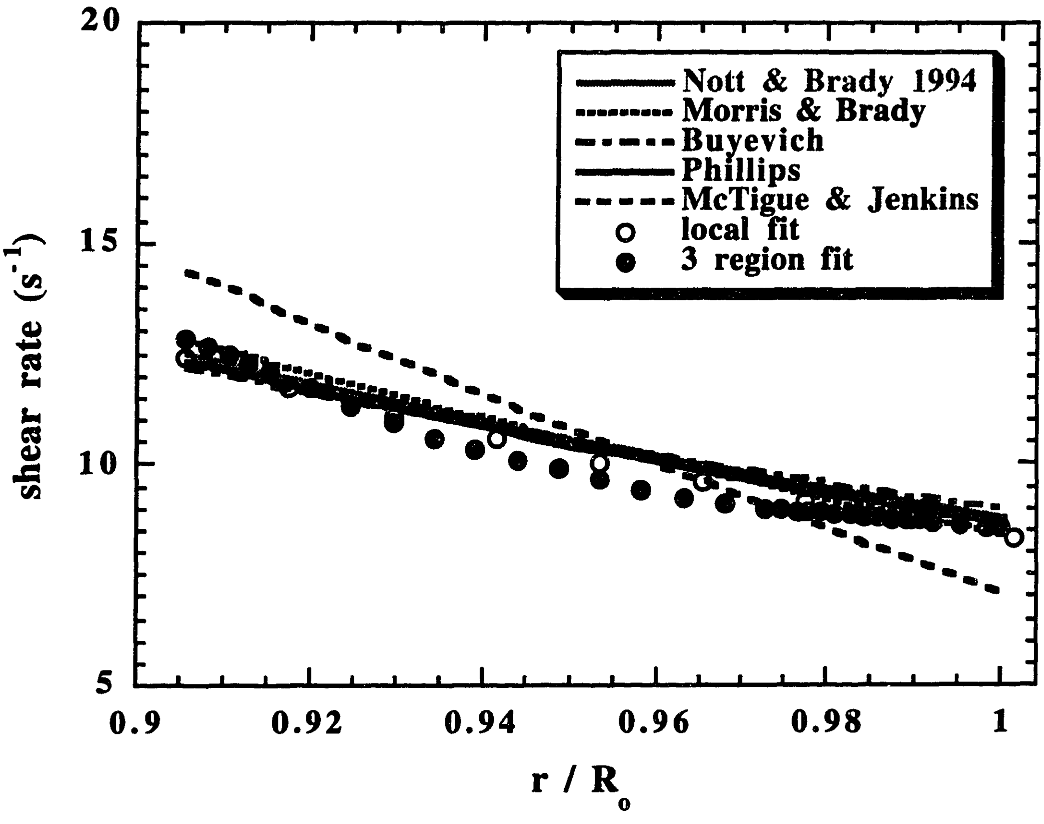

Figure 6.1 Comparison between model predictions and experimental measurements of the shear rate profile across the Couette gap, 30% particle concentration, average shear rate = 10s^{-1} (10 rpm). All the model predictions were multiplied by the wall slip correction factor of Jana et al. (1995). Note that the local fit and 3 region fit were calculated from two separate experiments.

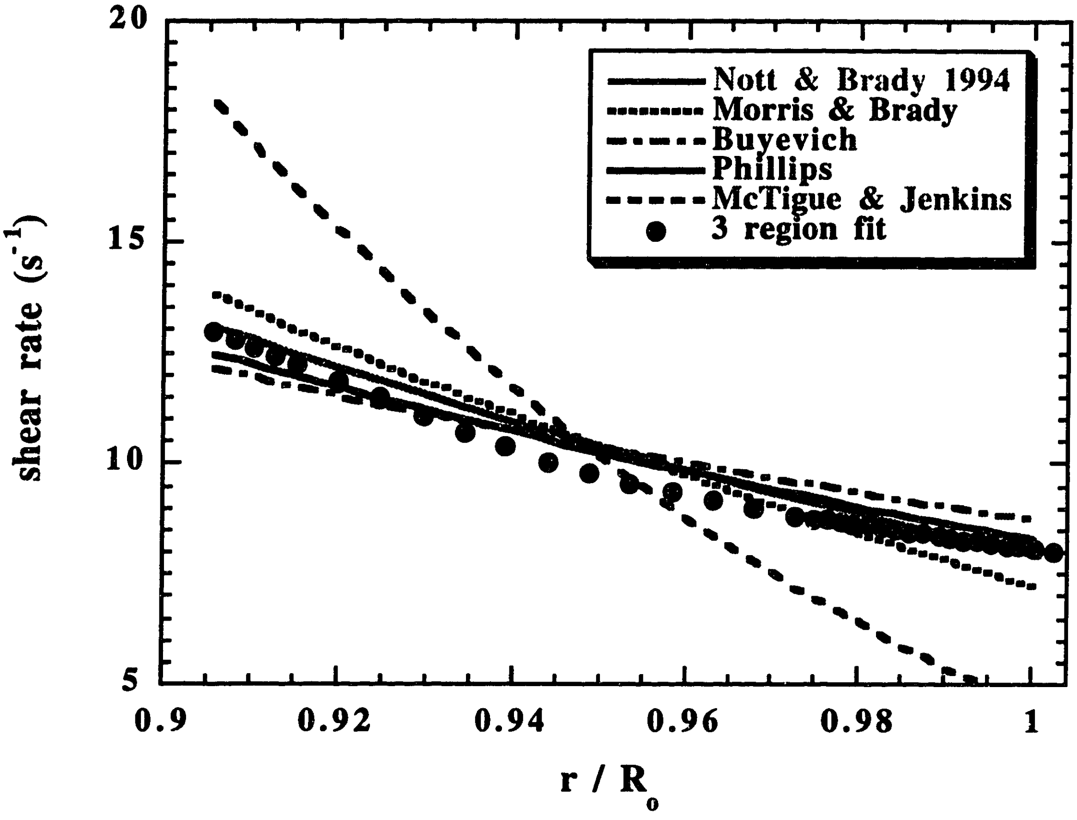

Figure 6.2 Comparison between model predictions and experimental measurements of the shear rate profile across the Couette gap, 40% particle concentration, average shear rate = $10s^{-1}$ (10 rpm). All the model predictions were multiplied by the wall slip correction factor of Jana et al. (1995).

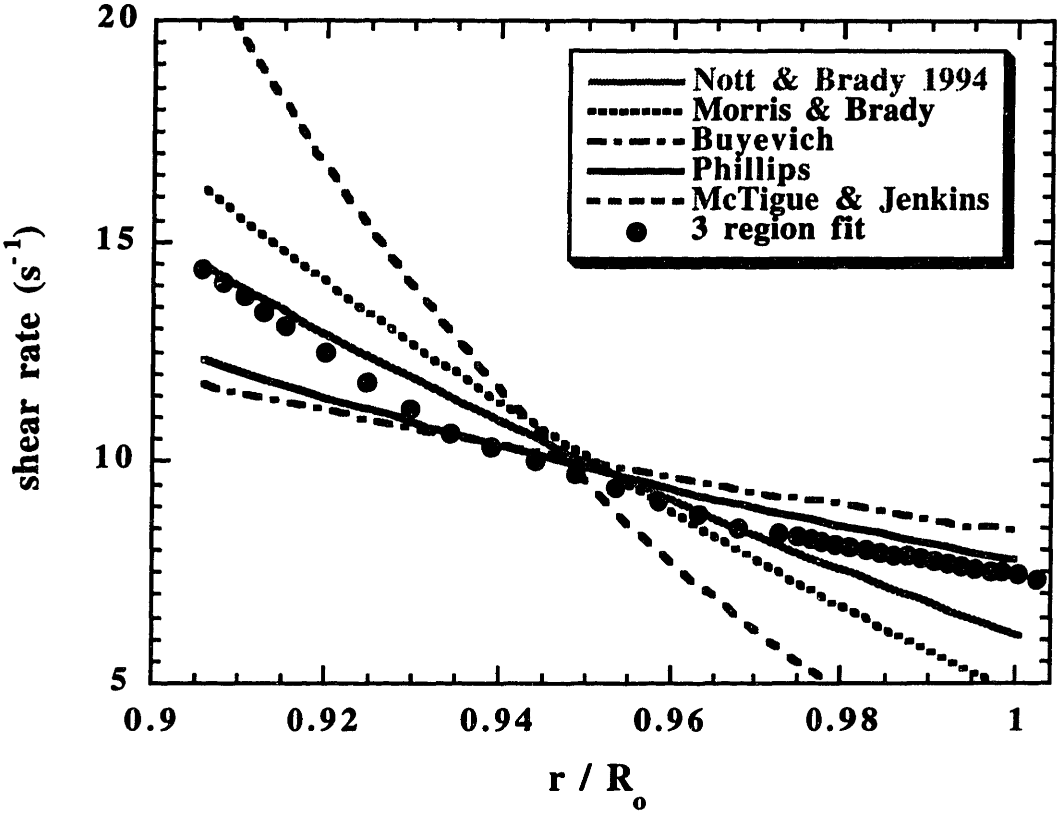

Figure 6.3 Comparison between model predictions and experimental measurements of the shear rate profile across the Couette gap, 50% particle concentration, average shear rate = $10s^{-1}$ (10 rpm). All the model predictions were multiplied by the wall slip correction factor of Jana et al. (1995).

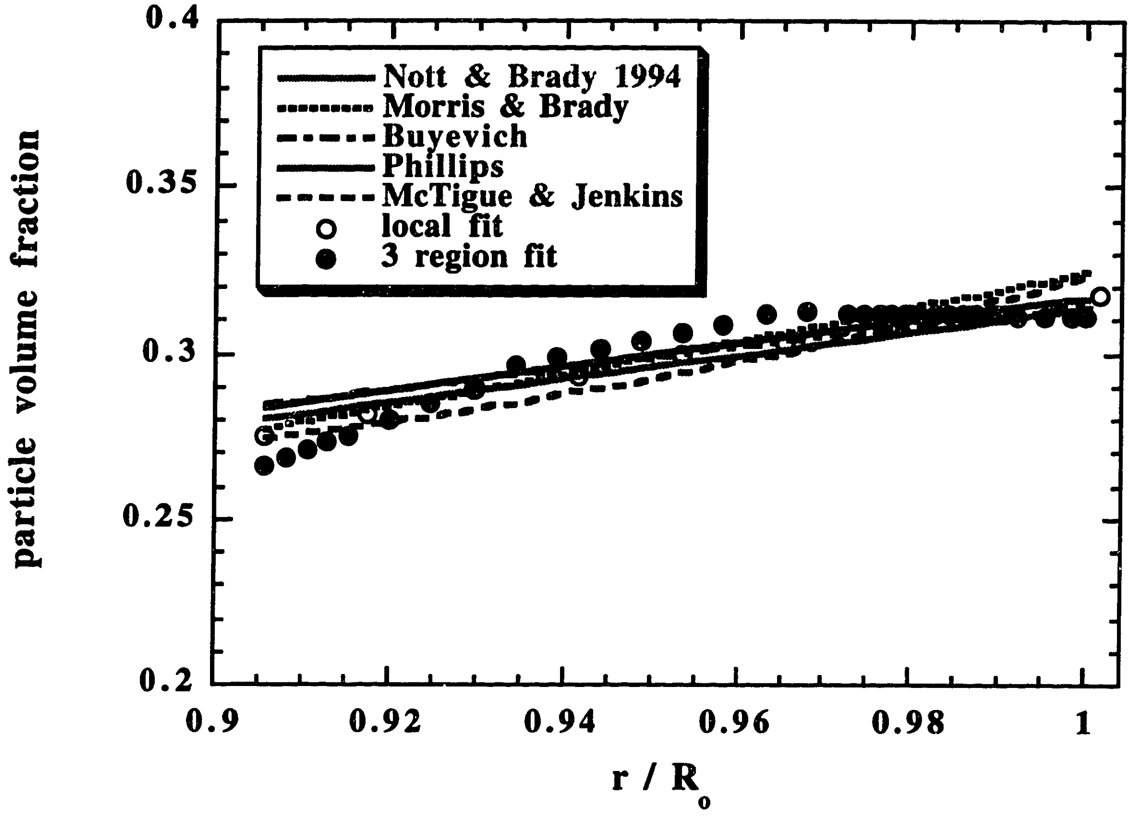

Figure 6.4 Comparison between model predictions and experimental measurements of the particle volume fraction profile across the Couette gap, 30% particle concentration, calculated from data with average shear rate = $10s^{-1}$ (10 rpm).

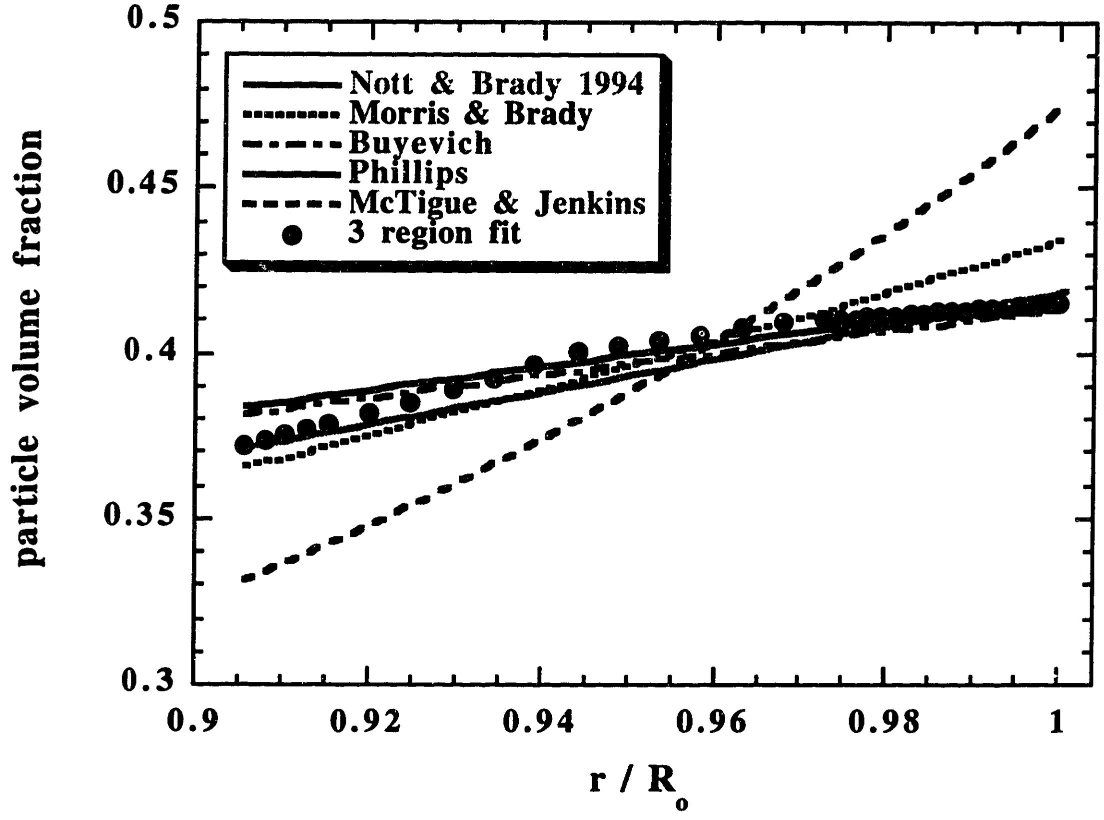

Figure 6.5 Comparison between model predictions and experimental measurements of the particle volume fraction profile across the Couette gap, 40% particle concentration, calculated from data with average shear rate = 10s^{-1} (10 rpm).

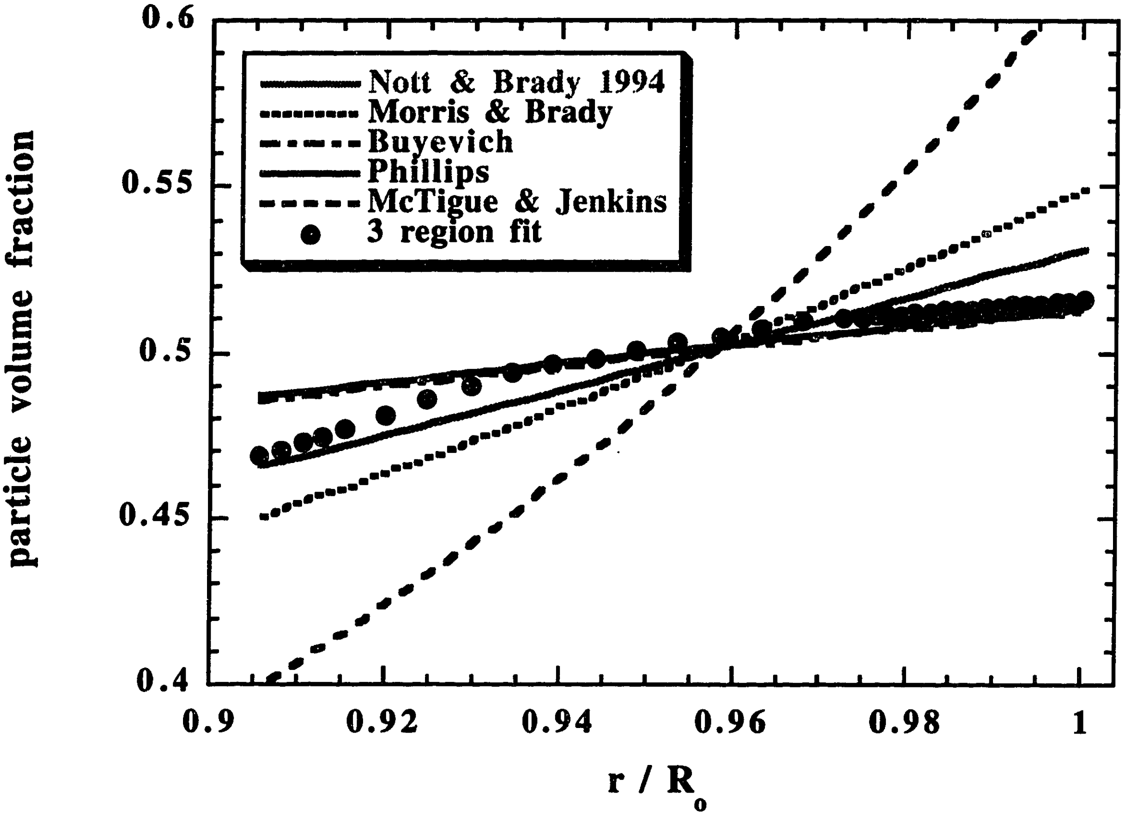

Figure 6.6 Comparison between model predictions and experimental measurements of the particle volume fraction profile across the Couette gap, 50% particle concentration, calculated from data with average shear rate = 10s^{-1} (10 rpm).

6.2 Comparison Between Observed Suspension Temperature and Model Predictions

This section contains an assessment of the models' assumptions and predictions of collisional particle velocity fluctuations, otherwise known as the suspension temperature. We extract the collisional velocity fluctuations from the LDV data by following the method outlined in section 3.5. We subtract the dilute 2% particle volume fraction baseline from the measured velocity variance to separate the collisional velocity fluctuations from other contributions, including particle rotation, LDV noise, and equipment vibration. As mentioned above, we compare several aspects of the models and data, beginning with the relative sizes of the collisional velocity fluctuation components.

6.2.1 Observed Suspension Temperature is Anisotropic

One of the original objectives in this research was to determine experimentally whether the suspension temperature is anisotropic, since the McTigue and Jenkins, Nott and Brady, and Morris and Brady models all assume that the suspension temperature is isotropic. It is demonstrated clearly in figures 4.24-4.26 that the suspension temperature components at an average shear rate of 10 s^{-1} (10 rpm) all have different magnitudes, for each of the 30%, 40% and 50% concentrated suspensions that we measured. The tangential (flow) component is overwhelmingly the largest at every concentration, followed by the vertical (neutral) and then the radial (gradient) components. The ratio between the average tangential and vertical components in these plots, which is easier to see in figures 4.30-4.32, is as large as 120 for the 30% concentrated suspension, and decreases to about 50 for the 40% and 50% concentrated suspensions. The ratio between the vertical and radial components lies in the range of 3 to 4, even for the 10% concentrated suspension, except near 40% concentration, where the ratio peaks at 8. These ratios are significant factors that show that the suspension temperature is extremely anisotropic; the degree of anisotropy is largest near 30% particle volume fraction.

At lower shear rates, the suspension temperature is less anisotropic, and the anisotropy varies little with concentration. However, even at an average shear rate of 2 s^{-1}, one of the lowest rotation speeds we measured, the ratio between the tangential and vertical components was still about 7, and the ratio between the vertical and radial components was about two, for all the concentrations. This set of data indicates that the models' concept of a scalar, isotropic suspension temperature does not exist in this real system.

If we compare either of the anisotropy ratios as a function of concentration with the data of Nicolai et al. (1995), who studied particle velocity fluctuations in settling suspensions, we find that their measured ratio of the vertical to horizontal fluctuations peaked at two at a particle concentration of about 10% and decreased at higher concentrations. We observe a different trend in the steady shear flow, where the anisotropy peaks around 30-40% concentration and is in general larger than two.

6.2.2 Comparison of Predicted and Measured Profiles of the Sum of the Suspension Temperature Components

The models only make predictions of the behavior of the scalar suspension temperature, defined as the sum of the suspension temperature components we measured. We derived the model predictions of how the scalar suspension temperature varies across the Couette gap in sections 5.2-5.4. Since we only were able to access the outer region of the gap with LDV, we cannot compare the entire measured and predicted profiles. However, we can test whether the models are in the right range of values at all for the positions that we were able to measure. It turns out that this is an important question, because the model predictions span a wide range.

Here, we compare model predictions of the scalar suspension temperature profile with comparable measured quantities, at an average shear rate of 10s^{-1} (10 rpm). Since the tangential component is much larger than the others (at least by a factor of 50) at this average shear rate, we use the tangential (flow) component to represent the sum of the three components. The correspondence of the models and data is shown in figures 6.7-6.9, for the 30%, 40%, and 50% concentrated suspensions, respectively. It is apparent in these figures that most of the models

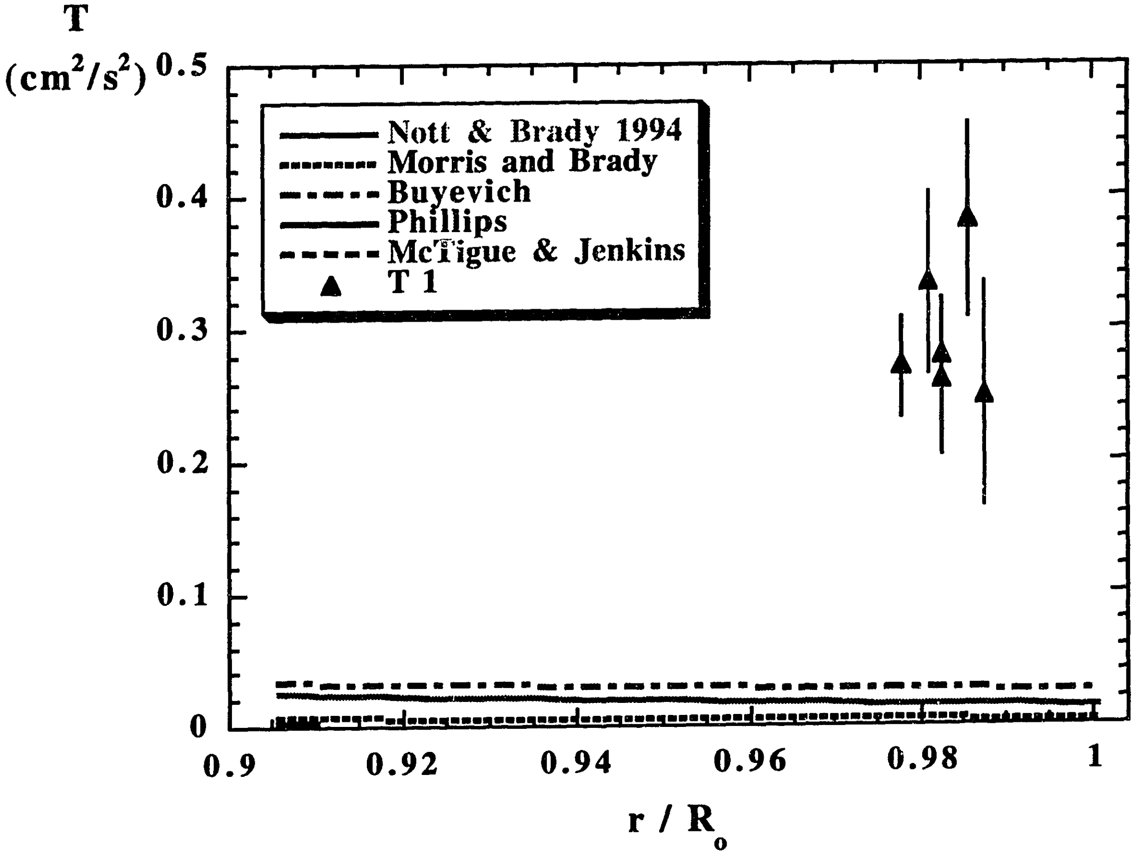

Figure 6.7 Comparison between model predictions of the scalar suspension temperature profile and experimental measurements of the tangential (flow, or 1 direction) suspension temperature component profile across the Couette gap, 30% particle concentration, average shear rate = $10s^{-1}$ (10 rpm).

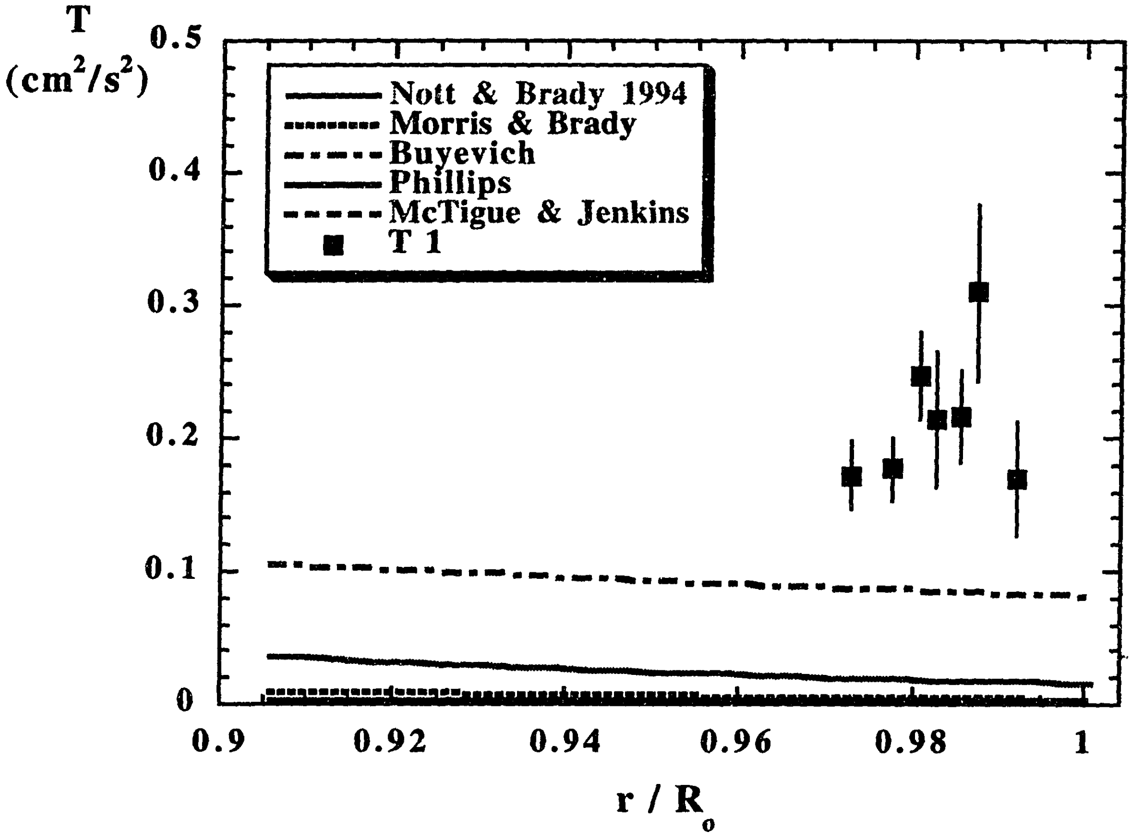

Figure 6.8 Comparison between model predictions of the scalar suspension temperature profile and experimental measurements of the tangential (flow, or 1 direction) suspension temperature component profile across the Couette gap, 40% particle concentration, average shear rate = 10s^{-1} (10 rpm).

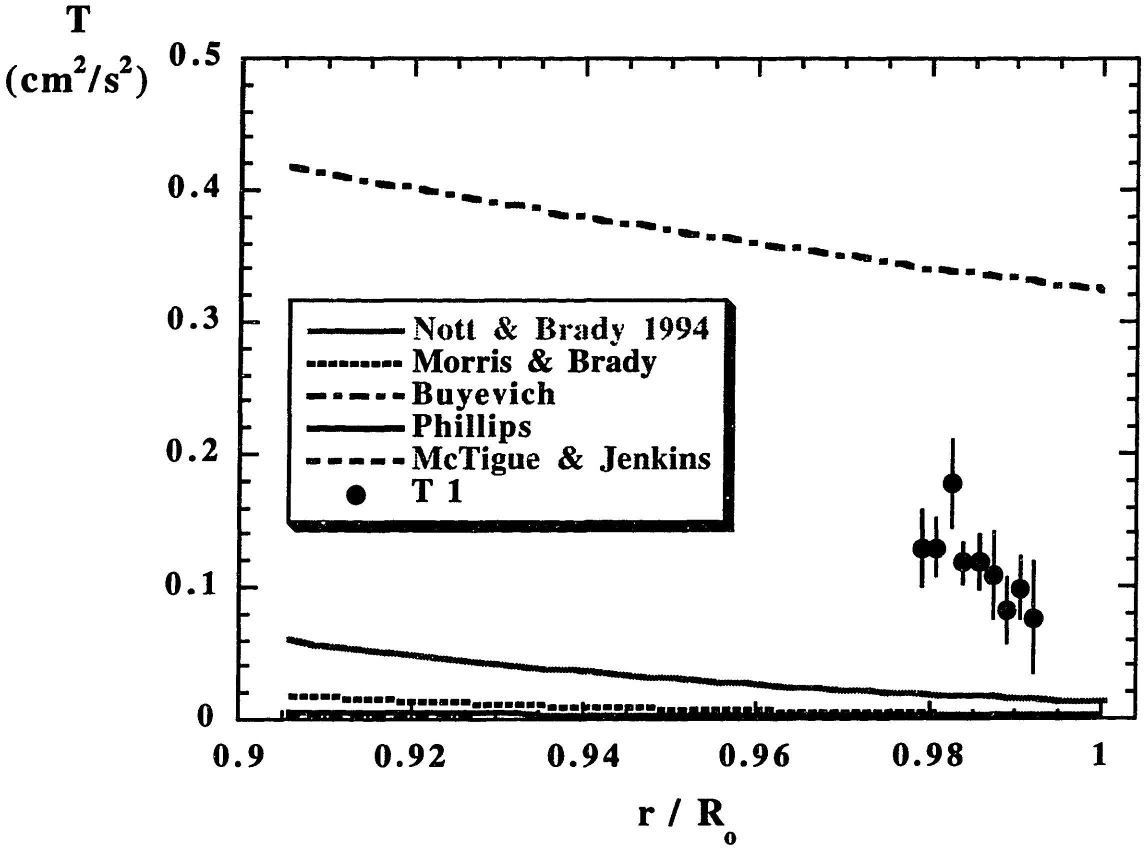

Figure 6.9 Comparison between model predictions of the scalar suspension temperature profile and experimental measurements of the tangential (flow, or 1 direction) suspension temperature component profile across the Couette gap, 50% particle concentration, average shear rate = $10s^{-1}$ (10 rpm).

underpredict the sum of the temperature components by a large factor. The model which approaches the data the most closely is the Buyevich model, which overpredicts the 50% concentrated suspension data but underpredicts the 30% and 40% concentrated suspension data.

All the other models predict suspension temperatures on the same order as the other two, much smaller, suspension temperature components. Another comparison we can make is between the model predictions of the scalar suspension temperature and the observed sum of the vertical (neutral) and radial (gradient) components, and this is displayed in figures 6.10-6.12 for the 30%, 40% and 50% concentrated suspensions. In each of these plots, the Morris and Brady model matches extremely well with the data, with the Phillips model the next closest curve. The good agreement between these measured components and the model predictions suggests that the models contain an assumption about the particle interactions in the suspension that applies to the gradient and neutral directions, but not to the flow direction.

6.2.3 Comparison of Predicted and Measured Variation of the Sum of the Suspension Temperature Components with Particle Volume Fraction

A feature of our physical observations which challenges the assumptions of all the models is the variation of the tangential, radial and vertical suspension temperature components with particle volume fraction. We observe that these components increase in size from low concentrations to about 30-40% concentration, and then decrease at 50% concentration, as demonstrated in figures 4.30-4.32. In contrast, all the models predict that the suspension temperature increases monotonically with concentration, as illustrated in figure 5.1.

This disagreement is illustrated in figure 6.13, where the observed variation of the tangential component (representing the sum of the three components) in concentration is compared to the models' predictions of the dependence of the scalar suspension temperature on concentration. Although the Buyevich model prediction covers the same range of values as the observed tangential component, for concentrations of 30%-50%, the Buyevich curve monotonically increases while the observed trend monotonically decreases.

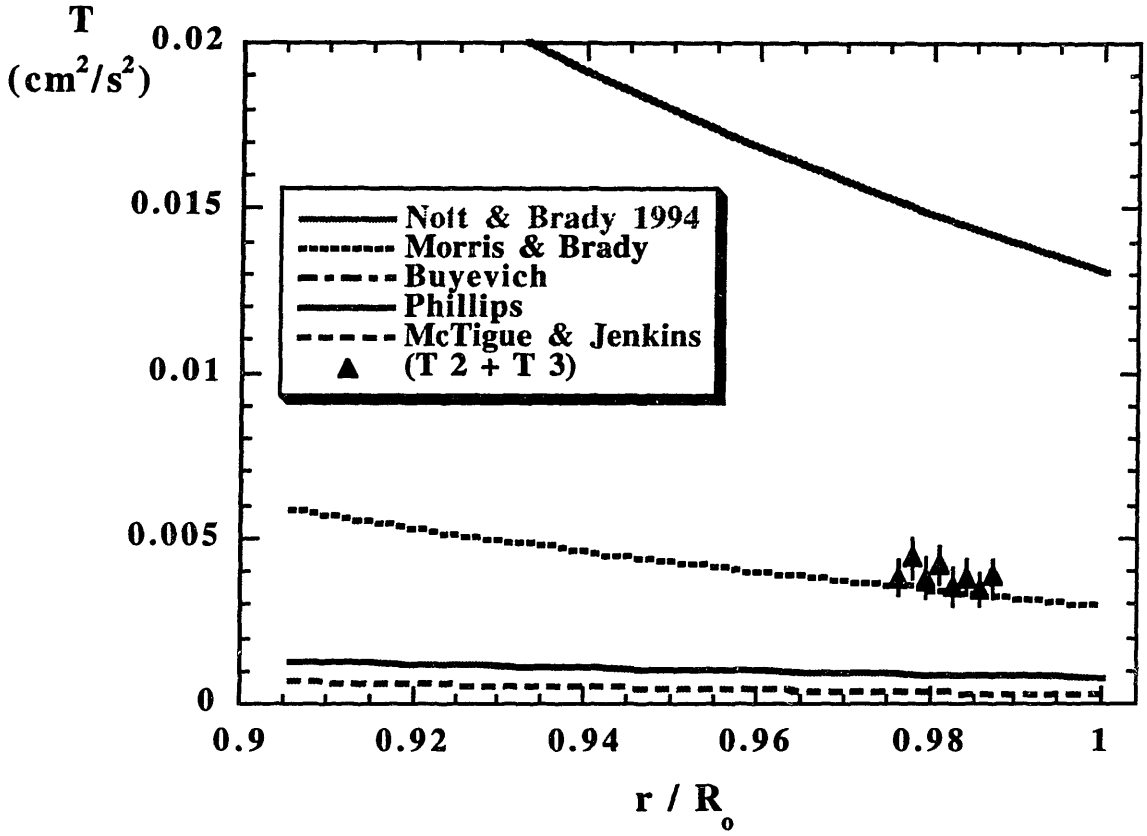

Figure 6.10 Comparison between model predictions of the scalar suspension temperature profile and experimental measurements of the sum of the radial (gradient, or 2 direction) and vertical (neutral, or 3 direction) suspension temperature components profile across the Couette gap, 30% particle concentration, average shear rate = $10s^{-1}$ (10 rpm).

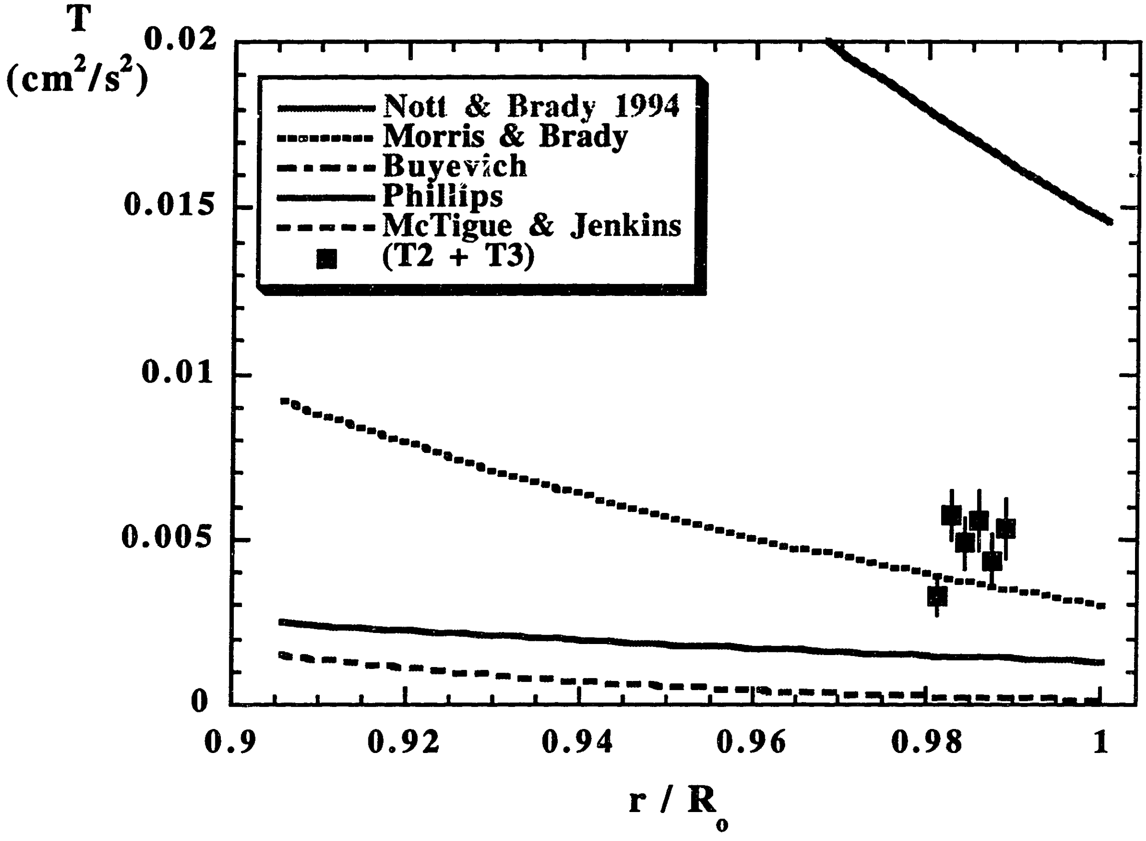

Figure 6.11 Comparison between model predictions of the scalar suspension temperature profile and experimental measurements of the sum of the radial (gradient, or 2 direction) and vertical (neutral, or 3 direction) suspension temperature components profile across the Couette gap, 40% particle concentration, average shear rate = $10s^{-1}$ (10 rpm).

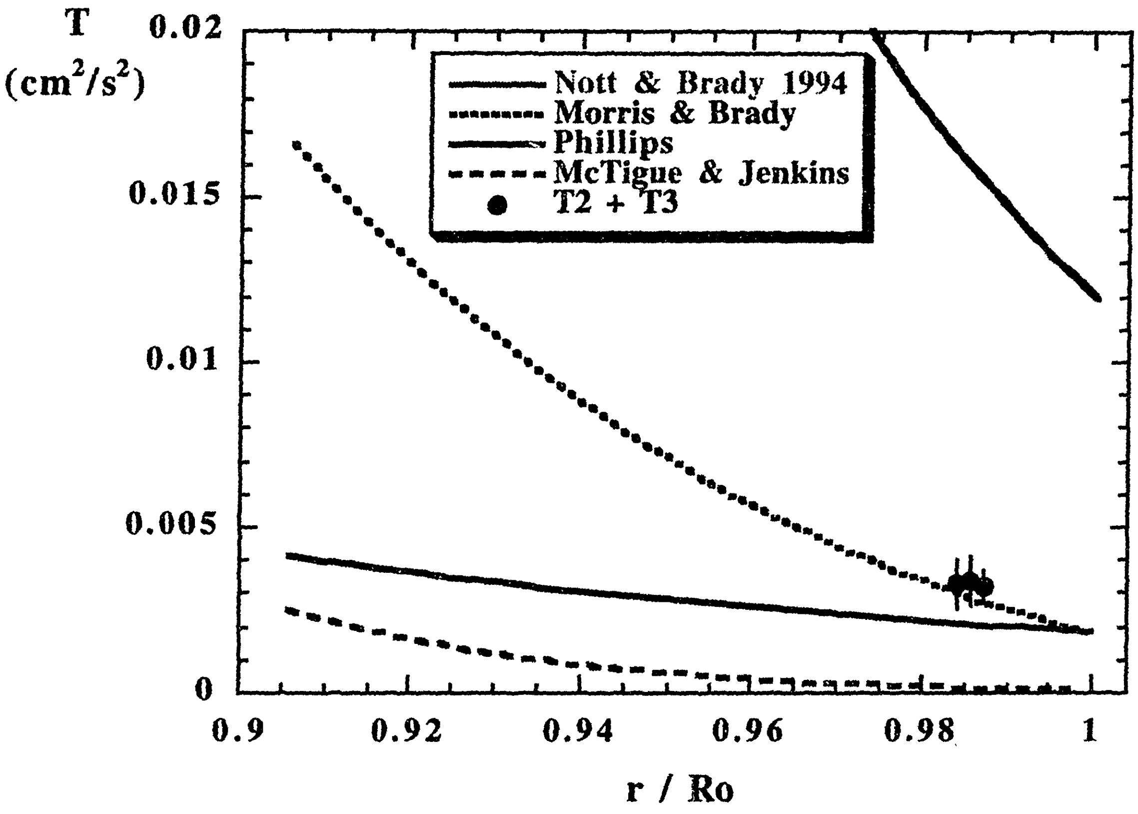

Figure 6.12 Comparison between model predictions of the scalar suspension temperature profile and experimental measurements of the sum of the radial (gradient, or 2 direction) and vertical (neutral, or 3 direction) suspension temperature components profile across the Couette gap, 50% particle concentration, average shear rate = $10s^{-1}$ (10 rpm).

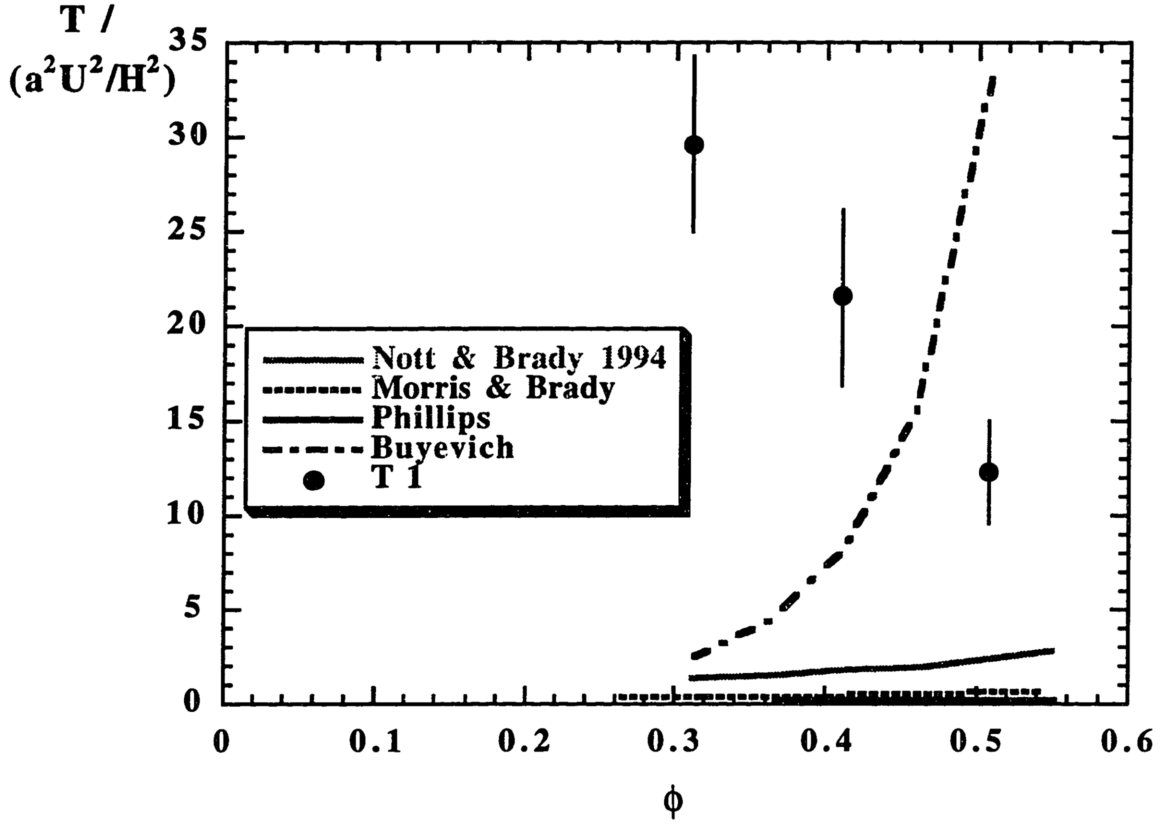

Figure 6.13 Comparison between the dependence on particle volume fraction of model predictions of the scalar suspension temperature and experimental measurements of the tangential (flow, or 1 direction) suspension temperature component, average shear rate = 10 s^{-1} (10 rpm), local shear rate = 8.7 s^{-1}. Both the model predictions and the data are made dimensionless by the particle radius squared multiplied by the average shear rate squared.

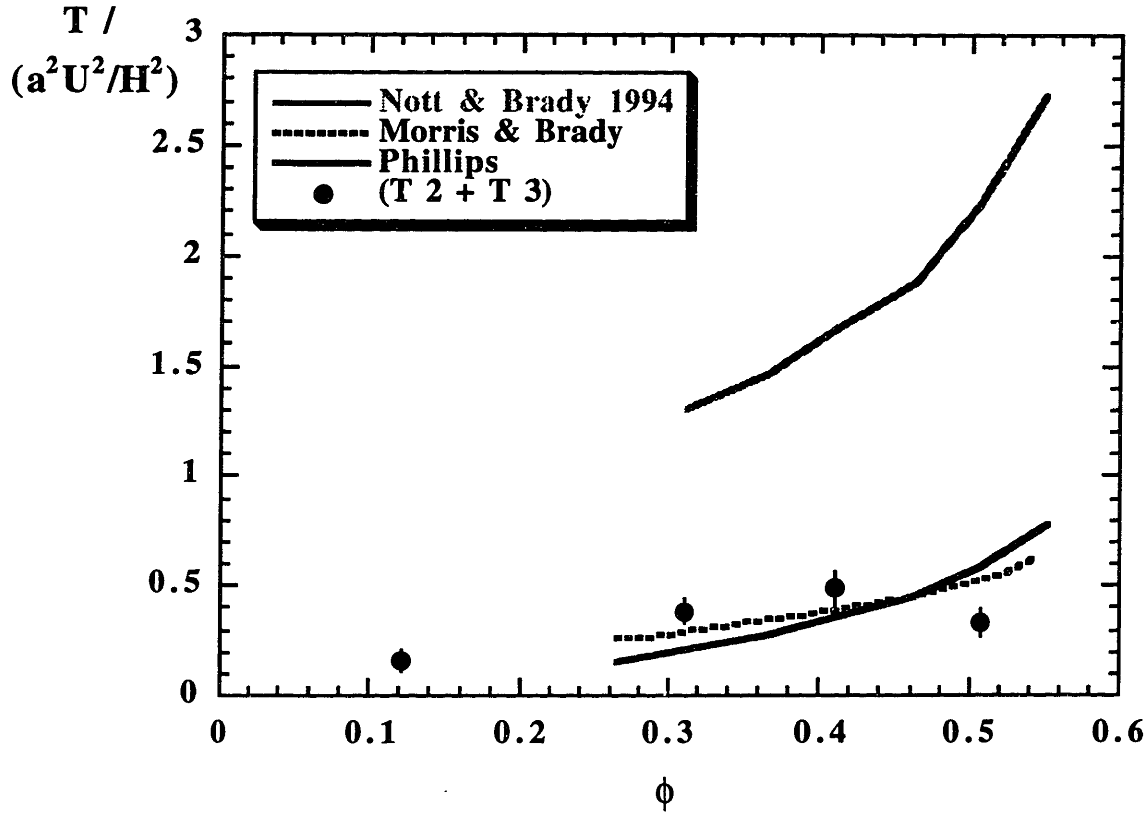

Figure 6.14 Comparison between the dependence on particle volume fraction of model predictions of the scalar suspension temperature and experimental measurements of the sum of the radial (gradient, or 2 direction) and vertical (neutral, or 3 direction) suspension temperature components, average shear rate = 10 s^{-1} (10 rpm), local shear rate = 8.7 s^{-1}. Both the model predictions and the data are made dimensionless by the particle radius squared multiplied by the average shear rate squared.

The comparison between the model predictions and the sum of the smaller two suspension temperature components is presented is figure 6.14. Although the Phillips and Morris and Brady model predictions lie close to the sum of the radial and vertical components, these models do not capture the increasing and decreasing behavior of the observed components.

The shape of the curves of the variation of the tangential, radial and vertical suspension temperature components with particle volume fraction in figures 4.30-4.32 may seem counterintuitive, but can be explained using a scaling argument in the manner of Phillips et al. (1992). The fluctuating velocity in each direction can be approximated by the ratio between the mean free path and the time interval between collisions. According to Jenkins and McTigue (1990) and Frankel and Acrivos (1967), the mean free path can be estimated by the average particle spacing, a function of the bulk concentration. According to Frankel and Acrivos (1967), the average particle spacing is approximated by

$$\frac{\text{spacing}}{a} \sim \frac{\phi}{\eta(\phi)} \tag{6.1}$$

where a is the particle radius and $\eta(\phi)$ is the relative viscosity function, such as that of Krieger (1972). According to Phillips et al. (1992), the time interval betwen collisions scales with $\frac{1}{(\phi\,\dot{\gamma})}$,

so the ratio becomes

$$v' \sim \frac{\text{mean free path}}{\text{collision time interval}} \sim \frac{\phi}{\eta(\phi)}\, a\, (\phi\,\dot{\gamma}) \sim \frac{\phi^2}{\eta(\phi)}\, \dot{\gamma}\, a \tag{6.2}$$

The suspension temperature is defined as the square of the fluctuating velocity, and so it can be approximated as

$$T \sim (v')^2 \sim \frac{\phi^4}{\eta^2(\phi)}\, a^2\, \dot{\gamma}^2 \tag{6.3}$$

As the concentration increases, there is a competition between increasing collision frequency and decreasing mean free path. At low to moderate concentrations, the viscosity function is slowly varying and so the collision frequency effect dominates, causing the suspension temperature to increase. However, at a higher concentration of about 45%, the viscosity curve suddenly starts to increase rapidly, and the mean free path decreases at a much faster rate than the collision rate can increase, and so the suspension temperature decreases at high concentrations. This behavior leads to a T(ϕ) curve with a maximum at moderate concentrations, which is what we observe. A plot of this curve is shown in figure 6.15.

In addition, a T(ϕ) curve with this shape already exists in the literature. Nicolai et al. (1995) observed in their settling experiments that a plot of the vertical (flow direction) fluctuating velocity increased at low concentrations, had a maximum at $\phi = 0.3$, and decreased at higher concentrations. This looks exactly like the shape of our curve for the tangential suspension temperature component, as indicated in figure 6.16, and is similar to the shapes of the other two components' curves.

6.2.4 Comparison of Predicted and Measured Scaling of the Suspension Temperature Components in Shear Rate

The last main subject of our observations is the scaling in shear rate of the three suspension temperature components. First of all, each component has a distinct variation with the shear rate, as is apparent in figures 4.33-4.35. Also, not all the components scale quadratically in the shear rate, as the models assume because of the definition of the suspension temperature. As discussed in chapter 4, only the tangential component for the 30% and 40% concentrated suspensions exhibits quadratic behavior. For the tangential component at these two concentrations, the models' assumed scaling is correct. In contrast, the radial component is nearly constant in the shear rate, and the vertical component displays a more complex scaling that is closer to a square root than a quadratic. Also, the tangential temperature component for the 50% concentrated suspension appears to have a scaling in between quadratic and the scaling of the vertical component. Figure 6.17 contains a comparison of several fits of the vertical suspension temperature component data plotted against the shear rate.

6.2.5 Comparison with the Anisotropic Buyevich Model

A unique feature of Buyevich's model is that it allows the suspension temperature to be an anisotropic tensor and a quadratic function of the rate of strain tensor, not just of the scalar shear

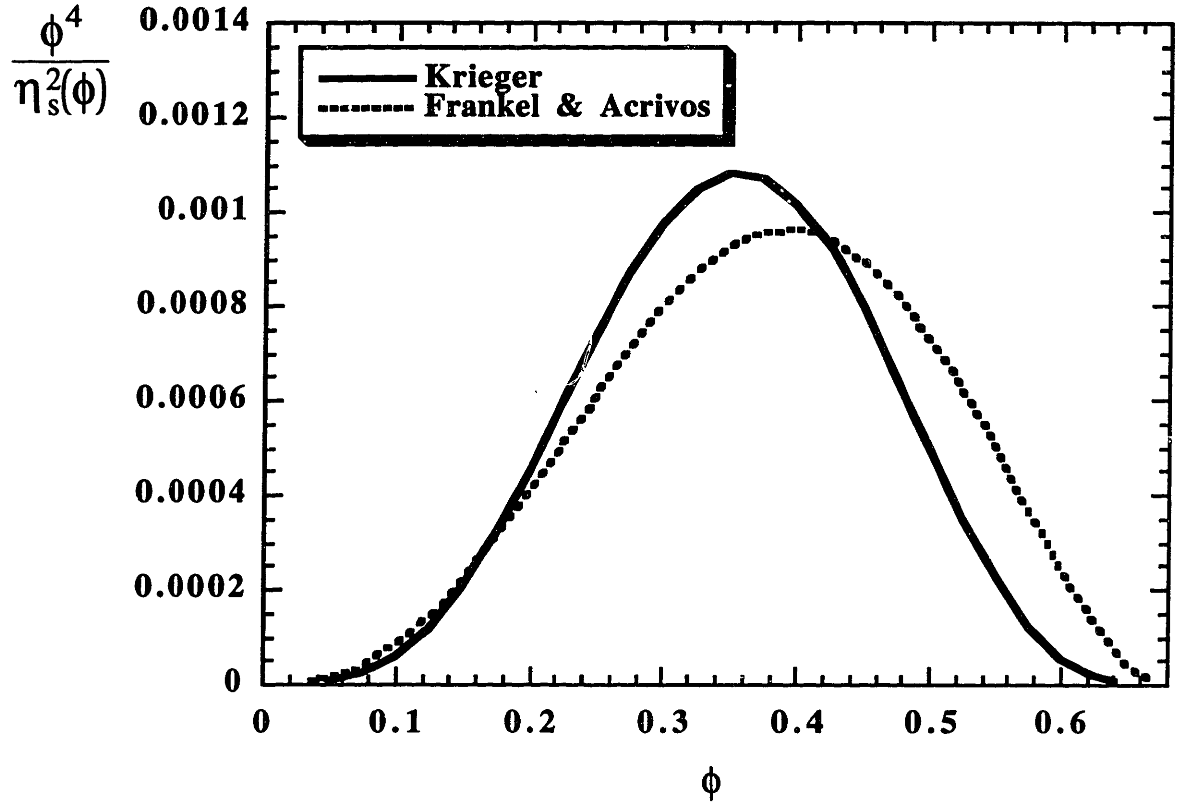

Figure 6.15 Plots of the estimated dependence of the suspension temperature on particle volume fraction. In section 6.2.3, the suspension temperature is approximated as the square of the product of the mean free path and the collision frequency, which leads to the functional form: $T \sim (v')^2 \sim \frac{\phi^4}{\eta^2(\phi)} a^2 \dot{\gamma}^2$.

The two curves shown only differ by the choice of the relative viscosity function, either that of Krieger (1972) or Frankel and Acrivos (1967). Although both curves contain values that are at least two orders of magnitude smaller than those observed experimentally, the curves capture qualitatively the dependence of the suspension temperature components on particle volume fraction.

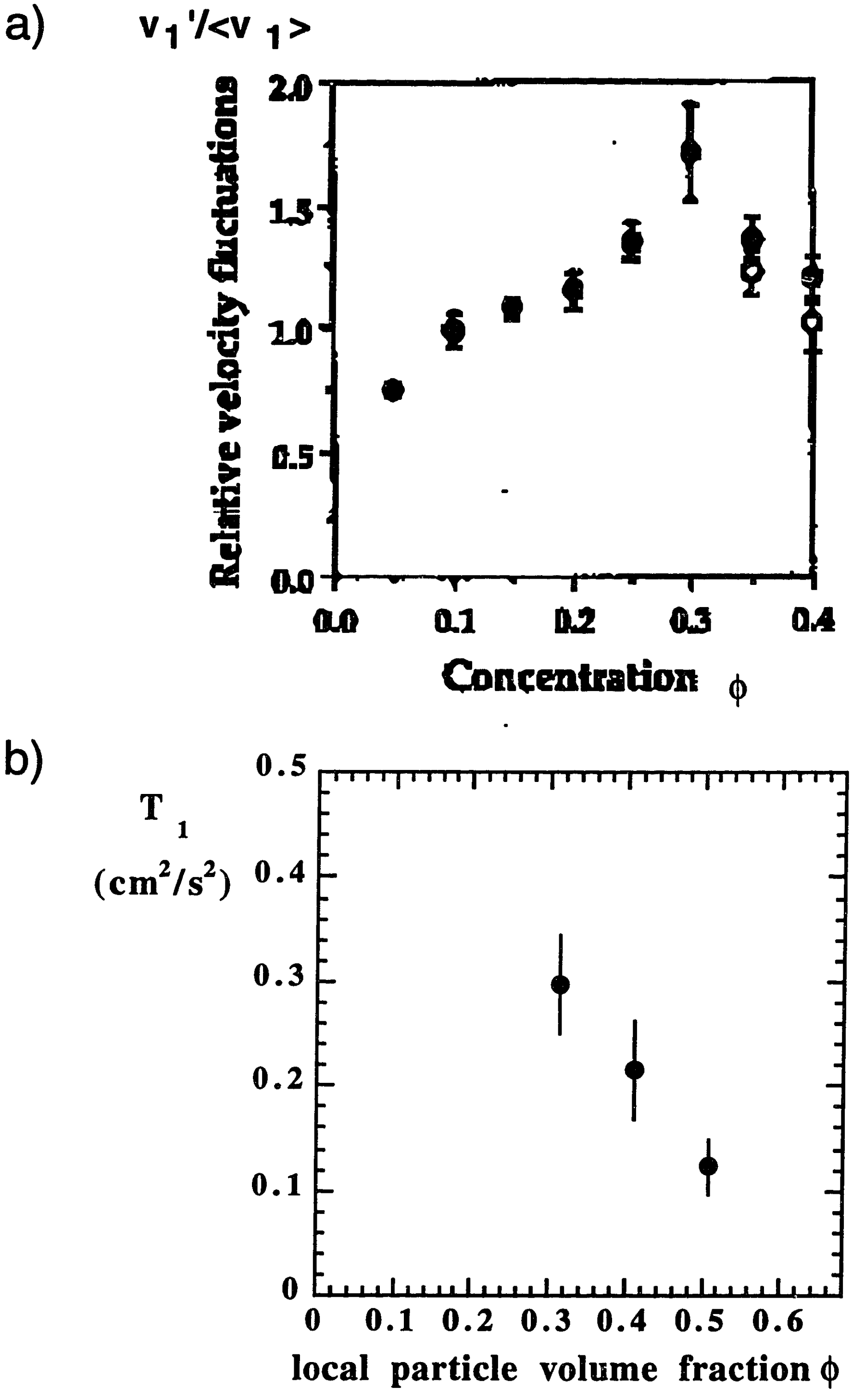

Figure 6.16 Dependence of the flow direction velocity fluctuation on particle volume fraction.

a) Reproduced from Nicolai et al. (1995). Vertical velocity fluctuation in a settling suspension, normalized by mean settling velocity.

b) Data from this study (same as figure 4.30). Collisional velocity fluctuation average shear rate = 10 s^{-1} (10 rpm), local shear rate = 8.7 s^{-1}.

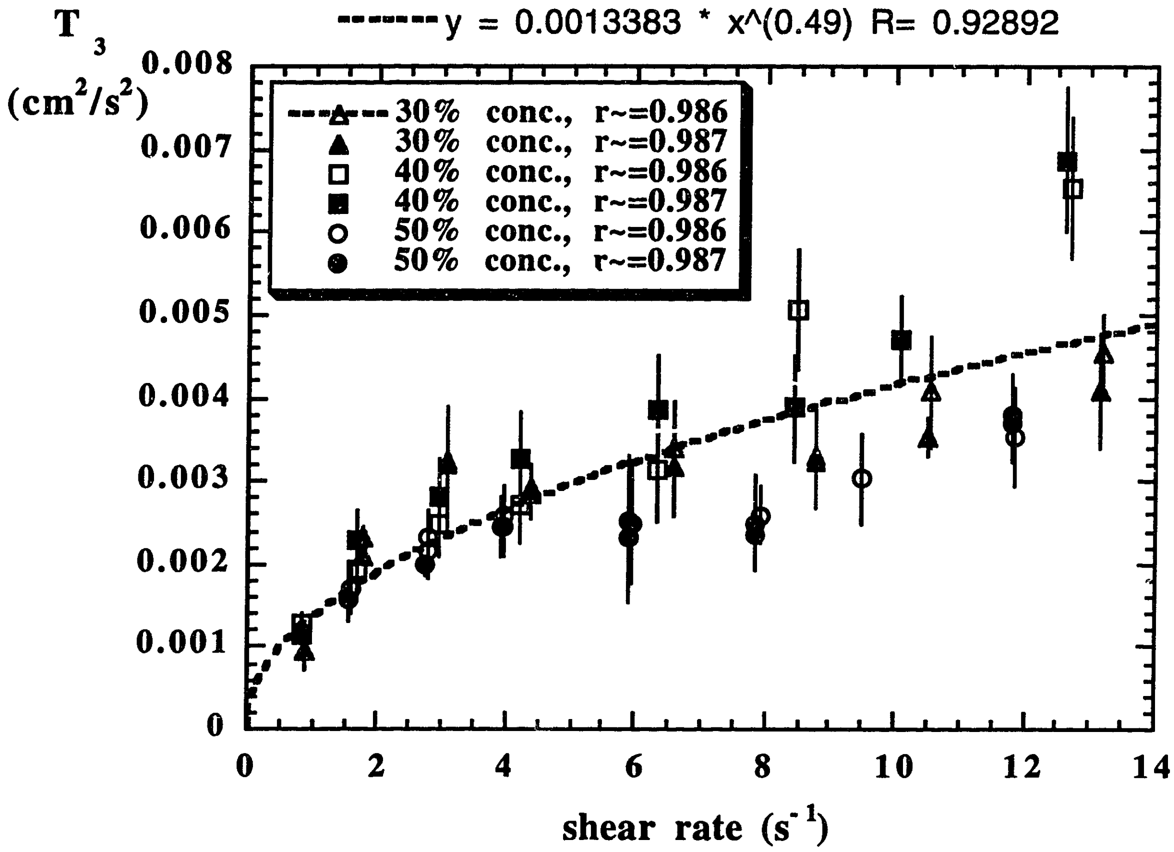

Figure 6.17 Vertical collisional velocity fluctuation (or suspension temperature component) for the 30%, 40% and 50% concentrated suspensions, measured at the ± 90° locations, plotted against local shear rate. These data were obtained at two adjacent radial positions (r/R_O = 0.986 and 0.987) while the local shear rate was varied by changing the inner cylinder rotation speed. A least-squares power law fit is drawn through one of the curves for the 30% concentrated suspension.

rate. Although we compared the model predictions to observations of the sum of the suspension temperature components above, a more detailed comparison is possible for this model, and that is the focus of this section.

Buyevich writes the suspension temperature tensor as the sum of two tensors that are quadratic in the rate of strain tensor,

$$\mathbf{T} = A(\boldsymbol{\gamma}:\boldsymbol{\gamma})\boldsymbol{\delta} + C[\boldsymbol{\gamma}\cdot\boldsymbol{\gamma}] \tag{6.4}$$

where A and C are dimensionless constants. For unidirectional shear flow in the concentric cylinder geometry and coordinate axes along the flow, gradient, and neutral directions, this expression results in a diagonal tensor where $T_{zz} \equiv \langle v'_z v'_z \rangle$ is smaller than the other two identical elements $T_{rr} \equiv \langle v'_r v'_r \rangle$ and $T_{\theta\theta} \equiv \langle v'_\theta v'_\theta \rangle$.

In Buyevich's model, $T_{rr} = T_{\theta\theta}$. Our data strongly contradict this statement, because the observed $T_{\theta\theta}$ is greater than T_{rr} by about two orders of magnitude. If we relax the constraint that tensor **T** must be a quadratic function of the rate of strain tensor and specify merely that the tensor **T** is a function of the rate of strain tensor only, then according to Aris (1962), **T** can be expressed as

$$\mathbf{T} = A(\mathrm{I},\mathrm{II},\mathrm{III})\boldsymbol{\delta} + B(\mathrm{I},\mathrm{II},\mathrm{III})\boldsymbol{\gamma} + C(\mathrm{I},\mathrm{II},\mathrm{III})[\boldsymbol{\gamma}\cdot\boldsymbol{\gamma}] \tag{6.5}$$

where A, B, and C are scalar functions of the three invariants (I, II, III) of the rate of strain tensor. For incompressible flow, $\mathrm{I} = \mathrm{tr}\,\boldsymbol{\gamma} = 0$. For unidirectional shear flow, $\mathrm{III} = \det\boldsymbol{\gamma} = 0$. The only remaining invariant quantity is related to II, $\dot{\gamma} = \sqrt{\frac{1}{2}(\boldsymbol{\gamma}:\boldsymbol{\gamma})}$. Accordingly, for the Couette flow problem,

$$\mathbf{T} = A(\dot{\gamma})\boldsymbol{\delta} + B(\dot{\gamma})\boldsymbol{\gamma} + C(\dot{\gamma})[\boldsymbol{\gamma}\cdot\boldsymbol{\gamma}] \tag{6.6}$$

The additional term in this expansion is proportional to the rate of strain tensor, and hence does not have any diagonal components in this coordinate system. Consequently, even without a constraint on the functional dependence of **T** on the rate of strain tensor, there is still the contradiction between the model predicting $T_{rr} = T_{\theta\theta}$ and the data indicating $T_{rr} \neq T_{\theta\theta}$.

The conclusion we draw is that **T**, the suspension temperature tensor, is not a function of the rate of strain tensor only. It is beyond the scope of this research to find the complete set of tensors on which the suspension temperature tensor may depend. However, another deformation tensor that the suspension temperature tensor **T** might depend on is the convected derivative of the rate of strain tensor, denoted as $\boldsymbol{\gamma}_{(2)}$ by Bird et al. (1987). For cylindrical Couette flow, the tensor $\boldsymbol{\gamma}_{(2)}$ has only one nonzero component in the flow coordinate system, namely $\gamma_{(2)_{\theta\theta}}$, which would allow the tensor components T_{rr} and $T_{\theta\theta}$ to vary independently. Adding this tensor to the expression for the suspension temperature tensor **T** would yield a relation like an ordered fluid expansion, which relates the stress tensor to the rate of strain tensor in a nonlinear viscoelastic material. The modified relation would be particularly similar to the Criminale-Ericksen-Filbey (CEF) stress tensor constitutive equation (Bird et al., 1987).

In addition, an example of another tensor that **T** could depend on is the suspension microstructure, specifically, the average pair orientation tensor, defined as $\langle \underline{u}\,\underline{u} \rangle$ by Phan-Thien (1995), where $\underline{u}$ is the unit vector pointing along the line of centers of two particles. This tensor has a similar definition to the structure tensor for liquid crystalline systems, where $\underline{u}$ represents the orientation of each rodlike crystal (Doi, 1981).

It is reasonable to suppose that the suspension temperature tensor **T** is a function of such a microstructure tensor. It is clear from figure 6.13 that the trace of **T** is a function of the particle volume fraction. Examination of the arrangement of particles at a higher level of detail suggests that an anisotropic arrangement of particles leads to an effectively anisotropic particle volume fraction, depending on the direction of observation. Consequently, it would be appropriate for the anisotropic suspension temperature tensor to depend on the anisotropic particle volume fraction, represented by the microstructure tensor $\langle \underline{u}\,\underline{u} \rangle$. This is analogous to the extension by Buyevich of the quadratic dependence of the scalar temperature on the shear rate to the quadratic dependence of the temperature tensor on the rate of strain tensor.

In chapter 7, we discuss the tensorial nature of the suspension temperature in more depth and describe and evaluate our own attempts to derive an anisotropic suspension temperature model.

6.3 Implications of Observations for Suspension Simulations

The physical observations we made of the collisional particle velocity fluctuations have implications for suspension simulations as well as for continuum models. The two observations with the greatest impact on simulations were the visualiztion by video imaging of particles undergoing "out-of-plane" binary collisions, shown in figure 4.3, and the LDV measurements indicating that the vertical fluctuating velocity component is larger than the radial component, shown in figures 4.25 and 4.26. The two observations together lead us to conclude that the neutral direction plays an important role in inter-particle interactions. This conclusion invalidates the idea employed in the original Stokesian dynamics simulations (Nott and Brady, 1994) that a monolayer is equivalent to an interior plane in a one-dimensional or two-dimensional flow. Our data indicates that three-dimensional simulations with all the physical degrees of freedom are needed to recreate the experimental environment.

6.4 Comparison with Other LDV Measurements of Particle Velocity Fluctuations in Shear Flows

In figures 4.25 and 4.26, which illustrate the dependence of the radial and vertical velocity fluctuations on local shear rate, at a fixed average shear rate of 10 s^{-1} (10 rpm), we compare our data to that of Tripathi (1998), who also measured suspension temperature components in narrow gap Couette flow. Tripathi made LDV measurements of particle velocity fluctuations in suspensions of 20% to 40% average particle volume fraction over a shear rate range of 3 to 16 s^{-1} and followed the same data reduction procedures that we did. There is a significant overlap between Tripathi's measurements and ours, in which the particle volume fraction varied from 10% to 50% and the average shear rate ranged from 1 to 12 s^{-1}.

The two sets of data are similar in several ways for shear rates close to 10 s^{-1}. We measured radial and vertical collisional velocity fluctuations of similar magnitude to Tripathi's data, and Tripathi observed, as we did, that the vertical (neutral) fluctuation component was larger than the radial (gradient) component, over the entire measured concentration and shear rate range.

Tripathi also measured the tangential (flow) velocity fluctuation component, but he used different conditions for these measurements, and the resulting observed velocity fluctuation component was nearly negligible. Accordingly, the tangential component measurements are not directly comparable to the data of this study. However, a final similarity is that Tripathi's plot of the dependence of the sum of the suspension temperature components on particle volume fraction has a very similar shape to the plot in figure 6.16 of the dependence of the sum of the two smaller suspension temperature components on particle volume fraction. Both curves rise from low particle volume fraction to a maximum at 40% particle volume fraction.

However, a discrepancy between Tripathi's observations and those presented here is that Tripathi found relatively quadratic dependence in the shear rate for the radial and vertical collisional velocity fluctuation components, which is different from what we observe. The source of the discrepancy is not easily detectable. We used Couette flows with very similar dimensions and very similar LDV systems, but different size particles, different particle and fluid materials, and measured at different places in the gap. Whereas our measurements were taken in the outer 25% of the gap for the concentrated suspensions, Tripathi obtained all his observations along the flow center line.

We also compare the tangential (flow direction) component of the collisional fluctuating velocity measurements presented here to the measurements made by Lyon and Leal (1998) of the collisional fluctuating velocity in the flow direction in channel flow.Since Lyon and Leal measured only this component, it is our only basis of comparison. It appears that our measured collisional velocity fluctuations were approximately an order of magnitude larger than Lyon and Leal 's.

However, it is difficult to compare the two flows, since the significant velocity fluctuations in channel flow occur near the wall, where the LDV signals are typically the noisiest and the local shear rate varies the most rapidly, so that the measurements are sensitive to small changes in position. Although some of our measurements also lie close to the outer cylinder wall, narrow gap Couette flow is designed to be nearly homogeneous in shear rate. We might expect that the measured velocity fluctuations could be different in nearly homogeneous and very inhomogenous flows, especially if the inhomogeneity is significant on the length scale of the LDV measuring volume.

Chapter 7

Anisotropic Suspension Temperature Model

In sections 4.3.2.1 and 6.2.1, we found that the suspension temperature components in the radial, tangential and vertical directions are unequal to each other. This means that the suspension temperature is anisotropic. If the suspension temperature were isotropic, then the components measured in any independent directions would be equal. More specifically, if tensor **T** is isotropic,

$$[\underline{n} \cdot \mathbf{T}] = T\,\underline{n} \quad \text{for all } \underline{n} \tag{7.1}$$

For an isotropic tensor, the choice of coordinate axes has no impact on the equality of the components.

7.1 What is the Structure of the Suspension Temperature Tensor T ?

In considering an anisotropic suspension temperature tensor, the first question that arises is what form the tensor has. If we define the suspension temperature tensor as

$$T_{ij} \equiv \langle v_i' v_j' \rangle \tag{7.2}$$

we have a symmetric 3x3 tensor, accordingly with six independent components. However, some of these independent components may vanish in a specific flow field, such as unidirectional shear flow.

In a simple homogeneous shear flow, with (x, y, z) replacing (θ, r, z) respectively, if we rotate the coordinate system by 180° about the vorticity axis, such that

$$x^* = -x \;; \qquad y^* = -y \;; \qquad z^* = z \tag{7.3}$$

then

$$T_{x^*x^*} = \langle v'_{x^*} v'_{x^*} \rangle = \langle (-v'_x)(-v'_x) \rangle = \langle v'_x v'_x \rangle = T_{xx} \tag{7.4}$$

Similarly,

$$T_{y^*y^*} = T_{yy} \text{ and } T_{x^*y^*} = T_{xy}, \tag{7.5}$$

and $T_{yx} = T_{xy}$, because tensor **T** is defined to be symmetric. The coordinate z does not change at all under the rotation, so T_{zz} remains unchanged.

However, T_{x*z*} does change under the rotation:

$$T_{x*z*} = \langle v'_{x*} v'_{z*} \rangle = \langle (-v'_x)(v'_z) \rangle = -\langle v'_x v'_z \rangle = -T_{xz} \tag{7.6}$$

And similarly,

$$T_{y*z*} = -T_{yz}. \tag{7.7}$$

However, the flow is invariant to rotations of 180° about the vorticity axis. This means that any tensor that depends on the flow kinematics is identical before and after the rotation (Bird et al., 1987). As a result,

$$T_{x*z*} = T_{xz} \tag{7.8}$$

$$T_{y*z*} = T_{yz}$$

This leads to

$$T_{xz} = -T_{xz} = 0 \tag{7.9}$$

$$T_{yz} = -T_{yz} = 0$$

Since the tensor **T** is defined to be symmetric, that means the T_{zx} and T_{zy} components are also zero.

Since narrow gap Couette flow is locally a simple shear flow, the same symmetry argument applies. Components T_{rz}, T_{zr}, $T_{\theta z}$, and $T_{z\theta}$ are zero. Therefore, the tensor **T** can contain at most four independent components: the three diagonal components (T_{rr}, $T_{\theta\theta}$, T_{zz}) and equal $T_{r\theta}$ and $T_{\theta r}$ components. The matrix representation of **T** is written in cylindrical coordinates as

$$\mathbf{T} = \begin{pmatrix} T_{rr} & T_{r\theta} & 0 \\ T_{r\theta} & T_{\theta\theta} & 0 \\ 0 & 0 & T_{zz} \end{pmatrix} \tag{7.10}$$

7.2 Dependence of Tensor T on the Rate of Strain Tensor: Comparison with the Anisotropic Buyevich Model

As was discussed in more detail in Chapter 6, if we assume that the tensor **T** is a function of the rate-of-strain tensor alone, then we can follow Aris (1962) in generalizing the quadratic form suggested by Buyevich (1996); and we can write the suspension temperature tensor as:

$$\mathbf{T} = A(\boldsymbol{\gamma}:\boldsymbol{\gamma})\boldsymbol{\delta} + B\boldsymbol{\gamma} + C[\boldsymbol{\gamma}\cdot\boldsymbol{\gamma}] \ . \tag{7.11}$$

Where A, B and C are functions of the three scalar invariants of **T**. Because of the form of the rate-of-strain tensor and its square in unidirectional shear flow, this reasoning leads to

$$T_{\theta\theta} = T_{rr} \ . \tag{7.12}$$

This result directly contradicts our observation that $T_{\theta\theta}$ and T_{rr} are different by a factor of between 25 and 120 for the concentrated suspensions we measured, with $T_{\theta\theta}$ being the largest and T_{rr} the smallest of the diagonal components. Consequently, our experimental observations do not support the idea that the tensor **T** is a function of the rate-of-strain tensor alone. The example given in Chapter 6 of another tensor that **T** could depend on was the suspension microstructure tensor, specifically, the average pair orientation tensor, analogous to $\langle \underline{u}\,\underline{u} \rangle$ for liquid crystals (Phan-Thien, 1995; Leighton and Rampall, 1993).

7.3 Relating the Experimental Measurements to the Invariants of Tensor T

The invariants of the suspension temperature tensor **T** are the trace, the determinant, and the second invariant, defined as

$$I_2 = \mathrm{tr}[\mathbf{T}:\mathbf{T}] \tag{7.13}$$

We can write three other quantities as functions of these three invariants only: T_{zz}, which is one of the eigenvalues, and the trace and determinant of the upper block of the **T** matrix involving r and θ components only, given respectively as:

$$(T_{rr} + T_{\theta\theta}) \ ; \quad (T_{rr}T_{\theta\theta} - T_{r\theta}^{\ 2}) \tag{7.14}$$

Now, we only measured the diagonal components of tensor **T** in the laboratory reference frame. We were not able to measure $T_{r\theta}$ because this is a covariance between two velocity components, and we only measured one velocity component at a time. Even if we had the capability of measuring two velocity components at once, the geometry of our system prohibits measuring $\langle v'_r \, v'_\theta \rangle$. The only way to measure this quantity would be to shine the LDV beams from the top or bottom of the flow, and the path length through the suspension to the center of the flow where end effects are minimized is far too long for any signals to pass through it, at least for the concentrated suspensions of interest. As mentioned in Chapter 3, measurement of $\langle v'_\theta\, v_r\rangle$ from the side of the flow is theoretically possible, but quite difficult in practice. Measuring $\langle v'_\theta\, v_r\rangle$ from the side involves comparing three fluctuation measurements, all with different path lengths that the beam must pass through in the suspension and different effective measuring volume sizes, with corresponding baselines in the 2% concentrated suspension. Accounting for all these factors is beyond the scope of this project.

We want to measure the invariants of the tensor, so that our observations are independent of an arbitrarily chosen reference frame. We measure the invariant quantities T_{zz}, which is one of the eigenvalues as noted previously, and the trace of **T** (sum of the diagonal components). We know the trace of **T** must be positive because it represents the total kinetic energy contained in velocity fluctuations in all directions, by definition a positive quantity. What about the determinant of **T**? When we diagonalize **T** in the principal axis coordinate system, it will not contain any off-diagonal terms which are covariances. It seems reasonable to associate each of the eigenvalues which appear in the diagonal tensor with the kinetic energy of velocity fluctuations along one of the principal axes. In that case, each of the eigenvalues should be positive, causing **T** to be a positive-definite tensor (i.e. the determinant of **T** is positive).We can use this judgement to put bounds on the value of the off-diagonal component $T_{r\theta}$. We can also bound the impact of nonzero $T_{r\theta}$ on the eigenvector directions.

If the determinant of **T** is positive, then

$$\det \mathbf{T} = T_{zz}\left(T_{rr}T_{\theta\theta} - T_{r\theta}{}^2\right) \geq 0 \tag{7.15}$$

Since T_{ZZ} is known to be positive from our measurements, and is positive by definition, we find

$$T_{rr}T_{\theta\theta} \geq T_{r\theta}{}^2 \tag{7.16}$$

T_{ZZ} is one of the eigenvalues of T. We find the other two from the upper left block of tensor **T** as follows,

$$\lambda^2 - \left(T_{rr} + T_{\theta\theta}\right)\lambda + \left(T_{rr}T_{\theta\theta} - T_{r\theta}{}^2\right) = 0 \tag{7.17}$$

Solving for λ gives

$$\lambda = \frac{T_{rr} + T_{\theta\theta} \pm \sqrt{\left(T_{rr} + T_{\theta\theta}\right)^2 - 4\left(T_{rr}T_{\theta\theta} - T_{r\theta}^{\ 2}\right)}}{2} \tag{7.18}$$

Now, $|T_{r\theta}|$ ranges from 0, where $\lambda = (T_{rr}, T_{\theta\theta})$, to $\sqrt{T_{rr}T_{\theta\theta}}$, where $\lambda = \left(\left(T_{rr} + T_{\theta\theta}\right), 0\right)$. If $T_{r\theta} = 0$, then the components we measured are the eigenvalues of the suspension temperature tensor. The worst case is $|T_{r\theta}| = \sqrt{T_{rr}T_{\theta\theta}}$, and $\lambda = \left(\left(T_{rr} + T_{\theta\theta}\right), 0\right)$. Now, we find the corresponding worst-case eigenvectors.

In the worst case, the eigenvectors must satisfy the equation

$$\mathbf{T}\ \underline{v}_i = \lambda_i\ \underline{v}_i \quad ; \qquad i = 1,2 \tag{7.19}$$

For $\lambda_1 = (T_{rr} + T_{\theta\theta})$, the equation becomes

$$\begin{pmatrix} T_{rr} & T_{r\theta} \\ T_{r\theta} & T_{\theta\theta} \end{pmatrix} \begin{pmatrix} 1 \\ v_1 \end{pmatrix} = (T_{rr} + T_{\theta\theta}) \begin{pmatrix} 1 \\ v_1 \end{pmatrix} \tag{7.20}$$

We set one of the eigenvector components to unity since we only need to solve for the ratio of the two components. Using the equation for the radial component, we obtain

$$T_{rr} + T_{r\theta}\, v_1 = T_{rr} + T_{\theta\theta} \tag{7.21}$$

which leads to

$$v_1 = \frac{T_{\theta\theta}}{T_{\ \theta}} = \frac{T_{\theta\theta}}{\pm\sqrt{T_{rr}T_{\theta\theta}}} = \pm\sqrt{\frac{T_{\theta\theta}}{T_{rr}}} \tag{7.22}$$

and

$$\underline{v}_1 = \begin{pmatrix} 1 \\ \pm\sqrt{\dfrac{T_{\theta\theta}}{T_{rr}}} \\ 0 \end{pmatrix} \tag{7.23}$$

which compares with $\begin{pmatrix} 0 \\ 1 \\ 0 \end{pmatrix}$ if $\lambda_1 = T_{\theta\theta}$.

For $\lambda_2 = 0$,

$$\begin{pmatrix} T_{rr} & T_{r\theta} \\ T_{r\theta} & T_{\theta\theta} \end{pmatrix} \begin{pmatrix} 1 \\ v_2 \end{pmatrix} = (0) \begin{pmatrix} 1 \\ v_2 \end{pmatrix} \tag{7.24}$$

Using the equation for the radial component, we find

$$T_{rr} + T_{r\theta}\, v_2 = 0$$

which leads to

$$v_2 = \frac{-T_{rr}}{T_{\ \theta}} = \frac{-T_{rr}}{\pm\sqrt{T\ \ T_{\theta\theta}}} = \mp\sqrt{\frac{T_{rr}}{T_{\theta\theta}}} \tag{7.25}$$

$$\underline{v}_2 = \begin{pmatrix} 1 \\ \mp\sqrt{\frac{T_{rr}}{T_{\theta\theta}}} \\ 0 \end{pmatrix} \tag{7.26}$$

which compares with $\begin{pmatrix} 1 \\ 0 \\ 0 \end{pmatrix}$ if $\lambda_2 = T_{rr}$.

From the experimental Couette flow data at the comparison average shear rate of 10 s^{-1}, we find that $T_{\theta\theta} \cong 0.1$ (cm^2/s^2), $T_{rr} \cong 0.0008$ (cm^2/s^2), and accordingly $\frac{T_{\theta\theta}}{T_{rr}} \cong 120$, so that $\sqrt{\frac{T_{\theta\theta}}{T_{rr}}} \cong 11$ and the eigenvectors become

$$\underline{v}_1 = \begin{pmatrix} 1 \\ \pm 11 \\ 0 \end{pmatrix} \quad \text{and} \quad \underline{v}_2 = \begin{pmatrix} 1 \\ \mp\frac{1}{11} \\ 0 \end{pmatrix}$$

or, normalizing,

$$\underline{v}_1 = \frac{1}{\sqrt{122}}\begin{pmatrix} 1 \\ \pm 11 \\ 0 \end{pmatrix} \quad \text{and} \quad \underline{v}_2 = \frac{1}{\sqrt{122}}\begin{pmatrix} 11 \\ \mp 1 \\ 0 \end{pmatrix} \tag{7.27}$$

The resulting principal axes are rotated only approximately 5° clockwise or counter clockwise from the lab axes, in the worst-case situation. We believe this indicates that our choice of measurement axes are nearly identical to the principal axes of the temperature tensor T. The corresponding maximum difference between the value $T_{\theta\theta}$ we measured and the eigenvalue $(T_{\theta\theta} + T_{rr})$ is only 0.8%. Also, the value of $|T_{r\theta}|$ is bounded by $0 \leq |T_{r\theta}| \leq 0.009$ (cm^2/s^2).

From the experimental Couette flow data, at the lowest average shear rate of 2 s^{-1}, $T_{\theta\theta} \cong 0.02$ (cm^2/s^2), $T_{rr} \cong 0.0008$ (cm^2/s^2), and accordingly $\sqrt{\frac{T_{\theta\theta}}{T_{rr}}} \cong 5$ and the normalized eigenvectors become

$$\underline{v}_1 = \frac{1}{\sqrt{26}}\begin{pmatrix} 1 \\ \pm 5 \\ 0 \end{pmatrix} \quad \text{and} \quad \underline{v}_2 = \frac{1}{\sqrt{26}}\begin{pmatrix} 5 \\ \mp 1 \\ 0 \end{pmatrix} \tag{7.28}$$

The resulting principal axes are rotated only approximately 11° clockwise or counterclockwise from the lab axes, in the worst-case situation. We believe this still indicates that our choice of measurement axes are nearly identical to the principal axes of the temperature tensor T. The corresponding maximum difference between the value $T_{\theta\theta}$ we measured and the eigenvalue $(T_{\theta\theta} + T_{rr})$ is only 4%. Also, the value of $|T_{r\theta}|$ is bounded by $0 \leq |T_{r\theta}| \leq 0.004$ $(\mathrm{cm}^2/\mathrm{s}^2)$.

7.4 Incorporating the Measured Anisotropy of the Suspension Temperature into the Models' Constitutive Relations

Now that we have some knowledge of the form of the anisotropic suspension temperature tensor, we attempt to apply it to the constitutive relations in the suspension models. In order to find constitutive relations that depend on a tensor **T** and are not completely arbitrary, we return to the statistical mechanics roots of the suspension temperature models. All the scalings and coefficients which appear in the models of McTigue and Jenkins (1992), Nott and Brady (1994), and Morris and Brady (1996) are based on those derived by Jenkins and Savage (1983) for a granular flow and Jenkins and McTigue (1990) for a concentrated suspension.

We pursued this modeling for several reasons. First, we wanted to determine whether the anisotropy of the suspension temperature has an impact on the macroscopic properties of the flow that is consistent with other observations through the constitutive equation for the stress tensor. Also, we felt that the existing conservation of fluctuation energy equation was missing a source term for neutral and gradient direction velocity fluctuations at flow startup, and a more realistic equation was needed, not only improved constitutive relations.

7.4.1 Incorporating the Measured Suspension Temperature Anisotropy into the Statistics for Calculating Averaged Properties

We modified the statistical mechanics model of Jenkins and McTigue (1990) to allow for an anisotropic suspension temperature. In this model, all the macroscopic observable quantities at a point in space are calculated as weighted averages of microscopic quantities, where the weighting factor is the particle distribution function. The distribution function indicates the probability of a particle, or multiple particles, being located at a certain point in space and having a certain velocity at that point. We made a simple approximation, that the anisotropic temperature only affects the single particle velocity distribution function. The anisotropic velocity fluctuations were not incorporated into the pair (position) distibution function, which indicates the probability of a selected particle finding a second particle at a given distance and direction. We left unchanged the isotropic pair orientation distibution function that Jenkins and McTigue used in their calculations.

The most important constitutive relation linking the anisotropic suspension temperature to other quantities is the stress tensor equation, since that is the only expression in the balance equations for macroscopic variables that contains T. Accordingly, this is the first constitutive relation we focus on, following the development of Jenkins and McTigue. We note that the model of Phan-Thien (1995) is derived in a similar manner.

7.4.1.1 Jenkins and McTigue's Derivation of the Stress Tensor

Jenkins and McTigue (1990) define the stress tensor at a given position as the average force transmitted through the fluid between two colliding particles, per unit area, multiplied by the unit vector connecting the line of particle centers. The average is taken over all the possible initial particle velocities and pair orientations, and expressed mathematically as

$$\tau(\underline{r}) = \frac{1}{2}(2\,a) \int_{\underline{k},\, \underline{v}_1,\, \underline{v}_2} \underline{F}\ \underline{k}\ f^{(2)}(\underline{v}_1, \underline{v}_2, \underline{k})\, d\underline{k}\, d\underline{v}_1\, d\underline{v}_2 \qquad (7.29)$$

where a is the particle radius, $\underline{k}$ is the unit vector along the line of particle centers and $f^{(2)}$ is the pair distribution function.

The force between particle 1, with its center located at $\underline{r}_1$ and with velocity $\underline{v}_1$, and particle 2, located with its center at $\underline{r}_2$ with velocity $\underline{v}_2$, can be written as (Jeffery and Onishi, 1984a,b)

$$\underline{F} = -3\,\pi\,(2\,a)\,\eta_f\,\mathbf{A}\cdot(\underline{v}_1 - \underline{v}_2) - \pi\,(2\,a)^2\,\eta_f\,\mathbf{B}\cdot\underline{\omega} \tag{7.30}$$

where **A** and **B** are tensors that depend on the average local inter-particle separation distance, a function of the average local particle volume fraction. $\underline{\omega}$ is the mean angular velocity of rotation of the particles due to the vorticity of the flow.

At contact, the two particles' centers are separated by a distance (2 a). Also, we separate each particle's velocity into mean and fluctuating parts as

$$\underline{v}_i \equiv \underline{u}(r_i) + \underline{v}'_i \tag{7.31}$$

In order to write the expression for the force at a single position, we expand linearly the velocity of particle 2 before contact as

$$\underline{v}_2 = \underline{v}_1 + (1+s)\,(2\,a)\,(\underline{k}\cdot\underline{\nabla})\,\underline{u} + \underline{v}' \tag{7.32}$$

where s is the inter-particle spacing, $\underline{u}$ is the mean velocity at point $\underline{r}_1$, and $\underline{v}'$ is the difference in the particles' fluctuating velocities, defined as $\underline{v}' \equiv \underline{v}'_1 - \underline{v}'_2$.

Substituting this expansion into the force expression, keeping only terms up to first order in $(a\,|\nabla\,u|)$, and assuming the particles' angular velocities are equal to the fluid vorticity yields

$$\underline{F}(\underline{r}_1, \underline{k}) = \pi\,(2\,a)\,\eta_f\,\Big[\underset{(1)}{\alpha_1\,(2\,a)\,(\underline{k}\cdot\boldsymbol{\gamma}\cdot\underline{k})\,\underline{k}} + \underset{(2)}{\alpha_2\,(2\,a)\,\boldsymbol{\gamma}\cdot\underline{k}} + \underset{(3)}{\alpha_1\,(\underline{k}\cdot\underline{v}')\,\underline{k}} + \underset{(4)}{\alpha_2\,\underline{v}'}\Big] \tag{7.33}$$

where we have numbered the four terms in order to facilitate the discussion below. The quantities α_1 and α_2 are functions of the inter-particle spacing s, which in turn is a function of the local particle volume fraction. These functions are given as (Jenkins and McTigue, 1990; Torquato et al., 1990)

$$\alpha_1(s) = \frac{1}{4}\left(\frac{3}{2\,s} + \frac{7}{10}\ln\left(\frac{1}{2\,s}\right)\right) \quad ; \qquad \alpha_2(s) = \frac{1}{2}\ln\left(\frac{1}{2\,s}\right) \quad ; \tag{7.34}$$

$$s(\phi) = \frac{(1-\phi)^3}{12\,\phi\,(2-\phi)}$$

Next, we describe Jenkins and McTigue's approximation to the pair distribution function

$f^{(2)}$. We write the pair distribution function as the product of the number of particles per unit volume $n(\underline{r})$, the isotropic pair orientational distribution function $A(\underline{r}, \underline{k})$, and the normalized single particle distribution functions of each of the particles, as follows

$$f^{(2)} = n(\underline{r})\ A(\underline{r}, \underline{k})\ f_0^{(1)}(\underline{v}_1, \underline{r})\ f_0^{(1)}(\underline{v}_2, \underline{r} + (2\,a\,\underline{k})) \tag{7.35}$$

where $A(\underline{r}, \underline{k})$ is defined as the average number of nearest neighbors per unit solid angle, or $A(\underline{r}, \underline{k}) = A \sim 6 / 4\pi$. The two single particle distributions are defined as Maxwellian functions by Jenkins and McTigue, in the form

$$f_0^{(1)}{}_i = \frac{1}{(2\,\pi\,T)^{\frac{3}{2}}} \exp\left(-\frac{v_i'^2}{2\,T}\right) \quad ; \qquad i = 1 \text{ or } 2 \tag{7.36}$$

Here, in the derivation of Jenkins and McTigue, the suspension temperature T is a scalar quantity. In our modified derivation, in section 7.4.1.2, we will identify this scalar temperature with the trace of the temperature tensor.

As with the velocity in the force expression, we expand the single particle distribution function for particle 2 about the position $\underline{r} = \underline{r}_1$. This is a standard procedure for correcting the statistics of dense systems (Hirschfelder et al., 1954; Chapman and Cowling, 1970). Here, the scalar suspension temperature T is the only function of position. Jenkins and McTigue's expansion yields

$$f^{(2)}(\underline{r}, \underline{k}, \underline{v}_1, \underline{v}_2) = \frac{n(\underline{r})\,A(\underline{r}, \underline{k})}{(2\,\pi\,T)^3}\left[1 + \frac{1}{2\,T}\left(\frac{\underline{v}_2'^2}{T} - 3\right)(2\,a)\,(\underline{k}\cdot\underline{\nabla}\,T)\right] \exp\left(-\frac{v_1'^2 + v_2'^2}{2\,T}\right) \tag{7.37}$$

Substituting this expression along with the equation for the inter-particle force into the definition of the stress above results in an integral that can be solved for the stress tensor. An important simplification can be made immediately. Since the integral over $\underline{k}$, the pair orientation vector, is decoupled from the other integration, we consider it independently. Because the distribution of $\underline{k}$ is isotropic, integrals of odd numbers of $\underline{k}$'s will vanish (Bird et al., 1987). This means that all the terms in the integral that contain the second term in the pair distribution function will vanish. Consequently, the pair distribution function effectively reduces to

$$f^{(2)}(\underline{r}, \underline{k}, \underline{v}_1, \underline{v}_2) = \frac{n(\underline{r})\, A(\underline{r}, \underline{k})}{(2\,\pi\,T)^3} \exp\left(-\frac{v_1'^2 + v_2'^2}{2\,T}\right) \quad . \tag{7.38}$$

After integration, the stress tensor is divided into two parts:

$$\boldsymbol{\tau} = -\pi(\phi, T)\,\boldsymbol{\delta} + \eta_s(\phi)\,\boldsymbol{\gamma} \tag{7.39}$$

The terms (1) and (2) in the force expression lead to the mean viscous deviatoric stress, $\eta_s(\phi)\,\boldsymbol{\gamma}$. The terms (3) and (4) in the force expression lead to the particle contribution to the pressure. The pressure is an isotropic contribution to the stress whose magnitude is given by

$$\pi(\phi, T) = \frac{6}{\sqrt{\pi}} \frac{\phi}{(2\,a)} \eta_f \left(\alpha_1(\phi) + \alpha_2(\phi)\right) T^{\frac{1}{2}} \tag{7.40}$$

The particle pressure calculated here is the link between the suspension temperature and the macroscopic properties. The deviatoric, that is, non-isotropic, stress results from the mean deformation and does not involve velocity fluctuations at all. Accordingly, any change we make in the velocity distribution function, to incorporate anisotropic velocity fluctuations, has no impact on this part of the stress. Only the particle pressure would be affected by such a change.

An important question we wish to answer in modifying the velocity distribution function is whether the resulting stress contribution will be anisotropic. Gadala-Maria (1979) observed normal stress differences in parallel plate rheometry experiments. It is not known whether the anisotropic suspension temperature contributes to these normal stress differences.

7.4.1.2 Modification of the Stress Tensor Derivation to Include Anisotropic Temperature

We modified Jenkins and McTigue's single particle velocity distribution function by incorporating the anisotropic suspension temperature in the following way. We replaced the isotropic Maxwellian velocity distribution with an anisotropically weighted form, written as

$$f^{(1)}{}_i = \frac{1}{(2\,\pi)^{\frac{3}{2}}(T_{rr}\,T_{\theta\theta}\,T_{zz})^{\frac{1}{2}}} \exp\left(-\frac{v_{ir}'^2}{2\,T_{rr}} - \frac{v_{i\theta}'^2}{2\,T_{\theta\theta}} - \frac{v_{iz}'^2}{2\,T_{zz}}\right) \tag{7.41}$$

This function has a similar form to the distribution function in the Bird-DeAguiar anisotropic drag model for concentrated polymer solutions and melts. This latter model describes the relative ease for a long polymer molecule to move along its backbone as opposed to perpendicular to it (Bird et al., 1987).

Expanding $f^{(1)}_2$ linearly about position $\underline{r} = \underline{r}_1$, forming the pair distribution function again with the isotropic pair orientation distribution, and eliminating the terms odd in $\underline{k}$ that vanish produces the following result for the pressure integral

$$\pi(\phi, T) = \frac{1}{2}(2a)\pi(2a)\eta_f \int (\alpha_1(\phi) + \alpha_2(\phi)) \frac{n(\underline{r})\, A(\underline{r}, \underline{k})}{(2\pi)^3 (T_{rr} T_{\theta\theta} T_{zz})} (\underline{v}'_2 - \underline{v}'_1)\underline{k} \\ \exp\left(-\frac{(v'^2_{1r} + v'^2_{2r})}{2T_{rr}} - \frac{(v'^2_{1\theta} + v'^2_{2\theta})}{2T_{\theta\theta}} - \frac{(v'^2_{1z} + v'^2_{2z})}{2T_{zz}}\right) d\underline{k}\, d\underline{v}_1\, d\underline{v}_2 \tag{7.42}$$

Now, we change the variables of integration to $\underline{v}'_1$ and $\underline{v}'_2$. This is possible because the mean velocity is only a function of $\underline{r}$, which is not a variable of integration. Also, we transform the fluctuating velocity variables into the center of mass reference frame of the pair of particles as follows.

$$\underline{\overline{v}}' = \frac{1}{2}(\underline{v}'_1 + \underline{v}'_2) \qquad ; \qquad \underline{v}' = \underline{v}'_2 - \underline{v}'_1 \tag{7.43}$$

Accordingly, the pressure integral becomes

$$\pi(\phi, T) = \frac{1}{2}(2a)^2 \pi \eta_f \frac{n(\underline{r})\, A(\underline{r}, \underline{k})\, (\alpha_1(\phi) + \alpha_2(\phi))}{(2\pi)^3 (T_{rr} T_{\theta\theta} T_{zz})} \\ \int \underline{v}'\underline{k} \exp\left(-\frac{\overline{v}'^2_r}{T_{rr}} - \frac{\overline{v}'^2_\theta}{T_{\theta\theta}} - \frac{\overline{v}'^2_z}{T_{zz}} - \frac{v'^2_r}{4T_{rr}} - \frac{v'^2_\theta}{4T_{\theta\theta}} - \frac{v'^2_z}{4T_{zz}}\right) d\underline{k}\; 2\, d\underline{\overline{v}}'\, d\underline{v}' \tag{7.44}$$

First, we attempt integration in $\underline{k}$. If $\underline{k}$ and $\underline{v}'$ are independent, the integral will vanish, since it will be odd in $\underline{k}$. The only way for this integral to be nonzero is if we assume that all the relative velocity fluctuations $\underline{v}'$ are in the direction of the line of centers $\underline{k}$. We write this assumed relation as a delta function within the pair distribution function $A(\underline{r}, \underline{k})$, given as $A(\underline{r}, \underline{k}) = A(\underline{r})\, \delta\!\left(\underline{k} - \frac{\underline{v}'}{|\underline{v}'|}\right)$.

$$\pi(\phi, \mathbf{T}) = \frac{1}{2}(2\,a)^2\,\pi\,\eta_f\,\frac{n(\underline{r})\,A(\underline{r})\,(\alpha_1(\phi)+\alpha_2(\phi))}{(2\,\pi)^3\,(T_{rr}\,T_{\theta\theta}\,T_{zz})}$$
$$\int \underline{v}'\,\underline{k}\;\delta\!\left(\underline{k}-\frac{\underline{v}'}{|\underline{v}'|}\right)\exp\left(-\frac{\overline{v}_r^{2}}{T_{rr}}-\frac{\overline{v}_\theta^{2}}{T_{\theta\theta}}-\frac{\overline{v}_z^{2}}{T_{zz}}-\frac{v_r'^2}{4\,T_{rr}}-\frac{v_\theta'^2}{4\,T_{\theta\theta}}-\frac{v_z'^2}{4\,T_{zz}}\right)d\underline{k}\;2\,d\overline{\underline{v}}\;d\underline{v}' \tag{7.45}$$

Also, we limit the range of $\underline{v}'$ to only half of space, since we assume that only the approach part of the collision ($\underline{k}\cdot\underline{v}' < 0$) contributes to the particle pressure.

Next, we integrate in $\overline{\underline{v}}$, the average fluctuating velocity of the two particles. Isolating the factors in the integrand that depend on $\overline{\underline{v}}$ results in

$$\int \exp\left(-\frac{\overline{v}_r^{2}}{T_{rr}}-\frac{\overline{v}_\theta^{2}}{T_{\theta\theta}}-\frac{\overline{v}_z^{2}}{T_{zz}}\right)2\,d\overline{\underline{v}} = 2\int e^{-(\mathbf{T}^{-1}\,:\,\overline{\underline{v}}\,\overline{\underline{v}})}\;d\overline{\underline{v}} \tag{7.46}$$

This is just a tensor version of a standard Gaussian integral, and the solution appears in Bird et al. (1987),

$$2\int e^{-(\mathbf{T}^{-1}\,:\,\overline{\underline{v}}\,\overline{\underline{v}})}\;d\overline{\underline{v}} = 2\,\frac{\pi^{\frac{3}{2}}}{\sqrt{\det(\mathbf{T}^{-1})}} = 2\;\pi^{\frac{3}{2}}\,(T_{rr}\,T_{\theta\theta}\,T_{zz})^{\frac{1}{2}} \tag{7.47}$$

The remaining integral is over $\underline{v}'$, the difference between the particles' flucutating velocitites, and is given as

$$\pi(\phi, \mathbf{T}) = (2\,a)^2\,\pi^{\frac{5}{2}}\,\eta_f\,\frac{n(\underline{r})\,A\,(\alpha_1(\phi)+\alpha_2(\phi))}{(2\,\pi)^3\,(T_{rr}\,T_{\theta\theta}\,T_{zz})^{\frac{1}{2}}}\int \frac{\underline{v}'\,\underline{v}'}{|\underline{v}'|}\;e^{-\left(\frac{1}{4}\mathbf{T}^{-1}\,:\,\underline{v}'\underline{v}'\right)}\;d\underline{v}' \tag{7.48}$$

This integral is difficult to solve, because it is odd in $|\underline{v}'|$, and is a tensor. Note that the integral only has three nonzero, diagonal tensor components. The off-diagonal terms are odd in the components of $\underline{v}'$, and vanish. We solve the integral by writing out each of the components,

$$\pi_{ii}(\phi, \mathbf{T}) = (2\,a)^2\,\pi^{\frac{5}{2}}\,\eta_f\,\frac{n(\underline{r})\,A\,(\alpha_1(\phi)+\alpha_2(\phi))}{(2\,\pi)^3\,(T_{rr}\,T_{\theta\theta}\,T_{zz})^{\frac{1}{2}}}\int \frac{v_i'^2}{|\underline{v}'|}\;e^{-\left(\frac{v_r'^2}{4T_{rr}}+\frac{v_\theta'^2}{4T_{\theta\theta}}+\frac{v_z'^2}{4T_{zz}}\right)}\;d\underline{v}' \tag{7.49}$$

where i = r, θ, z. We transform the integral into spherical coordinates, choosing the physical r axis as the polar axis (since it corresponds to the smallest temperature component). We make several assumptions based on the relative sizes of the suspension temperature components that make the integration possible. The rest of the integration is carried out with the aid of comprehensive integral tables (Abramowitz and Stegun, 1965; Gradshteyn and Ryzhik, 1965).

The pressure term was an isotropic tensor. Accordingly, it could be characterized by a single scalar π. With anisotropic suspension temperature, the pressure loses isotropy. Therefore, it must be described by an anisotropic tensor, which is symmetric according to the definition of the pressure in equation (7.48). In the cylindrical coordinate system of the flow, the tensor is diagonal, and its eigenvalues are given as

$$\pi_{rr}(\phi, T) = \frac{1}{2\pi^2}\,\frac{6\phi}{(2a)}\,\eta_f\big(\alpha_1(\phi) + \alpha_2(\phi)\big)\,\frac{T_{rr}^{\frac{3}{2}}}{(T_{\theta\theta}T_{zz})^{\frac{1}{2}}}\left[1 + \frac{2}{5}z + \frac{9}{35}z^2 + \frac{4}{21}z^3 + \dots\right] \tag{7.50}$$

where $z \equiv \dfrac{T_{rr}}{T_{zz}}$. Also,

$$\pi_{zz}(\phi, T) = \pi_{\theta\theta}(\phi, T) = \pi_{rr}(\phi, T)\left\{1 - \frac{4}{5}\,\frac{z}{1-z}\,\frac{\left[1 + \frac{2}{7}z + \frac{1}{7}z^2 + \frac{20}{231}z^3 + \dots\right]}{\left[1 + \frac{2}{5}z + \frac{9}{35}z^2 + \frac{4}{21}z^3 + \dots\right]}\right\} \tag{7.51}$$

For a value of $z = 1/3$, typically observed in a 50% concentrated suspension, the expressions for the stress components in (7.50) and (7.51) are well-approximated by

$$\pi_{rr}(\phi, T) \cong \frac{1\,[1.16]}{2\pi^2}\,\frac{6\phi}{(2a)}\,\eta_f\big(\alpha_1(\phi) + \alpha_2(\phi)\big)\,\frac{T_{rr}^{\frac{3}{2}}}{(T_{\theta\theta}T_{zz})^{\frac{1}{2}}} \tag{7.50a}$$

$$\pi_{zz}(\phi, T) = \pi_{\theta\theta}(\phi, T) \cong \pi_{rr}(\phi, T)\left\{1 - \frac{4}{5}\,\frac{z}{1-z}\right\} \cong \frac{3}{5}\,\pi_{rr}(\phi, T) \tag{7.51a}$$

The equal and opposite normal stress differences, $N_1 \equiv (-\pi_{\theta\theta}) - (-\pi_{rr}) > 0$ and $N_2 \equiv (-\pi_{rr}) - (-\pi_{zz}) < 0$, where the stresses are positive in tension, have signs that indicate an extra compression in the gradient direction and agree with observations in the literature. Gadala-Maria (1979) found in parallel plate rheometry experiments that $(N_1 - N_2) > 0$. Also, Phung (1996) calculated in 3-D Stokesian Dynamics simulations for a Brownian suspension that at the highest Peclet number computed, $Pe = 10^5$, $N_1 > 0$ and $N_2 < 0$. In addition, the normal stress differences reduce to the expected scaling of proportionality to the shear rate, if we assume all the suspension temperature components scale with the shear rate squared. Unfortunately, the normal stress differences we derived have negligible size, being smaller than the shear stress by a factor of about 1000, when we use the observed values of T_{ii} from the 50% concentrated suspension.

We also applied the anisotropic single particle velocity distribution function to the fluctuation kinetic energy conservation equation. Although we write the anisotropic suspension temperature as a tensor, the conserved quantity is the total kinetic energy contained in the velocity fluctuations; and this scalar quantity is still the sum of the three diagonal components (or the trace of **T**), as defined in the original models. Hence a scalar equation for its rate of change is appropriate. We applied the anisotropic single particle velocity distribution function to the constitutive relations in the fluctuation kinetic energy equation, including those for the fluctuation energy flux and the dissipation. We found that because all the macroscopic terms we computed depended on even functions of the fluctuating velocity, the new distribution function had no effect on the constitutive relations.

7.4.2 Including Rotational Dynamics of Particle Interactions

Another step in forming an anisotropic model is understanding how the dynamics of particle interactions affect the fluctuation kinetic energy conservation equation and cause the suspension temperature components to have the relative sizes we observe. Buyevich (1996) uses a simple geometric argument to estimate the paths of particles during a collision, which leads to an estimate of the relative sizes of the temperature components. We take the next step by computing an estimate of the magnitudes of the temperature components based on actual paths that particles take during a collision in a dilute suspension, according to the results of Okagawa et al. (1973), Brenner (1974), and Arp and Mason (1977a,b). We also utilize conservation of angular momentum and semi-dilute collision dynamics to calculate an additional rate of working term in the fluctuation energy conservation equation that acts as a source of neutral and gradient direction fluctuations at flow startup.

The picture of a binary particle collision that Arp and Mason (1977b) describe is very similar to the video image snapshots in figures 4.2 and 4.3. As the particles approach each other, typically along the compression direction of the shear flow, they translate with the mean velocity associated with their streamlines and rotate about the neutral direction (z) axis with the mean vorticity of the flow ($\omega = \frac{1}{2}\gamma$). The particles squeeze the fluid in the gap between them until the gap becomes arbitrarily thin, but the particles do not recoil. By conservation of linear momentum, the two joined particles act as one body translating at the average of their initial velocities.

In addition, angular momentum must be conserved during the collision because there are no external torques acting on that time scale. According to the experimental data of Arp and Mason, the two joined particles do not rotate relative to each other, and form a rigid doublet that rotates about the contact point between the particles at a new angular velocity. Although angular momentum is conserved, the moment of inertia has changed. We can calculate this instantaneous doublet angular velocity by equating the initial and final angular momentum. Initially, the particles each have angular momentum about the z axis from spinning at the mean flow vorticity. The particles also have angular momentum about the z axis from their linear translational motion about the center of mass of the pair. If the particles colliding were not in the same plane, they would also have angular momentum about the r-axis from their linear translational motion about the center of mass. When the particles form the rigid doublet, it instantly rotates at this new angular velocity. However, the net velocity of each particle in the doublet is different from that of the surrounding fluid. The suspending fluid exerts a torque on the doublet to make it rotate faster until each particle moves with the surrounding fluid. Since the particles are assumed to be inertialess, the torque acts instantly so that the doublet rotates at a constant, final angular velocity until it points along the extension axis of the shear flow. Then, the suspending fluid drags on the particles and separates them.

7.4.2.1 Estimate of the Relative Sizes of the Suspension Temperature Components

In a dilute suspension, the rotating doublet follows the trajectory of Okagawa et al. (1973) and Brenner (1974). We estimate the relative sizes of the suspension temperature components based on the actual paths that particles take during a collision in a dilute suspension, according to the derived trajectories above and experimental results of Arp and Mason (1977b). We estimate the velocity fluctuation in each direction with the product of the sphere radius (assuming uniform density) and the difference between the initial and the maximum or minimum values in the component of the angular velocity in that direction. We use the expressions of Okagawa et al. (1973) for the components of the angular velocity of the doublet.

$$\frac{d\Theta}{dt} = \frac{\gamma\left(r_e^{D2} - 1\right)}{4\left(r_e^{D2} + 1\right)} \sin 2\Theta \sin 2\varphi \; ; \qquad \frac{d\varphi}{dt} = \frac{\gamma}{\left(r_e^{D2} + 1\right)}\left(r_e^{D2} \cos^2\varphi + \sin^2\varphi\right) \quad , \tag{7.52}$$

$$\text{where } \tan\Theta = \tan\Theta_0 \frac{\left(r_e^{D2} \cos^2\varphi_0 + \sin^2\varphi_0\right)^{\frac{1}{2}}}{\left(r_e^{D2} \cos^2\varphi + \sin^2\varphi\right)^{\frac{1}{2}}} \tag{7.53}$$

and where r_e^D is the equivalent spheroidal axis ratio of the doublet (Arp and Mason, 1977a). r_e^D approaches a value of 1.9817 in the limit of osculating spheres. The angles (Θ, φ) describing the doublet orientation are defined in figure 7.1. (Θ_0 , φ_0) are the angles at which the particles initially contact each other.

Then, taking the components of these trajectories along the cylindrical coordinates of the Couette device in the laboratory reference frame gives

$$\begin{aligned} v'^2_{r,\,rot} &= a^2\left[(\underline{\omega}\cdot\underline{\delta}_r)_{min} - (\underline{\omega}\cdot\underline{\delta}_r)_0\right]^2 = a^2\left[\omega_r(\varphi{=}0) - \omega_r(\varphi{=}\varphi_0)\right]^2 \\ &= a^2\left[(\dot{\phi}\sin\Theta\sin\varphi)_{\varphi=0} - (\dot{\phi}\sin\Theta\sin\varphi)_{\varphi_0} + (\dot{\Theta}\sin\Theta\cos\varphi)_{\varphi=0} - (\dot{\Theta}\sin\Theta\cos\varphi)_{\varphi_0}\right]^2 \end{aligned} \tag{7.54}$$

$$v'^2_{z\ rot} = a^2\left[(\underline{\omega}\cdot\underline{\delta}_z)_{min} - (\underline{\omega}\cdot\underline{\delta}_z)_0\right]^2 = a^2\left[\omega_z(\varphi{=}0) - \omega_z(\varphi{=}\varphi_0)\right]^2 = a^2\left[(\dot{\Theta}\cos\Theta)_{\varphi=0} - (\dot{\Theta}\cos\Theta)_{\varphi_0}\right]^2 \tag{7.55}$$

$$\begin{aligned} v'^2_{\theta,\,rot} &= a^2\left[(\underline{\omega}\cdot\underline{\delta}_\theta)_{max} - (\underline{\omega}\cdot\underline{\delta}_\theta)_0\right]^2 = a^2\left[\omega_\theta(\varphi{=}0) - \omega_\theta(\varphi{=}\varphi_0)\right]^2 \\ &= a^2\left[(\phi\sin\Theta\cos\varphi)_{\varphi=0} - (\phi\sin\Theta\cos\varphi)_{\varphi_0}\right]^2 \end{aligned} \tag{7.56}$$

Here, the doublet angular velocity at different angles depends on the initial angles (Θ_0, φ_0) of contact.

In order to form an overall estimate of the velocity fluctuations in each direction, we substitute the expressions above for the rates of change of Θ and φ into the velocity fluctuation expressions and average the expressions over all possible initial contact angles $\Theta_0 = [0, \pi]$; $\varphi_0 = \left[-\frac{\pi}{2}, 0\right]$, assuming that all initial contact angles in the possible range are equally likely. The choice of this constant probability distribution function is based on the

a) Top view

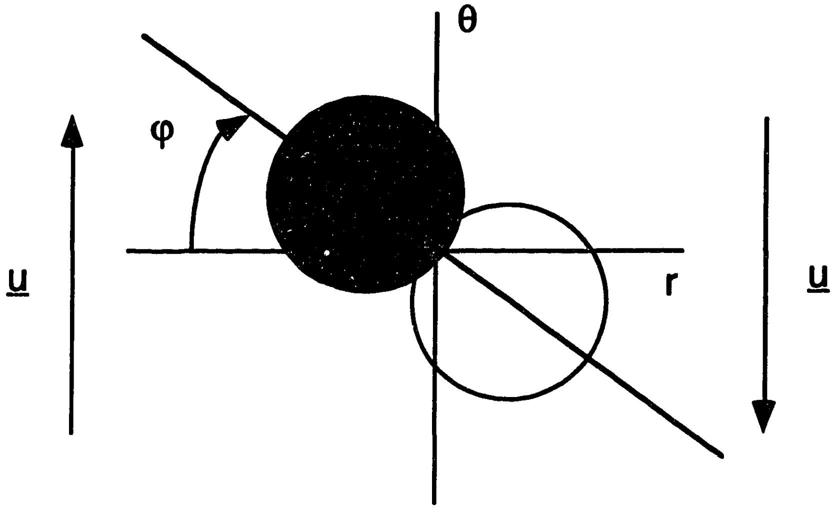

b) Side view

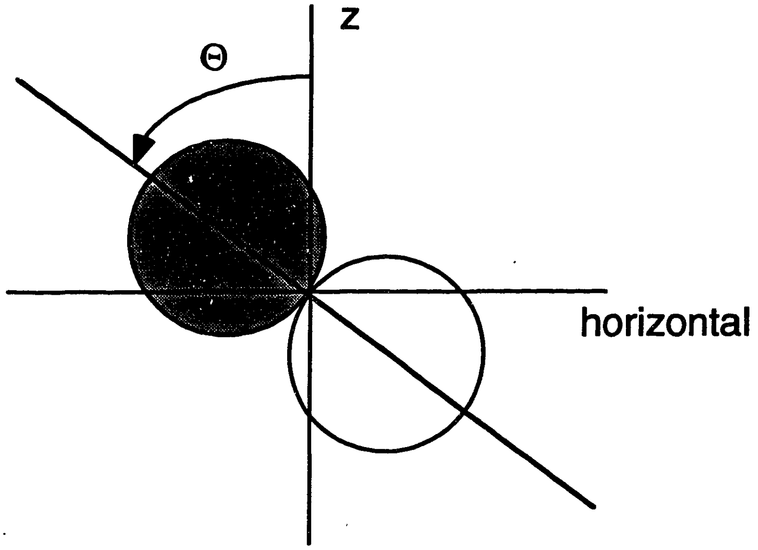

Figure 7.1 Definition of angles φ and Θ describing the orientation of a particle doublet in the reference frame of the center of mass of the two particles. The mean velocity of the shear flow is indicated by u̲. The top view (a) and side view (b) indicate the relation of φ and Θ to the cylindrical coordinate axes of the Couette device in the laboratory reference frame.

observations of Leighton and Rampall (1993). These authors found that the probability of observing a pair of particles at contact was roughly constant for azimuthal contact angles φ_0 in the compression quadrant and a much smaller value for azimuthal angles in the extension quadrant. Due to the kinematics of the unidirectional shear flow, it is aphysical for the particles to approach each other in the extension direction; hence, the angles $\varphi_0 = \left[0, \frac{\pi}{2}\right]$ in the extension quadrant are not included in the calculation of the average velocity fluctuations. Consequently, we assume an isotropic distribution of initial azimuthal contact angles in the compression quadrant $\varphi_0 = \left[-\frac{\pi}{2}, 0\right]$ and we average only over these angles. In addition, since data regarding the distribution of initial polar angles Θ_0 does not exist, we assume an isotropic distribution of initial polar angles. We were able to write analytical expressions for all the averages except the average over angle φ_0 for $v'^2_{\theta\ \mathrm{rot}}$, which was numerically integrated.

$$\left\langle v'^2_{r,\mathrm{rot}} \right\rangle = \frac{a^2\dot{\gamma}^2}{\left(r_e^{D2}+1\right)^2}\,\frac{2}{\pi}\int_{\Theta_0=0}^{\frac{\pi}{2}} \sin\Theta_0\,d\Theta_0 \int_{\varphi=-\frac{\pi}{2}}^{0} d\varphi_0$$
$$\left[\left(r_e^{D2}\cos^2\varphi_0+\sin^2\varphi_0\right)\sin\Theta_0\sin\varphi_0+\frac{\left(r_e^{D2}-1\right)}{4}\sin(2\Theta_0)\sin\Theta_0\sin(2\varphi_0)\cos\varphi_0\right]^2 \tag{7.57}$$

$$\left\langle v'^2_{z,\mathrm{rot}} \right\rangle = \frac{a^2\dot{\gamma}^2}{16}\,\frac{\left(r_e^{D2}-1\right)^2}{\left(r_e^{D2}+1\right)^2}\,\frac{2}{\pi}\int_{\Theta_0=0}^{\frac{\pi}{2}} \sin^2(2\Theta_0)\cos^2\Theta_0\sin\Theta_0\,d\Theta_0 \int_{\varphi=-\frac{\pi}{2}}^{0} \sin^2(2\varphi_0)\,d\varphi_0 \tag{7.58}$$

$$\left\langle v'^2_{\theta,\mathrm{rot}} \right\rangle = \frac{a^2\dot{\gamma}^2}{\left(r_e^{D2}+1\right)^2}\,\frac{2}{\pi}\int_{\Theta_0=0}^{\frac{\pi}{2}} \sin\Theta_0\,d\Theta_0 \int_{\varphi=-\frac{\pi}{2}}^{0} d\varphi_0$$
$$\left[r_e^{D2}\frac{C}{\sqrt{1+C^2}}-\left(r_e^{D2}\cos^2\varphi_0+\sin^2\varphi_0\right)\sin\Theta_0\cos\varphi_0\right]^2 \tag{7.59}$$

where the function C has the value $C = \tan\Theta_0\left[\frac{\left(r_e^{D2}\cos^2\varphi_0+\sin^2\varphi_0\right)}{r_e^{D2}}\right]^{\frac{1}{2}}$.

There is also a translational contribution to the estimated tangential velocity fluctuation, due to the particles exchanging linear momentum in a collision.

$$v'^2_{\theta,\mathrm{trans}} = \left[\frac{1}{2}\left(\underline{v}_2-\underline{v}_1\right)\right]^2 = \left[\frac{1}{2}\left(\dot{\gamma}\left(\underline{r}_2-\underline{r}_1\right)\cdot\underline{\delta}_r\right)\right]^2 = \left[a\,\dot{\gamma}\sin\Theta_0\cos\varphi_0\right]^2 \tag{7.60}$$

$$\langle v'^2_{\theta,\,\mathrm{trans}} \rangle = a^2 \gamma^2 \, \frac{2}{\pi} \int_{\Theta_0 = 0}^{\frac{\pi}{2}} \sin^2\Theta_0 \sin\Theta_0 \, d\Theta_0 \int_{\varphi = -\frac{\pi}{2}}^{0} \cos^2\varphi_0 \, d\varphi_0 = \frac{1}{3} a^2 \gamma^2 \qquad (7.61)$$

The resulting average values of the estimated velocity fluctuation components are

$$\langle v'^2_{r\ \mathrm{rot}} \rangle \cong 0.065\, a^2 \gamma^2 \; ; \quad \langle v'^2_{\theta\ \mathrm{rot+trans}} \rangle \cong (0.154 + 1/3)\, a^2 \gamma^2 \quad ; \quad \langle v'^2_{z\ \mathrm{rot}} \rangle \cong 0.0025\, a^2 \gamma^2 \qquad (7.62)$$

One important feature of this estimate is that it predicts a nonzero velocity fluctuation in the neutral (vertical) direction. The reason is that if two particles interact in an "out-of-plane" collision, where they are not initially in the same vertical plane, the doublet they form will rotate about an axis perpendicular to the long doublet axis. This rotation axis is oblique to the horizontal plane, so the rotation about the axis involves some up-and-down vertical motion of the particles. This vertical motion during the collision constitutes a vertical velocity fluctuation. If particles were only imagined to interact with neighbors in their own planes, no vertical velocity fluctuations would be predicted.

The velocity fluctuation components estimated in this way are all smaller than the components we observe. Of the three components estimated, the tangential component is the largest, followed by the radial component. The vertical component is much smaller than the others. This agrees with our observation that the tangential component is the largest, but disagrees with our observation that the radial component is the smallest. All the components of the fluctuating velocity scale with $a^2 \gamma^2$, just as in the suspension temperature models.

There are several likely explanations for the discrepancy between the semi-dilute calculation and the data from the concentrated suspensions. First, in a concentrated suspension, collisions are more frequent and of shorter duration than in the semi-dilute case. Also, the distribution of initial polar contact angles Θ_0 may be anisotropic, leading to some initial particle pair orientations in the compression quadrant being favored over others. Finally, the particles in the doublet may follow different trajectories in the concentrated suspension.

7.4.2.2 Rate of Suspending Fluid Working on a Doublet

When the suspending fluid exerts a torque on the rigid doublet, it is doing work on the doublet to make it rotate faster. The rate of working is equal to the product of the torque and the angular velocity. This is a change in the fluctuating (not the mean) kinetic energy of the particle pair, and therefore should be included in the fluctuation energy conservation equation. The work done by the suspending fluid to rotate the doublet is the source for particle velocity fluctuations in the neutral and gradient directions at flow startup in the fluctuation energy conservation equation. Without this contribution, there is no mechanism for fluctuations to arise in any direction other than the flow direction. Recall that fluctuations in the flow direction are fed by viscous dissipation from the mean flow.

Based on the conservation of angular momentum described above and the known flow field, we estimate the average rate of work done on the doublet per unit volume as

$$\frac{\dot{W}}{\mathrm{vol}} \cong \frac{15}{7}\,\eta_f\,\dot{\gamma}^2\,\phi = \frac{15}{7}\,\eta_f\,\Omega^2\,\tilde{\dot{\gamma}}^2\,\phi. \qquad (7.63)$$

Since this term represents a positive rate of change of the fluctuation kinetic energy, we add it to the right side of the fluctuation energy equation. Just as in the section above, we may have underestimated this term for a concentrated suspension, where the averaging statistics and particle volume fraction dependence are likely to be different from those in this semi-dilute approximation.

7.4.3 Combining the Anisotropic Stress and Doublet Rate of Working with the Nott and Brady Model

Once we have written new constitutive relations for the stress tensor and for the rate of the suspending fluid working on a rotating doublet, we incorporate these expressions into the Nott and Brady model. We then solve the Couette flow problem to determine how the predictions of the model are altered. The main features distinguishing this new model from the original Nott and Brady model are the replacement of the isotropic pressure tensor with an anisotropic, symmetric tensor, and the addition of the contribution of the rate of working due to the suspending fluid acting on a rotating doublet to the conservation of fluctuation kinetic energy equation. We chose to modify the Nott and Brady model because its predictions match neither the measured sum of the suspension temperature components nor the sum of the two smaller temperature components. For this model, it will be clear whether the modifications described here improve the accuracy of its predictions.

First, we solve the radial momentum equation in the Nott and Brady model, including the normal stress difference N_1. In chapter 5, equation (5.63) set the particle phase pressure contribution constant across the gap. Here, the radial component of the momentum equation has another term added to it and is now written as

$$0 = \frac{\partial}{\partial r}\{-\pi_{rr}\} + \frac{(-\pi_{rr}) - (-\pi_{\theta\theta})}{r} \tag{7.64}$$

Then,

$$\frac{d}{dr}\pi_{rr} = \frac{\pi_{\theta\theta} - \pi_{rr}}{r} = \left\{ -\frac{4}{5}\,\frac{z}{1-z}\,\frac{\left[1 + \frac{2}{7}z + \frac{1}{7}z^2 + \frac{20}{231}z^3 + \ldots\right]}{\left[1 + \frac{2}{5}z + \frac{9}{35}z^2 + \frac{4}{21}z^3 + \ldots\right]} \right\} \frac{\pi_{rr}}{r} \quad , \tag{7.65}$$

where $z \equiv \frac{T_{rr}}{T_{zz}}$. We also identify the factor in curly braces as

$$F \equiv \left\{ \frac{4}{5}\,\frac{z}{1-z}\,\frac{\left[1 + \frac{2}{7}z + \frac{1}{7}z^2 + \frac{20}{231}z^3 + \ldots\right]}{\left[1 + \frac{2}{5}z + \frac{9}{35}z^2 + \frac{4}{21}z^3 + \ldots\right]} \right\} \tag{7.66}$$

If we assume z = constant, which is reasonable since z ranges only from approximately 1/8 to 1/2 in the suspension observations, then the solution is

$$\pi_{rr} = p_2 r^{-F} + p_0 \tag{7.67}$$

Since p_0 is an arbitrary constant, we set it to zero.

Also, from our anisotropic version of the Jenkins and McTigue (1990) model, given in equation (7.50), we find that

$$\pi_{rr}(\phi, T) = \frac{1}{2\pi^2}\,\frac{6\eta_f}{(2a)}\left[\phi\left(\alpha_1(\phi) + \alpha_2(\phi)\right)\right]\,\frac{T_{rr}^{\frac{3}{2}}}{(T_{\theta\theta}T_{zz})^{\frac{1}{2}}}\left[1 + \frac{2}{5}z + \frac{9}{35}z^2 + \frac{4}{21}z^3 + \ldots\right] \tag{7.68}$$

In order to simplify this expression, we assume the suspension temperature components all have the same dependence on radial position, that is

$$T_{ii} \equiv A_{ii}\,T(r) \tag{7.69}$$

where the A_{ii}, for i = r,θ,z (with no summation implied), are constants, and T contains the radial dependence of all the components. The A_{ii} actually depend on the particle volume fraction, but we treat them as constant for a single concentration of $\phi = 0.5$.

Then, equating the two expressions above (7.67 and 7.68) for the radial normal stress yields

$$\frac{1}{2\pi^2}\,\frac{6\eta_f}{(2a)}[p(\phi)]\,\frac{A_{rr}^{\frac{3}{2}}}{(A_{\theta\theta}A_{zz})^{\frac{1}{2}}}\,T^{\frac{1}{2}}\left[1+\frac{2}{5}z+\frac{9}{35}z^2+\frac{4}{21}z^3+\ldots\right] = p_2\,r^{-F} \tag{7.70}$$

where we have identified

$$p(\phi) = [\phi\,(\alpha_1(\phi)+\alpha_2(\phi))] \tag{7.71}$$

Defining a new dimensionless constant,

$$\tilde{p}_3 \equiv \frac{3}{2\pi^2}\,\frac{A_{rr}^{\frac{3}{2}}}{(A_{\theta\theta}A_{zz})^{\frac{1}{2}}}\left[1+\frac{2}{5}z+\frac{9}{35}z^2+\frac{4}{21}z^3+\ldots\right] \tag{7.72}$$

setting

$$p_2 = \eta_f\,\Omega\,R_0{}^F\,\tilde{p}_2 \tag{7.73}$$

and then nondimensionalizing the equation (7.70) above results in

$$\tilde{T} = \frac{\tilde{p}_2{}^2}{\tilde{p}_3{}^2}\,\frac{\tilde{r}^{-2F}}{[p(\phi)]^2} \tag{7.74}$$

Turning to the reduced fluctuation energy equation (5.81) and adding the new doublet rate of working term produces

$$\tilde{T} = \frac{\left(\eta_p(\phi)+\frac{15}{7}\phi\right)}{\alpha(\phi)}\left[\frac{1}{\left(\displaystyle\int_k^1 \frac{1}{\tilde{r}^3\,\eta_s(\phi)}\,d\tilde{r}\right)}\right]^2\left(\frac{1}{\eta_s^2(\phi)\,\tilde{r}^4}\right) \tag{7.75}$$

Substituting for $\tilde{T}$ from the modified radial momentum equation (7.74) leads to

$$\frac{\tilde{p}_2{}^2}{\tilde{p}_3{}^2}\,\frac{\tilde{r}^{-2F}}{[p(\phi)]^2} = \frac{\left(\eta_p(\phi)+\frac{15}{7}\phi\right)}{\alpha(\phi)}\left[\frac{1}{\left(\displaystyle\int_k^1 \frac{1}{\tilde{r}^3\,\eta_s(\phi)}\,d\tilde{r}\right)}\right]^2\left(\frac{1}{\eta_s^2(\phi)\,\tilde{r}^4}\right) \tag{7.76}$$

and rearranging the terms yields

$$\tilde{r}^{4-2F} = \tilde{p}'^{2}_{2} \, \frac{\left(\eta_p(\phi) + \frac{15}{7}\phi\right)}{\alpha(\phi)} \, \frac{[p(\phi)]^2}{[\eta(\phi)]^2} \tag{7.77}$$

Here we have defined a new dimensionless constant

$$\tilde{p}'^{2}_{2} \equiv \left[\frac{1}{\left(\int_k^1 \frac{1}{\tilde{r}^3 \eta_s(\phi)} \, d\tilde{r} \right)} \right]^2 \frac{\tilde{p}_3^{2}}{\tilde{p}_2^{2}} \tag{7.78}$$

Equation (7.77) gives the new expression for the dimensionless radius as a function of particle volume fraction for the anisotropically modified Nott and Brady model. Below we use all the same functions of particle volume fraction as before, in order to determine the impact of the normal stress difference N_1 and the additional doublet rate of working term.

7.4.4 Comparison of the Anisotropically Modified Nott and Brady Model Predictions with the Original Model Predictions and the Experimental Data

We compute the predictions of the anisotropically modified Nott and Brady model for shear rate and scalar suspension temperature T profiles in narrow gap Couette flow, using the same approximation in the fluctuation kinetic energy equation as in section 5.3.4. We find that the original and modified models yield identical predictions for the shear rate, a macroscopic property. For the sum of the suspension temperature components, the models give only slightly different predictions. These comparisons are shown in figure 7.2. The original and modified Nott and Brady models are also compared to the experimentally observed trace of the suspension temperature components in figure 7.3.

Consequently, allowing the temperature to be anisotropic in the single particle distribution function alone does not account for the discrepancies between the original model predictions and our observations. It seems likely that an anisotropic pair orientation distribution function, which has been measured in shear flow (Leighton and Rampall, 1993), plays a major role, with an anisotropic temperature possibly feeding into it, such that the velocity fluctuation size in a given direction affects the probability of encountering a neighbor at a given distance in that direction.

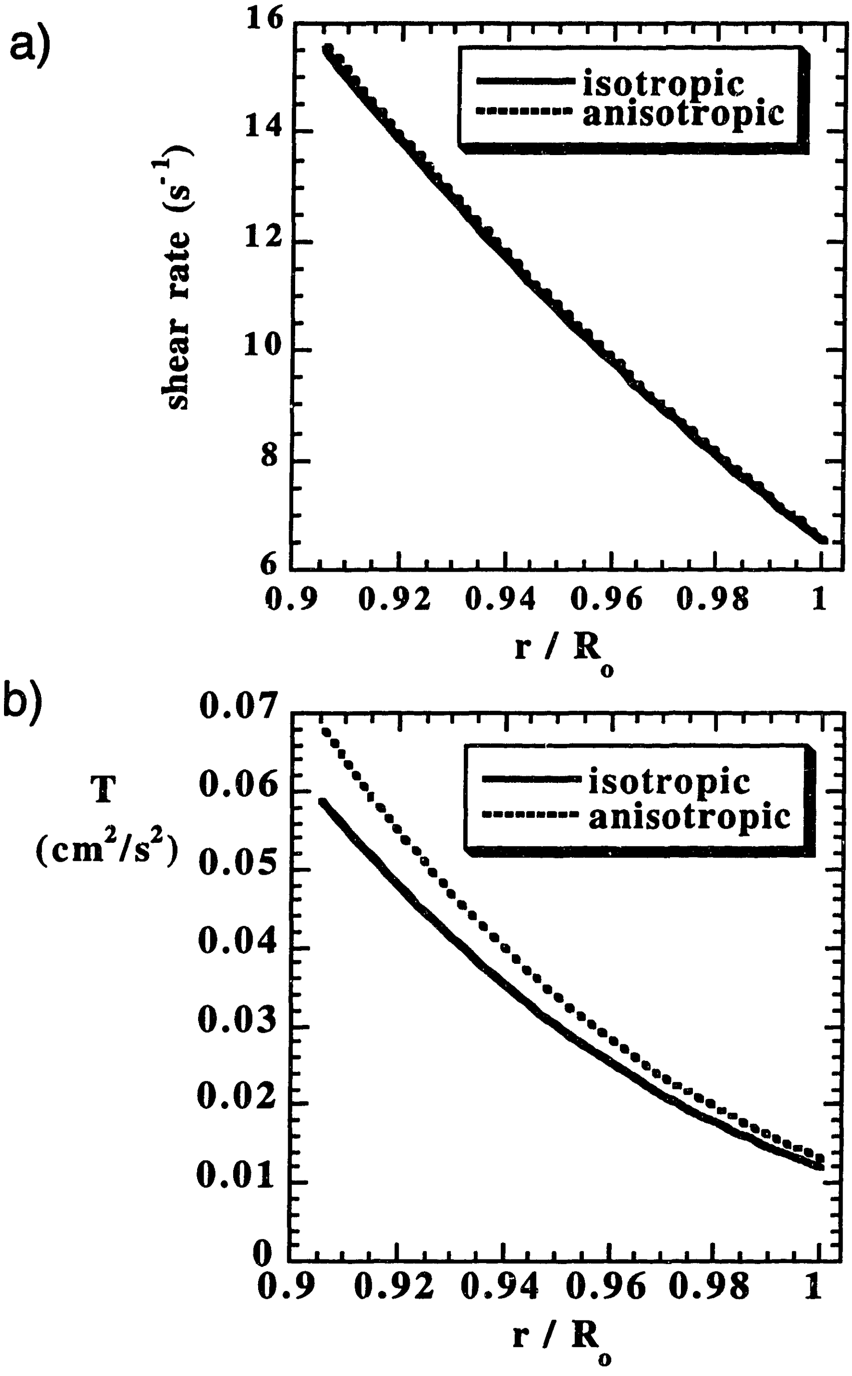

Figure 7.2 Comparison of the anisotropically modified Nott and Brady model predictions with those of the original Nott and Brady model (1994) for a 50% particle volume fraction suspension at an average shear rate of 10 s^{-1} (10 rpm).

a) Shear rate profile
b) Scalar suspension temperature profile

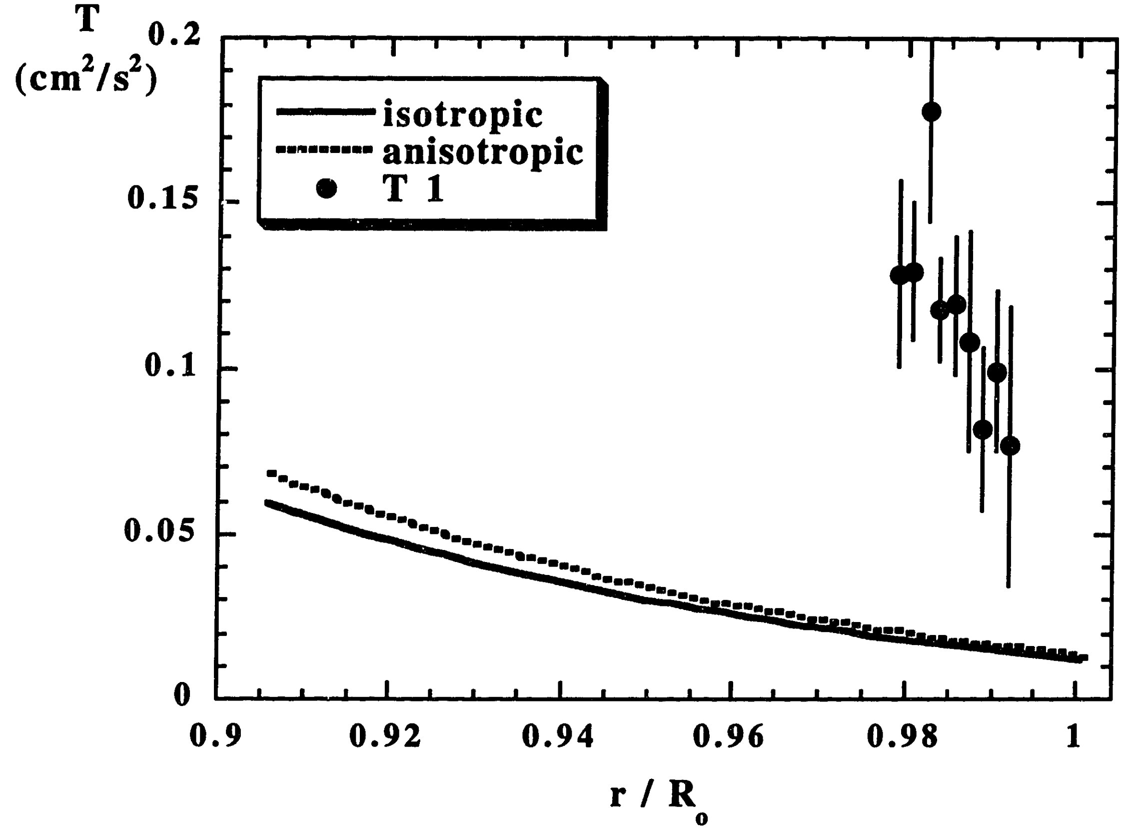

Figure 7.3 Comparison of the anisotropically modified Nott and Brady model predictions with those of the original Nott and Brady model (1994) and with experimental measurements of the tangential (flow, or 1 direction) suspension temperature component, for a 50% particle volume fraction suspension at an average shear rate of 10 s^{-1} (10 rpm). The anisotropic modification shifts the Nott and Brady prediction only slightly toward the observed values.

Chapter 8

Conclusions

This thesis reports a set of physical observations of particle velocity fluctuations from inter-particle collisions in a nearly homogeneous shear flow of a concentrated non-colloidal suspension. We compared the relative sizes of the fluctuating velocity components and observed the variation of each component with particle volume fraction, shear rate, and radial position. In addition, we studied the implications of these observations for suspension temperature models. Finally, we attempted to account for the discrepancies between the suspension temperature model predictions and our observations by incorporating an anisotropic suspension temperature tensor into the temperature models.

One of the objectives of this research was to determine experimentally whether the suspension temperature is anisotropic, since the McTigue and Jenkins (1992), Nott and Brady (1994), and Morris and Brady (1998) models all assume that the suspension temperature is isotropic. It is demonstrated clearly in figures 4.24-4.29 that the suspension temperature components at an average shear rate of 10 s^{-1} (10 rpm) all have different sizes, for the 30%, 40% and 50% concentrated suspensions that we measured. The tangential (flow) component is overwhelmingly the largest at every concentration, followed by the vertical (neutral) and then the radial (gradient) components. The ratio between the average tangential and vertical components in these plots ranges from about 50 to 120. The ratio between the average vertical and radial components lies in the range of 3 to 8. These ratios are significant factors that cause the suspension temperature to be extremely anisotropic. The maximum anisotropy occurs near 30% particle volume fraction.

Furthermore, we find that the velocity fluctuation components increase in size from low particle volume fraction to about 30-40% particle volume fraction, and then decrease at higher concentrations, as demonstrated in figures 4.27-4.29. In contrast, all the suspension temperature models predict the suspension temperature to be monotonically increasing with concentration, as illustrated in figure 5.1. A $T(\phi)$ curve with the shape we observe already exists in the literature, in the work of Nicolai et al. (1995) on settling suspensions. The authors attribute the decreasing velocity fluctuations at high particle volume fractions to particle cluster formation. We offer a different interpretation of the shape of the $T_i(\phi)$ plot in shear flow as the indication of a competition between decreasing mean free path and increasing collision frequency, as particle volume fraction increases.

Meanwhile, each fluctuating velocity component has a distinct variation with the shear rate, as is apparent in figures 4.33-4.35. This means that not all the components scale quadratically in the shear rate, as the temperature models assume because of the definition of the suspension temperature. As discussed in chapter 4, only the tangential component for the 30% and 40% concentrated suspensions exhibits quadratic behavior. For the tangential component at these two concentrations, the models' assumed scaling is correct. In contrast, the measured radial component is nearly independent of the shear rate, and the vertical component displays a more complex scaling that is closer to a square root than a quadratic. Also, the tangential temperature component for the 50% concentrated suspension appears to have a scaling in between quadratic and the scaling of the vertical component.

In comparing the measured profiles of the field variables to those predicted by the suspension models, we began with macroscopic variables, such as the shear rate and particle volume fraction, and then examined the sum of the suspension temperature components. It is apparent in comparison graphs at three bulk particle volume fractions that the Phillips, Nott and Brady, and Buyevich models capture qualitatively the approximate range and average slope of the shear rate profiles. However, none of the models captures the slightly curved shape of the experimental three-region-fit shear rate profiles. This is especially noticeable for the 50% concentrated suspension, which has the largest slope and the most curvature in the shear rate profile. It is also noticeable that the model predictions diverge from each other increasingly with particle concentration, since the differences in their coefficients which are functions of concentration become significant there.

Turning to the particle volume fraction profile, almost all the models in figure 6.4 capture the average slope of the experimental three-region-fit profile for a 30% concentrated suspension. As the concentration increases to 40% and 50% in figures 6.5 and 6.6, the model predictions separate and agree poorly with the data. This is true especially in the case of the 50% concentrated suspension profile, which again has the most curvature. Among the models, as before, the Phillips, Nott and Brady, and Buyevich models capture best the approximate size and slope of the particle volume fraction profiles. Overall, the trend we observe is that the models tend to capture the behavior of moderately concentrated suspensions like the 30% concentrated suspension better than that of highly concentrated suspensions like the 50% concentrated suspension.

Finally, in comparing the predicted scalar suspension temperature profiles to the sum of the measured velocity fluctuation components, it is apparent that most of the models underpredict the sum of the temperature components by a large factor. The model which approaches the data the most closely is the Buyevich model, which overpredicts the 50% concentrated suspension data but underpredicts the 30% and 40% concentrated suspension data.

When the predicted scalar suspension temperature profiles are compared to the sum of only the two smaller measured temperature components, the Morris and Brady model matches extremely well with the data, with the Phillips model the next closest curve. The good agreement between these measured components and the models suggests that the models contain an assumption about the particle interactions in the suspension that applies to the gradient and neutral directions, but not to the flow direction.

A different type of model that our measurements relate to is the suspension simulation. The observation of both out-of-plane collisions in video imaging of the flow and significant vertical velocity fluctuations in LDV measurements together lead us to conclude that the neutral direction plays an important role in inter-particle interactions. This conclusion invalidates the idea employed in the original Stokesian Dynamics simulations (Nott and Brady, 1994) and more recent simulations (Dratler et al., 1997; Bilodeau and Bousfield, 1998) that a monolayer is equivalent to an interior plane in a one-dimensional or two-dimensional flow. Our data indicate that three-dimensional simulations with all the real degrees of freedom are needed to recreate the experimental environment.

A final set of conclusions relate to our attempts to incorporate an anisotropic suspension temperature tensor **T** into the suspension models. First, we established the most general form that the tensor **T** could have and confirmed that, for a positive definite tensor **T**, the observed suspension temperature components were nearly identical to the principal components of the tensor.

In addition, because we found that the tangential and radial diagonal components of suspension temperature tensor **T** are not equal, we concluded that Buyevich's assertion that **T** is only a function of the rate of strain tensor is not possible. Another tensor that **T** could depend on is the suspension microstructure, specifically, the average pair orientation tensor, defined as $\langle \underline{u}\, \underline{u} \rangle$ by Phan-Thien (1995), where $\underline{u}$ is the unit vector pointing along the line of centers of two particles. This tensor describes the tendency of pairs of particles to align preferentially in certain directions relative to the flow, gradient, and neutral directions.

Finally, when we incorporated the anisotropic suspension temperature tensor and the rotational dynamics of inter-particle collisions into the Nott and Brady model through the stress tensor (Jenkins and McTigue, 1990) and the fluctuation energy equation, we found that the new model cannot account for observed normal stress differences and relative sizes of the suspension temperature components. We believe that a more complicated model formulated with an anisotropic pair orientation distribution function would be much more capable of resolving these discrepancies.

The modification with the greatest apparent impact on the suspension temperature models is a change in the choice of transport coefficients that are functions of ϕ, the particle volume fraction . No single existing model has all the right functions so that its predictions match well with all the data. Also, it appears that functions chosen for one flow geometry may not be able to be generalized to other flow geometries.

For example, pressure-driven channel flow and Couette flow have quite similar kinematics, since they are both unidirectional shear flows. This similarity suggests that the suspension temperature models should be able to capture the behavior of both of these flows with the same transport coefficients. However, this was not true of the models we examined. For example, the functions of the Nott and Brady model were originally optimized to fit pressure-driven channel flow data. The resulting predicted suspension temperature profile here does not match the observed sum of the temperature components (or the sum of the minor components) as well as the other models' profiles. In addition, the Morris and Brady model, which also contains functions optimized for channel flow, predicts a suspension temperature profile which matches the observed sum of the minor temperature components very well, but predicts more inaccurate shear rate and concentration profiles than three of the other models. The fact that these temperature models are not able to capture the behavior of both the Couette and channel flows by using the same transport coefficients implies that the structure of the models in incorrect.

The original promise of suspension temperature models was the potential they had to be more general than the phenomenological shear rate models. This generality would be a great advantage in the study of complex flows with elongation as well as shearing present. According to our results, the models require at least experimental measurements of the transport coefficient functions as phenomenological inputs. This challenges the models' claim of greater generality than the phenomenological shear rate models. More likely, the suspension temperature models are missing some important physics of inter-particle interactions that is related to the anisotropic suspension temperature. In order to characterize these interactions by evaluating the transport coefficient functions and validating or refuting different suspension models, it is necessary to pursue further detailed measurements similar to the ones described in this study.

References

Abbott, J. R., N. Tetlow, A. L. Graham, S. A. Altobelli, E. Fukushima, L.A. Mondy and T. S. Stephens, "Experimental observations of particle migration in concentrated suspensions : Couette flow," J. Rheol. **35**, 773-797 (1991).

Abbott, J. R., L. A. Mondy, A. L. Graham and H. Brenner, "Techniques for analyzing the behavior of concentrated suspensions," in *Particulate Two-Phase Flow*, ed. M. C. Roco (Butterworth-Heinemann, Boston, 1993), pp. 3-30.

Abramowitz, M., and I. A. Stegun, ed., *Handbook of Mathematical Functions* (Dover, New York, 1965).

Acrivos, A., "The rheology of concentrated suspensions of non-colloidal particles," in *Particulate Two-Phase Flow*, ed. M. C. Roco (Butterworth-Heinemann, Boston, 1993), pp. 169-187.

Adrian, R. J., "Laser velocimetry," in *Fluid Mechanics Measurements*, ed. R. J. Goldstein (Taylor & Francis, 1996), pp.175-293.

Altobelli, S. A., R. C. Givler and E. Fukushima, "Velocity and concentration measurements of suspensions by nuclear magnetic resonance imaging," J. Rheol. **35**, 721-734 (1991).

Altobelli, S. A., E. Fukushima and L. A. Mondy, "Nuclear magnetic resonance imaging of particle migration in suspensions undergoing extrusion," J. Rheol. **41**, 1105-1115 (1997).

Aral, B. K. and D. M. Kalyon, "Effects of temperature and surface roughness on time-dependent development of wall slip in steady torsional flow of concentrated suspensions," J. Rheol. **38**, 957-972 (1994).

Aris, R., *Vectors, Tensors, and the Basic Equations of Fluid Mechanics* (Dover, New York, 1962).

Arola, D. F., R. L. Powell, G. A. Barrall and M. J. McCarthy, "Pointwise observations for rheological characterization using nuclear magnetic resonance imaging," J. Rheol. **43**, 9-30 (1999).

Arp, P. A. and S. G. Mason, "The kinetics of flowing dispersions: doublets of rigid spheres (theoretical)," J. Colloid Interface Sci. **61**, 21-43 (1977).

Arp, P. A. and S. G. Mason, "The kinetics of flowing dispersions: doublets of rigid spheres (experimental)," J. Colloid Interface Sci. **61**, 44-61 (1977b).

Averbakh, A., A. Shauly, A. Nir, and R. Semiat, "Slow viscous flows of highly concentrated supensions - Part I: Laser Doppler velocimetry in rectangular ducts, Intl. J. Multiphase Flow 23,409-424 (1997).

Batchelor, G. K., "The stress in a suspension of force-free particles," J. Fluid Mech. **41**, 545-570 (1970).

Bagnold, R. A., "Experiments on a gravity-free dispersion of large solid spheres in a Newtonian fluid under shear," Proc. R. Soc. London, Ser. A **225**, 49-63 (1954).

Bekefi, G. and A. H. Barrett, "Electromagnetic waves and radiation," Massachusetts Institute of Technology, Department of Physics (course notes) (1976).

Bilodeau, R. R. and D. W. Bousfield, "Shear-thinning predictions from particle motion modeling," J. Rheol. **42**, 743-764 (1998).

Bird, R. B., R. C. Armstrong and O. Hassager, *Dynamics of Polymeric Liquids.* (Wiley, New York, 1987) Vols. 1, 2.

Bobroff, S. and R. J. Phillips, "Nuclear magnetic resonance imaging investigation of sedimentation of concentrated suspensions in non-Newtonian fluids," J. Rheol. **42**, 1419-1436 (1998).

Brady, J. F. and G. Bossis, "Stokesian Dynamics," Ann. Rev. Fluid Mech. **20**, 111-157 (1988).

Brenner, H., "Rheology of a dilute suspension of axisymmetric Brownian particles," Int. J. Multiphase Flow **1**, 195-341 (1974).

Burst Spectrum Analyzer User's Guide, Dantec Corporation, Mahwah, New Jersey, 1993.

Buyevich, Y. A., "Particle distribution in suspension shear flow," Chem. Eng. Sci., **51**, 635-647 (1996).

Cargille Specialty Optical Liquids Catalog, R. P. Cargille Laboratories, Inc., Cedar Grove, New Jersey, 1994.

Chapman, S. and T. G. Cowling, *The Mathematical Theory of Non-Uniform Gases* (Cambridge University Press, Cambridge, England, 1970).

Chow, A. W., S. W. Sinton, J. H. Iwamiya, and T. S. Stephens, "Shear-induced particle migration in Couette and parallel-plate viscometers : NMR imaging and stress measurements," Phys. Fluids **6** (8), 2561-2576 (1994).

Corbett, A. M., R. J. Phillips, R. J. Kauten and K. L. McCarthy, "Magnetic resonance imaging of concentration and velocity profiles of pure fluids and solid suspensions in rotating geometries," J. Rheol. **39**, 907-924 (1995).

Drain, L. E.,*The Laser Doppler Technique*. (Wiley, New York, 1980).

Dratler, D. I., W. R. Schowalter, and R. L. Hoffman, "Dynamic simulation of shear thickening in concentrated colloidal suspensions," J. Fluid Mech. **353**, 1-30 (1997).

Durst, F., A. Melling and J. H. Whitelaw, *Principles and Practice of Laser-Doppler Anemometry* (Academic Press, New York, 1981).

Eckstein, E. C., D. G. Bailey and A. H. Shapiro, "Self-diffusion of particles in shear flow of a suspension," J. Fluid Mech. **79**, 191 (1977).

Einstein, A. (1906) "For a theory of Brownian motion," Ann. Phys. **19**, 289.

Ennis, B. J., J. Green, and R. Davies, "Particle technology: The legacy of neglect in the U.S.," Chem. Eng. Progress **April,** 32-43 (1994).

Fingerson, L. M., R. J. Adrian, R. K. Menon, S. L. Kaufman and A. A. Naqwi, "Data analysis, laser Doppler velocimetry and particle image velocimetry," *TSI Short Course Text,* 1993.

Frankel, N. A. and A. Acrivos, "On the viscosity of a concentrated suspension of solid spheres," Chem. Eng. Sci. **22**, 847-853 (1967).

Gadala-Maria, F., "The rheology of concentrated suspensions," Ph.D. Thesis, Stanford University, 1979.

Gadala-Maria, F. and A. Acrivos, "Shear induced structure in a concentrated suspension of solid spheres," J. Rheol. **24**, 799 (1980).

Genieser, L. H., "Stress- and velocity-field evolution in viscoelastic planar contraction flow," Ph.D. Thesis, Massachusetts Institute of Technology, 1997.

Gondret, P., L. Petit and G. Bossis, "Static and dynamic viscosity of macroscopic suspensions of solid spheres," Proc. XIIth Int. Congr. on Rheology, 554-555 (Quebec City, Canada, August 1996).

Gradshteyn, I. S., and I. M. Ryzhik, *Table of Integrals, Series, and Products* (Academic Press, New York, 1965).

Graham, A. L., S. A. Altobelli, E. Fukushima, L. A. Mondy and T. S. Stephens, "NMR imaging of shear-induced diffusion and structure in concentrated suspensions undergoing Couette flow," J. Rheol. **35** (1), 191-201 (1991).

Haan, J. J. and P. S. Steif, "Particle-phase pressure in a slow shearing flow based on the numerical simulation of a planar suspension of rough contacting cylinders," J. Rheol. **42**, 891-916 (1998).

Haff, P. K., "Grain flow as a fluid-mechanical phenomenon," J. Fluid Mech. **134**, 401-430 (1983).

Hampton, R. E., A. A. Mammoli, A. L. Graham et al., "Migration of particles undergoing pressure-driven flow in a circular conduit," J. Rheol. **41**, 621-640 (1997).

Hirschfelder, J. O., C. F. Curtiss and R. B. Bird, *Molecular Theory of Gases and Liquids* (Wiley, New York, 1954).

Iwamiya, J. H., A. W. Chow and S. W. Sinton, "NMR flow imaging of Newtonian liquids and a concentrated suspension through an axisymmetric sudden contraction," Rheol. Acta **33**, 267-282 (1994).

Jana, S. C., B. Kapoor and A. Acrivos, "Apparent wall slip velocity coefficients in concentrated suspensions of noncolloidal particles," J. Rheol. **39**, 1123-1132 (1995).

Jeffrey, D. J. and Y. Onishi, "The force and couples acting on two nearly touching spheres in low-Reynolds-number flow," Z. agnew. Math. Phys. **35**, 634-641 (1984 a).

Jeffrey, D. J. and Y. Onishi, "Calculation of the resistance and mobility functions for two unequal rigid spheres in low-Reynolds-number flow," J. Fluid Mech. **139**, 261-290 (1984 b).

Jenkins, J. T. and D. F. McTigue, "Transport processes in concentrated suspensions : the role of particle fluctuations," In *Two Phase Flows and Waves* , ed. D. D. Joseph and D.G. Schaeffer, (Springer-Verlag, New York, 1990) pp.70-79.

Jenkins, J. T. and D. F. McTigue, "Viscous flucutations and the rheology of concentrated suspensions," submitted to J. Fluid Mech. (1990).

Jenkins, J. T. and S. B. Savage, "A theory for the rapid flow of identical, smooth, nearly elastic, spherical particles," J. Fluid Mech. **130**, 187-202 (1983).

Kapoor, B. and A. Acrivos, "Sedimentation and sediment flow in settling tanks with inclined walls," J. Fluid Mech. **290**, 39-66 (1995).

Karnis, A., H. L. Goldsmith and S. G. Mason, "The kinetics of flowing dispersions, 1. Concentrated suspensions of rigid particles," J. Colloid Interface Sci. **22**, 531-553 (1966).

Knowlton, T. M., J. W. Carson, G. E. Klinzing and W. Yang, "Particle Technology: The importance of storage, transfer, and collection," Chem. Eng. Progress **April**, 44-54 (1994).

Kodak High Speed Camera Catalog, Eastman Kodak Company, Motion Analysis Systems Division, San Diego, California, 1996.

Koh, C. J., "Experimental and theoretical studies on two-phase flows," Ph.D. Thesis, California Institute of Technology, 1991.

Koh, C. J., P. Hookham and L. G. Leal, "An experimental investigation of concentrated suspension flows in a rectangular channel," J. Fluid Mech. **266**, 1-32 (1994).

Krieger, I. M., "Rheology of monodisperse latices," Adv. Colloid Interface Sci. **3**, 111-136 (1972).

Krishnan, G. P., "Structure and migration in concentrated suspensions of non-colloidal particles," Ph.D. Thesis, University of Notre Dame, 1994.

Krishnan, G. P., S. Beimfohr and D. Leighton, "Shear-induced radial segregation in bidisperse suspensions," J. Fluid Mech., **321**, 371-393 (1996).

Kundu, P. K., *Fluid Mechanics* (Academic Press, New York, 1990).

Leighton, D. and A. Acrivos, "Viscous resuspension," Chem. Eng. Sci. **41**, 1377-1384 (1986).

Leighton, D. and A. Acrivos, "Measurement of self-diffusion in concentrated suspensions of spheres," J. Fluid Mech. **177**, 109 (1987a).

Leighton, D. and A. Acrivos, "The shear-induced migration of particles in concentrated suspensions," J. Fluid Mech. **181**, 415-439 (1987b).

Leighton, D. and I. Rampall, "Measurement of the shear-induced microstructure of concentrated suspensions of non-colloidal spheres," in *Particulate Two-Phase Flow*, ed. M. C. Roco (Butterworth-Heinemann, Boston, 1993), pp. 190-208.

Liu, A. W., "Viscoelastic flow of polymer solutions around arrays of cylinders: comparison of experiment and theory," Ph.D. Thesis, Massachusetts Institute of Technology, 1997.

Lyon, M. K., "Experimental studies of noncolloidal suspensions undergoing two-dimensional flow," Ph. D. Thesis, University of California, Santa Barbara, 1997.

Lyon, M. K. and L. G. Leal, "An experimental study of the motion of concentrated suspensioons in two-dimensional channel flow. Part 1. Monodisperse systems," J. Fluid Mech. **363**, 25-56 (1998).

Lyon, M. K. and L. G. Leal, "An experimental study of the motion of concentrated suspensioons in two-dimensional channel flow. Part 2. Bidisperse systems," J. Fluid Mech. **363**, 57-77 (1998 b).

Madanshetty, S. I., A. Nadim and H. A. Stone, "Experimental measurement of shear-induced diffusion in suspensions using long-time data," Phys. Fluids **8**, 2011-2018 (1996).

McTigue, D. F.and J. T. Jenkins, "Channel flow of a concentrated suspension," In *Advances in Micromechanics of Granular Materials* , ed. H. H. Shen et al., (Elsevier Science Publishers B. V., 1992) pp.381-390.

Melrose, J. R., and R. C. Ball, "The pathological behavior of sheared hard-spheres with hydrodynamic interactions," Europhys. Lett. **32**, 535-540 (1995).

Morris, J. F., and J. F. Brady, "Self-diffusion in sheared suspensions," J. Fluid Mech. **312**, 223-252 (1996).

Morris J. F., and J. F. Brady, "Pressure-driven flow of a suspension: buoyancy effects, Intl. J. Multiphase Flow **24**, 105-130 (1998).

Nicolai, H., B. Herzhaft, E. J. Hinch, L. Oger and E. Guazzelli, "Particle velocity fluctuations and hydrodynamic self-diffusion of sedimenting non-Brownian spheres," Phys. Fluids **7**, 12-23 (1995).

Nott, P. R., and J. F. Brady, "Pressure-driven flow of suspensions: simulations and theory," J. Fluid Mech. **275**, 157-199 (1994).

Ogawa, S., "Multitemperature theory of granular materials," In *Proc. U.S.-Japan Symp. on Continuum Mechanics and Statistical Approaches in the Mechanics of Granular Materials.*, ed. S. C. Cowin and M. Satake, (Gakujutsu Bunken Fukyu-kai, Tokyo, 1978) pp. 208-217.

Okagawa, A., R. G. Cox and S. G. Mason, "The kinetics of flowing dispersions: transient orientation and rheological phenomena of rods and discs in shear flow," J. Colloid Interface Sci. **45**, 303-329 (1973).

Phan, S. E. and D. T. Leighton, "Measurement of the shear-induced tracer diffusivity in concentrated suspensions," submitted to J. Fluid Mech. (1993).

Phan-Thien, N., "Constitutive equation for concentrated suspensions in Newtonian liquids," J. Rheol. **39**, 679-695 (1995).

Phillips, R. J., R. C. Armstrong, R. A. Brown, A. L. Graham and J. R. Abbott, "A constitutive model for concentrated suspensions that accounts for shear-induced particle migration," Phys. Fluids A **4**, 30-40 (1992).

Phung, T. N., J. F. Brady, and G. Bossis, "Stokesian Dynamics simulation of Brownian suspensions," J. Fluid Mech. **313**, 181-207 (1996).

Powell, R. L., J. E. Maneval, J. D. Seymour, K. L. McCarthy and M. J. McCarthy, "Nuclear magnetic imaging for viscosity measurements," J. Rheol. **35**, 1465-1470, (1994).

Quinzani, L. M., "Birefringence studies of entry flows of concentrated polymer solutions," Ph.D. Thesis, Massachusetts Institute of Technology, 1991.

Rigord, P., E. Charlaix and L. Petit, "Dynamic viscosity of non Brownian suspensions in Poiseuille flow," Proc. XIIth Int. Congr. on Rheology, 460-461 (Quebec City, Canada, August 1996).

Shauly, A., A. Averbakh, A. Nir and R. Semiat, "Slow viscous flows of highly concentrated suspensions-part II: Particle migration, velocity and concentration profiles in rectangular ducts," Int. J. Multiphase Flow **23**, 613-629 (1997).

Silbert, L. E., J. R. Melrose and R. C. Ball, "The rheology and microstructure of concentrated, aggregated colloids," J. Rheol., **43**, 673-700 (1999).

Sinton, S. W., and A. W.Chow, "NMR flow imaging of fluids and solid suspensions in Poiseuille flow," J. Rheol. **35**, 735-772 (1991).

Tetlow, N., A. L. Graham, M. S. Ingber, S. R. Subia, L. A. Mondy and S. A. Altobelli, "Particle migration in a Couette apparatus: experiment and modeling," J. Rheol. **42**, 307-327 (1998).

Toivakka, M., D. Eklund and D. W. Bousfield, "Prediction of suspension viscoelasticity through particle motion modeling," J. Non-Newtonian Fluid Mech. **56**, 49-64 (1995).

Torquato, S., B. Lu and J. Rubinstein, "Nearest-neighbor distribution functions in many-body systems," Phys. Rev. A **41**, 2059-2075.

Tripathi, A., "Experimental investigations of shear-induced particle migration in concentrated suspensions undergoing shear," Ph.D. Thesis, City University of New York, (1998).

Yilmazer, U. and D. M. Kalyon, "Slip effects in capillary and parallel disk torsional flows of highly filled suspensions," J. Rheol. **33**, 1197-1212 (1989).

Yoshimura, A. and R. K. Prud'homme, "Wall slip corrections for Couette and parallel disk viscometers," J. Rheol. **32**, 53-67 (1988).

THESIS PROCESSING SLIP

FIXED FIELD: ill. ______ name ______

index ______ biblio ______

▶ **COPIES:** [✓ Archives] Aero Dewey Eng Hum

Lindgren Music Rotch [✓ Science]

TITLE VARIES: ▶☐ ______

NAME VARIES: ▶☐ ______

IMPRINT: (COPYRIGHT) ______

▶ **COLLATION:** 251 p

▶ **ADD: DEGREE:** ______ ▶ **DEPT.:** ______

SUPERVISORS: ______

NOTES:

cat'r: date:

page:

▶ F50

▶ **DEPT:** Chem. Eng

▶ **YEAR:** 2000 ▶ **DEGREE:** Ph. D.

▶ **NAME:** SHAPLEY, Nina Claire